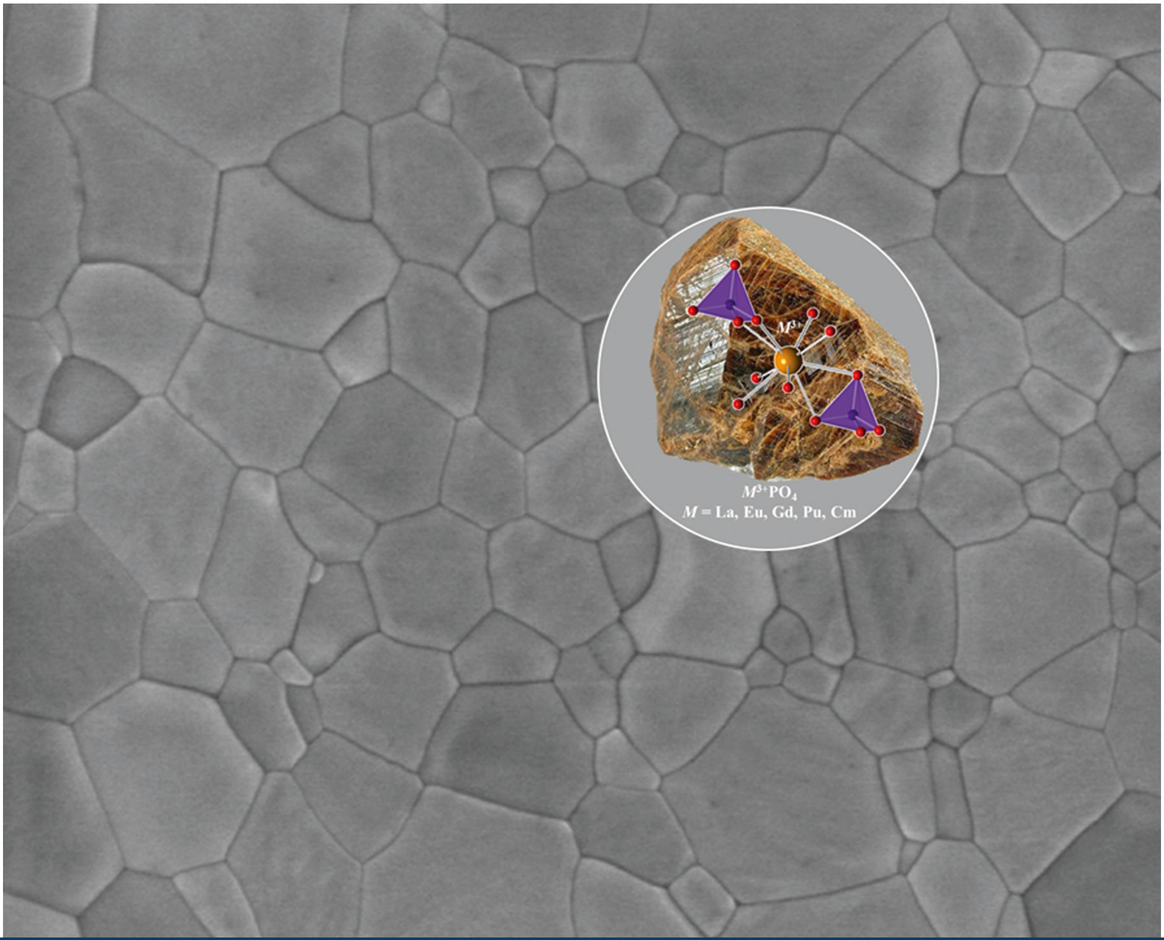

Monazite-type ceramics as nuclear waste form: crystal structure, microstructure and properties

Yulia Arinicheva

Energie & Umwelt / Energy & Environment
Band / Volume 459
ISBN 978-3-95806-397-6

Mitglied der Helmholtz-Gemeinschaft

JÜLICH
Forschungszentrum

Schriften des Forschungszentrums Jülich
Reihe Energie & Umwelt / Energy & Environment Band / Volume 459

Forschungszentrum Jülich GmbH
Institute of Energy and Climate Research
Nuclear Waste Management and Reactor Safety (IEK-6)

Monazite-type ceramics as nuclear waste form: crystal structure, microstructure and properties

Yulia Arinicheva

Schriften des Forschungszentrums Jülich
Reihe Energie & Umwelt / Energy & Environment Band / Volume 459

ISSN 1866-1793 ISBN 978-3-95806-397-6

Bibliografische Information der Deutschen Nationalbibliothek.
Die Deutsche Nationalbibliothek verzeichnet diese Publikation in der
Deutschen Nationalbibliografie; detaillierte Bibliografische Daten
sind im Internet über http://dnb.d-nb.de abrufbar.

Herausgeber und Vertrieb: Forschungszentrum Jülich GmbH
Zentralbibliothek, Verlag
52425 Jülich
Tel.: +49 2461 61-5368
Fax: +49 2461 61-6103
zb-publikation@fz-juelich.de
www.fz-juelich.de/zb

Umschlaggestaltung: Grafische Medien, Forschungszentrum Jülich GmbH

Druck: Grafische Medien, Forschungszentrum Jülich GmbH

Copyright: Forschungszentrum Jülich 2019

Schriften des Forschungszentrums Jülich
Reihe Energie & Umwelt / Energy & Environment, Band / Volume 459

D 82 (Diss., RWTH Aachen University, 2019)

ISSN 1866-1793
ISBN 978-3-95806-397-6

Vollständig frei verfügbar über das Publikationsportal des Forschungszentrums Jülich (JuSER)
unter www.fz-juelich.de/zb/openaccess.

This is an Open Access publication distributed under the terms of the Creative Commons Attribution License 4.0,
which permits unrestricted use, distribution, and reproduction in any medium, provided the original work is properly cited.

Table of Contents

Abstract

In the last decades, various single- and polyphase ceramic materials have been proposed as potential waste forms for the immobilisation of specific nuclear waste streams, such as separated plutonium from civilian or military sources unsuitable for further use, or separated minor actinides. Among them, phosphate-based materials with monazite structure emerged as promising candidates for ceramic nuclear waste forms due to their specific physico-chemical properties including high structural flexibility allowing for significant waste loadings, high chemical durability, and high resilience against radiation damage.

This work focuses on synthesis and fabrication of monazite-type ceramics for the immobilisation of Pu and minor actinides, and their properties. Key points addressed comprise the formation of monazite and rhabdophane solid solutions by structural incorporation of actinides (Cm^{3+}, Pu^{3+}) or their non-radioactive surrogates (Eu^{3+}, Gd^{3+}), studied by combined X-ray diffraction, spectroscopic and computational techniques; the comparison of various synthesis methods, leading to monazite precursors with different crystal structure and morphology; the effect of precursor morphology on the microstructural evolution of monazite-type ceramics during sintering; as well as correlations between microstructure, texture effects and mechanical properties. Besides the mechanical properties (elastic moduli, microhardness and fracture toughness), thermal properties (thermal expansion, and heat capacity) of monazite solid solutions were studied in detail. Particular attention is paid to the properties that govern the long-term stability of the waste form under conditions relevant to geological disposal. The enthalpies of formation and mixing of single phase monazite $La_{1-x}Ln_xPO_4$ (Ln = Eu and Gd) solid solution series, determined in this work using high temperature oxide melt solution calorimetry, provide key input parameters for calculation of stability and solubility of the monazite solid solutions as a function of temperature, thus contributing to the long-term stability prediction of monazite nuclear waste forms. Additionally, the dissolution kinetics of $LaPO_4$ of the monazite structure-type was systematically studied in dynamic dissolution experiments in acidic media at different temperatures to gain a deeper insight into the mechanism governing the dissolution of monazite waste forms. The potential formation of La-rhabdophane as secondary phase in the dissolution experiments was explored here in the temperature range of interest by thermodynamic modelling.

In conclusion, this work provides a perspective on the recent advancements in the understanding of the properties of monazite ceramics in respect to their application as nuclear waste forms.

Kurzzusammenfassung

In den letzten Jahrzehnten wurden verschiedene ein- und mehrphasige keramische Materialien als potentielle Abfallformen für die Immobilisierung spezifischer Kernabfallströme, wie z.B. abgetrenntes Plutonium aus zivilen oder militärischen Quellen, das für weitere Verwendungen ungeeignet ist, oder abgetrennte minore Actiniden, in Betracht gezogen. Phosphat-basierte Keramiken mit Monazit Struktur erwiesen sich als vielversprechende Kandidaten für die Anwendung als nukleare Abfallformen aufgrund ihrer spezifischen physikalisch-chemischen Eigenschaften, wie hohe strukturelle Flexibilität, die eine signifikante Abfallbeladung ermöglicht, chemische Beständigkeit und eine hohe Widerstandsfähigkeit gegen Strahlenschäden.

Im Fokus dieser Arbeit stehen die Synthese, Fabrikation und Eigenschaften von Monazit-Keramiken für die Immobilisierung von Pu und minoren Actiniden. Die adressierten Schwerpunkte beinhalten die Untersuchung der Monazit- und Rhabdophan-Mischkristallbildung durch den strukturellen Einbau der Actiniden (Cm^{3+}, Pu^{3+}) oder deren nicht-radioaktiven Surrogaten (Eu^{3+}, Ga^{3+}) mit Hilfe von kombinierten Röntgenbeugungs-, spektroskopischen und rechnerischen Techniken; den Vergleich verschiedener Syntheseverfahren, die zu Monazit-Präkursoren mit unterschiedlicher Kristallstruktur und Morphologie führen; die Auswirkung der Morphologie der Präkursorpulver auf die Mikrostrukturentwicklung von Monazit-Keramiken während des Sinterns; sowie die Untersuchung der Zusammenhänge zwischen der Mikrostruktur, den Textureffekten und den mechanischen Eigenschaften. Neben den mechanischen Eigenschaften (Elastizitätsmodul, Mikrohärte und Bruchzähigkeit) wurden thermische Eigenschaften (Wärmeausdehnung und Wärmekapazität) von Monazit-Mischkristallen im Detail untersucht. Besondere Aufmerksamkeit wurde den Eigenschaften gewidmet, die die Langzeitstabilität von Monazitkeramiken bestimmen. Die Bildungs- und Mischenthalpien von einphasigen Monazit-Mischkristallen $La_{1-x}Ln_xPO_4$ (Ln = Eu und Gd), die in dieser Arbeit mittels Hochtemperatur-Oxidschmelzlösungs-Kalorimetrie bestimmt wurden, liefern wichtige Ausgangsparameter für die Berechnung der thermodynamischen Stabilität und der Auflösungsbeständigkeit der Monazit-Mischkristalle als Funktion der Temperatur, und tragen somit zur langfristigen Stabilitätsprognose von nuklearen Abfallformen mit Monazitstruktur bei. Darüber hinaus wurde die Auflösungskinetik von $LaPO_4$ vom Monazitstrukturtyp systematisch in dynamischen Auflösungsexperimenten in sauren Medien bei verschiedenen Temperaturen untersucht, um einen tieferen Einblick in den Mechanismus zu erhalten, der die Auflösung

von Monazit-Abfallformen steuert. Die potentielle Bildung einer La-Rhabdophan-Sekundärphase in den Auflösungsexperimenten in einem endlager-relevanten Temperaturbereich wurde in dieser Arbeit mittels thermodynamischer Modellierung untersucht.

Zusammenfassend leistet diese Arbeit einen erheblichen Beitrag zum Verständnis der Eigenschaften von Monazit-Keramiken in Bezug auf deren Anwendung als nukleare Abfallform.

List of publications

An abridged version of the present work has been published in following journals / book chapter:

Y. Arinicheva, C. Gausse, S. Neumeier, F. Brandt, K. Rozov, S. Szenknect, N. Dacheux, D. Bosbach, G. Deissmann *Influence of temperature on the dissolution kinetics of synthetic $LaPO_4$-monazite in acidic media between 50 and 130°C.* J. Nucl. Mater. *509* (**2018**) 488-495. https://doi.org/10.1016/j.jnucmat.2018.07.009

Y. Arinicheva, S. Neumeier, F. Brandt, D. Bosbach, G. Deissmann *Dissolution kinetics of synthetic $LaPO_4$-monazite in acidic media.* MRS Advances *3, 21* (**2018**) 1133-1137. https://doi.org/10.1557/adv.2018.205

Y. Arinicheva, N. Clavier, S. Neumeier, R. Podor, A. Bukaemskiy, M. Klinkenberg, G. Roth, N. Dacheux, D. Bosbach *Effect of powder morphology on sintering kinetics, microstructure and mechanical properties of $La_{0.5}Eu_{0.5}PO_4$ monazite ceramics.* J. Eur. Ceram. Soc. *38, 1* (**2018**) https://doi.org/10.1016/j.jeurceramsoc.2017.08.008

N. Huittinen, A. Scheinost, Y. Ji, P. Kowalski, **Y. Arinicheva**, A. Wilden, S. Neumeier, T. Stumpf, *A spectroscopic and computational study of Cm^{3+} incorporation in lanthanide phosphate rhabdophane ($LnPO_4{\cdot}nH_2O$) and monazite ($LnPO_4$).* Inorg. Chem. *57, 11* (**2018**) 6252 – 6265. https://pubs.acs.org/doi/10.1021/acs.inorgchem.8b00095

Y. Arinicheva, K. Popa, A.C. Scheinost, A. Rossberg, O. Dieste-Blanco, P. Raison, A. Cambriani, S. Neumeier, J. Somers, D. Bosbach *Structural investigations of (La,Pu)PO_4 monazite solid solutions: XRD and XAFS study.* J. Nucl. Mater. *493* (**2017**) 404 – 411. https://doi.org/10.1016/j.jnucmat.2017.06.034

Y. Arinicheva, N. Huittinen, S. Neumeier *Eu^{3+} and Cm^{3+} time-resolved laser fluorescence spectroscopy for studies on materials relevant for nuclear waste management.* In: C. Degueldre (ed.) "The analysis of nuclear materials and their environments". Springer (**2017**). https://www.springer.com/de/book/9783319580043

S. Neumeier, **Y. Arinicheva**, Y. Ji, J.M. Heuser, P.M. Kowalski, P. Kegler, H. Schlenz, D. Bosbach, G. Deissmann, New insights into phosphate based materials for the immobilisation of actinides. Radiochim. Acta *105, 11* (**2017**) 961 – 984. https://doi.org/10.1515/ract-2017-2819

N. Huittinen, **Y. Arinicheva**, P. Kowalski, V. Vinograd, S. Neumeier, D. Bosbach *Probing structural homogeneity of* $La_{1-x}Gd_xPO_4$ *monazite-type solid solutions by combined spectroscopic and computational studies.* J. Nucl. Mater. *486* (**2017**) 148 – 157. https://doi.org/10.1016/j.jnucmat.2017.01.024

P.M. Kowalski**,** Y. Ji, Y. Li, **Y. Arinicheva**, G. Beridze, S. Neumeier, A. Bukaemskiy, D. Bosbach *Simulation of ceramic materials relevant for nuclear waste management: Case of* $La_{1-x}Eu_xPO_4$ *solid solution*. Nucl. Instrum. Meth. B. *393* (**2017**) 68 – 72. https://doi.org/10.1016/j.nimb.2016.09.029

N. Huittinen, **Y. Arinicheva**, M. Schmidt**,** S. Neumeier, Th. Stumpf *Using* Eu^{3+} *as an atomic probe to investigate the local environment in* $LaPO_4$*–*$GdPO_4$ *monazite end-members.* J. Coll. Interf. Sci. *483* (**2016**) 139 – 145. https://doi.org/10.1016/j.jcis.2016.08.027

S. Neumeier, **Y. Arinicheva**, N. Clavier, R. Podor, A. Bukaemskiy, G. Modolo, N. Dacheux, D. Bosbach *The effect of the synthesis route of monazite precursors on the microstructure of sintered pellets.* Prog. Nucl. Energ. *92* (**2016**) 298 – 305. https://doi.org/10.1016/j.pnucene.2016.07.011

B. Klobes, **Y. Arinicheva**, S. Neumeier, R.E. Simon, A. Jafari, D. Bosbach, R.P. Hermann *Quadrupole splitting and Eu partial lattice dynamics in europium orthophosphate* $EuPO_4$. Hyperfine Interact. *237* (**2016**) 31 – 37. https://doi.org/10.1007/s10751-016-1211-y

S. Neumeier, P. Kegler, **Y. Arinicheva**, A. Shelyug, P.M. Kowalski, Ch. Schreinemachers, A. Navrotsky, D. Bosbach *Thermochemistry of* $La_{1-x}Ln_xPO_4$*-monazites (Ln = Gd, Eu).* J. Chem. Thermodyn. *105* (**2016**) 396 – 403. https://doi.org/10.1016/j.jct.2016.11.003

A. Thust, **Y. Arinicheva**, E. Haussühl, J. Ruiz-Fuertes, L. Bayarjargal, S.C. Vogel, S. Neumeier, B. Winkler *Physical properties of* $La_{1-x}Eu_xPO_4, 0 \leq x \leq 1$*, monazite-type ceramics*. J. Am. Ceram. Soc. *98(12)* (**2015**) 4016 – 4021. https://doi.org/10.1111/jace.13841

Y. Arinicheva, A. Bukaemskiy, S. Neumeier, G. Modolo, D. Bosbach *Studies on thermal and mechanical properties of monazite-type ceramics for the conditioning of minor actinides*. Prog. Nucl. Energ. *72* (**2014**) 144 – 148. https://doi.org/10.1016/j.pnucene.2013.09.004

F. Brandt, S. Neumeier, T. Schuppik, **Y. Arinicheva**, A. Bukaemskiy, G. Modolo, D. Bosbach *Conditioning of minor actinides in lanthanum monazite ceramics: A surrogate study with europium*. Prog. Nucl. Energ. *72* (**2014**) 140 – 143. https://doi.org/10.1016/j.pnucene.2013.07.019

1 Introduction

Radioactive wastes, that have to be disposed of safely, arise throughout all stages of the nuclear fuel cycle as well from a variety of other sources such as industrial and medical applications of radioisotopes and research or in industries handling and processing naturally occurring radioactive materials. High-level radioactive wastes related to the nuclear fuel cycle include spent nuclear fuels from nuclear power plants (i.e. in open "once-through" fuel-cycles) and research reactors, liquid waste streams from spent fuel reprocessing, and materials separated in the course of reprocessing (e.g. separated civilian Pu or minor actinides arising from innovative partitioning concepts).

The safe and sustainable management of high-level nuclear wastes poses major scientific/technical and societal challenges, in particular to countries with large nuclear programs. In Germany the government has meanwhile decided complete renunciation of nuclear energy by 2022. The safe disposal of nuclear waste accumulated from nuclear plants operation and dismantling reactors in Germany has to be managed [1].

Several strategies for management and disposal of radioactive waste in deep geologic formations have evolved over the course of nuclear power development. A growing number of countries including Germany are pursuing policy of an open or once-through fuel cycle [2]. This policy involves the direct disposal of spent nuclear fuel (SNF) due to nuclear non-proliferation and economic considerations. In the closed cycle SNF is reprocessed and partially reused. In the established SNF reprocessing technology the spent nuclear fuel pellets are removed from the cladding and dissolved in nitric acid; uranium and plutonium are selectively extracted from the solution in the PUREX process to be recycled as fresh fuel, the fission/activation products including minor actinides are conditioned by vitrification. Immobilisation of radionuclides in a durable waste form as one of the engineered barriers in the deep geological repository is called Conditioning [2]. There are two innovative complementary strategies for the closed cycle: Partitioning and Conditioning and Partitioning and Transmutation. In the innovative Partitioning process the PUREX process is followed by the coextraction with the subsequent separation of minor actinides and lanthanides (e.g. in DIAMEX and SANEX processes, respectively). Recycling of actinides by neutron bombardment in a nuclear reactor or accelerator-driven device (Transmutation) enables efficient and sustainable management of resources and reduces the volume and radio-toxicity of the waste for the following geological disposal.

The safe disposal of radioactive wastes requires the long-term isolation of the waste from the biosphere to protect humans and the environment against dangers arising from ionizing radiation, until radioactive decay has reduced the radioactivity to acceptable levels. At the international level experts came to the consensus that disposal in deep underground engineered facilities — geological disposal — provides the best solution for the management of high level waste allowing long-term safety for periods of millions years without surveillance and maintenance [3]. In a geological disposal facility, the long-term isolation and containment of the radioactive wastes is achieved by a defence-in-depth multi-barrier system, combining various engineered barriers, i.e. durable waste forms and waste containers, buffer and backfill materials, and tunnel/shaft seals, with a suitable repository host rock providing the geological barrier. An in-depth understanding of the often highly coupled processes, that govern the long-term evolution of the repository system and its components, the (slow) release of radionuclides from the wastes, and the radionuclide migration in the repository near- and far-field on a molecular level, is a prerequisite to demonstrate the long-term safety of the disposal facility for the required timescales of up to one million years [4].

Nuclear waste forms for the conditioning of specific radioactive waste streams or separated radionuclides have to comply with a variety of requirements such as a high long-term durability and leaching resistance besides a sufficiently high waste loading. Depending on the nature of the waste streams that have to be immobilised, waste forms have to offer a certain chemical flexibility to accommodate a wide range of radionuclides and to retain also daughter nuclides in the decay chains. The generation of heat due to the decay of radionuclides and self-heating by release of stored Wigner-energy (resulting from structural changes inflicted by radiation damage) requires an appropriate thermal stability and thermal conductivity of the waste form. Moreover, a waste form has to exhibit a high tolerance against damages arising from self-irradiation from the incorporated radionuclides, such as amorphisation of a (crystalline) waste matrix, which may be accompanied by an enhanced leachability of the waste form. In addition, a sufficient resistance against adverse effects induced, for example, by the build-up of helium from alpha decay and associated pressure build-up and mechanical disruption of the matrix is essential. Further important issues comprise the homogenous distribution of fissile radionuclides in the matrix and criticality control, i.e. the potential for incorporation of neutron absorbers into the waste form. The waste form should be recalcitrant against recovery of radioactive constituents, especially fissile materials such as ^{239}Pu or ^{235}U, to reduce proliferation risks. Moreover, a reliable, safe and mature fabrication technology is required. In this context, low processing temperatures are advantageous to avoid losses of relatively volatile radionuclides into the off-gas. Key issue with respect to the post-closure safety is the dissolution behaviour and leaching resistance of the waste form under the environmental conditions encountered in the disposal facility in the long-term, and the radionuclide release rates, which constitute the source term for the subsequent radionuclide migration in the near- and far-field of the disposal site. In general, each waste form offers distinctive strengths and weaknesses and no immobilisation matrix can satisfy all of the requirements.

Historically, in the 1980's ceramics and borosilicate glasses were discussed competitively for the immobilisation of HLW. In the US in 1981 a decision was made to use borosilicate glasses as preferred waste matrix for the immobilisation of HLW at Savannah River Laboratory [5, 6] mainly because of the chemical flexibility and existing fabrication technology of glasses. Worldwide borosilicate glass is established as waste form for spent nuclear fuel reprocessing and under investigation for IL waste streams. Thus vitrification became the best-demonstrated available technology for solidification of highly radioactive liquors after the reprocessing of spent fuel for the subsequent isolation in a deep geological formation [7].

However, ceramic waste forms can be tailor-made for the immobilisation of specific radioactive waste streams consisting of single elements or element groups with similar chemical properties. Due to the fact that specific waste streams already exist (e.g. I, collected in filters of the exhaust from reprocessing processes, and weapon-grade Pu) or can be generated in selective waste separation processes by liquid-liquid extraction, ceramic waste forms are of particular interest. Moreover, application of advanced industrial scale sintering techniques, such as hot isostatic pressing, offered opportunities to immobilise several HLW's and ILW's, discerned to be unsuitable for vitrification, e.g. Tc- and I-rich waste streams [8, 9], in ceramic waste forms.

Thus in the last decades, various single- and polyphase ceramic materials have been examined as potential nuclear waste forms for the immobilisation of specific nuclear waste streams, such as separated Pu from civilian or military sources unsuitable for further use, or separated minor actinides (MA = Am, Cm, Np) from HLW concentrate [10, 11]. In addition to oxide based ceramics (e.g. polyphase Synroc materials or single-phase zirconolite, perovskite, and pyrochlore ceramics), special attention has been paid to silicates like zircon ($ZrSiO_4$) and/or thorite ($ThSiO_4$) and phosphates, such as monazite, beside various other phases [12-15].

Complementary to the development of ceramic waste forms for actinides, specific ceramic matrices for the immobilisation of long-lived fission products such as ^{135}Cs [16, 17], ^{99}Tc [16, 18] or ^{129}I (u. a. [19, 20]) based inter alia on the structures of hollandite, perovskite and apatite have been developed and investigated in recent years.

For many years, phosphate-based ceramic materials and particularly monazites (LnPO$_4$) were subjected to extensive studies regarding their suitability as nuclear waste forms, due to their specific physico-chemical properties [21, 22] including high structural flexibility allowing for significant waste loadings [23], high chemical durability [24, 25] and high resilience against radiation damage [26-28].

This work is dedicated to the investigation of synthesis, fabrication and properties of monazite-type ceramics. The emphasis is placed especially on the formation of solid solutions by structural incorporation of actinides or their non-radioactive surrogates and properties that govern the long-term stability of the waste form under conditions relevant to geological disposal such as thermodynamic stability and aqueous durability.

2 Scientific and theoretical background

2.1 Monazite-type ceramics for conditioning of actinides

The strategies for the safe management and disposal of radioactive waste in deep geologic formations include immobilisation of radionuclides in a durable waste form as one of the engineered barriers. In the last decades monazite-type orthophosphates have been subject to extensive investigations as they fulfil most of the selection criteria for suitable ceramic waste forms such as high achievable waste loading, high chemical and thermal durability, sufficient chemical flexibility and high radiation resistance [10, 15, 21, 22, 25, 29-31].

From a geological point of view, monazite is known to be a metamorphic mineral, i.e. which is formed from the alteration of other phases (such as apatites or pelitic rocks) by hydrothermal fluids [32, 33]. Monazite is the most abundant lanthanide phosphate mineral [30, 34]. It appears in granites, gneisses and pegmatites [30] as well as in alluvial deposits and beach sands.

Monazite ceramics are being considered to be promising materials for various technological applications as thermal barrier coatings for gas-turbine engines [35], proton conductors [36, 37], heterogeneous catalysts [38], highly efficient light traps/photon convertors for solar cells [39], negative contrast agent for magnetic resonance imaging [40] as well as nuclear waste form [15, 21, 22, 26].

The outstanding properties of this material have been demonstrated by the natural analogues being exposed to geological events for several hundred millions of years. Natural monazite minerals can contain up to 27 wt% natural radioelements, such as tetravalent Th and U and trivalent ^{228}Ac as a daughter product from the ^{232}Th series, for several hundred millions of years without suffering from amorphisation due to radiation damages [30, 34] and significant weathering due to chemical alteration [41].

The lighter and larger lanthanide orthophosphates (LnPO$_4$, Ln = La – Gd), crystallize in the monoclinic monazite structure with space group P21/n. The monazite crystal structure, depicted in **Figure 1**, is represented by LnO$_9$-polyhedra (Ln = La – Gd) interpenetrated by phosphate tetrahedra building edge-connected chains along the c-axis [23, 42]. In contrast, the heavier and smaller lanthanides (Ln = Tb – Lu) adopt the zircon-type tetragonal structure of xenotime with the space group I41/amd [23, 42]. The limits between the monazite and xenotime structure for the lanthanides located in the middle of series is not strictly defined and seems to be strongly dependent on the synthesis procedures. The actinides (Am, Cm, Pu) considered for immobilisation exhibit ionic radii comparable to the lighter lanthanides and are known to form phosphates with a monazite structure [43]. Therefore, monazite is the preferred crystal structure for trivalent actinides such as Am^{3+}, Cm^{3+} and Pu^{3+} to be incorporated in a phosphate host matrix.

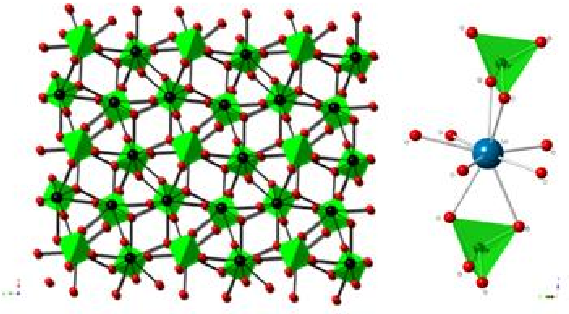

Figure 1. Representation of the monazite structure. (Green: phosphate anionic site; blue spheres: Ln^{3+} cationic site; red spheres: oxygen ions).

The incorporation of trivalent actinides on lattice sites of the monazite structure allows high loading rates and offers certain advantages over other waste forms (incl. borosilicate glasses and spent fuel) in terms of long-term stability including chemical durability and irradiation resistance [10, 21, 22, 31]. Monazites are also attractive in terms of criticality issues. For the immobilisation of fissile ^{239}Pu, stable isotopes of Gd, possessing extremely large neutron-cross-sections ($\sigma(^{157}Gd)$ = 254,000 barn), can be incorporated in a tailored $LnPO_4$ host-crystal system.

Besides radiation tolerance the outstanding chemical resistance of natural monazites demonstrates the long-term stability of these materials. For instance, recent studies on natural monazites which have been exposed to weathering since several hundred millions of years show significant modifications due to mechanical abrasion but not due to chemical alteration [41]. Synthetic monazites have been investigated extensively in recent decades with a focus on their structure, dissolution behaviour and response to ionising radiation [23, 42, 44-47]. Chemical durability is one of the most important properties for the long-term stability of a ceramic waste form since immobilized radionuclides may be dissolved out of the waste matrix and migrate into the geo- and biosphere if the waste matrix comes into contact with groundwater. Migration can occur in the aqueous phase or for strongly sorbing radionuclides associated on mobile solid colloids or nanoparticles [48, 49]. The dissolution behaviour of ceramic materials depends on several parameters, such as composition, homogeneity, crystallinity, and microstructure of the waste matrix, the pH, temperature, ionic strength as well as the composition of the aqueous environment [50-52]. As instance, recent results from geochemical modelling calculations indicate that trace components such as fluorine may affect the aqueous *Ln*-speciation scheme and *Ln*-solubility distinctively [15].

However, to date, the highly complex relationships between structure and stability with regard to the long-term behaviour of ceramic waste forms under conditions relevant to end-storage have not been described in detail.

2.2 Rhabdophane compounds

Lanthanide phosphates with rhabdophane structure ($LnPO_4\cdot xH_2O$, Ln = La to Gd, x = 0, 0.5, 0.667) play an important role for the consideration of monazite-type ceramics for nuclear waste management applications. As rhabdophane is formed in aqueous environments at low temperature it appears as the precursor material for the fabrication of monazite waste matrices derived from wet chemistry methods. The rhabdophane phases can potentially also be neo-formed by dissolution of monazite in aqueous media, such as groundwater in a repository, and thus control the radionuclide release from monazite-type waste matrices due to dissolution [53]. Rhabdophane nano-wires and nano-rods draw also a particular technological interest as precursors for the preparation of quasi-one-dimensional monazite nanomaterials with unique electronic, optical and catalytic properties associated with the reduced dimensionality [54, 55], as well as of textured monazite ceramics with optimized thermal and mechanical properties [56-58].

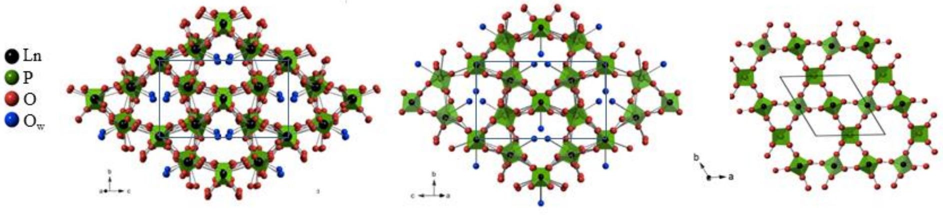

$LnPO_4\cdot 0.667H_2O$ $LnPO_4\cdot 0.5H_2O$ $LnPO_4$

Figure 2. Representation (from the left to the right) of the hydrated, hemihydrated and anhydrous rhabdophane structures. Green: phosphate anionic site; black spheres: Ln^{3+} cationic site; red spheres: oxygen ions. Figure modified from [59, 60].

Rhabdophane compounds were considered to crystallize in the hexagonal lattice with an eight-fold coordination of lanthanide cations by oxygen atoms [61]. According to a recent re-examination of the rhabdophane crystal structure by high resolution synchrotron X-ray diffraction [59, 60] there are three distinct rhabdophane structures with different hydration states depending on the synthesis conditions: monoclinic hydrated $LnPO_4\cdot 0.667H_2O$, monoclinic hemihydrated $LnPO_4\cdot 0.5H_2O$, and hexagonal anhydrous $LnPO_4$ rhabdophane phases (**Figure 2**). The crystal structure of the anhydrous rhabdophane compounds represents interconnected chains of interpenetrated polyhedra, consisting of lanthanide cations eight-fold coordinated by oxygen atoms, and phosphate tetrahedra, forming hexagonal channels. In the hydrated rhabdophane phases a distortion of the hexagonal channels due to the accommodation of water molecules leads to the low-symmetry monoclinic structures with mixed eight- and nine-fold coordination of the lanthanide cations by oxygen atoms (**Figure 3**). In an eight-fold coordinated site all the oxygen atoms are provided by phosphate groups, whereas in the nine-fold coordinated site one additional coordinating oxygen atom originates from a water molecule.

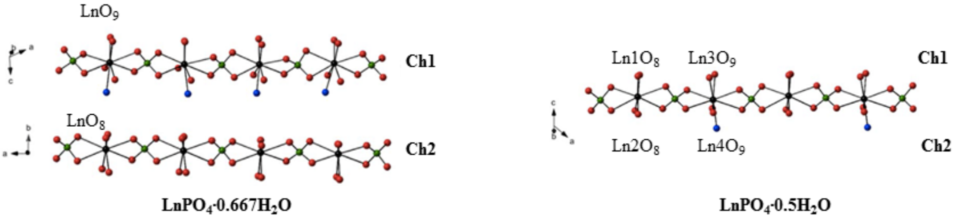

Figure 3. Representaion of the interconnected chains consisting of interpenetrated lantanide-oxygen polyhedra and phosphate tetrahedra in the compounds $\mathit{Ln}PO_4\cdot0.667H_2O$ (left) and $\mathit{Ln}PO_4\cdot0.5H_2O$ (right). Figure modified from [60].

The interrelation between rhabdophane- and monazite-type phases is schematically represented in **Figure 4**. A reversible two-step dehydration of the low-temperature hydrated rhabdophane phases between RT and approximately 523 K as well as an irreversible phase transition from anhydrous rhabdophane to monazite between 773 K and 1173 K occur during thermal treatment [62]. The temperature of these processes strongly depends on the chemical composition. Additionally rhabdophane can form from monazite in aqueous environments at low temperature (363 K (La) $< T_{lim} <$ 433 K (Nd-Gd)) [53]. Since these conditions can be expected in a deep geological repository in the long-term, the rhabdophane-type phase can occur as a potential neo-formed phase on the surface of monazite waste forms in contact with groundwater in a repository (i.e. after failure of the waste canister). Hence, the rhabdophane phase is of particular interest concerning the application of monazite waste forms as it might control the radionuclide release from monazite-type ceramics due to dissolution [53].

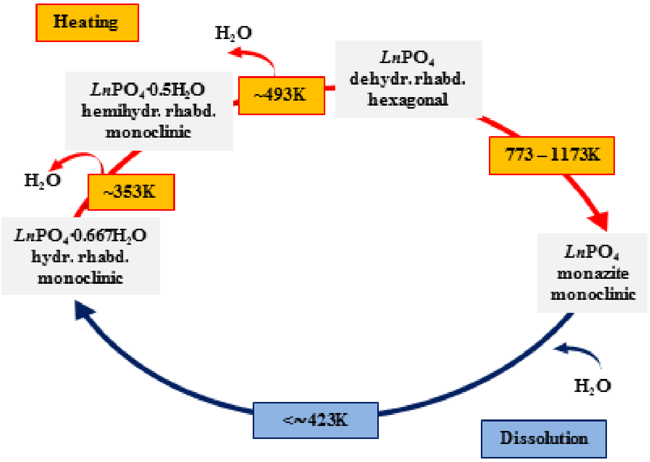

Figure 4. Schematic description of stability and interrelation of monazite- and rhabdophane-type lanthanide orthophosphates (modified after [63]).

The formation of rhabdophane and the phase transition to monazite is well described in the literature for several pure lanthanide phosphates [53, 64-66] as well as for solid solutions [67-69]. However, information about phase transition of *An* phosphates is rare so far. Rai et al. [70] discussed the solubility of $AmPO_4 \cdot xH_2O$ and a phase transition at higher temperatures. Keller and Walter [71] reported about a monoclinic phase after thermal treatment at >473 K. From the work of Mesbah et al. [59, 60] it can be concluded that the dehydrated rhabdophane was observed. Finally, only Björklund [72] published a measurement of a phase transition of Pu-rhabdophane to monazite after thermal treatment at 1223 K.

The short-range order investigations of rhabdophane structure are limited to the Raman-data on the rhabdophane endmembers considering hexagonal symmetry. Thermodynamic data of $LnPO_4 \cdot 0.667H_2O$-rhabdophane endmembers, derived from solubility experiments, have been reported in the work [65]. Thermodynamic data for anhydrous rhabdophanes and hydrated rhabdophane solid solutions is absent in the literature. Moreover the actual population of the lattice sites by actinide dopants within the crystal structure of rhabdophane compounds with different hydration states is currently not understood. Thus, for a sound understanding of the long-term performance of monazites as immobilisation matrices for especially trivalent actinides (Am^{3+}, Cm^{3+}, Pu^{3+}), knowledge of the fate of actinides within the solid monazite ceramic should be complemented with a detailed understanding of their uptake within rhabdophane-type secondary phases.

2.3 Synthesis and fabrication of monazite ceramics

The long-term stability of phosphate ceramic waste forms under conditions relevant to end-storage is determined by a complex interrelation between its crystal structure, microstructure and properties. Synthesis and fabrication methods influence the phase purity and homogeneity of phosphate solid solutions as well as their microstructure. As microstructure significantly impacts physico-chemical properties of ceramic materials such as thermal conductivity [56, 73], resistance to aqueous corrosion [50, 74-76] and mechanical strength [73], it is important to control the microstructure development, in order to meet the particular technological requirements linked with the various applications of monazite-type lanthanide phosphates.

The morphology of the starting powders used for sintering have a significant influence on the final pellets microstructure [68]. Powder morphology can be tuned thanks to the numerous methods reported in the literature for the synthesis of monazite ceramics including solid state chemistry [77, 78], solid-liquid reaction [79] and wet chemical synthesis [62, 69, 80-83]. Among them, wet chemistry routes exhibit several advantages, such as homogeneity of cations' distribution by synthesis of solid solutions, low synthesis temperatures and avoidance of dust formation [84, 85]. Also, a variety of precursor morphologies can be achieved by applying different reaction conditions, such as needle-like [81], spherical [81], rice-shaped [83] or dandelion-like particles [86].

Sintering of monazite-type lanthanide phosphates is often addressed in the literature towards the production of highly densified pellets. The optimum sintering temperature for $Ln\mathrm{PO}_4$ monazites was usually reported to range between 1623 and 1773 K [80, 87-89], and led to densities up to 98% of the theoretical density. Nevertheless, sintering of $Ln\mathrm{PO}_4$ ceramics also appeared to be limited by phosphate decomposition at high temperatures leading to volatile P_4O_{10} and/or by the presence of remaining impurities [90]. Particularly, the presence of residual polytrioxophosphate species, $Ln(\mathrm{PO}_3)_3$, can induce the formation of a glassy phase surrounding the grains [91] as well as the establishment of an abnormal grain growth regime correlated with the apparition of intragranular porosity [80]. More recent works have focused on the use of nanopowders [92], as well as hot-pressing [56, 93] or Field Assisted Sintering Techniques (FAST) to overcome such drawbacks [57, 94]. Yet, little attention was given to the control of microstructure and consequently on the properties of interest [56, 95]. The development of the microstructure during the sintering step has only been assessed by Bregiroux *et al.* [96] who established a sintering map for $LaPO_4$ and proposed comparative values of activation energy for densification (480 $\mathrm{kJ{\cdot}mol^{-1}}$) and grain growth (around 600 kJ·mol^{-1}) processes. On this basis they stated that slow heating rates are needed to reach high density values and to avoid the inhibition of grain growth by porosity [96]. However, nothing was said about the impact of the initial powder morphology in both densification and grain growth steps.

2.4 Structural investigations of solid solutions with monazite and rhabdophane structures

A real monazite-type waste form is at least a ternary system comprising of: (i) the main cation of the host material (Ln^{3+}), (ii) the immobilised actinide (e.g. An^{3+}) and (iii) a neutron absorber providing criticality safety (e.g. Gd^{3+}). Therefore a particular attention was paid in this work to a detailed investigation of structure and properties of solid solutions with monazite and rhabdophane structures.

2.4.1 Surrogates for minor actinides and plutonium

The performance of specific waste forms developed for actinide immobilisation under conditions relevant for geological disposal should ideally be evaluated with actinides-bearing materials. However, the use of radioactive elements in experimental work regarding the development and testing of nuclear waste forms is generally costly, requires a high level of safety measures, and can only be performed in specialised laboratories. Thus often inactive surrogates for the radioactive elements are employed in fundamental investigations and in initial steps of waste form development. The chemical behaviour (oxidation state, ionic radii and electronic configuration) of the selected surrogate has to be sufficiently similar to the radioelement of interest to provide meaningful insights into the chemical and physical behaviour of a waste form. For example $Ce^{+3/+4}$ is often used as surrogate for Pu because it is the most useful redox-active Pu-surrogate (e.g. [97]), although substantial differences in the redox potential from $Pu^{+3/+4}$ have to be taken into account (**Table 1**) [98]. Surrogates cannot mimic all chemical properties of the radioactive element of interest. Therefore, a multi-surrogate approach is advisable for waste form development.

Table 1. Criteria for selection of surrogates for $Pu^{+3/+4}$ and Am^{+3} exemplarily for actinides.

Element	**Valence state**	**Electronic configuration**	**Ionic radius (pm) [43]**		**Redox potential (V) [98]**
			[CN6]	[CN8]	
Pu	(III)	[Rn] $5f^5$	100		$Pu^{4+} + e^- \leftrightarrow Pu^{3+}$
	(IV)	[Rn] $5f^4$	86	96	1.006
Ce	(III)	[Xe] $4f^1$	101	114.3	$Ce^{4+} + e^- \leftrightarrow Ce^{3+}$
	(IV)	[Xe]	87	97	1.72
Th	(IV)	[Rn]	94	105	
Nd	(III)	[Xe] $4f^3$	98.3	110.9	
Am	(III)	[Rn] $5f^6$	97.5	109	
Sm	(III)	[Xe] $4f^5$	95.8	107.9	
Eu	(III)	[Xe] $4f^6$	94.7	106.6	
Gd	(III)	[Xe]$4f^7$	93.8	105.3	

In the present work Eu^{3+} and Gd^{3+} served as inactive surrogates for trivalent minor actinides and Pu. The results of the surrogate studied were confirmed with Cm^{3+} doped monazite and hydrated rhabdophane and Pu^{3+} doped monazite solid solutions.

2.4.2 Actinide incorporation into the monazite structure

The flexible monazite structure can incorporate varying compositions of practically all light trivalent lanthanide elements which endmembers crystallize in the monazite structure, typically La-Tb [23]. By carefully selecting the dopant cation and the composition of the monazite, the material can be employed in a number of technologies such as phosphors [81, 99] and photonic materials [100, 101] due to the favorable electronic properties of the 4f elements. The monazite structure is also capable of incorporating ions with differing oxidation states in coupled substitution reactions [78, 102]. An important reaction in this respect is the coupled substitution of the tetravalent actinides Th^{4+} and U^{4+} with a divalent cation, often Ca^{2+}, to preserve charge neutrality within the crystal lattice. Very old, naturally occurring monazites containing more than 20 wt% uranium and thorium are known to exist [26, 103] and they rarely show any metamictization due to radiation damage despite the high concentration of alpha emitting actinide elements [104]. This strong resistance towards ionizing radiation and the good chemical durability of the monazites make these materials attractive as potential waste forms for the conditioning of high-level radioactive wastes [15, 21, 105]. Especially the transuranics including Am, Cm, and Pu, originating from specific waste streams such as the treatment and reprocessing of spent nuclear fuel or dismantled nuclear weapons, will require durable host matrices for their immobilisation over long time periods. Irrespectively of the application, whether as hosts for luminescent substituents in optoelectronic devices or actinides in nuclear waste disposal, it is clear that a sound understanding of the incorporations processes within the monazite material is required.

Thus the structure and properties of pure monazite-type endmembers [46, 80, 88, 106-108] and of mixed solid solutions containing mainly non-radioactive analogues of trivalent [44, 69, 109, 110] and tetravalent [102, 111-114] actinides (*An*) have been investigated in numerous studies. In contrast, studies on actinides-bearing monazite materials are rather rare. As expected based on the surrogate studies, Pu [72, 115], Am- [70, 116, 117], Cm- [71, 118, 119] as well as Cf-, Bk-, and Es-orthophosphates [120] were reported to crystallize in a monoclinic monazite structure because the ionic radii of these actinides fit into the range between La and Gd [43]. The formation of $Pu^{III}PO_4$ [117, 121, 122] and $Np^{III}PO_4$ [123] monazites gained particular interest because they were synthesised in absence of additional reactants to reduce the oxidation state of $An^{IV} \rightarrow An^{III}$ (An = Pu, Np) during reaction. The formation of $Pu^{III}PO_4$ and $Np^{III}PO_4$ was confirmed by Popa et al. [124] and Begg et al. [123], respectively by X-ray Absorption Near Edge Structure (XANES) spectroscopy measurements. Additionally, the thermal behaviour of $Pu^{III}PO_4$, such as lattice expansion and thermal decomposition during heat treatment was studied by Jardin et al. [125].

The solid state synthesis route has already been adopted successfully to synthesize $La_{1-x}Pu_xPO_4$ (x = 0.01 – 0.1) solid solutions by Popa et al. [126] and Zhang et al. [127]. XRD analysis for all compositions revealed single phase materials with monoclinic structure and the oxidation state +III of Pu was confirmed by diffuse reflectance spectroscopy [127]. Finally for self-irradiation studies $PuPO_4$ (7.2 wt% ^{238}Pu) and $(La,Pu)PO_4$ (8.1 wt% ^{238}Pu) were synthesised by wet chemical method based on precipitation from aqueous nitrate solutions by Burakov et al. [115]. However, the incorporation of pure Pu^{IV} by coupled substitution into a monazite-cheralite system $Ln_{1-x}Ca_{0.5x}Th_{0.5x}PO_4$ as well as the synthesis of pure $CaPu^{IV}PO_4$ failed so far. Instead Bregiroux et al. [78] and Deschanels et al. [128] prepared mixed-valence compounds such as $Pu_{0.4}{}^{III}Pu_{0.3}{}^{IV}Ca_{0.3}{}^{II}PO_4$ and $Ca_{0.09}Pu_{0.09}La_{0.73}Th_{0.09}PO_4$, respectively.

2.4.3 Actinide incorporation into the rhabdophane structure

Data existing in literature on rhabdophane phase for trivalent actinides and in particular for plutonium is scarce. The phase transition from rhabdophane to monazite for Pu, Am and Cm phosphates are not reported in the literature in detail. Rai et al. [70] published the solubility of $AmPO_4{\cdot}xH_2O$ and mentioned the phase transition at higher temperatures. Keller and Walter [71] reported a monoclinic phase after thermal treatment at >473 K. $AmPO_4$ with monazite structure was described to be stable above 1273 K [129]. Also, Hobart et al. [120] synthesised monazite-type Am, Cm, Cf, Bk and Es by precipitation and subsequent heat treatment at 1373 K. A phase transition of rhabdophane-like $PuPO_4{\cdot}nH_2O$ to $PuPO_4$ monazite was reported by Bjorklund [72] after thermal treatment at 1223 K. However a refined crystal structure of the hydrated Pu-phosphate compound as well its XRD pattern have not been reported so far. Therefore it can be assumed, that the “rhabdophane” phase for the precipitation product was suggested in the literature solely from analogy to *Ln*-rhabdophane [61]. Taking into account the recently reported dehydrated *Ln*-rhabdophane structure [59] further investigations of wet chemical routes for synthesis of actinide-bearing monazite compounds might potentially lead to the discovery of new structures of actinide phosphates.

2.4.4 Analytical methods for probing the structural homogeneity of solid solutions

In the present work the long-range order characterization of monazite and hydrated rhabdophane solid solutions by X-ray diffraction analysis was complimented by short-range order spectroscopic studies. The structural homogeneity of monazite- and rhabdophane-type La(Gd/Eu)PO_4($\cdot 0.667H_2O$)(:Cm^{3+}) solid solutions was evaluated by a combination of Raman (particularly addressing the local distortions of the phosphate tetrahedra) and time-resolved laser fluorescence spectroscopy (accessing the local environment of cations) techniques. The laser-spectroscopic investigations of the Cm-doped (La,Gd)PO_4 monazite solid solutions were complemented with Cm^{3+} LIII-edge X-ray absorption fine structure (XAFS) spectroscopy analysis in order to examine the Debye-Waller factor, an indicator for thermal and structural disorder. XAS analysis at the Pu-L_{III} and La-L_{III} edges was used to determine the valence state of plutonium and the local environment of La and Pu in the monazite solid solutions. In this chapter the theoretical background of the analytical methods mentioned above is briefly described.

2.4.4.1 X-ray diffraction

X-ray diffraction (XRD) analysis is a non-destructive analytical long-range order technique for quantitative and qualitative determination of phase composition and phase characterization (unit cell dimensions) of a crystalline material. The analytical method is based on the interaction of monochromatic incident X-Ray beam with a crystalline sample causing constructive interference when conditions satisfy Bragg's Law (**Equation 1**).

Equation 1

$n\lambda = 2d \sin\theta$,

(λ is the wavelength of electromagnetic radiation, θ the diffraction angle, d the lattice spacing in a crystalline sample.)

All possible diffraction directions of the lattice can be attained by scanning the polycrystalline sample through a range of 2θ angles. The resulting diffraction pattern of a polycrystalline substance is regarded as a mathematical function of the intensity of the diffraction peaks and the diffraction angle, which in turn depends on the parameters of the crystal structure and the parameters of the instrument. Based on this, the crystal structure (or structures in samples containing more than one phase) is refined using the Rietveld refinement method (the least squares method) to achieve the best fitting of the theoretically calculated profile of the diffraction patterns to the experimentally obtained profile and the smallest value of the difference factors [130].

2.4.4.2 Raman spectroscopy

Raman spectroscopy can be used to study solid, liquid and gaseous samples and is based on inelastic scattering of monochromatic light from a laser source by an interaction with a sample. Photons of the laser light absorbed by the sample are subsequently reemitted. The frequency of the reemitted photons is changed in comparison to the frequency of the incident monochromatic beam. This frequency shift is called the Raman effect. The Raman shift provides information about vibrational, rotational and other low frequency transitions in molecules.

Structural information and order-disorder phenomena in solids can be studied using Raman spectroscopy [131, 132]. Decreased short-range order in terms of Raman band broadening (full width at half maximum, FWHM) and shifted band positions have been correlated to the degree of actinide substitution in monazite materials causing a deviation from the ideal chemical composition [111, 133].

2.4.4.3 Time resolved laser fluorescence spectroscopy

Time-resolved laser fluorescence spectroscopy (TRLFS) is a non-invasive *in situ* technique, allowing for a direct detailed probing of the local coordination environment of luminescent ions (e.g. Eu^{3+}, Cm^{3+}, $Am^{3+}$and U^{6+}) in aqueous solutions as well as on the surface and within crystalline and amorphous solids. The TRLFS method is based on the excitation of electrons of luminescent atoms with tunable laser light and the subsequent collection of the emitted luminescence upon relaxation. Depending on the electronic configuration of the luminescent ion, the number of non-equivalent species in a given system, incorporation site symmetries, and potential quenching entities in the proximity of the luminescent ion can be obtained from recorded excitation spectra, emission spectra, and luminescence lifetimes, respectively. This allows for molecular level understanding of the speciation of the luminescent ion in the investigated system.

Eu^{3+} and Cm^{3+} ions are often applied as luminescent probes in studies dealing with radionuclide incorporation mechanisms in envisioned immobilisation matrices [108, 119, 134-137] and the interaction of radionuclides with minerals [138, 139] and ground water [140-143] in the geosphere. Europium serves as an inactive surrogate for trivalent minor actinides and Pu. The use of curium as a luminescent probe allows for trace concentration measurements due to its low detection limit [144] and serves for a verification of surrogate studies with Eu^{3+}. The theoretical background of the Eu^{3+} and Cm^{3+} TRLFS method and further experimental examples can be found e.g. in the reviews [145] and [146], respectively. Here, only a short description of luminescent parameters for Eu^{3+}, required to understand the spectroscopic findings in this work, and for Cm^{3+} for comparison is provided. The number of non-equivalent Eu^{3+} or Cm^{3+} species in the system under investigation can be obtained from excitation spectra of the $^7F_0 \rightarrow ^5D_0$ or $^6D_{7/2} \rightarrow ^8S_{7/2}$ transitions, respectively. Collection of the excitation spectra is performed by varying the excitation wavelength and directly probing the $^7F_0 \rightarrow ^5D_0$ energy gap of Eu or $^6D_{7/2} \rightarrow ^8S_{7/2}$ of Cm. The integration of the collected luminescence signal is plotted against the excitation wavelength. In the case of Eu, the transition is non-degenerate and therefore results in a single peak for a single Eu environment. The splitting in the excitation spectra of Cm^{3+}-doped $LaPO_4$: is more complex due to the degenerate ground state. The identified species can thereafter be selectively excited at the corresponding excitation peak maxima, yielding emission spectra characteristic for the individual species. In the case of the Eu^{3+} doped compounds the splitting pattern of especially the $^7F_1$ and $^7F_2$ bands in the emission spectra depends on the symmetry of the Eu^{3+} ion in the investigated solid. For low symmetries, such as the C_1 symmetry of the cation site in monazites, a full three-fold and five-fold splitting of the $^7F_1$ and $^7F_2$-bands, respectively, is expected for Eu^{3+} incorporation.

Lifetime measurements can be obtained by monitoring the luminescence emission as a function of delay time between the laser pulse and the camera gating. Monoexponential (single slope) luminescence decay curves for both Eu^{3+}- and Cm^{3+}-doped compounds would confirm the presence of only one Eu^{3+} or Cm^{3+} species in the structure. If there are water molecules in the first coordination shell of the luminescent ions, oscillating OH-groups absorb energy inducing a faster return of the electron to the ground state. The fluorescence lifetimes (τ) and the number of water molecules (n (H_2O)) in the first coordination sphere of Eu or Cu ions can be correlated using empirical equations **Equation 2** and **Equation 3**, respectively.

Equation 2

$n(H_2O) = 1.07\ \tau^{-1} - 0.62$ [147]

Equation 3

$n(H_2O) = 0.65\ \tau^{-1} - 0.88$ [148]

2.4.4.4 X-ray absorption fine structure spectroscopy

X-ray absorption fine structure (XAFS) spectroscopy is a general term for two spectroscopic methods: extended X-ray absorption fine structure (EXAFS) and X-ray absorption near-edge structure (XANES) techniques. EXAFS gives information about the interatomic distances, near neighbor coordination numbers, and lattice dynamics. XANES allows determination of the valence state, energy bandwidth and bond angles [149].

In XAFS spectroscopy, the absorption coefficient of X-ray photons by electrons in a tightly bound quantum core level of an atom in a sample is measured as a function of the energy of the radiation resulting in the X-ray absorption spectrum of the sample [150].

The absorption coefficient μ is the measure of the probability of X-rays absorption according to Beer's Law (**Equation 4**).

Equation 4

$$I = I_0 e^{-\mu t}$$

(I_0 is the intensity of incident X-ray, t is the sample thickness, and I is the intensity transmitted through the sample.)

μ is inversely proportional to X-ray energy E and also depends on the sample density ρ, the atomic number Z and atomic mass A of the atoms of the sample (**Equation 5**).

Equation 5

$$\mu \approx \rho Z^4 / AE^3$$

In XAFS technique the energy dependence of μ at and above the binding energy of a certain core level of an atom of interest is measured. When the energy of the incident X-ray corresponds to the binding energy of a core-level electron, a sharp rise in absorption takes place resulting in an absorption edge. The binding energies of core-level electrons of every atom are well defined and the absorption edge energies are tabulated. Therefore the X-ray energy can be tuned to a desired absorption edge of an element of interest.

Following an X-ray absorption event, an electron is excited in the continuum and leaves the absorber atom as a photoelectron. Above the absorption edges, a periodic modulation of the absorption coefficient up to about 2000 eV (X-ray absorption fine structure, EXAFS) is observed. It is caused by the interaction of the photoelectron with the surrounding atoms. The emitted electron wave is backscattered on the adjacent atoms and interferes with itself. Depending on the energy of the photoelectron (difference between the energy of the absorbed photon and the binding energy of the electron), the wavelength of the electron wave changes. If interference occurs at the location of the absorber atom, a maximum of the absorption coefficient is found, a minimum corresponds to the destructive interference (spectrum provides information on the distance, the type and number of neighboring atoms of an absorber atom). The oscillations close to the absorption edge region (0 – 50 eV above the edge) differ from the described EXAFS oscillations by higher amplitudes and frequencies (X-ray absorption near edge structure (XANES)). XANES analysis is used inter alia to determine the oxidation state of the atoms, as elements show significant edge shifts (binding energy shifts) with oxidation state.

XAFS spectra can be recorded in transmission ($\mu(E) = \log(I_0/I)$) or fluorescence ($\mu(E) \propto I_f/I_0$, I_f – monitored intensity of fluorescence line) mode [150].

2.5 Properties of monazite-type ceramics

In general, an application of ceramic materials as nuclear waste forms requires a refined understanding of the long-term behaviour of these materials under repository relevant conditions. It includes a description and prediction of the waste form stability over very long-time scales on the basis of reliable data regarding the chemical thermodynamics, the chemical durability, mechanical stability and the radiation resilience of the waste form.

2.5.1 Thermodynamic properties

The application of solid solutions as nuclear waste form requires a reliable thermodynamic model because the safety performance assessment demands the demonstration of waste form stability over a very long period of time under repository relevant conditions. A refined understanding of the thermochemistry of the mixed lanthanide orthophosphates solid solutions allows for description of the monazites' stability, the tendency of destabilization due to immiscibility and phase separation and therefore for estimation of the maximal loading of the waste form.

Thermodynamic properties of synthetic analogues of natural phosphate minerals have been of general interest since the early 1950ies. The data of these early studies are compiled in extensive tabulations [151-153]. The data are often limited to single phases (endmembers) and therefore provide only a limited view on the complete thermodynamic behaviour of series of phases or solid solutions in, for example, binary or ternary systems. In spite of the age of these publications these datasets are very valuable tools being in some cases the only available source for a complete thermodynamic description of materials including standard enthalpies of formation (ΔH°_f), Gibbs free energy of formation (ΔG°_f), entropy (ΔS°) and heat capacity (C°_P).

Thermodynamic data are experimentally accessible from calorimetric measurements [154, 155] or can be derived from solubility data [65]. The calorimetry technique has been significantly developed and progressed over the last decades [154, 156, 157] to expand the abilities to collect thermodynamic data from mg amounts of materials under different environmental conditions (e.g. oxygen atmosphere, argon atmosphere) and up to very high temperatures (2273 K) [158]. Generally, calorimetric techniques can be divided into three main groups [159]. The first group includes differential scanning calorimetry to collect data about heat capacities of materials and phase transitions with a very limited capability to investigate chemical reactions. Thermodynamic data of phase transitions and heat capacities can be also obtained from the second class including the conventional drop calorimetry that has to be clearly distinguished from the third group, the drop solution calorimetry. This method allows for the direct determination of the enthalpy dissolution by measuring the heat-flow of dissolving a sample dropped in an appropriate solvent. Suitable thermochemical cycles are than applied to determine enthalpies of formation. Among them the Calvet-type twin calorimeter e.g. for oxide melt solution calorimetry or low-temperature solution calorimetry is the most advanced system [154, 155, 160].

Thermodynamic properties of lanthanide phosphates (*Ln*PO$_4$) have been the objective of several experimental and computational investigations. These studies include investigations of pure *Ln*PO$_4$ materials [106, 107, 161-165], as well as *Ln*PO$_4$ solid solutions containing tri- and tetravalent lanthanides/actinides. Popa et al. [109] observed excess properties from enthalpy increment measurements of phosphate solid solutions ($La_{1-x}Ln_xPO_4$; *Ln* = Nd, Eu, Gd) using high temperature calorimetry. These data, however, do not represent enthalpies of mixing but, rather, the integral of excess heat capacity from ambient to high temperature. The enthalpies of formation of pure *Ln*PO4 follow a roughly linear trend consistent with the decrease of ionic radii of lanthanides and the ionic binding in these materials [107, 166-168]. Thus the solid solutions of these phosphate series were found to be regular solid solutions and the observed non-ideal behaviour was ascertained to the mismatch in size of substituting ions. Very recently the excess enthalpy of mixing of $La_{1-x}Pr_xPO_4$ solid solutions were obtained from drop solution calorimetry [169].

With respect to the use of phosphate materials as potential nuclear waste forms the thermodynamic data of solid solutions are of particular interest since they can provide insight into the excess properties of materials that are close to the chemical composition of a realistic waste form after the incorporation of e.g. actinides into the crystal structure of the host matrix.

Mogilevsky [170] considered the relative solubilities of monazite and xenotime phases which require information on the excess enthalpies of mixing that were modelled by simple strain energy-based model taking ionic radii of *Ln* cations and Young's moduli of the respected phases as input parameters. With this model Mogilevsky [170] was able to reproduce well the solubilities measured for various monazite-xenotime systems. Recently *ab initio* methods were used to compute the Margules interaction parameters and resulting excess enthalpies of mixing for series of monazite solid solutions [171, 172]. Kowalski and Li [172] derived a simple model with which the excess enthalpies of mixing can be estimated from measured or computed volumes of endmembers and Young's moduli. However, all these studies require further validation by direct measurements of the excess enthalpies of mixing.

For actinide-bearing solid solutions only relatively few thermochemical data are available due to the radioactivity of such samples (experimental measurements can exclusively be performed in radiochemical laboratories and are therefore extremely costly). Thiriet et al. [173] and Beneš et al. [174] investigated the heat capacity of $PuPO_4$ in the low (3 – 300 K) and high (530 – 1386 K) temperature range providing the temperature dependencies. Additionally, the derived standard entropy data for $PuPO_4$ [173] allowed for the evaluation of a semi-empirical method to estimate missing data for $AmPO_4$ and $CmPO_4$. Popa et al. measured the low temperature heat capacity of a monazite-type $La_{0.9}Pu_{0.1}PO_4$ solid solution and reported about an antiferromagnetic effect of the Pu^{3+} in the solid solution system explaining anomaly effects in the low T range (4 K) [126]. Drop solution calorimetry measurements of the $CaTh(PO_4)_2$ endmember as well as the $Ca_xTh_xLn_{1-2x}PO_4$ (*Ln* = La, Ce) solid solution series were performed by Popa et al. [175] and Konings et al. [112] showing typical excess properties of regular solid solutions with a slight influence of the smaller Th^{4+} ions compared to the lanthanide ions. Very recently results of the heat capacity and standard molar enthalpies of formation were reported by Rawat et al. [176] indicating a stabilisation of the solid solution by the incorporation of 12.5 mol% of Th^{4+} which is an appropriate waste load for the disposal of tetravalent actinides.

The thermodynamic data of $LnPO_4\cdot0.667H_2O$-rhabdophane endmembers *(Ln* = La-Dy), derived from solubility experiments, have been reported by Gausse et al. [65]. According to these results, the solubility ranges from $\log K°_{s,0}\ (298\ K) = -25.6 \pm 0.8$ (Pr) to -24.9 ± 1.7 (Eu) with a minimum from Pr to Sm, which is in very good agreement with data of the associated monazite. The $\Delta_f H°$ were determined to be between (-2151 ± 13) and (-2130 ± 12) $kJ\cdot mol^{-1}$ with an exception of Eu (-2057 ± 9) $kJ\cdot mol^{-1}$. Estimations by simply adding the formation enthalpy of $0.667H_2O$ molecules to the values of the monazite compositions [107] revealed the same trend. Thermodynamic data for hydrated rhabdophane solid solutions and anhydrous rhabdophanes is absent in the literature.

2.5.2 Thermal and mechanical properties

Thermal (specific heat, thermal conductivity, coefficient of thermal expansion) and mechanical (elastic moduli, flexural strength, hardness and fracture toughness) properties are of particular importance considering various technological applications of monazite ceramics.

Several works dedicated to the thermal and mechanical properties of *Ln*PO_4 have been published [56, 73, 177-180]. The thermal and mechanical properties of monazite ceramics depend on their composition [179, 180] and are directly related to the microstructure (porosity, crystallographic grain orientation) of the material [56, 73]. Thus for *Ln*PO_4 endmembers Young's modulus varies between 150 and 200 GPa and the coefficient of thermal expansion ($\approx 9.5 \cdot 10^{-6}$ K^{-1}) increases with an increasing atomic number of the lanthanide element. However systematic studies on the variation of thermal and mechanical properties of monazite-type solid solutions are absent in the literature to the best of our knowledge.

2.5.3 Dissolution kinetics

The long-term containment and isolation of the wastes from the biosphere is generally ensured by a complementary and redundant system of engineered barriers including waste forms, waste containers, and backfill materials, in combination with a suitable repository host rock acting as geological barrier. In geological disposal facilities in crystalline or clay rocks the waste packages are generally expected to come into contact with groundwater in the long-term after resaturation of the repository. Even in repositories in salt rocks, the presence of water cannot be completely ruled out for less probable scenarios, for example, an early failure of shaft seals and plugs. After failure of the waste containers due to aqueous corrosion, radionuclides can be released from the degrading waste forms into the near-field water and subsequently migrate into the geo-/biosphere via the water pathway.

Thus insight into the aqueous durability of nuclear waste forms and the radionuclide source term are essential perquisites for the long-term safety assessment of an underground repository, requiring a mechanistic understanding of the dissolution processes. The long-term performance of the waste forms in a deep geological repository and their aqueous durability are controlled to a varying degree by thermodynamics and reaction kinetics and can be affected by the near-field hydro-(geo)chemistry and the hydrodynamic regime. Geochemical conditions affecting waste form durability comprise in particular pH and redox conditions as well as ionic strength and composition of the near-field water as well as the thermal regime at the time of canister failure.

The dissolution rates of minerals or waste forms are often described by empirical formulations based on Transition State Theory (TST) and considering contributions from different factors. According to TST the dissolution rate r of a phase i can be written in simplified form as:

Equation 6

$$r_i = k_0 A_S e^{-E_a/RT} a_{H^+}^{n} \prod_j a_j^{n_j} f(\Delta G_r) \ ,$$

where k_0 is an intrinsic rate constant, A_s is the reactive surface area, E_a is the apparent activation energy of dissolution, RT is the product of the gas constant and the absolute temperature, $a(H^+)^n$ is the hydronium ion activity in solution with the reaction order n, the product term comprises the activity and reaction order of all ions in solution catalysing or inhibiting the dissolution reaction and $\mathbf{f(\Delta G_r)}$ describes the deviation from thermodynamic equilibrium (e.g. [181]).

Dissolution rates can be derived from standardised static laboratory dissolution tests, e.g. MCC-1 [182] and/or dynamic single-pass flow through (SPFT) tests [183]. All standardised static dissolution tests are typically short-term laboratory tests, usually run for less than 1 month at drifting conditions, which occur according to the progress of the waste matrix dissolution. The dynamic SPFT set-up prevents the progressive accumulation of reaction products which may affect element release rate. During the experiment, a continuous flow of fresh influent solution maintains constant, well defined chemical conditions within the flow-through reactor. The dissolution rate can be derived by quantification of the concentration of dissolved species in the leaching media in relation to the original inventory in the solid. Finally the dissolution rate can be expressed as the elemental loss by mass normalised per unit surface area per unit time. Claperede et al. and Horlait et al. reported that the dissolution rate of monazite ceramics significantly depends on pH, temperature, chemical composition, etc. [50, 52]. Furthermore, the influence of microstructure, phase transformations due to radiation damages, strength and species of ions in the water have to be considered.

Several studies were carried out on the dissolution kinetics of natural monazite or synthetic lanthanide orthophosphates with monazite structure. Sales et al. [184] and Ishida et al. [185] found in independent dissolution tests a dissolution rate of synthetic monazite that is three orders of magnitude lower than that of borosilicate glasses. Natural monazite from Madagascar was systematically investigated by Oelkers&Poitrasson [47] at pH 2 in the temperature range of 50 – 473 K. The dissolution rate was determined to be $5 \cdot 10^{-7}$ $g \cdot m^{-2} \cdot d^{-1}$ – 10^{-4} $g \cdot m^{-2} \cdot d^{-1}$, respectively with an activation energy of 40 $kJ \cdot mol^{-1}$ indicating a surface-controlled dissolution mechanism [186]. Du Fou de Kerdaniel [53] investigated the dissolution behaviour of LnPO$_4$ monazite (Ln = La, Ce, Nd, Eu and Gd) in static experiments in 0.1 M HNO$_3$ at 363 K obtaining almost the same normalised dissolution rate ($1\cdot10^{-3}$ to $1.8\cdot10^{-3}$ $g\cdot m^{-2}\cdot d^{-1}$) for all lanthanides consistent to the data determined by Oelkers and Poitrasson. After 10 days a rapid decrease of the normalised dissolution rate was observed due to saturation processes and precipitation of neoformed phases. The structure of the neoformed phase is mainly governed by the temperature and the ionic radius of the lanthanide elements as has been discovered by du Fou de Kerdaniel et al. [53] (cf. **Figure 4**). At 423 K they reported a reprecipitation of lanthanide phosphates with monazite structure for the light lanthanides La and Ce and in contrast with rhabdophane structure for lanthanides from Nd to Dy. Taking into account other temperatures it can be concluded that at temperatures above ~423 K the monazite phase will be stabilised while rhabdophane is the low-temperature phase of $LnPO_4$.

The dissolution rate of monazite-type solid solution has been investigated for $La_{1-x}Gd_xPO_4$ [69] in dependence of pH at 363 K in static dissolution experiments. It significantly decreases from pH 1_{HCl} ($3.8\cdot10^{-4}$ $g\cdot m^{-2}\cdot d^{-1}$) to pH$4_{HCl}$ ($4.8\cdot10^{-6}$ $g\cdot m^{-2}\cdot d^{-1}$). The same tendency was observed for $Ce_{0.5}Pr_{0.5}PO_4$ [95]. The dissolution rate varied between ~10^{-3} $g\cdot m^{-2}\cdot d^{-1}$ at pH 3 and ~10^{-7} $g\cdot m^{-2}\cdot d^{-1}$ at pH 7 with no significant change with increasing the temperature from 363 K to 473 K and no significant influence of the fabrication method (i.e. either using conventional sintering or hot-pressing) [95, 187]. Brandt et al. [44] investigated the dissolution behaviour of $La_{1-x}Eu_xPO_4$ solid solutions in dynamic dissolution experiments at pH 2 and 363 K. They reported a normalised dissolution rate between $5\cdot10^{-5}$ $g\cdot m^{-2}\cdot d^{-1}$ and $1.7\cdot10^{-3}$ $g\cdot m^{-2}\cdot d^{-1}$ in dependence on the Eu content with a minimum at $x_{Eu} = 0.2$. Kowalski et al. [172] showed an interesting correlation between the measured dissolution rate for the $La_{1-x}Eu_xPO_4$ solid solution [44] and the simulated threshold displacement energy. Both parameters show a minimum at x~0.2, which points towards a common origin of these phenomena. In the case of simulations it is explained by the interplay of the two effects: (i) the lowering of the volume along the solution series and (ii) the weakening of the interaction between the *Ln* and O atoms with increase in x (i.e. weaker interaction between Eu-O than La-O).

Moreover, experiments with ^{241}Am-doped La-monazite revealed a normalised dissolution rate in a similar order of magnitude compared to the synthetic monazite [116] and 300 times lower as reported for borosilicate glasses [188].

In conclusion, these investigations revealed that the steady state dissolution rates of monazite-type materials are several orders of magnitude lower compared to borosilicate glasses at corresponding conditions [31]. However, so far only few studies were dedicated to the temperature dependence of the dissolution kinetics of monazite-type materials. Oelkers and Poitrasson [47] studied the dissolution kinetics of natural monazite from Manangotry, Madagaskar, as a function of temperature from 323 to 503 K at pH 2. Terra et al. [69] determined the apparent activation energy of the dissolution of synthetic $GdPO_4$ with monazite structure from the normalised dissolution rates measured at room temperature and 363 K under more acidic conditions (pH 1).

Gausse et al. (2016) demonstrated that in low temperature aqueous environments at temperatures below about 363 K, the hydrous *Ln*-orthophosphate rhabdophane ($LnPO_4 \cdot xH_2O$) is more stable than the corresponding monazite-type phase. Therefore it is presumed that rhabdophane could occur as a potential neo-formed phase on the surface of monazite waste forms in contact with groundwater in a repository after failure of the waste container, potentially controlling also the release of actinide elements from the waste form (cf. [53, 59, 60, 65, 189, 190]).

Thus, in the present work Raman investigations have been employed to provide information on potential variations in the crystalline structure as a function of Gd^{3+}/Eu^{3+} substitution in the $La_{1-x}(Gd/Eu)_xPO_4$ solid solution series.

3 Aim of the work

The aim of this work is to contribute to a deeper fundamental understanding of the molecular level processes involved in the long-term stability of monazite-type ceramic waste forms and their retention capacity for radionuclides (in particular actinides) under repository relevant conditions. Thus, in the context of this work experimental investigations of structure-property relationships of monazite-type solid solutions were linked to complementary model calculations.

The flexibility of the monazite and rhabdophane structures of $(La,M)PO_4(\cdot 0.667H_2O)$ (M = Eu^{3+}, Gd^{3+}, Cm^{3+}, Pu^{3+}) solid solutions was systematically studied by a combination of X-ray diffraction, spectroscopic and computational methods. Eu^{3+} and Gd^{3+} served thereby as inactive surrogates for trivalent minor actinides and Pu. The results of the surrogate studied were confirmed with Cm^{3+} doped monazite and hydrated rhabdophane and Pu^{3+} doped monazite solid solutions.

The enthalpies of formation and mixing of single phase monazite $La_{1-x}Ln_xPO_4$ (Ln = Eu and Gd) solid solution series were measured directly using high temperature oxide melt solution calorimetry. Additionally, heat capacity of $La_{1-x}Gd_xPO_4$ solid solutions was determined from microcalorimetric measurements. The obtained data provide key input parameters for calculation of stability and solubility of the monazite solid solutions as a function of temperature, thus contributing to the long-term stability prediction of monazite nuclear waste forms.

This work focuses also on the comparison of various synthesis methods, leading to precursors with different crystal structure and morphology, and on the effect of precursor morphology on the microstructural evolution of monazite-type lanthanum-europium phosphate ceramics during sintering, including grain growth rate, as well as correlations between microstructure, texture effects and mechanical properties (elastic moduli, microhardness and Vicker's hardness).

Besides the thermodynamic and mechanical properties, the dissolution kinetics of $LaPO_4$ of the monazite structure-type was systematically studied to gain a deeper insight into the mechanism governing the dissolution of monazite waste forms. The potential formation of La-rhabdophane as secondary phase in the dissolution experiments was explored here in the temperature range of interest by thermodynamic modelling using the Gibbs energy minimization (GEM) approach.

4 Materials and methods

4.1 Synthesis and aftertreatment

Within this work a number of methods have been established to synthesize homogeneous and single phase solid solutions of monazite-type materials with high crystallinity and to fabricate dense pellets by sintering. Besides the conventional solid state method, particular attention has been paid to wet chemistry routes such as precipitation and hydrothermal methods. These methods allow for a safe handling of radionuclides since dust formation and therefore the risk of contamination is mainly prevented. The methods and the conditions of treatment (calcination, palletisation and sintering) have been adjusted to the experimental requirements of the investigations. A great deal of experiments was performed on solid solutions containing lanthanides serving as non-radioactive surrogates for actinides. An overview of the materials prepared is summarised in **Table 2**.

Table 2. Overview of synthesised materials and performed investigations.

Composition	**Synthesis method**	**Specimen**	**Characterisation method**	**Investigations**
Structural & microstructural characterisation:				
$La_{1-x}Eu_xPO_4$ $La_{1-x}Gd_xPO_4$, Eu^{3+} doped (500 ppm)	Prec.	Powder	XRD, Raman, TRLFS	Solid solution formation
$La_{0.5}Eu_{0.5}PO_4$	Prec., HTS	Powder	XRD, SEM	Influence synthesis method → structure, morphology
	Prec.	Powder	HT-Raman[d], HT-XRD[e]	Phase transition rhabdophane → monazite
	HTS	Powder	Dilatometry, *In situ* HT-ESEM[d]	Sintering kinetics
Mechanism of An-incorporation:				
$La_{1-x}Pu_xPO_4$[c]	Solid state synthesis	Powder	XRD, SEM, EXAFS[a], XANES[a]	Solid solution formation Oxidation state
$PuPO_4{\cdot}xH_2O$[c]	Prec.	Powder	XRD HT-XRD	Structure of Pu-rhabdophane Phase transition rhabdophane → monazite
$La_{1-x}Gd_xPO_4$ Cm^{3+} doped (50 ppm)	Prec.	Powder	XRD, TRLFS[f], EXAFS[a] Atomistic modelling	Mechanism of *An*-incorporation (Eu^{3+} serves as surrogate for trivalent *An)*
Thermodynamic and physical properties:				
$La_{1-x}Eu_xPO_4$	Prec.	Powder	Drop solution calorimetry[g],	Enthalpy of formation, Excess properties
$La_{1-x}Gd_xPO_4$	Prec.		TG-DSC	
$La_{1-x}Eu_xPO_4$			Atomistic modelling	
	HTS-10	Pieces from pellets	Microcalorimetry[b]	Heat capacity
$La_{1-x}Eu_xPO_4$		Pellets	RUS[b;] Microindentation	Young's modulus
				Vickers hardness, fracture toughness
$La_{0.5}Eu_{0.5}PO_4$	Flux-growth	Single crystal		

Continuation of **Table 2**. Overview of synthesised materials and performed investigations.

Composition	**Synthesis method**	**Specimen**	**Characterisation method**	**Investigations**
Aqueous durability:				
$LaPO_4$; $LaPO_4 \cdot 0.667H_2O$	HTS	Powder	SEM, BET, ICP-MS	Dissolution rate

HTS: hydrothermal synthesis; Prec.: precipitation (cf. **Chapter 4.1**).

Experiments have been performed in cooperation with: [a]Rossendorf beamline at ESRF, Grenoble; [b]Goethe-University, Frankfurt am Main (IFG-GUH); [c]European Commission - Joint Research Centre (JRC), Karlsruhe; [d]ICSM, Marcoule, France, [e]Aachen University (RWTH-GHI); [f]Helmholtz-Zentrum Dresden – Rossendorf (HZDR-IRO); [g]University of California Davis, CA, USA; [h]Inter-University Accelerator Centre (IUAC), New-Delhi, India; [i]University of Tennessee, Knoxville, TN, US

4.1.1 Synthesis of rhabdophane and monazite samples for structural and thermodynamic studies of solid solutions formation

4.1.1.1 *Synthesis of $La_{1-x}Ln_xPO_4$ (Ln = Eu, Gd; x = 0 – 1) solid solutions with rhabdophane and monazite structures by precipitation (Prec.)*

This method includes the direct precipitation of solid phosphates from a mixture of aqueous lanthanide nitrate solutions with phosphoric acid according to the desired composition. It is noticeable that the structure of the precipitate can be controlled by the temperature. A precipitation at $T < 363$ K yields rhabdophane while the phosphates crystallise as a pure monazite by precipitation at $T > 413$ K.

The lanthanide phosphates $La_{1-x}Eu_xPO_4$ and Eu^{3+}-doped (500 ppm) $La_{1-x}Gd_xPO_4$ (x = 0 – 1) crystallising in the rhabdophane and monazite structure were synthesised by precipitation similar to the procedure described in Roncal-Herrero et al. [191]. The doping of the $La_{1-x}Gd_xPO_4$ solid solution by 500 ppm Eu^{3+} was performed for the TRLFS-measurements. For other measurements this amount of Eu^{3+}-doping is neglectable. Lanthanide nitrate salts were dissolved in deionized water (MilliQ) in concentrations of 0.3 – 0.5 M and then mixed in desired proportions. A 14.8 M aqueous solution of H_3PO_4 was slowly added to the solution, causing precipitation of lanthanide orthophospates. The suspension was heated at 90°C for 1 week to complete the precipitation and increase the degree of crystallisation of the solid. The precipitate was separated by centrifugation (10,000 rpm, 10 min) and washed with MilliQ water. The washing step was repeated several times until the supernatant was free of nitrate ions (NO_3^- test strips). Subsequently the powders were dried in an oven at 363 K for 12 hours. The dry powders were ground in an agate mortar and calcined for 2 hours at 873 K in order to remove any nitrate residues. As a final step, sintering of *Ln*PO₄ was carried out at 1723 K for 5 hours to yield the crystalline monazite product.

4.1.1.2 *Synthesis of Cm^{3+}-doped (50 ppm) $La_{1-x}Gd_xPO_4$ (x = 0 – 1) solid solutions with rhabdophane and monazite structures by precipitation (Prec.)*

Cm^{3+}-doped $La_{1-x}Gd_xPO_4$ (x = 0.0, 0.24, 0.54, 0.83, 1.0) rhabdophane and monazite solid solutions were synthesised by precipitation similair to the procedure described in **Subchapter**

4.1.1.1. La and Gd nitrate salts were dissolved in deionized water in desired relative concentrations. A small aliquot of a 10^{-4} M $^{248}Cm^{3+}$ stock solution was pipetted to the solution, followed by slow addition of H_3PO_4, causing precipitation of $La_{1-x}Gd_xPO_4{\cdot}0.667H_2O$ rhabdophane doped with approximately 50 ppm Cm^{3+}. The rhabdophane-suspension was kept at 363 K for 1 week to complete the precipitation and allow for better crystallisation of the solid phase. Subsequently, the solid was recovered and repeatedly washed with MilliQ water to remove nitrate ions, followed by drying at 363 K for 12 hours and grinding in an agate mortar. Part of the obtained rhabdophane material was further calcined for 2 hours at 873 K to remove any nitrate residues, followed by sintering at 1723 K for 5 hours to finally obtain the crystalline monazite ceramic.

4.1.1.3 Synthesis of $PuPO_4$ with monazite structure by precipitation

Pu^{4+} in the nitrate stock solution was reduced to Pu^{3+} by hydrazine. The reduction was accompanied by change of the colour of the solution from brown to green. Then an excess of concentrated phosphoric acid was added causing precipitation of the phosphate compound. The reaction mixture was filtered and the precipitate was washed with distilled water.

4.1.1.4 Synthesis of $La_{1-x}Pu_xPO_4$ ($x = 0 – 0.15$) solid solutions with monazite structure by the solid state method

$La_{1-x}Pu_xPO_4$ solid solutions were synthesised by conventional solid state method under inert atmosphere in order to avoid possible formation of traces of tetravalent plutonium phosphate [117, 124]. The synthesis was carried out in alpha-tight glove box designed to handle radioactive materials. Lanthanum oxide (Aldrich. 99.9%), plutonium(IV) oxide (>98% Pu, metal basis), diammonium hydrogen phosphate (Aldrich, 99%) were used as starting reagents without further purification. La_2O_3, PuO_2 in corresponding stoichiometric ratios and $(NH_4)_2HPO_4$ (10% molar excess) were mixed and ground in an agate mortar. Subsequently the synthesis of the $La_{1-x}Pu_xPO_4$ compounds was performed in inert atmosphere (Ar or N_2) for reduction of Pu^{IV} using the following conditions:

- for the desired molar fraction of Pu x = 0.50: 1273 K, 1373 K and 1473 K, 12 hours, Ar-atmosphere with subsequent grinding after each sintering step.

- for the desired molar fraction of Pu x = 0.01, 0.05, 0.10, 0.15: 1573 K, 5 hours, N_2-atmosphere.

By increasing the temperature of the synthesis up to 1573 K the reaction time was reduced to avoid phosphate decomposition leading to volatile P_4O_{10}.

4.1.2 Synthesis and fabrication of $La_{1-x}Eu_xPO_4$ (x = 0 – 1) samples for studies on sintering and/or physical and mechanical properties of monazite-type ceramics

Lanthanum-europium phosphates were synthesised by three different synthesis methods in order to obtain powders with variable particle morphologies for studies on sintering and/or physical and/or mechanical properties. As starting materials, $La(NO_3)_3 \cdot 6H_2O$(Alfa Aesar), $Eu(NO_3)_3 \cdot 6H_2O$ (Alfa Aesar), NH_4OH (GPR RECTAPUR), HNO_3 (Merck), and H_3PO_4 (Merck) of analytical grade were used without additional purification.

4.1.2.1 Hydrothermal synthesis

The hydrothermal synthesis, a precipitation from aqueous solution applying temperature and pressure, is an attractive method that allows for the preparation of uniform precursor particles with high crystallinity and homogeneity directly after synthesis at relatively low temperatures.

Hydrothermal precipitation in basic conditions (HTS-10)

$La_{0.5}Eu_{0.5}PO_4$-powder was synthesised hydrothermally at pH = 10.5 according to Meyssamy et al., 1999 [81]. The precursor material is prepared using a two-stage method that can be described as follows:

1) $0.5\ La(NO_3)_3 + 0.5\ Eu(NO_3)_3 + 3\ NH_4OH \rightarrow 0.5\ La(OH)_3 + 0.5\ Eu(OH)_3 + 3\ NH_4NO_3$

2) $0.5\ La(OH)_3 + 0.5\ Eu(OH)_3 + (NH_4)_2HPO_4 \rightarrow La_{0.5}Eu_{0.5}PO_4 + 2\ NH_4OH + H_2O$

In the first synthesis step, lanthanide hydroxides were precipitated from 0.5 M aqueous solution of nitrates using NH_4OH. The hydroxides were transformed into mixed lanthanide phosphates using $(NH_4)_2HPO_4$ and hydrothermal conditions. In this aim, the final pH was adjusted to 10.5 by adding drops of 25% NH_4OH solution, and the resulting mixture was poured into Teflon-lined steel autoclaves (Parr instruments) and treated at 473 K for 2 hours (p = 35 bar). After centrifugation (10,000 rpm, 10 min), the powder was stirred at pH 1 (adjusted with 1 M HNO_3) for 3 days at room temperature in order to remove lanthanum/europium hydroxide byproducts.

Hydrothermal precipitation in acidic conditions (HTS-1)

$La_{0.5}Eu_{0.5}PO_4$-powder was also obtained by hydrothermal precipitation at pH 1 according to Meyssamy et al., 1999 [81]:

$0.5\ La(NO_3)_3 + 0.5\ Eu(NO_3)_3 + (NH_4)_2HPO_4 \rightarrow La_{0.5}Eu_{0.5}PO_4 + 2NH_4NO_3 + HNO_3$.

Mixed lanthanide phosphate was precipitated from 0.5 M aqueous lanthanide nitrate solution with aqueous $(NH_4)_2HPO_4$ solution. The resulting pH of the reaction mixture was 1. Subsequently the reaction mixture was treated hydrothermally in steel Teflon-lined autoclaves at 473 K for 2 hours (p = 35 bar).

4.1.2.2 Synthesis by direct co-precipitation from acidic solution (Prec-1)

$La_{0.5}Eu_{0.5}PO_4$ powder was synthesised by direct precipitation in excess concentrated H_3PO_4 at 413 K according to Schatzmann et al. [83] by dropping a 0.5 M aqueous solution of lanthanide nitrates slowly into heated H_3PO_4:

$0.5\ La(NO_3)_3 + 0.5\ Eu(NO_3)_3 + H_3PO_4 \rightarrow La_{0.5}Eu_{0.5}PO_4 + 3\ HNO_3$

All pristine precipitates from both hydrothermal methods as well as from the precipitation route were centrifuged and washed by suspending them in 100 mL deionised water for 30 min in order to remove nitrates coming from the starting materials prior to thermal treatment. The washing step was repeated three to five times until the supernatant was free of nitrate ions (NO_3^- test strips).

4.1.2.3 Calcination and sintering of samples for sintering studies

After washing, the HTS-1, HTS-10 and Prec-1 powders were dried in an oven at 373 K for 12 hours. They were then hand-grinded in an agate mortar and fired for 2 hours at 873 K or 1073 K in order to remove residues of nitrates in the case of the two hydrothermal synthesis methods. The temperature was selected based on the TG-DSC measurements (see Section 5.1). Ground raw powders obtained after calcination were pelletized in an uniaxial press at 250 MPa, and finally sintered in a high-temperature furnace at 1723 K for 5 hours (heating and cooling rate: 3 K min^{-1}). The compaction pressure was chosen based on the results reported in [192]. The green bodies were then sintered by four different methods:

1. Sintering in a high-temperature furnace at 1723 K for 5 hours (heating and cooling rate: 3 K min^{-1}) after calcination at 873 K.
2. *In situ* sintering using HT-ESEM (details provided in section 4.2.3) to study sintering kinetics at 1623 K for 8 hours with a heating rate of 30 K·min^{-1} under water vapour at an operating pressure of 120 Pa after calcination at 1073 K.
3. Conventional sintering in a high-temperature furnace at 1623 K for 7 hours (heating and cooling rate: 30 K·min^{-1}) in air after calcination at 1073 K.
4. Uniaxial hot-pressing with a sintering temperature of 1623 K and a maximum compaction pressure of 50 MPa for 3.5 hours (heating and cooling rate: 10 K·min^{-1}) under nitrogen atmosphere after calcination at 1073 K.

4.1.2.4 Preparation of pellets for studies on physical properties

The synthesised HTS-10 powders were calcined at 873 K for 2 hours. Afterwards, the calcined powders were ground manually and pelletized in an uniaxial press (150 to 350 MPa) at ambient temperature. The green pellets were then hot-pressed using a vacuum hot-press (FCT Systeme GmbH) with a maximum pressure of 50 MPa and a sintering temperature of 1623 K for 2 hours. The use of graphite pressing tools in a nitrogen atmosphere gave rise to a dark grey colour, and possibly a slight oxygen deficit due to the low oxygen fugacity. To balance this and to remove the fine outer carbon impurities, some pellets were later re-sintered in air for several hours (4 – 18 hours) at a temperature of 1273 K. Additionally, the HTS-1 powder with the desired composition $La_{0.5}Eu_{0.5}PO_4$, calcined at 873 K for 2 hours, was also hot-pressed according to the procedure described above.

4.1.2.5 Flux growth of $La_{0.5}Eu_{0.5}PO_4$ single crystals

$La_{0.5}Eu_{0.5}PO_4$ single crystals with monazite structure used as reference material for measurements of pysical-mechanical properties were synthesised by the conventional Pb-free Na_2CO_3–MoO_3 flux method [193] in cooperation with partners from RWTH Aachen University (RWTH-IFK). An excess of a water-soluble flux (75 mole% of MoO_3 and 25 mole% of Li_2CO_3) was thoroughly mixed with fresh precipitated $La_{0.5}Eu_{0.5}PO_4$ powder in a ratio of 50:1. The mixture was melted at 1273 K in a platinum crucible and the crystal growth was achieved by heating at 1623 K for 15 hours and subsequent controlled cooling with a rate of 3 K·hours^{-1}. The flux was dissolved with deionised water.

4.1.2.6 Preparation of the defined LaPO$_4$-monazite powder of 100 – 180 µm fraction for dissolution experiments

LaPO$_4$ precursor powder was prepared hydrothermally by the HTS-1 method. The obtained powder was calcined at 873 K for two hours prior the sintering in order to remove water of crystallisation and ground in a mortar. 500 mg of the calcined powder were then pelletized by uniaxial pressing with 350 MPa and sintered at 1723 K for 5 hours. The pellets were coarsely crushed and sieved in order to obtain a particle size fraction of 100 to 180 µm. These powders were additionally washed several times with deionised water in an ultrasonic bath to remove finer particles from the materials surface.

4.2 Experimental and computational methods

Technical details and parameters of the experimental and computational techniques, used in the present work, are given in this chapter.

4.2.1 Elemental analysis

4.2.1.1 Inductively coupled plasma mass spectrometry

The concentration of lanthanide ions in the corresponding nitrate aqueous solutions used for the synthesis of lanthanide phosphates with rhabdophane and/or monazite structure as well as in the outlet solution samples after dissolution experiments were determined by inductively coupled plasma mass spectrometry (ICP-MS) using an ICP-MS ELAN 6100 DRC (PerkinElmer SCISX) instrument. All the analysed samples were acidified by adding 1 vol% HNO_3 suprapur (Merck Millipore) prior the ICP-MS measurements.

4.2.1.2 Energy dispersive X-ray spectroscopy

The actual chemical compositions of the synthetic $(La,Eu/Gd)PO_4$ rhabdophane and monazite solid solutions were determined using scanning electron microscopy with energy dispersive X-ray spectroscopy (SEM-EDS) on powders without any specific sample preparation prior to the measurements. The energy dispersive X-ray spectroscopy (EDS) for elemental spot analysis was performed on a FEI Quanta 200 FEG scanning electron microscope equipped with an EDAX Apollo X Si-drift detector in low vacuum mode at p = (0.4 – 0.6) mbar with an accelerating voltage between U = (7 and 20) kV.

The actual chemical compositions of the synthetic monazites $La_{1-x}Pu_xPO_4$ with x = 0.01, 0.04, 0.10, 0.14 were determined by SEM-EDS. The SEM observations were performed on a Philips XL40 SEM ((Philips, Amsterdam, Netherlands), which has been adapted for the examination of highly active or irradiated nuclear materials [194, 195]: the high voltage unit, column, chamber and turbomolecular pump are mounted inside a glove-box in order to keep the contaminated pieces in a confined space. The primary vacuum system, water cooling circuit and acquisition electronic are placed outside, preventing those parts from contamination by the active samples. The microscope is equipped with a secondary electron detector (SE), which gives a morphology-related signal, a backscattered electron detector (BSE) which provides images with Z-related contrast, and EDS used to obtain elemental analysis of the samples; the beam was always operated at 20 kV. As the samples were in the form of powders, the coating of the same to avoid the electronic charging was not necessary. No further preparation was required for the samples.

4.2.1.3 X-ray fluorescence spectroscopy

The X-ray fluorescence (XRF) spectra were collected on finely ground (La,Eu/Gd)PO_4-monazite powders using an EDAX Eagle II l-probe equipped with a Rh anode X-ray tube and a lithium-drifted Si-detector to confirm the results of elemental analysis by EDS.

4.2.2 X-ray diffraction and Rietveld refinement

The crystal structure of the synthesised (La,Gd/Eu)PO_4 and (La,Pu)PO_4 compounds were characterized by powder X-ray diffraction (PXRD) at room temperature using a Bruker D8 diffractometer mounted in a Bragg-Brentano configuration with a curved Ge (1, 1, 1) monochromator, a copper tube (40 kV, 40 mA) equipped with a LynxEye position sensitive detector adopting the parallel geometry (reflection mode) and using Cu $K_{\alpha 1,2}$ radiation (λ = 1.54184 Å). The data were collected by step scanning in the angle range $10^{\circ} \leqslant 2\theta \leqslant 120^{\circ}$ with a 2θ step size of 0.02° or of 0.0092°. For the measurement of the (La,Pu)PO_4 compounds, the powder was deposited on a silicon wafer to minimize the background and dispersed on the surface with several drops of isopropanol. The radioactive sample holders were covered by Mylar film to prevent any material dispersal. The phase composition and crystal lattice constants were refined with the Topas software (Bruker AXS GmbH) using the Rietveld technique.

4.2.3 Environmental scanning electron microscopy

Scanning electron microscope (SEM) observations were conducted on powdered samples using a FEI Quanta 200 environmental scanning electron microscope (ESEM) coupled with a gaseous secondary electron detector (GSED). The high voltage ranged between 15 kV and 30 kV, and the remaining gas pressure in the chamber was 50 – 300 Pa. These conditions were chosen to compensate the charging effects on the surface of the ceramic materials during SEM imaging. For sintered, polished and thermally etched (1273 K, 4 hours) pellets, a FEI Quanta 200 FEG scanning electron microscope (SEM) equipped with backscattered electron detector (BSED) was used in low vacuum mode (20 kV, 60 Pa). The particle size of the pristine powders, as well as the grain size of the sintered pellets was analysed using ImageJ Software [196].

Dynamic aspects of sintering were studied *in situ* using an Environmental Scanning Electron Microscope (model FEI Quanta 200 ESEM FEG) equipped with a 1773 K hot stage. The experimental procedure was adapted from [197]: green pellets of $La_{0.5}Eu_{0.5}PO_4$ were coarsely crushed, then the smallest fractions (i.e. with a diameter about 2 mm) were placed in a MgO ceramic crucible with a 5 mm inner diameter covered with platinum paint and heated up to 1613K with a heating rate 30 $K \cdot min^{-1}$. This temperature was subsequently retained for 8 hours. The temperature control was carried out by a custom thermocouple placed near the MgO crucible [198]. The experiment was performed under water vapour at an operating pressure of 120 Pa and a specific detector was used for *in situ* gaseous secondary electron imaging at high temperature. Micrographs with magnification up to 20,000× were recorded every 2 – 5 min during the heat treatment on a representative part of the sample.

4.2.4 Spectroscopic methods for short-range structural studies on solid solutions formation

4.2.4.1 Raman spectroscopy

Raman spectra of the $La_{1-x}Ln_xPO_4$ (Ln = Eu, Gd) orthophosphate powders with hydrated rhabdophane and monazite structures were recorded with a Horiba Jobin-Yvon Aramis spectrometer equipped with Olympus BX41 microscope. The 632.8 nm line of a He-Ne laser was used as the excitation wavelength with a 1 cm^{-1} resolution of spectra. The calibration of the apparatus was performed with the first-order Si line at 520.7 cm^{-1} of a silicon wafer. For each spectrum, an acquisition time of 35 s was considered with an average of 4 scans. The collected Raman data were fitted with the Voigt function using the open-source curve-fitting and data analysis software fityk 0.9.8.

4.2.4.2 Time resolved laser fluorescence spectroscopy

The Time resolved laser fluorescence spectroscopy (TRLFS) measurements were performed at the Helmholtz-Zentrum Dresden-Rossendorf (HZDR).

In the present study selective excitation of the Eu^{3+} ion from the $^7F_0$ ground state directly to the emitting $^5D_0$ excited state was performed using a pulsed Nd:YAG (Spectra Physics) pumped dye laser set-up (Radiant dyes Narrow Scan K). The emitted Eu^{3+} luminescence light was directed into a monochromator (Acton SpectraPro 300i) with a 300 or 1200 lines·mm^{-1} grating and the emission was monitored with an intensified CCD camera (Princeton Instruments) 10 ms after the exciting laser pulse in a time window of 10 ms. The laser pulse energy and the exact excitation wavelength were monitored in every measurement with an optical power meter (Newport 1918-R) and a wavelength meter (High Finesse WS-5), respectively. To achieve the desired spectral resolution the solid samples were cooled to approximately 10 K with liquid helium in a cryostat.

Direct excitation of Cm^{3+} from the ground state ($^8S_{7/2}$) to the emitting excited state ($^6D_{7/2}$) was performed with a pulsed Nd:YAG (Spectra Physics) pumped dye laser set-up (Radiant Dyes Narrow Scan K). The emitted luminescence light was directed into a spectrograph (Shamrock 303i) equipped with a polychromator with 300, 600, and 1200 lines/mm gratings and the emission was monitored with an intensified CCD camera (Andor iStar) 10 μs after the exciting laser pulse in a time window of 10 ms. The laser pulse energy and the exact excitation wavelength were monitored in every measurement with an optical power meter (Newport 1918-R) and a wavelength meter (High Finesse WS-5), respectively. To achieve the desired spectral resolution the solid samples were cooled to approximately 10 K with liquid helium in a cryostat.

4.2.4.3 X-ray absorption fine structure spectroscopy (XAFS)

XAFS measurements of Cm^{3+}-doped (La,Gd)PO_4 and (La,Pu)PO_4 monazite-type solid solutions were performed at the Rossendorf Beamline (ESRF, Grenoble, France) in order to determine the local environment of Pu- and Cm-cations and the oxidation state of Pu in the envestigated solid solutions.

The finely ground Cm^{3+}-doped monazite powders were placed in sample holders consisting of polyethylene (inner confinement) and Teflon (outer confinement) for X-ray absorption measurements. Powdered (La,Pu)PO_4 samples were diluted with boron nitride powder, pressed into pellets and encapsulated in a double sealed confinement prior the experiment.

Cm-L_{III} edge (18970 eV), Pu-L_{III} edge (18057 eV) or La-L_{III} edge (5483 eV) XAFS spectra were collected. Due to the very low Cm^{3+} doping of 50 ppm in the monazite samples, the collection of approximately 30 spectra per sample was necessary to achieve a satisfactory quality of data. XAFS spectra were collected at ambient temperature. Due to the very low Cm^{3+} doping of 50 ppm in the monazite samples, the collection of approximately 30 spectra per sample was necessary to achieve a satisfactory quality of data. The high noise level and subsequently necessary accumulation of many spectra limited the total number of samples to be analysed, i.e. of the five synthesised monazite samples only the Cm^{3+}-doped $LaPO_4$, $La_{0.46}Gd_{0.54}PO_4$, and $GdPO_4$ compositions were measured.

A flat, meridionally-bent, 140-cm long Rh-coated silicon mirror was used to collimate the X-ray beam into a Si(111) double-crystal monochromator. The monochromatic X-ray beam was thereafter focused onto the sample by a 1.3-m long, Rh-coated, toroidal silicon mirror, achieving a rejection of higher order harmonics by at least four orders of magnitude.

The measurements were done in transmission (T) or fluorescence (F) mode using gas-filled ionization chambers and a high-purity, 13-element Ge detector (Canberra) with a digital spectrometer (XIA XMap). The collected spectra were energy-calibrated using the absorption edge of a simultaneously measured Zr foil (17998 eV) for each sample, and averaged to improve the signal-to-noise ratio using Sixpack43 [199]. The acquired spectra were analysed according to a standard procedure of the program WinXAS (version 3.2). EXAFS theoretical fitting was performed both in k-space (i.e. EXAFS oscillation spectra) and R-space (i.e. Fourier transforms: FTs). EXAFS theoretical phase and amplitude functions required for the theoretical fitting were calculated by the program code FEFF 8.2045 based on the structure of La monazite.

4.2.5 Atomistic modelling

4.2.5.1. *Ab initio* and force-field simulations of $La_{1-x}Gd_xPO_4$ solid solutions

The impact of the $La_{1-x}Gd_xPO_4$ solid solution composition on the distribution of Gd-O bond lengths in the monazites was investigated in coupled *ab initio* and force-field simulations. The calculations were performed by the Atomistic modelling group of Dr. Piotr Kowalski. So called quasi random structures were applied to represent homogeneous $La_{1-x}Gd_xPO_4$ solid solutions following a modified procedure of Zunger et al. [200] (see Li et al. (2014) [171] for a detailed description). *Ab initio* calculations using the Quantum ESPRESSO code [201] were performed on a $La_{1-x}Gd_xPO_4$ 2 · 2 · 2 supercell consisting of 192 atoms (8 elementary units). This setup comprising 32 Ln^{3+} cation sites [171], i.e. 32 possible doping sites for a single Eu^{3+} cation resulted in a set of 32 average Eu-O bond distances. To improve the statistics, *ab initio* calculations were combined with force-field-based calculations on a 1536 atom 4 · 4 · 4 supercell resulting in 256 average Eu-O bond lengths. These calculations were performed using the GULP code [202] and a set of simple Buckingham force fields together with a shell model to account for the polarisability of O^{2-} anions in the monazite structure. The applied force field parameters for La-O, Gd-O, and Eu-O interactions were fitted to the *ab initio* structures and the energetics taken from Blanca-Romero et al. [166] and the parameters for O-O and P-O interactions were taken from Girard et al. [203] (see also Ji et al. [204] and Kowalski et al. [205]). The force fields parameters are compiled in **Table 3**.

Table 3. The Buckingham and shell model force field parameters used in the force-field simulations

	La-O	Gd-O	Eu-O	P-O	O-O
A (E_v)	18854	13271	13911	877.34	22764
B (Å)	0.26	0.26	0.26	0.3594	0.149
C (eV·Å^6)	0	0	0	0	27.879
Spring constant (eV·Å^{-2})	-	-	-	-	74.92
Atomic charge (core/shell)	+3	+3	+3	+5	+0.869020/ -2.869020

4.2.5.2. *Atomistic simulations of Cm^{3+} incorporation in monazite and rhabdophane*

The lattice parameters of $La_{1-x}Gd_xPO_4$ monazite and $La_{1-x}Gd_xPO_4·0.667H_2O$ rhabdophane solid solutions were investigated by *ab initio* simulations. Furthermore, the bond-length distribution (Cm-O) in the monazite solid solutions doped with Cm^{3+} were investigated and compared to the collected spectroscopic data. The calculations were performed with the DFT-based plane-wave Quantum ESPRESSO code [201] on $La_{1-x}Gd_xPO_4$ monazite and $La_{1-x}Gd_xPO_4·0.667H_2O$ rhabdophane solid solutions represented by supercells consisting of 192 atoms. In order to get the converged wavefunctions, 2 · 2 · 2 and 1 · 3 · 2 Methfessel-Paxton k-points grids were applied. The ionic arrangements of solid solutions were built with the aid of special quasirandom structures using the procedure described in Li et al. [171] and Huittinen et al. [136]. We used

PBEsol exchange correction functional which was successfully applied to the previous studies of lanthanide-phosphates [166, 168, 171]. The plane-wave energy cutoff was 30 Ry.

The set of energies of Cm^{3+} incorporated on different hydrated (24 positions) and non-hydrated (8 positions) sites of $La_{1-x}Gd_xPO_4 \cdot 0.667H_2O$ rhabdophane (x = 0, 0.25, 0.5, 0.75, 1) were calculated. The energy of Cm incorporation into the hydrated and non-hydrated configuration was then derived applying the Boltzmann distribution

Equation 7

$$\langle E \rangle = \frac{\sum_{i=1}^{M} \varepsilon_i e^{-\varepsilon_i/kT}}{\sum_{i=1}^{M} e^{-\varepsilon_i/kT}},$$

where ε_i are the energies of the different Cm ionic configurations with respect to the lowest energy structure, k is the Boltzmann constant, and T = 363 K is the synthesis temperature. Having these incorporation energies, the abundances of Cu on non-hydrated and hydrated lattice sites were computed, assuming a Boltzmann distribution between the two sites. To account for temperature effects on the lattice site occupancy, another set of calculations was performed for T = 1200 K. This high temperature was chosen to obtain an adequate difference between the site occupancies as a function of temperature.

Finally, for a better understanding of the Cm^{3+} distribution on the various lattice sites in rhabdophane matrices, the MPO_4 formula unit volume was calculated based on the optimized rhabdophane structures for pure phase $LaPO_4$, $GdPO_4$, and $CmPO_4$ rhabdophane as well as for Cm^{3+}-doped $LaPO_4 \cdot 0.667H_2O$ and $GdPO_4 \cdot 0.667H_2O$.

4.2.6 Methods for studies on physical, thermodynamic and mechanical properties

4.2.6.1 Thermal analysis and calorimetric methods

TG-DSC

The transition in precursor powders from rhabdophane to monazite phase was investigated by thermogravimetric analysis (TG) coupled with differential scanning calorimetry (DSC) using the thermo-analyser Netzsch STA449C Jupiter in the temperature range 373 – 1423 K with a heating rate of 10 $K\cdot min^{-1}$. The TG-DSC data analysis was carried out using NETZSCH Proteus® Software for thermal analysis.

Microcalorimetry

The heat capacity measurements of the $La_{1-x}Eu_xPO_4$ ceramics (HTS-10, hot-pressed, see **Section 4.1.2**) and of a single crystal with the composition $La_{0.5}Eu_{0.5}PO_4$ were performed with a PPMS instrument (Quantum Design, San Diego, CA) at temperatures between 2 and 395 K in cooperation with the Institut für Geowissenschaften, Goethe Universität Frankfurt. Small pieces with dimensions of about 2mm · 2mm ·1.5 mm and masses between 8 and 30 mg were cut from the pellets. The accuracy of the mass determination was 0.02 mg. At each temperature, the heat capacity was measured three times by the relaxation method. The accuracy of the measurements was established by measurements of standard reference materials SRM-720 (Al_2O_3) and Cu (99.999%; Alfa Aesar). The experimental error of the data for SRM720 is in the range of 395 to 50 K is 2%, and 6% below 5 K, as determined by comparison of the data from this work with those obtained by Ditmars et al. [206]. A comparison of the data from the present work to that of Lashley et al. [207] gives an experimental error of the measurement of the heat capacity of Cu of < 1% in the range from 300 to 40 K, and of ~ 2% below 40 K [207].

The standard molar entropy $S°_{298.15}$ and the molar enthalpy $\Delta H°_{298.15}$ of the samples were calculated by analytical integration of high-order polynomials fitted to the data (**Equation 8** and **Equation 9**).

Equation 8

$$S°_{298.15} = S^{T\,=\,298.15} - S^{T\,=\,0K} = \int_0^{298.15} \frac{C_p}{T} dT$$

Equation 9

$$\Delta H^\circ_{298.15} = H^{T\,=\,298.15} - H^{T\,=\,0K} = \int_0^{298.15} C_p \mathrm{dT}$$

High temperature oxide melt solution calorimetry

High temperature oxide melt solution calorimetry was performed at the Peter A. Rock Thermochemistry Laboratory at UC Davis using a custom build Tian-Calvet twin calorimeter [156, 208]. Pelletized samples with a mass of about 5 mg were dropped from room temperature into molten sodium molybdate ($3Na_2O\cdot 4MoO_3$) solvent in a platinum crucible in the calorimeter at 973 K. The methodology has been described previously in [154-156, 208]. Sodium molybdate solvent was prepared according to Navrotsky et al. [209] using MoO_3 (Fisher, 99.5% purity) and $Na_2MoO_4\cdot 2H_2O$ (EMD Millipore, 99.5% purity) as reagents. Always a batch of 100 g of the solvent was synthesised at once. Thus the uncertainty of solvent composition is due to the standard uncertainty of the used balance of 0.01 g. Prior to the calorimetric measurements all samples were thermally treated at 1073 K for at least 8 hours to remove possible adsorbed water from the surface. At least 8 – 10 drops were performed per composition to optimize the accuracy. To prevent saturation of the solvent, a maximum of m = (50 – 60) mg of sample material was dropped into one batch of 20 g solvent. During the measurement, the melt was stirred by bubbling with oxygen (rate 5.9 $\mathrm{mL\cdot min^{-1}}$). This assures an oxidative environment and enhances the dissolution and prevents a local saturation of the solvent [154]. In addition, a constant flow of O_2 gas was flushed through the calorimeter chamber (40 $\mathrm{mL\cdot min^{-1}}$) to generate a constant gas environment above the solvent and to remove any other gases. On average, the time which was needed to return to the baseline level (i.e. time of experiment) was 30 min. This time is a function of the dissolution rate, the magnitude of the heat effect and the time constant of the calorimeter. The measured signal of heat flow over time was integrated using the software CALISTO by Setaram to calculate ΔH_{ds}. The achievable accuracy of ΔH_{ds} is in the range of ± 1 $\mathrm{kJ\cdot mol^{-1}}$. Using appropriate thermochemical cycles, enthalpies of formation from oxides and elements as well as the enthalpy of mixing were calculated.

4.2.6.2 Dilatometry

Densification studies

For the dilatometric measurements, powders obtained after heat treatment at 873 K or 1073 K were uniaxially pelletized at 250 MPa. The densification of the specimens was studied in a Setaram Setsys Evolution apparatus (Caluire, France) in air with a heating rate of 10 $K{\cdot}min^{-1}$ up to 1723 K in order to determine the optimal sintering temperature. The densification of the specimens calcined at 1073 K during the conventional sintering at 1613 K was studied isothermally by dilatometry at identical conditions (heating rate 30 $K{\cdot}min^{-1}$, dwell of 7 hours).

Determination of the linear coefficients of thermal expansion

The linear coefficients of thermal expansion (CTE = a) of the $La_{1-x}Eu_xPO_4$ solid solutions were measured with a push rod dilatometer equipped with a high-temperature furnace (DIL 402C; Netzsch, Hanau, Germany) using air as a purge gas. The dilatometer was calibrated with ceramic corundum rods. The samples had different geometries (pellets, cuboid, etc.) and different thicknesses ranging from 3.797(4) to 7.890(2) mm. CTEs were obtained from subsequent heating-/cooling cycles, where the temperature was first increased from ambient temperature up to 373.15 K followed by a temperature decrease back to ambient temperature. In the subsequent heating/cooling cycles, the maximum temperature was increased in steps of 100 K up to 773.15 K. Heating-/cooling rates were 1 $K{\cdot}min^{-1}$. Additionally, two samples with endmembercompositions were measured in a single heating run up to 1373.15 K with a heating-/cooling rate of 2 $K{\cdot}min^{-1}$. The linear CTE were calculated by fitting the data with a third order polynomial function (**Equation 10**).

Equation 10

$$f(T) = A + \alpha(T - T_{ref}) + \beta(T - T_{ref})^2 + \gamma(T - T_{ref})^3$$

4.2.6.3 Density measurements

The green density of the pellets was determined geometrically. The density of sintered bodies was measured using Archimedes principle with water as the immersion liquid at ambient temperature and with a He pycnometer (Micromeritics ACCUPYC 1340) for the determination of total and closed porosity, respectively.

4.2.6.4 Plane wave/parallel plate ultrasound spectroscopy

Elastic stiffness coefficients were determined at ambient temperatures (293 – 296 K) by plane wave/parallel plate ultrasound spectroscopy at the Institut für Geowissenschaften, Goethe-Universität, Frankfurt am Main, Germany. The method and the setup employed have been previously described by Arbeck et al. [210]. In the case of ceramic materials with random crystallographic orientation, there is no need to orient the samples. The absence of a texture was concluded from neutron diffraction experiments using the HIPPO diffractometer at LANSCE 16 and electron backscattering diffraction experiments. The resonance frequencies were obtained by the excitation of mechanical oscillations of the sample using an ultrasound transducer driven by an impedance analyzer (HP 4395A network analyzer; Hewlett Packard, Palo Alto, CA). The resonant frequencies were determined by measuring the phase angle between the current and the voltage. For the acoustic coupling of the sample to the transducer, paraffin oil or resin was employed. The sound velocities, v, were obtained by calculating the separation between neighboring resonant frequencies, Δf (**Equation 11**).

Equation 11

$v = 2D\Delta f,$ (D is the thickness of the sample).

The relation between the sound velocities and the elastic stiffness coefficients is given by **Equation 12**:

Equation 12

$\mathrm{v} = \sqrt{\rho / c}_{\mathrm{ij}}$,

where c_{ij} are elastic stiffness coefficients and q is the sample density [211]. For isotropic materials it is sufficient to obtain the longitudinal and shear acoustic velocities in order to be able to calculate other mechanical properties, such as the bulk modulus (K), shear modulus (G), Poisson's ratio (η) or Young's modulus (E) [212]:

Equation 13

$\mathrm{K} = \mathrm{c}_{11} - \frac{4}{3}\mathrm{c}_{44}$

Equation 14

$\mathrm{G} = \mathrm{c}_{44}$

Equation 15

$$\eta = \frac{3K-2G}{6K+2G}$$

Equation 16

$$E = 2G(1+\eta)$$

4.2.6.5 Vickers indentation

Microhardness was measured with a Vickers diamond indenter (Anton Paar MHT 10). The thoroughly polished and thermally etched surface of hot-pressed pellets as well as (100) face of reference single crystals was indented between with loading forces 0.5 and 3.5 N to determine the optimal loading force. The full indentation load was applied for 10s. For each indenting force, fifteen measurements were performed. Based on these measurements, values were determined for the average microhardness, fracture toughness and their experimental dispersions. The equations, applied for the microhardness and fracture toughness determination are given in the work [67]. The Young's modulus used for $La_{0.5}Eu_{0.5}PO_4$ was 168 GPa [213].

4.2.7 Dissolution experiments

4.2.7.1 Dynamic dissolution of $LaPO_4$

Dynamic dissolution experiments were performed with the prepared $LaPO_4$-monazite powder (see the sample preparation in **Subchapter 4.1.2.6**) using two different experimental set-ups depending on the temperature conditions. A single pass flow through (SPFT) experimental set-up adapted from Dacheux et al. [214] and Neeway et al. [215], and used in recent studies by Brandt et al. [44] was used for dissolution tests at 323, 333, and 353 K, respectively. The set-up consists of a perfluoroalkoxy polymer (PFA) reactor (Savillex) with a total volume of 50 mL placed inside a thermostatic oil bath, and a peristaltic pump, passing the inlet solution through the reactor. All experiments were carried out using 0.01M HNO_3 (Merck, Suprapur®) and employing 0.8 g of monazite powder. A flow rate between 0.18 and 0.7 mL min^{-1} was set and monitored by weighing the outflowing solution mass before sampling. The outlet solution was sampled regularly. The La-concentrations in the filtered and acidified samples were determined by ICP-MS (see **Subchapter 4.2.1.1**).

Moreover, experiments to temperatures up to 403 K were conducted in a hydrothermal mixed flow setup using a reactor system similar to the one used by Oelkers and Poitrasson [47] and described in detail by Finkeldei et al. [216]. The experimental setup consisted of a pressurised titanium reactor (Parr Instruments) with a total volume of 50 mL, equipped with a pressure gauge, an externally driven stirring system and a thermocouple. The acidic inlet solution was passed into the reactor by a high pressure liquid chromatography pump. The outflow of the reactor was regulated by a computer controlled pressure valve and was filtered through a Ti-cylinder frit with a pore size of 2 μm and an in-line Ti-filter with 0.5 μm pore size to avoid the loss of fines. At the start of a dissolution experiment, about 0.8 g of the $LaPO_4$ powder and 35 mL of 0.01 N HNO_3 (Merck) were placed into the reactor, which was pressurised with He and heated up to the desired temperature. During the experiment the reactor was continuously stirred at a low stirring rate of 100 rpm. The pressure was kept constant by pumping fresh solution into the reactor at pump rates of 0.5 to 0.6 mL min^{-1} and continuously releasing solution through the pressure valve. Samples were taken, filtered and analysed in the same way as for the experiments in the SPFT experimental setup with the PFA reactors.

Normalised steady state monazite dissolution rates (r_{mon}) were calculated from the outlet solution concentrations of La ($C_{(La)}$) using **Equation 17**, where F equals the fluid flow rate, $X_{(La)}$ is the stoichiometric factor representing the mass fraction of La in $LaPO_4$, and A_S represents the total surface area of the powder present in the reactor at the start of the experiment.

Equation 17

$$r_{mon} = F \cdot C_{(La)} / X_{(La)} \cdot A_S$$

4.2.7.2 Thermodynamic modelling with GEM-Selektor software

The preferential stability of anhydrous and hydrated La-orthophosphate phases in the temperature range from 298 to 368 K was addressed using a thermodynamic modelling approach to support the interpretation of the dissolution experiments. The modelling was performed using the GEM-Selektor software ver. 3.3. [217]. In GEM-Selektor, the phase equilibrium is found via direct minimisation of the total Gibbs energy of the system defined by its bulk elemental composition, temperature, pressure and standard Gibbs energy per mole of all chemical species. The chemical thermodynamic database implemented in GEM-Selektor based on SUPCRT92 [218] and the

PSI/NAGRA Chemical Thermodynamic Database 12/07 [219] was extended to include data for the relevant solid phases (cf. **Table 4**). Thermodynamic properties of $LaPO_4$-monazite were taken from Tardy and Vieillard [220], Popa and Konings [161] and Neumeier et al. [110], respectively, and added to the GEM thermodynamic database; for La-rhabdophane ($LaPO_4 \cdot 0.667H_2O$) data from Gausse et al. [65] were employed. For the thermodynamic modelling an input recipe reflecting the experimental conditions in the dissolution experiments was used by adding 20 g La-monazite to 1 kg 0.01 molar HNO_3 solution (i.e. solid to liquid ratio 1:50). Both La-rhabdophane and La-monazite were specified as possible stable phases under these conditions.

Table 4. Thermodynamic data for La-monazite ($LaPO_4$) and La-rhabdophane ($LaPO_4 \cdot 0.667H_2O$) used for GEMS modelling. Coefficients a, b and c refer to the polynomial coefficients describing the temperature dependence of the heat-capacity C_p according to $C_p = a + b \cdot 10^{-3}T - c \cdot 10^{-6}T^{-2}$.

	$\Delta G_f°$ (kJ mol^{-1})	$\Delta H_f°$ (kJ mol^{-1})	S° (J mol^{-1} K^{-1})	*a*	*b*·10^3	*c*·10^{-6}
La-monazite	-1843.8[a]	-1994.36	108.28	121.1275	30.1156	-2.5625
La-rhabdophane	-2004 ± 2	-2151 ± 13	170 ± 36			

[a] average value from Tardy and Vieillard [220] and Popa and Konings [161]

5 Results and discussions

The **Chapter 5** is thematically divided in four parts. The effect of the synthesis route on crystal structure and shape of phosphate precursor powders and the subsequent sintering of the obtained monazite precursors are discussed in detail in the **Subchapters 5.1** and **5.2** respectively on the example of the equimolar $La_{0.5}Eu_{0.5}PO_4$ composition. Eu served thereby as a surrogate for actinides. The **Subchapter 5.3** is dedicated to the structural investigations of the formation of the monazite- and rhabdophane-type solid solutions by incorporation of surrogates for actinides (Eu^{3+}, Gd^{3+}) and actinides (Cm^{3+}, Pu^{3+}) into $LaPO^4$ matrix. The results of systematic studies on thermodynamic, physical and mechanical properties, as well as dissolution behaviour of monazite-type ceramics are presented in the **Subchapter 5.4**.

5.1 The effect of the synthesis route on crystal structure and morphology of monazite precursor powders

The present Subchapter focuses on the effect of the synthesis route on crystal structure and morphology of $La_{0.5}Eu_{0.5}PO_4$ monazite precursors, where europium serves as a nonradioactive surrogate for trivalent actinides. The intermediate $La_{0.5}Eu_{0.5}PO_4$ composition was chosen to prove the independence of formation of pure phase monazite-type solid solutions on synthesis route. The monazite precursor powders with different particle morphologies were synthesised by three different synthesis methods: HTS-1, HTS-10, Prec-1. A variation of morphologies of precursor powders is required for fabrication of monazite-type ceramics with controlled microstructure (please, refer to **Subchapter 5.2**).

5.1.1 Thermal behaviour of monazite precursor powders from different synthesis methods

It is well known from the literature that the lanthanide phosphates tend to precipitate in a rhabdophane structure as a low-temperature precursor (see **Chapter 2.2**). The phase composition, crystallinity and morphology of the precursor powders strongly depend on the synthesis conditions and compositions chosen [53]. The first step of the phase transition from rhabdophane ($Ln\text{PO}_4{\cdot}0.667\text{H}_2\text{O}$) to monazite ($Ln\text{PO}_4$) is the dehydration of the rhabdophane phase which goes along with a weight loss of about 4.7%. The temperature of the subsequent transition from anhydrous rhabdophane to monazite depends on the composition and is expected to occur between 923 K and 1173 K [62, 66, 69]. Thermogravimetric measurements were performed in order to investigate the dependency of the transition temperature on the synthesis route and to choose the calcination and sintering temperatures for the precursor materials. In **Figure 5**, the thermograms of precursors with the nominal composition $La_{0.5}Eu_{0.5}PO_4$, synthesised by different hydrothermal synthesis routes (HTS-1 and HTS-10), are plotted. A major mass loss of 4% for HTS-1 and 6% for HTS-10.5 was measured up to 673 K due to desorption of adsorbed water [221] and the transformation from a hydrated to anhydrous rhabdophane due to complete elimination of water molecules [59]. Between 873 K and 1323 K, there is a reaction in the material which results in a significant exothermic signal in the thermogram. This exothermic effect can be assigned to the rhabdophane-monazite phase transition and is in very good agreement with the literature [62, 67]. For the coprecipitated material (Prec-1), no thermogram was plotted since the precipitate crystallizes in a monazite crystal structure right after synthesis (**Figure 6**). Thus the thermogram is mostly horizontal.

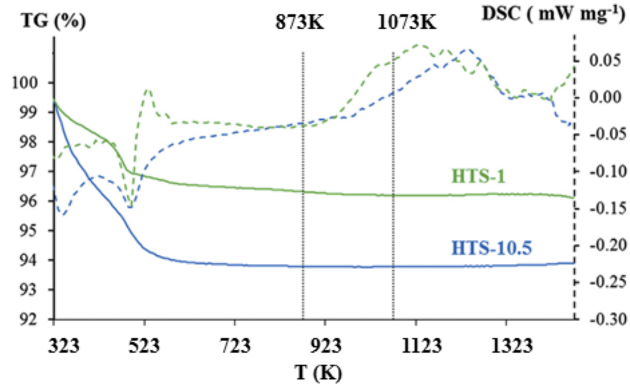

Figure 5. TG-DSC curves of $La_{0.5}Eu_{0.5}PO_4$ powders synthesised by the hydrothermal method: HTS-10.5 (blue) and HTS-1 (green).

5.1.2 Crystal structure of monazite precursor powders from different synthesis methods

Powder X-ray diffraction

PXRD measurements were carried out on $La_{0.5}Eu_{0.5}PO_4$ powders in dependence on the synthesis route and temperature in order to investigate the crystal structure of the precursor materials right after synthesis and to follow the conversion process. Therefore, the crystal structure of the powders was analysed at different stages of the crystallisation process: directly after synthesis and after thermal treatment at 873 K, 1073 K and 1723 K. These temperatures were chosen based on TG-DSC measurements and the literature [62, 69]. The results are summarised in **Figure 6**. As can be seen from the XRD patterns, the crystal structure and degree of crystallinity of the precursor materials after drying at 373 K, 12 hours differ significantly. The Prec-1 sample (orange line) crystallizes in a monazite structure and exhibits a high crystallinity, as evidenced by the narrow full width at half maximum (FWHM) of the XRD reflexes. According to the literature [53] the formation of the monazite-type precursor solid solution can be attributed to the fact that the precipitation occurred at elevated temperature (413 K). In contrast, the diffractograms of the precursors synthesised hydrothermally (HTS-10 (a) and HTS-1 (b)) in addition to monazite reflexes of low intensity show typical reflections assigned to a rhabdophane XRD pattern (e.g. at 20° 2θ) although the precursors were synthesised at 473 K. Obviously, the phase transition from rhabdophane to monazite is suppressed by the pressure applied under hydrothermal conditions (p ~35 bar) even at higher temperatures. However, the spherical precursor material (i.e. HTS-10) exhibits broad reflexes, which are assigned to the less pronounced degree of crystallinity, on the one hand, and to the nanosized dimensions of the spherical grains compared to the needle-like particles, on the other hand. The XRD pattern of the precipitation sample (Prec-1) does not change significantly after thermal treatment at 873 K, 1073 K and 1723 K since a monazite structure of high crystallinity was already evident for the untreated precursor material. In contrast, the crystal structures of the hydrothermally synthesised samples (HTS-10 and HTS-1) showed a phase transition from a rhabdophane to monazite structure when the samples were heated from 873 K to 1073 K. Characteristic reflections of the rhabdophane structure at 15°2θ and 20°2θ vanish, while characteristic reflexes of the monazite structure at 27°2θ and 35°2θ appear after thermal treatment at 1073 K. Since the PXRD patterns collected from crushed pellets prepared after sintering at 1723 K are similar for all synthesis routes only one is inserted in **Figure 6** exemplarily. It shows a monazite pattern of pure single-phase $La_{0.5}Eu_{0.5}PO_4$ solid solution with high crystallinity. As can be seen from the data listed in **Table 5** the refined unit-cell parameters of the $La_{0.5}Eu_{0.5}PO_4$ solid solution from this study and data of the pure endmembers from literature are in very good agreement assuming that the solid solutions follow Vegard's law.

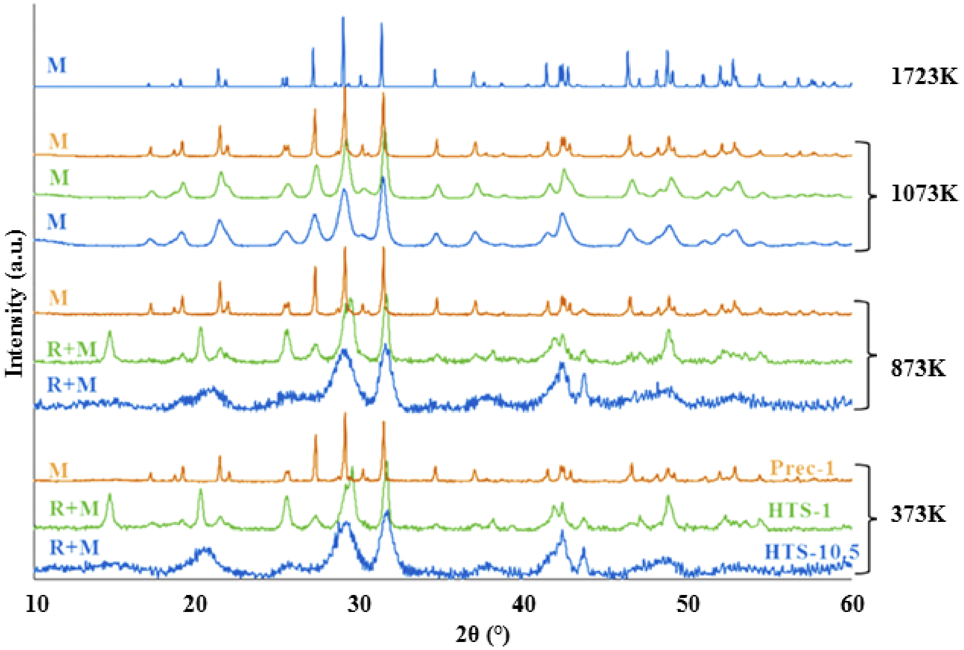

Figure 6. PXRD patterns of $La_{0.5}Eu_{0.5}PO_4$ samples in dependence on synthesis route and temperature.

Table 5. Unit cell parameters of $La_{0.5}Eu_{0.5}PO_4$ in comparison with reference data.

Composition	a (Å)	b (Å)	c (Å)	β (°)	V_{uc} (Å^3)	Ref.
$LaPO_4$	6.8313(1)	7.0705(9)	6.5034(9)	102.27(1)	305.7(3)	a
$La_{0.5}Eu_{0.5}PO_4$	6.7521(9)	6.9664(1)	6.4332(1)	103.63(7)	294.0(7)	b
$EuPO_4$	6.6613(1)	6.8618(9)	6.3491(8)	103.96(1)	281.6(4)	a
$La_{0.9}Pu_{0.1}PO_4$	6.8396(8)	7.0777(1)	6.5008(2)	103.2(7)		c
$PuPO_4$	6.7641(2)	6.9841(2)	6.4536(2)	103.640(2)	296.28	d
$AmPO_4$	6.73	6.93	6.41	103.50	290.29	e
$CmPO_4$	6.72	6.93	6.37	104.63	287.70	f

V_{uc}: unit cell volume

Ref.: a: [42]; b: this work; c: [126]; d: [125]; e: [71]; f: [118]

Of interest is the fact that the solid solution investigated here consists of a $4f^0$element (La^{3+}) and a $4f^6$ element (Eu^{3+}). In addition a pure single phase solid solution formation of a $La_{(1-x)}Gd_xPO_4$ (x = 0 – 1) series consists of a $4f^0$ element (La^{3+}) and a $4f^7$ element (Gd^{3+}) has been published by Terra et al., 2003 [69]. It can be concluded that the solid solution formation depends mainly on the ionic radius and the oxidation state of the ions and not on the electronic configuration of the elements. Since monazite structure of pure $PuPO_4$ [125], $AmPO_4$ [71], $CmPO_4$ [118] as well as of $La_{0.9}Pu_{0.1}PO_4$ solid solution [126] has been published a structural incorporation of Pu^{3+} ($5f^5$), Am^{3+} ($5f^6$) and Cm^{3+} ($5f^7$) on defined lattice sites of the $LaPO_4$ matrix with high loadings and a single phase solid solution formation can be expected. The ionic radius of Eu^{3+} is smaller compared to those of the minor actinides, Am^{3+} and Cm^{3+} [43]. Therefore, a lattice expansion will occur due to partially incorporation of the bigger trivalent actinide ions. This effect will yield a shift to lower 2θ values in the PXRD and to lower wavenumber in Raman spectra but a miscibility gap of a monazite-type $La_{(1-x)}An_xPO_4$, An = Am^{3+}, Cm^{3+},Pu^{3+} solid solution can be excluded because the $AnPO_4$ monazites reveal smaller lattice parameter compared to the pure $LaPO_4$ monazite matrix (**Table 5**). However, studies on actinides bearing ceramics are essentially needed.

Raman spectroscopy

The results from PXRD investigations were confirmed by Raman measurements recorded on the precursors and compounds thermally treated at 1073 and 1723K. For all samples, the usual bands corresponding to the internal vibration modes of phosphate entities were observed (**Figure 7**). The main bands for the monazite compound after sintering are compiled in **Table 6** in comparison to the modes of the pure $LaPO_4$ and $EuPO_4$ monazites [222] . The ν_2 (P-O) symmetrical bending mode from 400 cm^{-1} to 500 cm^{-1} with a central band at 467 cm^{-1}, the ν_4 (P-O) asymmetrical bending mode from 540 cm^{-1} to 650 cm^{-1} with the maximum band at 622 cm^{-1} as well as the η_1 (P-O) symmetrical stretching mode at 978 cm^{-1} and the ν_3 (P-O) asymmetrical stretching modes between 1050 cm^{-1} and 1100 cm^{-1} with the maximum band at 1061 cm^{-1} are evident. The positions of the normal modes of the $La_{0.5}Eu_{0.5}PO_4$ solid solutions are as expected between those of the pure $LaPO_4$ and $EuPO_4$ endmembers and in good agreement with the literature [46, 111, 222]. In the range of 700 – 800 cm^{-1} no characteristic vibration bands associated to the P-O-P bridge of diphosphate entities or polytrioxophosphate groups are evident [223]. Additionally, some less intense vibration bands were detected from 100 cm^{-1} to 300 cm^{-1} and were assigned to lattice vibration modes. Even though rhabdophane and monazite phases presented similar Raman spectra, some differences were obvious between the various samples investigated. First, the precursor compounds obtained from the hydrothermal synthesis routes (HTS-10 and HTS-1) exhibited a shift towards higher wavenumbers for the symmetrical stretching mode (ν_1) compared to the Prec-1 sample. In addition, the band assigned to the asymmetrical stretching vibration (ν_3) appeared to be very weak. Such features argue in favour of the formation of rhabdophane-type compounds in the preparation conditions considered here, as they are fully consistent with the data reported in the literature for $Ln\mathrm{PO_4{\cdot}0.5H_2O}$ samples [64]. On the other hand, all the other samples, i.e. Prec-1 precursor and fired compounds, appeared to exhibit typical Raman spectra of monazites [46, 111]. Furthermore, the comparison of the width of the vibration bands confirmed that the best crystallisation state was obtained when the samples were precipitated at 413 K.

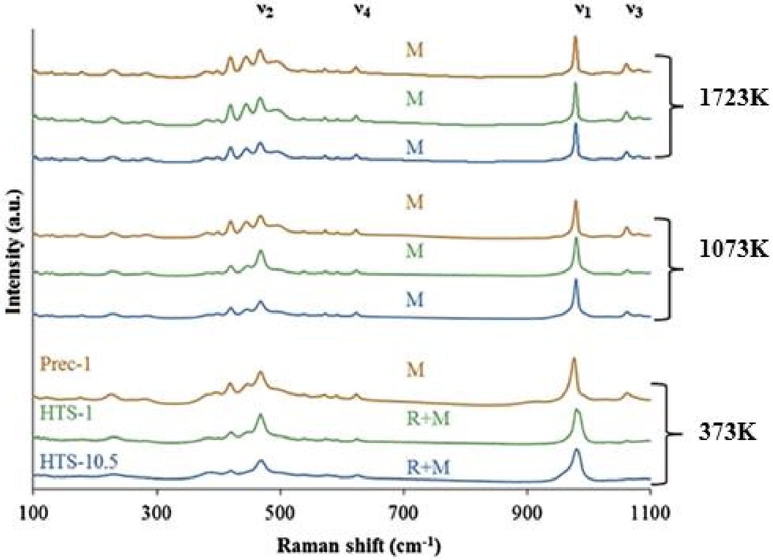

Figure 7. Raman spectra of $La_{0.5}Eu_{0.5}PO_4$ precursors after drying at 373 K, 12 h; after calcination at 1073 K, 2 hours and after sintering at 1723 K, 5 hours in dependence on the synthesis route.

Table 6. Experimental Raman shifts (cm^{-1}) of $La_{0.5}Eu_{0.5}PO_4$ (HTS-10, HTS-1, Prec-1) monazite samples after sintering at 1723 K, 5 hours, in comparison to pure endmembers [222]

		Raman shift (cm^{-1})				
Normal modes	Vibration	$LaPO_4$	HTS-10	HTS-1	Prec-1	$EuPO_4$
ν_2	sym. bending (δ_S)	466	467.5	467.5	467.2	472
ν_4	asym. bending (δ_{AS})	620	622.9	622.7	622.6	631
ν_1	sym. stretching (ν_S)	968	979	978.8	978.5	990
ν_3	asym. stretching (ν_{AS})	1054	1061.4	1061.3	1060.9	1069

5.1.3 Morphology of monazite precursor powders from different synthesis methods

The morphology of powder precursors was investigated by SEM after calcination at 873 K for 2 hours (before the phase transition). The micrographs (**Figure 8**) reveal significant differences in the morphology. In the HTS-10 precursor, nanosized spherical particles form soft but relatively dense agglomerates. In comparison, HTS-1 crystallises in a needle-like shape that is typical of rhabdophane-type compounds, and the precipitation method (Prec-1) yields rice-shaped precursors. As the size of particles formed by HTS-10 method is smaller compared to that from HTS-1 method (**Table 7**) a larger surface area is present to adsorb more water molecules on the surface which clarifies the larger water release from the HTS-10 product compared to HTS-1 (**Figure 5**). From EDS measurements, the chemical composition of all precursors were found to be exactly the nominal composition $La_{0.5}Eu_{0.5}PO_4$ taking into account an uncertainty of EDS results of 2 – 10%. The EDS results of precursor compositions are summarised in **Table 7**.

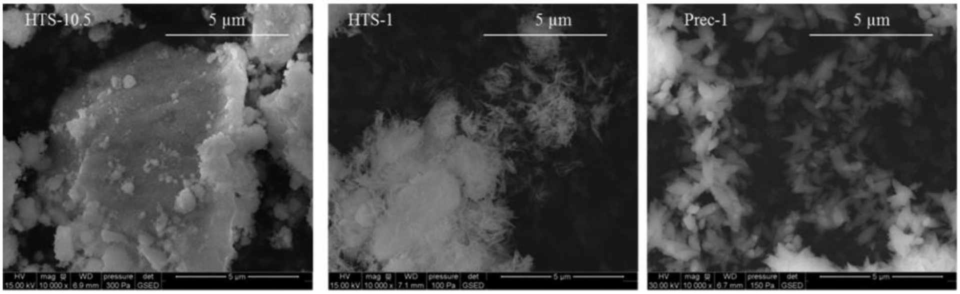

Figure 8. SEM micrographs of $La_{0.5}Eu_{0.5}PO_4$ precursors synthesised by different routes after calcination at 873 K, 2 h. Left: hydrothermal synthesis (pH 10.5, HTS-10), spherical grains; middle: hydrothermal synthesis (pH 1, HTS-1), needle-like grains; right: Co-precipitation (Prec-1), rice-shaped grains.

Table 7. Overview of synthesised samples: chemical composition (EDS); shape of precursors (SEM); crystal structure of precursor and sintered pellets (XRD).

Sample	Chemical composition	Shape of precursor	Particle size (µm)	Crystal structure	
				Prec.	Pel.
HTS-10	$La_{0.495}Eu_{0.505}PO_4$	Spheres	Nanosized	R/M	M
HTS-1	$La_{0.496}Eu_{0.504}PO_4$	Needles	L: 1.0(2) W: 0.10(5)	R/M	M
	$La_{0.504}Eu_{0.496}PO_4$	Rice grains	L: 1.0(3) W:0.5(1)	M	M

R: rhabdophane; M: Monazite; L: length; W: width; Prec.: precursor; Pel.: sintered pellet

5.1.4 Résumé of Chapter 5.1

In **Chapter 5.1** the effect of the synthesis route on crystal structure and shape of phosphate precursor materials for subsequent sintering (sintering is discussed in detail in **Chapter 5.2**) was discussed in detail. $La_{0.5}Eu_{0.5}PO_4$ precursor powders with spherical, needle-like and rice-shaped particles were successfully synthesised by hydrothermal precipitation at basic (pH 10) and acidic (pH 1) conditions as well as by co-precipitation at pH 1 and 413 K, respectively. From TG-DSC, temperatures for thermal treatment were selected. It was found that the phase transition occurs between 873 K and 1073 K which is in good agreement with the literature. XRD and Raman analysis showed that the precursor from precipitation crystallizes in a monazite structure right after synthesis, while the precursor materials from hydrothermal synthesis have an additional rhabdophane phase. The PXRD of the spherical particles showed broad signals due to lower crystallinity and particle size. After cold pressing and sintering at 1723 K for 5 h, all solid solutions showed a pure single-phase monazite structure with high crystallinity.

5.2 The effect of powder morphology on sintering kinetics and microstructure of sintered pellets

The importance of pellets fabrication with defined microstructure by sintering is very important for an application of ceramic materials as a nuclear waste form and often underestimated. The microstructure of a pellet is mainly governed by the synthesis method and conditions of sintering. Moreover, the sintering kinetics is dominated by the morphology of the precursor powder that can be tuned by the synthesis conditions.

The effect of the synthesis route on the shape of phosphate precursor materials for subsequent sintering was investigated and described in detail in **Chapter 5.1**. Within this chapter the influence of the precursor morphology on sintering kinetics and on the final microstructure of sintered pellets are described. Moreover, the microstructural dependence of the mechanical properties of the pellets will be discussed in **Section 5.4.3**.

5.2.1 Characterization of monazite powders and green specimens.

XRD patterns of the as synthesised, calcined and sintered powders from the hydrothermal synthesis route (i.e. HTS-1 and HTS-10) are presented in **Figure 6**. As discussed in **Chapter 5.1**, a mixture of rhabdophane and monazite phases was obtained after synthesis for both precursor powders. Powders were then fully converted into the monoclinic monazite-type structure (space group $P2_1/n$) after heating at 1073 K. The unit cell parameters determined from Rietveld refinement (cf.

Table 8) also confirmed the formation of a pure monazite phase for both powders studied. Indeed, the values obtained are in very good agreement with the average of the unit cell parameters reported for pure $LaPO_4$ and $EuPO_4$ endmembers [23].

Morphological investigation conducted by SEM on $La_{0.5}Eu_{0.5}PO_4$ powders were discussed in **Chapter 5.1**. Apparently, the observed higher green density (58% TD) for the HTS-10 specimen in comparison to the green density of the HTS-1 specimen (55% TD), obtained after pelletization of calcined powders using uniaxial pressing at 250 MPa, is mainly linked to the morphology of the powders. Indeed, dense packing of small spherical particles of the HTS-10 powder is more favorable in comparison to that of larger needle-like particles of the HTS-1 powder.

Table 8. Crystallographic data and physico-chemical properties of monazite-type $La_{0.5}Eu_{0.5}PO_4$ samples prepared after calcination of precursor powders at 1073 K for 2 hours.

	HTS-1	HTS-10
x_{Eu}, molar fraction	0.505(5)	0.504(5)
a (Å)	6.7615 (5)	6.7521(9)
b (Å)	6.9796(4)	6.9664(1)
c (Å)	6.4417(4)	6.4332(1)
β (°)	103.623(5)	103.63(7)
V ($Å^3$)	295.45(6)	294.0(7)
Spec. surface area ($m^2 \cdot g^{-1}$)	155(1)	110(1)
Green density (% TD)	55.3(1)	58.2(2)
Grain size	W: 0.05(5) µm; L: 1.1(2) µm	0.01-0.05 µm [81]

5.2.2 Sintering kinetics and microstructure evolution

5.2.2.1 General grain growth kinetics determination from HT-ESEM data

The impact of the morphologies of the starting powders on the development of the microstructure and sintering kinetics of the compacted specimens by conventional isothermal sintering were studied by an *in situ* high temperature environmental scanning electron microscopy (HT-ESEM) technique. Prior to HT-ESEM *in situ* observations, preliminary dilatometry experiments were performed in order to estimate the optimal temperature for the densification of $La_{0.5}Eu_{0.5}PO_4$ monazite pellets (**Figure 9**). Both samples investigated exhibited similar densification profiles but with slightly different characteristic temperatures. Indeed, while the densification onset was detected around 1193 K for both powders, a maximal shrinkage rate was reached at a lower temperature for the HTS-10 sample (1443 K) than for the HTS-1 sample (1503 K), probably due to the higher reactivity of the nanoscale powder obtained in basic conditions. As a consequence, complete densification of the pellet was achieved at lower temperature for HTS-10 (1573 K) than for HTS-1 (1613 K). This result is in good agreement with the data reported in the literature which frequently indicates 1623 K as the optimal temperature to sinter monazite-type compounds, that can be lowered by the use of nanoscale powders (such as HTS-10 sample). On this basis, the operating conditions for *in situ* HT-ESEM experiments were set to a heating rate of 30 K·min^{-1} with an isothermal dwell of 7 hours at 1613 K to specifically study the grain growth step (**Figure 9**, pink area).

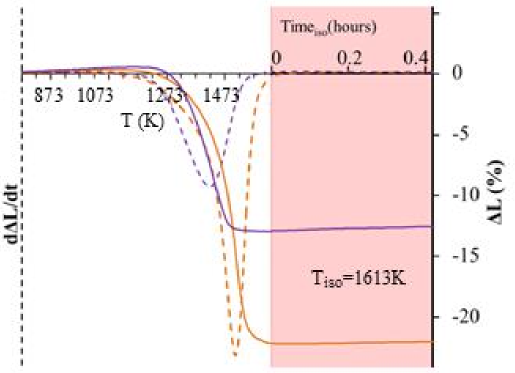

Figure 9. Dilatometric curves (solid line) and their derivatives (dashed line) for the two precursors (HTS-1, orange; HTS-10, purple) as a function of temperature (heating rate 30 K·min^{-1}) or time (pink area, T_{iso} = 1613 K).

The grain growth kinetics and microstructure evolution of the HTS-10 and HTS-1 samples were then assessed through direct observation of their surface during *in situ* experiments. ESEM image stacks were recorded at T = 1613 K on the same part of the sample. As an example, selected images from the series obtained *in situ* for the HTS-1 and HTS-10 powders are reported in **Figure 10** and depict the grain growth processes during sintering. Both grain growth and grain elimination dynamics can be observed in the associated videos. The latter, corresponding to the stacking of the images, are available online [224, 225]. It is important to note that prior to any exploitation of the images series, *in situ* microstructure observations on the pellet surface were compared with those of pellets sintered *ex situ* under analogous conditions. The grain size and morphology observed during *in situ* experiments were in good agreement with those obtained from *ex situ* experiments (**Figure 10**). This confirms that there is no effect of the sampling of the green pellets as well as of the electron beam.

At the end of the 7-hour isothermal heat treatment at 1613 K, the bulk microstructure of the HTS-10 pellet consists of well-sintered agglomerates surrounded by less dense regions (**Figure 10**, a). The heterogeneous microstructure is presumably due to the agglomerates already noticed in the starting powder (**Figure 8**). A preliminary mechanical milling sequence could then be required to improve the homogeneity of the microstructure [80]. Well sintered agglomerates consist of spherical grains up to 1.3 µm in diameter with minor intergranular porosity (**Figure 10**, a). On the other hand, the microstructure of the HTS-1 sintered pellet is more homogeneous and represents elongated grains with typical length up to 50 µm and width up to 20 µm, consisting of smaller subgrains with an average grain diameter of 3.6(5) µm with trapped intragranular pores and minor porosity in the grain interstices (**Figure 10**, b). Nevertheless, the relative density of the samples was measured to 94% TD and 96% TD for the HTS-10 and HTS-1 pellets, respectively, which is characteristic of the final stage of sintering and confirmed the completion of the densification process for such operating conditions.

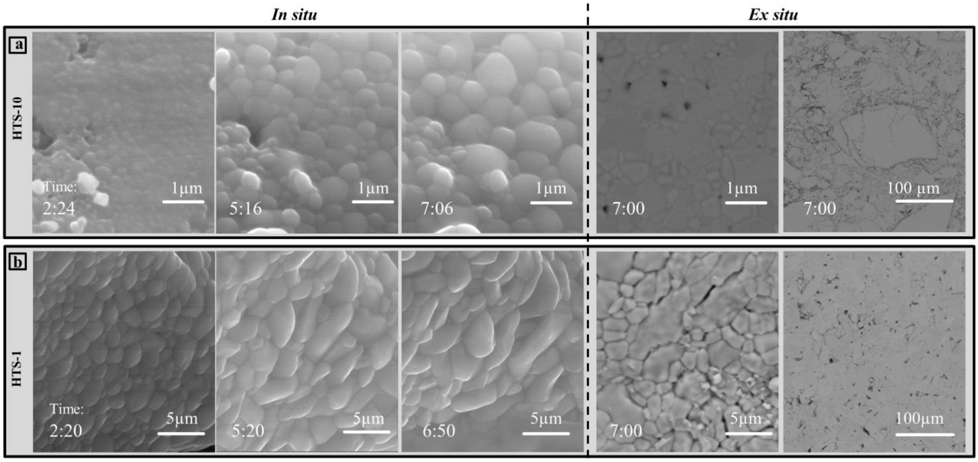

Figure 10. SEM micrographs of $La_{0.5}Eu_{0.5}PO_4$ pellets (HTS-10 (a); HTS-1 (b)) sintered isothermally at T = 1613 K *in situ* for 2, 5 and 7 hours and *ex situ* at T = 1613 K for 7 hours.

The evolution of the average grain diameters was also determined for the HTS-1 and HTS-10 specimens from HT-ESEM experiments performed at 1613 K (**Figure 11**). An about three times higher grain growth rate was observed for the HTS-1 in comparison to that estimated for the HTS-10 specimen (5.0 nm·min^{-1} and 1.5 nm·min^{-1} (initial grain growth rate), respectively).

Nevertheless, one should note that the nanoscale character of the HTS-10 sample precludes accurate grain size determination during the first hours of heat treatment. The logarithmic representation of the holding time dependence of the grain sizes (**Figure 11**, b) was then used for the determination of the grain growth kinetics.

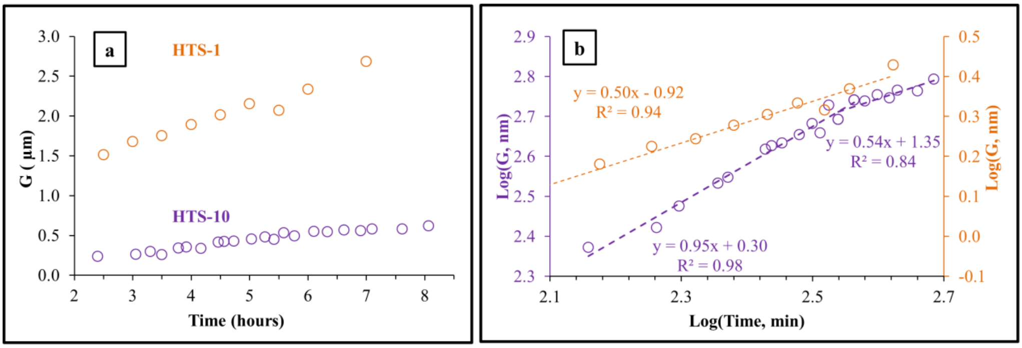

Figure 11. Variation of average grain diameters determined *in situ* from HT-ESEM at T = 1613 K versus holding time for HTS-1 and HTS-10 specimens (a). The log-log plot (b) served for the determination of the n coefficient in the grain growth kinetic equation.

The grain growth kinetic law in the case of the normal grain growth can be represented by **Equation 18** [226]:

Equation 18

$(G^n - G_0^n) = k\,t$

where G is the average grain size at time t, G_0 the initial grain size, k a kinetic constant and n a whole number whose value depends on the mechanism responsible for grain growth [227].

Equation 18 is valid in the case of normal grain growth, i.e. when the granulometric distribution is similar for all the sintering durations [228]. The invariance of the normalised grain size distribution as a function of time of each grain class (with a constant ratio $x = G/G_{average}$), also called self-similarity, was demonstrated experimentally for ceramic materials in a number of references [80, 197, 229-231]. **Figure 12** shows the conservation of grain size distribution as self-similarity for the $La_{0.5}Eu_{0.5}PO_4$ monazite samples HTS-1 and HTS-10 sintered *in situ* (open symbols) and *ex situ* (solid symbols). All the grain size distributions followed similar trends independent of the dwell time (2 – 7 hours). It can be concluded that the grain growth in the

$La_{0.5}Eu_{0.5}PO_4$ ceramic samples remained constant under the given conditions of the *ex situ* and *in situ* experiments with the HTS-10 specimen and of the *in situ* experiments with the HTS-1 specimen. The more pronounced deviation of the self-similarity graph for the HTS-1 specimen from the *ex situ* experiment might be an indication of an abnormal grain growth. The grain size distribution at the surface of the pellet could then be considered as a normal distribution for these cases. For the HTS-10 specimen a significantly narrower grain size distribution was observed for the holding time up to 5 hours compared to that of HTS-1 (**Figure 12**, a). Broadening of the grain size distribution for the HTS-10 specimen after 5 hours of sintering coincides with the deceleration of the grain growth (**Figure 11**).

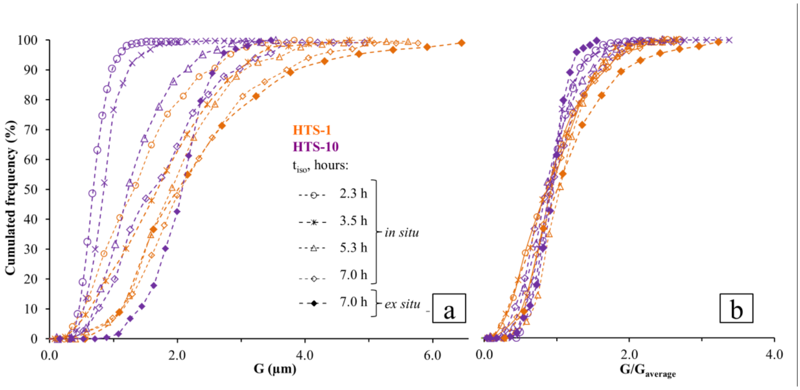

Figure 12. Average grain size distribution (a) and grain distribution self-similarity graphs (b) for different durations of sintering of the precursor specimens (HTS-1, orange; HTS-10, purple) from the *in situ* HT-ESEM experiment (open symbols) and from the *ex situ* experiment after 7 hours (solid symbols).

The grain size in the advanced phase of sintering (0.2 – 0.6 µm for HTS-10 and 1.5 – 2.7 µm for HTS-1, **Figure 11**, a, left) is significantly larger than the corresponding initial grain size for both samples (10 – 50 nm and 0.1 µm, respectively,

Table 8), G_0 can therefore be neglected and **Equation 18** takes the form:

Equation 19

$G^n \approx k\ t$

Using logarithmic representation of **Equation 19**,

Equation 20

$$\mathrm{Log}\,(G) \approx 1/n\ \mathrm{Log}\,(t) + k',$$

the value of the constant n was determined from the slope of the log-log plot of the data of the HT-ESEM experiments (**Figure 11**, b, right) [197, 227, 232].

It led to n = 2 for both HTS-10 (in the advanced stage of sintering) and HTS-1 (for the entire sintering duration) specimens. According to the literature, in a pure and dense ceramic, this number corresponds to the control of grain growth through grain-boundary mobility [227]. The value n = 2 obtained for both samples excludes the possibility of a prevailing abnormal grain growth mechanism. Due to the grain boundary motion the total amount of grain boundary surface area and thereby the total energy of the system decreases. For the HTS-10 specimen, faster grain growth rate was observed and a value of n = 1, usually considered as anomalous in classical grain growth models, was determined in the initial stage of sintering, presumably due to the nano-sized character of the powder. Indeed, several authors already pointed out the particular behavior of nanograins during sintering, notably through the possibility of growth by an oriented attachment process (i.e. mechanical reorientation of the crystalline domains [233-235]). As an effect, the correlated activation energies are generally lowered while the corresponding diffusion mechanism cannot be determined by the classical models anymore [236, 237].

5.2.2.2 Effect of sintering in a hot uniaxial press

Studies of conventional isothermal sintering demonstrated that the morphology of the starting powders significantly affects the sintering kinetics and therefore, the final microstructure of the sintered pellets, even if the mechanisms involved in the densification process remain mostly unchanged. Moreover, *in situ* sintering experiment allows for the optimisation of the sintering time at the given conditions to achieve a desired grain size. Nevertheless, the results obtained also demonstrate that densification of the samples was not sufficient enough to fully eliminate residual porosity and that microstructural heterogeneity can occur when using nanoscale powders. Additional steps such as preliminary grinding and/or sieving could then be needed, but could appear unsuitable in several application cases, such as conditioning of minor actinides in the back-end of the nuclear fuel cycle, due to the generation of highly radiotoxic dust.

The hot-pressing approach allows for increasing the contact between the precursor particles of the green compact by applying pressure during the sintering. It generally lowers the sintering temperature and/or time and leads to the elimination of microstructural heterogeneities and residual porosity. Therefore, the effect of hot-pressing on the sintering capability of HTS-1 and HTS-10 monazite powders at 1613 K was evaluated and the concsequences on the mechanical properties of the resulting pellets were assessed.

In order to avoid potential phosphate decomposition due to the contact with graphite pressing tools (die and punches) while sintering [238], the holding time for the hot-pressing experiments was reduced to 3.5 hours. Nevertheless dense ceramics were obtained for both powders, with density values reaching 99% of the calculated theoretical value. The hot-pressed (HP-) pellets (**Figure 13**) reveal significantly larger grain sizes than samples obtained from conventional sintering. However, the grains of the hot-pressed HTS-10 pellet are smaller than those of the corresponding HTS-1 sample (G = 9 ± 4 μm vs 20 ± 10 μm determined from analysis of 250 and 220 grains, respectively). Minor intergranular porosity remained within both pellets.

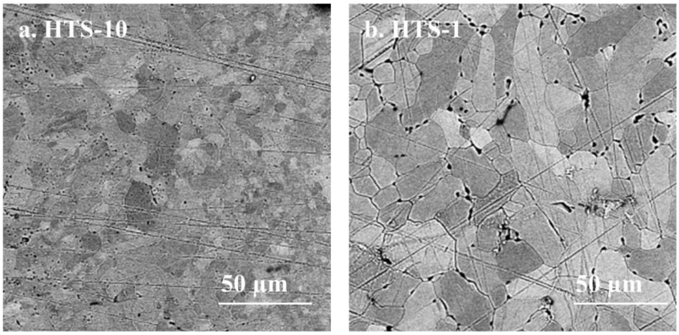

Figure 13. SEM micrographs of $La_{0.5}Eu_{0.5}PO_4$ pellets hot-pressed at T = 1623 K and under a maximum compaction pressure of 50 MPa for 3.5 hours (heating and cooling rate: 10 $K \cdot min^{-1}$ (a. HTS-10, b. HTS-1).

Besides the significant differences in grain size between HTS-1 and HTS-10 HP-pellets, elongation of the grains of the HTS-1 sample was noticeable (aspect ratio 2.0 ± 0.6; **Figure 13**, b). This microstructural feature was already observed for the pellets prepared through conventional sintering and appeared to be directly inherited from the starting powder morphology. The preparation of monazite samples as needle-like grains then significantly impacts the microstructure of final pellets, even when using hot-pressing methods.

Microstructural and structural anisotropic effects of needle-shaped particles of the HTS-1 powder can also be increased by the use of uniaxial pressing for pellet preparation [56]. Thus texture effects in the hot-pressed HTS-1 and HTS-10 pellets were studied by XRD. In order to obtain polycrystalline monazite, i.e. a reference powder with random crystal orientation, calcined HTS-10 powder without prior pelletization was sintered at 1723 K for 2 hours and subsequently ground. XRD data were collected for the HTS-10 powder sample as well as on polished surfaces of the HTS-1 and HTS-10 hot-pressed pellets (**Figure 14**). Analysis of the XRD data revealed a significant increase of the relative intensity of the 200 reflection with simultaneous decrease of the 012 reflection for the HTS-1 HP sample compared to that of sintered HTS-10 powder. It indicates the preferential orientation of the grains along the (100) plane. Such preferential orientation and elongation parallel to the c axis were also observed as one of the common growth habits of idiomorphic natural monazites [239, 240]. For the HTS-10 sintered pellet, this texture effect is less pronounced indicating apparently random crystal orientation. Thus, even when using hot-pressing for pellets fabrication, microstructural and textural properties were still inherited from the initial grain morphology of the starting powders, which can significantly impact the physico-chemical properties of the material.

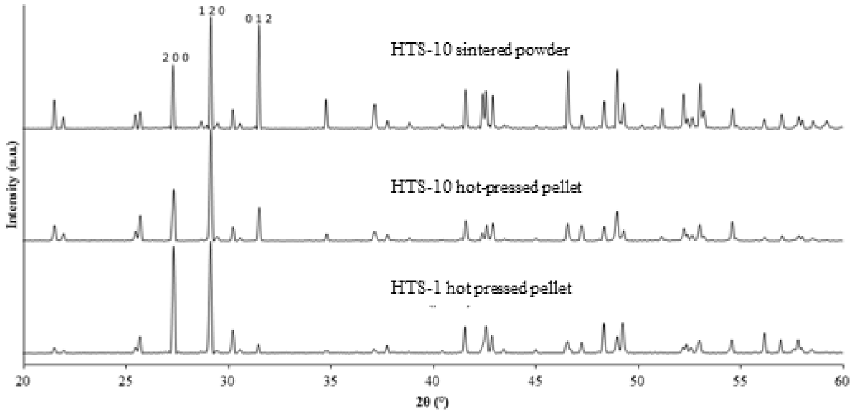

Figure 14. XRD patterns recorded on the HTS-10 powder sample as well as on polished surfaces of the HTS-1 and HTS-10 hot-pressed pellets, normalised to the most intense 120 reflection.

5.2.3 Résumé of Chapter 5.2

Ex situ conventional sintering and *in situ* HT-ESEM experiments demonstrated the dependence of sintering kinetics of $La_{0.5}Eu_{0.5}PO_4$ monazite-type specimens on the morphology of precursor powders. The grain growth rate was significantly higher for the precursor containing needle-shaped micrometric particles compared to that composed of nano-sized spherical particles. In the advanced stage of sintering the grain growth is apparently controlled by grain-boundary mobility in both cases. Therefore, *in situ* sintering experiments allowed for the determination of the holding time needed to achieve a desired grain size for the two powders at the given sintering conditions. High-density pellets (99% of the calculated theoretical density) were obtained from both powders by hot uniaxial pressing. The average grain size determined for the HTS-1 specimen was significantly larger than for the HTS-10 specimen (50 µm vs 15 µm). Analysis of the XRD data collected for the hot-pressed pellets revealed preferential orientation of grains along the (100) plane in the case of the needle-shaped precursor. The microstructural and textural dependence of mechanical properties of the HTS-1 and HTS-10 hot-pressed materials is discussed in detail in **Section 5.4.3**.

The results of this work together with the available literature data on the influence of microstructure and texture on physical properties [56, 58, 73] clearly demonstrate, that the choice of the starting precursor, of the sintering method and of the sintering conditions are essential for the fabrication of material with tailored microstructure and hence allow for an optimization of properties.

5.3 Structural characterization

Within this work formation of $La_{1-x}Ln_xPO_4$ (Ln = Gd, Eu; x = 0 – 1) monazite- and $La_{1-x}Gd_xPO_4$ (x = 0 – 1) rhabdophane-type solid solutions was studied in detail by the combination of XRD and spectroscopic techniques (Raman, TRLFS). To obtain information on the incorporation process of the minor actinide curium (Cm^{3+}) in a series of synthetic $La_{1-x}Gd_xPO_4$ (x = 0, 0.24, 0.54, 0.83, 1) monazite and rhabdophane solid solutions on the molecular scale and to understand the distribution of the dopant in the synthetic phosphate phases, combined time-resolved laser fluorescence spectroscopy (TRLFS) and X-ray absorption fine structure (XAFS) spectroscopy investigations have been conducted and complemented with *ab initio* atomistic simulations. The incorporation of Pu in $La_{1-x}Pu_xPO_4$ (x = 0 – 0.15) monazite-type was investigated by XRD and XAFS analysis. Spectroscopic methods allow for direct probing of the dopant and its local environment in host matrices, providing for a better understanding of potential lattice defect formations, lattice strain or disordering phenomena, and site population deviances with regard to the composition of the host structure, which may occur in the solid phase upon introduction of the dopant. *Ab initio* calculations further deliver descriptions and explanations for spectroscopic findings, thus, contributing to a better understanding of the incorporation processes on a molecular level.

5.3.1 $La_{1-x}Ln_xPO_4$-monazite solid solutions (*Ln* = Gd, Eu)

Phase analysis and chemical composition

$La_{1-x}Ln_xPO_4$-monazite solid solutions (Ln = Gd, Eu; x = 0 – 1) were synthesised by precipitation method followed by thermal treatment (**Section 4.1.1.1**). The actual compositions of the synthesised solid solutions were determined by averaging the results from SEM-EDS and XRF spectroscopy. Since both methods show very similar, data, which are compiled in **Table A 1** of the Appendix**,** the XRF measurements were not performed for all samples.

X-ray diffraction

PXRD patterns of $La_{1-x}Ln_xPO_4$-monazites (Ln = Gd, Eu; x = 0, 0.5, 1) with the corresponding reference from ICSD data base of the pure endmembers are exemplarily plotted in **Figure 15**. PXRD-analysis confirmed the formation of pure monazite solid solutions. The PXRD-patterns show a typical linear shift of reflection positions to higher 2θ values with increasing content of the smaller Eu^{3+} and Gd^{3+} ions [67]. The lattice parameter of $La_{1-x}Ln_xPO_4$ solid solutions were determined by Rietveld refinement and listed in **Table A 2** of the **Fehler! Verweisquelle konnte nicht gefunden werden.**. They are in good agreement with refined data from $LnPO_4$ monazite single crystals and powders existing in the literature [23, 42, 69, 241, 242]. Lattice constants of $(La,Eu)PO_4$ and $(La,Gd)PO_4$ depend linearly on composition and therefore follow Vegard's law (**Figure 16**) confirming the formation of solid solutions.

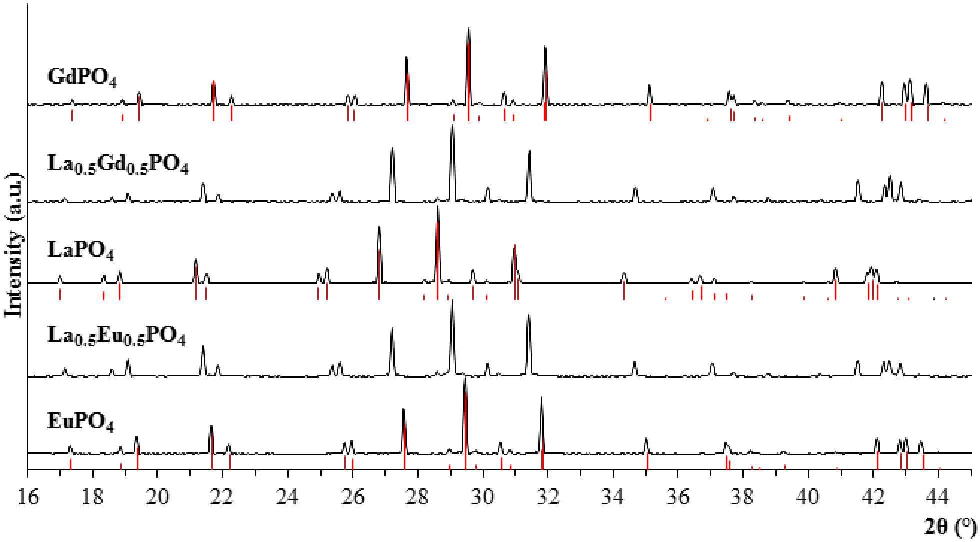

Figure 15. PXRD patterns of $La_{1-x}Ln_xPO_4$-monazites (Ln = Gd, Eu; x = 0, 0.5, 1) with the corresponding reference reflexes [243] for the endmembers.

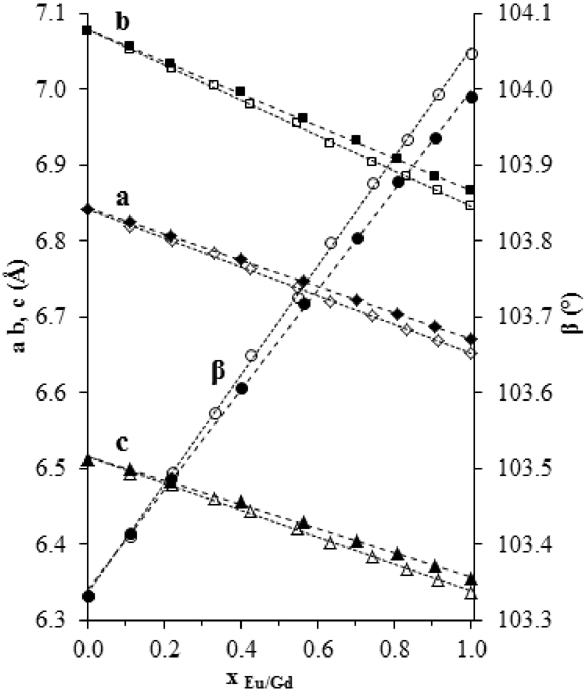

Figure 16. Dependence of lattice constants from composition. Lattice constants for (La,Eu)PO_4 and (La,Gd)PO_4 solid solutions are marked with closed and open symbols, respectively. The uncertainties are within the size of the symbols.

Raman spectroscopy

The Raman spectra of rare earth orthophosphates with monazite structure have been studied extensively for the endmembers [46, 111, 133, 222, 244] as well as for some solid solutions. In the present work, the Raman spectra of $La_{1-x}Ln_xPO_4$-monazites (*Ln* = Eu, Gd) were systematically analysed. Representative spectra of $La_{1-x}Ln_xPO_4$-samples with *Ln* = Gd, Eu, x = 0, 0.5, 1 are presented in **Figure 17** and is in a good agreement with the existing literature data [46, 111, 133, 222, 244]. The spectra of Eu-containing monazites reveal additional discrete fluorescence bands (*). The assignment of the main bands for the monazite structure is discussed in detail in the **Section 5.1.2**. **Table A 3** of the Appendix contains the Raman shift positions of the main modes. The absence of characteristic vibrational bands associated to P-O-P bridge of diphosphate entities or polytrioxophosphate groups (700 – 800 cm^{-1}) [223] proves the purity of the materials. The normal modes of the $La_{0.5}(Eu/Gd)_{0.5}PO_4$ solid solutions are shifted as expected between those of the pure $LaPO_4$ and $EuPO_4/GdPO_4$ endmembers and are in good agreement with the literature [111, 222]. The maxima of symmetrical, anti-symmetrical stretching and bending vibrations $\nu_1 - \nu_4$ as well as of external lattice vibration modes ($I\nu_1 - I\nu_3$) are plotted vs. composition for $(La,Eu)PO_4$ (closed symbols) and $(La,Gd)PO_4$ (open symbols) solid solutions (**Figure 18**). As can be seen by the regression lines, the Raman bands shift linearly to higher wavenumbers with increasing the Eu or Gd content. The incorporation of smaller Eu and Gd cations yields a decrease of the *Ln*-O bond length and hence a lattice contraction [42, 111]. Finally, the lattice contraction leads to an increase of the vibration frequencies and therefore to the observed shift to higher wavenumber. These results are in very good agreement with the XRD data and further confirm the formation of $La_{1-x}(Eu/Gd)_xPO_4$ solid solutions.

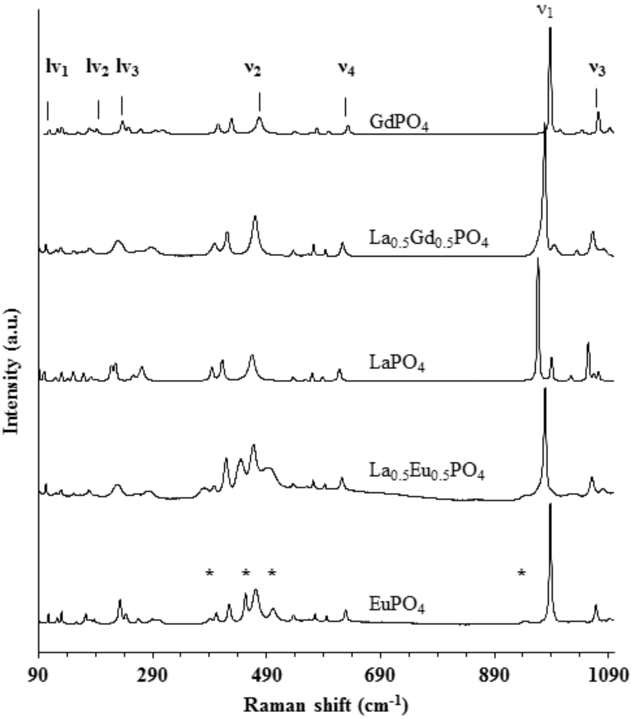

Figure 17. Representative Raman spectra of $La_{1-x}Ln_xPO_4$-monazites (*Ln* = Gd, Eu; x = 0, 0.5, 1) and indications of external lattice (lv_i) and phosphate group vibration modes. ‘‘*” points to the fluorescence modes of $EuPO_4$.

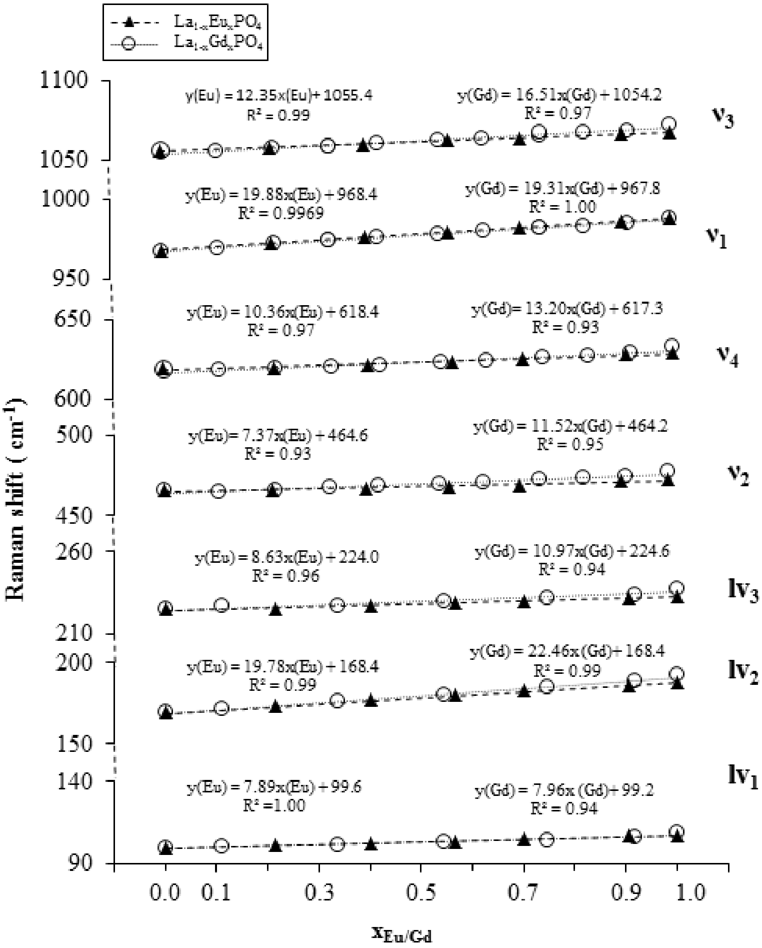

Figure 18. Raman band positions as a function of (La,Eu)PO$_4$ (solid triangles) and (La,Gd)PO$_4$ (open circles) composition for the vibrations of the lattice (lν$_1$ – lν$_3$) and the phosphate tetrahedra (ν$_1$ – ν$_4$).

The evolution of the shape of the Raman peaks along the solid solutions was studied in detail. From the Raman spectra the band half width (FWHM) of the main vibration modes were determined and plotted as a function of composition of the (La,Eu)PO$_4$ and (La,Gd)PO$_4$ solid solutions (**Figure 19**). According to Gouadec and Colomban [132], especially the Raman stretching modes (ν$_1$ and ν$_3$) are sensitive to the disorder of their nearest neighbor atoms in the structure. The FWHM of the symmetrical bending vibration (ν_2) does not depend on the solid solution composition and is between 12 and 13 cm^{-1}. The symmetrical stretching vibration (ν_1) shows a broadening effect when going from the pure endmembers $LaPO_4$ and $(Gd/Eu)PO_4$ towards the composition with x = 0.5. The FWHM of the Raman bands ν_1, ν_3, ν_4 varies from 3 – 4 cm^{-1} for the endmembers up to 8 – 9 cm^{-1} for the solid solutions with x = 0.5. This effect is more pronounced for the antisymmetric bending vibration (ν_4), while the largest Raman peak broadening is observed for the antisymmetric stretching vibration (ν_3).

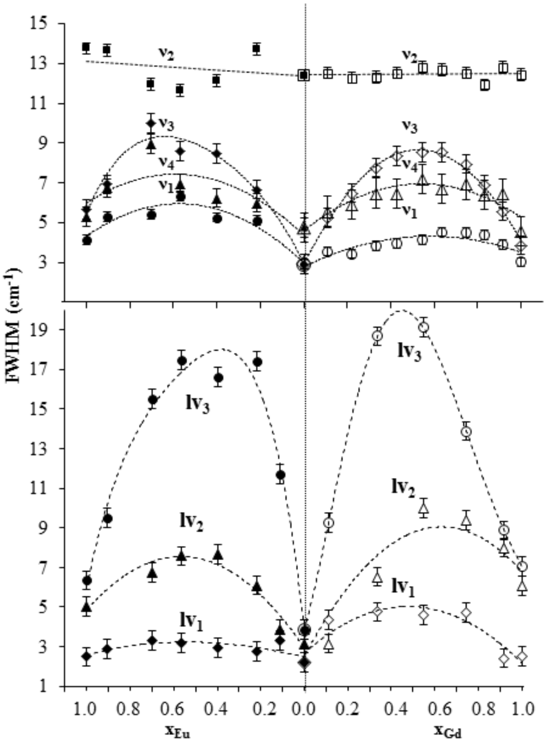

Figure 19. Raman band width as a function of $La_{1-x}(Gd/Eu)_xPO_4$ composition for the internal vibrations of the phosphate tetrahedron ($\nu_1 – \nu_4$) and chosen lattice vibrations ($l\nu_1 – l\nu_3$).

Raman peak broadening has previously been observed in the works [111, 245] investigating the coupled substitution of Ca^{2+} and An^{4+} in the monazite structure. Both authors could show a significant broadening of the Raman bands with increasing actinide content. According to Raison et al. [245], the strong broadening of the ν_1 Raman band indicates that the P-O distance in the cheralites is less well-defined than in the pure endmember monazite-(Ce). The ν_1 band broadening in the present study is not very pronounced, however, the large influence of the $La_{1-x}(Gd/Eu)_xPO_4$ composition on especially the antisymmetric stretching vibration points toward a local distortion of the phosphate tetrahedron when going from the $LaPO_4$ and $(Gd/Eu)PO_4$ endmembers toward the composition with $x = 0.5$. Whether this distortion is due to variations in the P-O distances only, or due to distortions of the cation site, cannot be deduced from the Raman data of the vibrational normal modes alone.

Thus, FWHM of chosen lattice vibrations were plotted against the degree of substitution, x, in **Figure 19**. Raman band broadening when going from the $LaPO_4$ and $(Gd/Eu)PO_4$ endmembers towards the $La_{0.5}(Gd/Eu)_{0.5}PO_4$ composition is visible, to slightly different extents, for all lattice vibrations, **Figure 19**. The FWHM shows a much more pronounced compositional dependency for the LnO_9 associated phonons than the lattice vibrations arising from the phosphate tetrahedron. This would imply that the $La_{1-x}(Gd/Eu)_xPO_4$ solid solution series shows a stronger distortion around the lanthanide cation than around the phosphate anion, which is in concordance with the structural parameters in terms on *Ln*-O and P-O bond lengths in the $LaPO_4$ and $(Gd/Eu)PO_4$ endmembers as discussed above.

The structure and bond lengths of the pure endmembers $LaPO_4$, $EuPO_4$ and $GdPO_4$ are well defined due to the complete ordering of atoms. In the solid solutions the lanthanides of two different sizes are probably distributed close to randomly since the heats of mixing are small (**Section 5.4.1**). The number of different bonding environments is presumably maximized at a mole fraction of 0.5. The influence of different local environments appears to be more pronounced for the external lattice vibration modes ($l\nu_1 - l\nu_3$) because the bond length between the lanthanide cation and the oxygen of the phosphate tetrahedron is more affected by the substitution of a La-cation (r_{La} = 1.216 Å) by other ions with much smaller ionic radii (r_{Eu} = 1.12 Å; r_{Gd} = 1.107 Å) [43]. Moreover, some different behaviour of Eu and Gd during precipitation as instance from the kinetic point of view cannot be excluded. In very recent studies lanthanum was found to precipitate faster compared to gadolinium and europium [65] which may affect the homogeneity of lanthanide distribution within the samples. Finally, the band widths are larger for the Gd compared to Eu substituted compounds, which reflects the larger mismatch of ionic radii within the La,Gd solid solution compared to the La,Eu system. However, the overall results for both solid solutions are very similar with only slightly larger distortions in the case of $La_{1-x}Gd_xPO_4$.

To gain further insight into structural differences in the lanthanide cation environment in the $La_{1-x}Gd_xPO_4$ solid solution series, TRLFS measurements were performed providing exclusive information on the local environment of the trivalent Eu^{3+} dopant. The results obtained from these TRLFS measurements are discussed below.

Time-resolved laser fluorescence spectroscopy

The excitation spectra of all synthesised $La_{1-x}Gd_xPO_4$ solid solution compositions doped with 500 ppm Eu^{3+} are presented in **Figure 20** (solid or dashed lines). The pure endmembers $LaPO_4$ and $GdPO_4$ show one narrow excitation peak with a half width around 1 cm^{-1}, corresponding to Eu^{3+} incorporation on the host lattice sites in the highly crystalline monazite ceramics. The excitation peak maximum is found at 17268 cm^{-1} for $GdPO_4:Eu^{3+}$, i.e. slightly red shifted to lower energy in comparison to the excitation peak at 17289 cm^{-1} for Eu^{3+}-doped $LaPO_4$. This phenomenon we attributed to the longer average *Ln*-O bond distance of 2.579 Å in $LaPO_4$ in comparison to 2.476 Å in the $GdPO_4$ solid [108]. The closer located oxygen ligands in $GdPO_4$ are, thus, exerting a stronger ligand field on the incorporated Eu^{3+} ion, causing a slight decrease in the excitation energy and a subsequent shift of the excitation peak to lower energies. Huittinen et al. [108] have shown that this shift follows a linear trend within the pure monazite endmemberseries ($LaPO_4$, $SmPO_4$, $EuPO_4$, $GdPO_4$) as a function of both ionic radius of the host cation and the average *Ln*-O bond distance. A linear trend depending of the excitation energy is also apparent in the solid solution series when plotting the excitation peak maximum, x_c (values indicated in **Figure 20**), as a function of the Gd^{3+} substitution in $La_{1-x}Gd_xPO_4$, **Figure 21** (left). The excitation peak maxima were obtained by Gaussian fitting of the excitation peaks, and the values are compiled in **Table A 4** in **Appendix**.

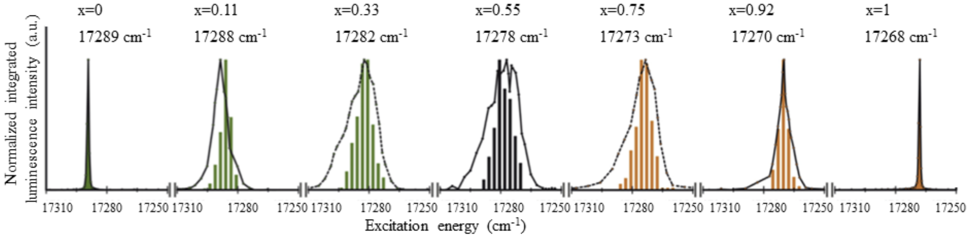

Figure 20. Experimental (solid or dashed lines) excitation spectra of the synthetic $La_{1-x}Gd_xPO_4$ monazite solid solutions doped with 500 ppm Eu^{3+} and simulated average Eu-O bond length distributions (colored or black bars). The simulated profiles are calculated for x-values of 0.1, 0.3, 0.5, 0.7, and 0.9.

The linear fit of the experimental data yields an expression for the excitation peak maximum given by **Equation 21**.

Equation 21

$$x_c(^5D_0 \rightarrow {}^7F_0)\ (\mathrm{cm}^{-1}) = 17290.1 - 21.7 \cdot x\ (La_{1-x}Gd_xPO_4)$$

This allows to predict the excitation peak maximum for known solid solution compositions or conversely, the composition of an Eu^{3+}-doped $La_{1-x}Gd_xPO_4$ solid solution for which the Eu^{3+} excitation peak maximum has been obtained.

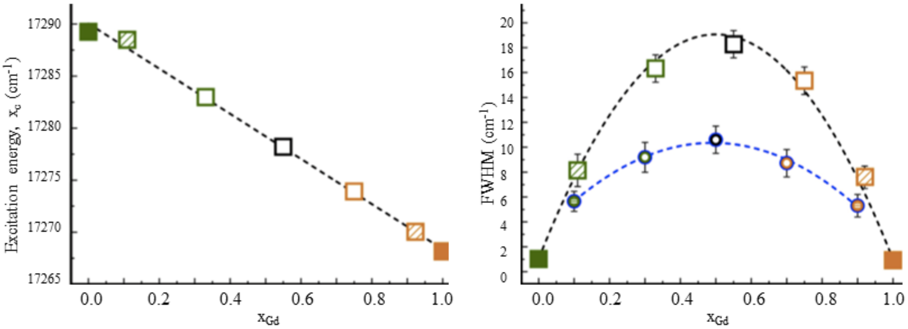

Figure 21. The Eu^{3+} excitation peak maximum (x_c) (left) and the experimental (square symbols) excitation peak line widths (FWHM) and broadening widths of the simulated average Eu-O bond length distributions (circles) (right) of Eu^{3+}-doped $La_{1-x}Gd_xPO_4$ solid solutions plotted as a function of the Gd^{3+} fraction, x_{Gd}.

In addition to the linear shift of the excitation peak position across the synthetic $La_{1-x}Gd_xPO_4$ solid solution series as described above, a second order polynomial trend can be perceived when plotting the line width of the Eu^{3+} excitation peaks as a function of the $La_{1-x}Gd_xPO_4$ composition (**Equation 22**).

Equation 22

$$\mathrm{FWHM}\ (\mathrm{cm}^{-1}) = 1.0 + 72.3 \cdot x - 72.3 \cdot x^2$$

This excitation peak broadening trend is in perfect concordance with the recorded Raman peak broadening discussed above. The FWHM increases from approximately 1 cm^{-1} for the pure endmembers $LaPO_4$ and $GdPO_4$ to 18 cm^{-1} for the $La_{0.45}Gd_{0.55}PO_4$ composition.

The increasing excitation line-widths indicate increasing local disorder in the monazite solid solutions or in general a less well defined structure around the incorporated Eu^{3+} ion. In addition, the line widths for the $La_{1-x}Gd_xPO_4$ with $x < 0.5$ (i.e. higher La^{3+} than Gd^{3+} content) are slightly larger than the line widths for $x > 0.5$ (lower La^{3+} than Gd^{3+} content). To explain this asymmetry it has to be kept in mind that that Eu^{3+} has cation radius very close to that of Gd^{3+} ($r^{IX}_{Eu(III)}$ = 112.0 p.m., $r^{IX}_{Gd(III)}$ = 110.7 p.m.) [43]. La^{3+} on the other hand is more than 8% larger ($r^{IX}_{La(III)}$ = 121.6 p.m.) [43] than both Eu^{3+} and Gd^{3+}. Because of the similar sizes of Eu^{3+} and Gd^{3+} cations, the monazite compositions with higher Gd^{3+} concentrations have probably a slightly higher local order around the Eu^{3+} luminescent center than the corresponding compositions with higher La^{3+} concentration. This is supported by the atomistic simulations described further in the text.

A similar trend can be observed when considering the emission line intensities of emission spectra recorded after excitation of the incorporated Eu^{3+} species at the excitation peak maximum (**Figure 22**). All emission spectra are very similar showing a full three-fold and five-fold splitting of the $^7F_1$ and $^7F_2$ bands, respectively, corresponding to Eu^{3+} incorporation on a low symmetry site, in accordance with the monoclinic (C1) lattice site in the monazites. The relative intensities of these bands reflect the coordination symmetry around the Eu^{3+} ion. The $^5D_0$ / $^7F_2$ transition has a predominant electric dipole character that is sensitive to changes in the ligand environment. In contrast, the $^5D_0$ / $^7F_1$ transition retains its magnetic dipole character even in low symmetry systems and its radiative transition is not significantly influenced by the ligand environment.

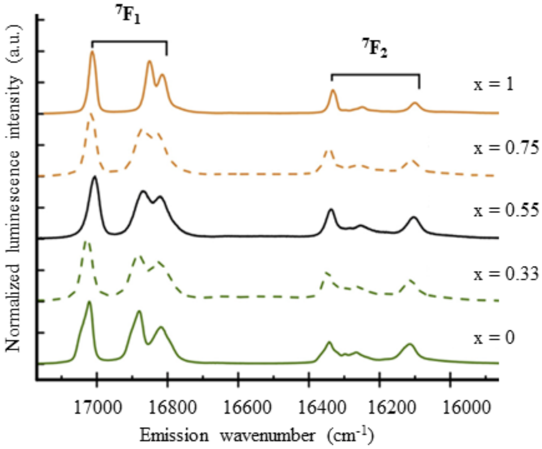

Figure 22. Selected emission spectra of the synthetic Eu^{3+}-doped $La_{1-x}Gd_xPO_4$ monazite solid solutions.

Thus, when the site symmetry decreases, the relative intensity of the hypersensitive transition ($^5D_0$ / $^7F_2$) increases, resulting in a higher $^7F_2/^7F_1$ ratio. The $^7F_2/^7F_1$ ratio follows an almost linear trend when going from the pure $GdPO_4$ composition toward the $La_{0.45}Gd_{0.55}PO_4$ composition, **Figure 23**. Similarly, the transition from $LaPO_4$ towards the $La_{0.45}Gd_{0.55}PO_4$ composition yields an almost linear increase of the $^7F_2/^7F_1$ ratio. This behavior can, in concordance with the witnessed trend for the excitation line width discussed above, be explained by the slight distortion of the crystal lattice and the subsequent lowering of the site symmetry upon increasing dopant concentration. An error between 7% and 10% is introduced from the integration of the emission peaks that depend on the chosen boundaries for the integrals. It is, however, obvious that the solid solutions compositions with an excess of La^{3+} yield larger values for the $^7F_2/^7F_1$ ratio, i.e. larger distortions around the Eu^{3+} cation than the corresponding solid solutions containing more Gd^{3+}. The origin of the broadening of the excitation spectra and the asymmetry in the FWHM along the solid solution series will be further discussed in terms of the Eu-O bond length distribution obtained by the aid of the atomistic simulations.

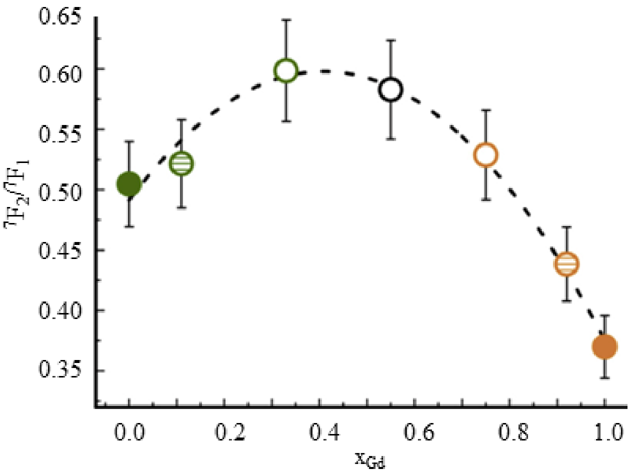

Figure 23. The $^7F_2/^7F_1$ ratio in the Eu^{3+}-doped $La_{1-x}Gd_xPO_4$ solid solutions plotted as a function of the Gd^{3+} fraction, x.

Results from atomistic modelling

With the atomistic simulations, a distribution of average Eu-O bond lengths was computed for five $La_{1-x}Gd_xPO_4$ (x = 0.1, 0.3, 0.5, 0.7, 0.9) compositions and 256 doping sites for each special quasi random structure that represent a homogeneous solid solutions. Due to the computational intensity of the *ab initio* method limiting the size of the supercell to 2·2·2 with only 32 doping sites resulting in rather poor statistics, the *ab initio* calculations were performed for the 50:50 compositions only. However, obtained distributions resemble the ones derived by the force-field calculations as indicated in **Figure 24**.

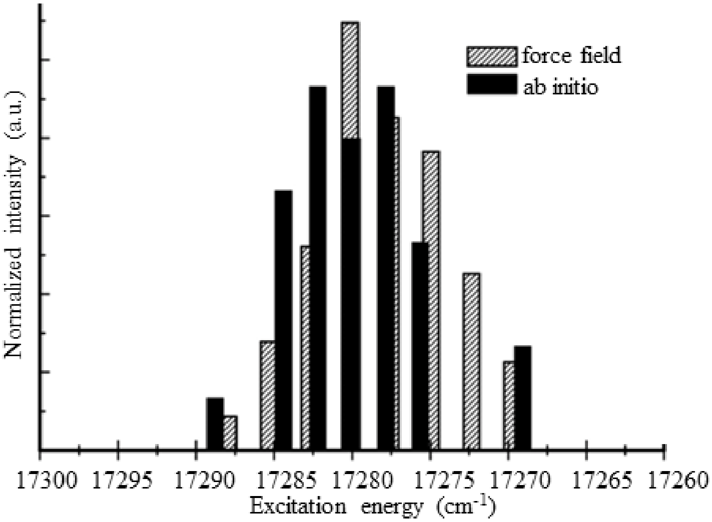

Figure 24. Comparison of computed excitation energy probabilities (intensities) for $La_{0.5}Gd_{0.5}PO_4$ using *ab initio* calculations (solid bars) and force field simulations (dashed bars).

The obtained bond lengths were converted to wavenumbers assuming the linear relationship between the excitation peak maximum and the average Eu-O bond length, observed for pure monazite-phases [108] (**Equation 23**).

Equation 23

$$E({}^7F_0 \rightarrow {}^5D_0)\ (\mathrm{cm^{-1}}) = 16759.04681 + 205.60539 \cdot Ln\text{-O}\ (\text{Å})$$

In order to make a quantitative analysis a Gaussian distribution was fitted to the computed excitation energy profiles as well as to the measured excitation lines. The used Gaussian function, normalised to a peak height of 1, has the form:

Equation 24

$$f(\mathrm{x}) = e^{-\frac{(x-x_c)^2}{2\sigma^2}},$$

where x_c is the peak position and σ represents the broadening. The broadening can be related to the half-width (FWHM) through (**Equation 25**).

Equation 25

$$\mathrm{FWHM} = \sqrt{2ln2}\cdot\sigma = 2.3548\cdot\sigma$$

The parameters of the fits are given **Table A 4**. The obtained excitation energy distributions are plotted in **Figure 20** together with the experimental Eu^{3+} excitation spectra for $La_{1-x}Gd_xPO_4$. The computational results show that the distribution of Eu-O bond-lengths in the solid solutions becomes systematically wider when going from the solid solutions with lower doping ($La_{0.1}Gd_{0.9}PO_4$ and $La_{0.9}Gd_{0.1}PO_4$) towards the equimolar $La_{0.5}Gd_{0.5}PO_4$ compositions, resulting in a broadening of the Eu^{3+} excitation line. In general, the calculated distributions of Eu-O bond lengths have smaller half-widths than the experimental data, but the variation of the width with Gd^{3+} substitution (x) matches the variation of FWHM. Interestingly, the widths of the Eu-O distributions for $x > 0.5$ are also slightly smaller than for $x < 0.5$ which shows that this asymmetry is produced by the slightly larger distortion in Eu-O bonds in a La^{3+}-rich matrix than in a Gd^{3+}-rich matrix as already discussed in connection to the TRLFS data above.

As already mentioned, this supports the conclusion that the larger differences in sizes between Eu^{3+} and La^{3+} cations than Eu^{3+} and Gd^{3+} cations and the associated larger volume distortion upon substitution of La^{3+} by Eu^{3+} in a La-rich matrix are responsible for this asymmetry.

5.3.2 Rhabdophane-type solid solutions

5.3.2.1 Phase analysis and chemical composition

Powder X-ray diffraction

The conventional low-temperature precipitation method from lanthanide nitrates aqueous solutions (0.3 M) with concentrated phosphoric acid, applied previously in [59, 136, 246] (Prec., **Section 4.1.1.1**) was used in this work to obtain $La_{1-x}Gd_xPO_4$ rhabdophane solid solutions. PXRD patterns of the resulted compounds are shown in **Figure 25**.

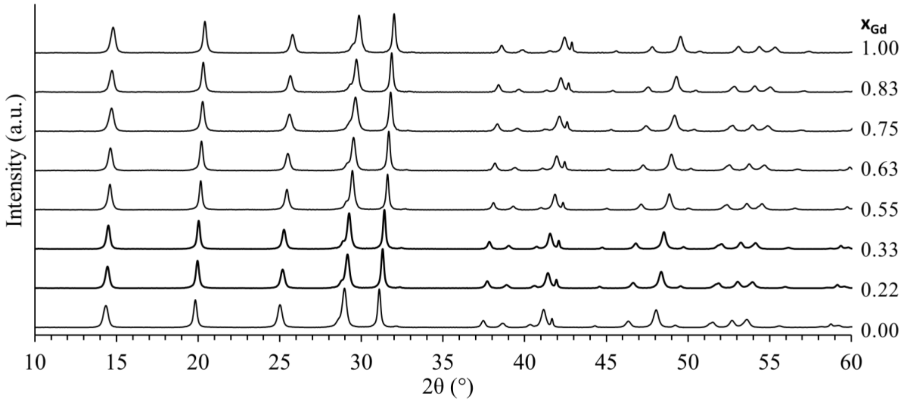

Figure 25. X-ray diffraction patterns of the synthesised $La_{1-x}Gd_xPO_4 \cdot 0.667H_2O$ rhabdophane solid solutions.

No reflections other than those belonging to the hydrated monoclinic rhabdophane can be seen in the diffractograms (**Figure 25**), indicating that single-phase rhabdophane solid solutions are formed during the synthesis. In addition, no evidence of monazite in the rhabdophane diffractograms can be seen, implying that rhabdophane to monazite transformation has not occurred during synthesis. The observed linear shift of the Bragg reflections is caused by the lattice contraction due to the incorporation of the slightly smaller Gd^{3+} ions compared to La^{3+} (1.20 Å and 1.09 Å, respectively (average lanthanide radii given for the mixed nine- and eight-fold coordinated environment (1/3 rLn_{CN8} + 2/3 rLn_{CN9}) [247]). As a consequence the lattice parameters decrease linearly as a function of Gd-content confirming solid solution formation according to Vegard's law (**Figure 26**). For hydrated $La_{1-x}Gd_xPO_4$ rhabdophane solid solutions, in the present work (see also **Section 5.3.2.2**) the lattice parameters are reported for the first time.

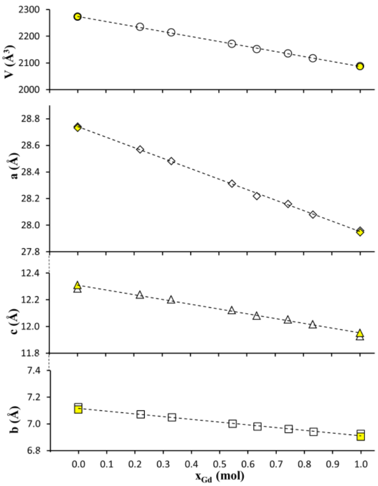

Figure 26. Evolution of the lattice parameters and of the cell volume of the $La_{1-x}Gd_xPO_4{\cdot}0.667H_2O$ solid solutions with rhabdophane structure (x = 0.0 – 1.0). Lattice parameters and cell volume calculated by Rietveld refinement of the XRD data are marked with open symbols. Lattice parameters and cell volume of $LaPO_4{\cdot}0.667H_2O$ and $GdPO_4{\cdot}0.667H_2O$ [59] are marked with yellow symbols.

The lattice strain determined from the Rietveld refinement of the XRD data demonstrates a parabolic trend increasing from the endmembers towards the intermediate composition (**Figure 27**).

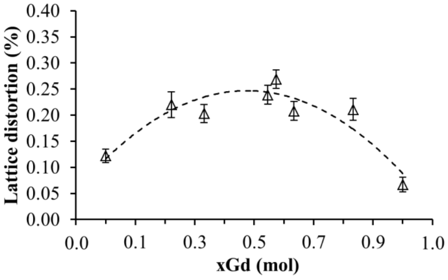

Figure 27. Lattice strain determined by Rietveld refinement of the XRD data as a function of $La_{1-x}Gd_xPO_4{\cdot}0.667H_2O$ composition.

Scanning electron microscopy with energy dispersive spectroscopy

The chemical composition of the precipitate was investigated using SEM-EDS. The EDS analysis confirmed the homogeneity of the samples as well as the actual compositions (ratio La-Gd-P). The actual compositions of the synthesised solid solutions determined by averaging the results from SEM-EDS and XRF spectroscopy with the corresponding refined unit cell parameters are summarised in **Table A 5**.

5.3.2.2 Spectroscopic investigations of $La_{1-x}Gd_xPO_4{\cdot}0.667H_2O$ rhabdophane solid solutions

Raman spectroscopy

A free PO_4^{-3} tetrahedron has a T_d symmetry resulting in four normal degenerate fundamentals (ν_1 to ν_4) with nine vibrational degrees of freedom, all being Raman active [248]. In the monoclinic structure of hydrated rhabdophane compounds *Ln*$PO_4{\cdot}H_2O$ (*Ln* = La to Dy), reported by [59], five of the seven $(PO_4)^{3-}$ anions in the unit cell occupy sites with a C_1 symmetry while two of the $(PO_4)^{3-}$ anions belong to the C_2 point group, resulting in a higher number of active internal modes. Factor group theoretical analysis predicts 237 vibrational modes for *Ln*$PO_4{\cdot}0.667H_2O$ crystallizing in the monoclinic C_2 space group. These modes are distributed among the irreducible representations of the factor group C_2 as 118A + 119B. 108 of these Raman active modes are internal modes of the phosphate tetrahedra, namely stretching ν_1 (7A + 5B), ν_3 (17A + 19B) and bending ν_2 (14A + 10B), ν_4 (17A + 19B) (**Figure 28**). The remaining modes were not assigned due to the complexity of the structure. The assignment of the Raman bands corresponding to the vibrational modes of phosphate tetrahedra is reported in the literature assuming hexagonal structure of rhabdophane compounds [64]. In the present work, we are mainly concerned with the compositional effect in the $La_{1-x}Gd_xPO_4$ rhabdophane solid solutions on the fundamental Raman vibrations.

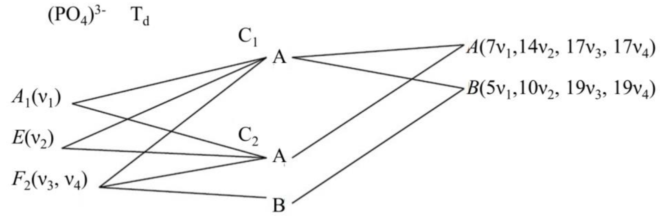

Figure 28. Correlation table of the internal vibrational modes of the phosphate group in *Ln*$PO_4 \cdot 0.667H_2O$.

Raman spectra of $La_{1-x}Gd_xPO_4 \cdot 0.667H_2O$ rhabdophane solid solutions (x = 0, 0.22, 0.33, 0.55, 0.64, 0.75, 0.83, 1) are presented in **Figure 29**. In agreement with the previous studies of hydrated rhabdophane compounds (La – Dy) [64], the most intensive Raman band appearing between 970 and 1000 cm^{-1} corresponds to the symmetric stretching vibration of the phosphate tetrahedron (ν_1). At higher wavenumbers (≈ 1020 – 1130 cm^{-1}) the components of the (ν_3) mode appear. The Raman bands appearing below approximately 400 cm^{-1} correspond to lattice vibrations. Due to the low intensity of the Raman bands corresponding to lattice vibrational modes, they were not fitted (**Figure 29**). The Raman bands ν_2 and ν_4 can be found between the regions of modes assigned to ν_1 and lattice vibrations.

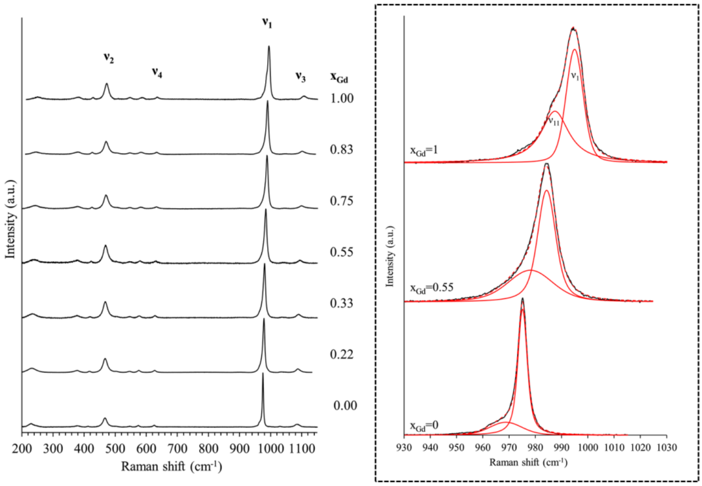

Figure 29. Raman spectra of $La_{1-x}Gd_xPO_4·0.667H_2O$ solid solutions and indications of phosphate group vibration modes.

In the literature only one Raman band has been reported for the ν_1 vibrational mode in agreement with one crystallographic position of the phosphate group considering the hexagonal structure [61]. Taking into account the re-examination of the rhabdophane structure, the hydrated rhabdophane compounds crystallize in monoclinic symmetry and $(PO_4)^{3-}$ anions occupy crystallographic sites with two different site symmetries (C_1 and C_2) resulting in (7A + 5B) stretching vibrational modes ν_1 (**Figure 28**). In this work the best fit for the ν_1 band was obtained by fitting a minimum of two Voigt functions (insert of **Figure 29**). The less intensive Raman band at a slightly lower wave number than the ν_1 band will further be named ν_{11}.

Positions of Raman bands corresponding to the symmetrical and anti-symmetrical stretching and bending vibrations of the phosphate tetrahedra (ν_1 – ν_4) are plotted as a function of $La_{1-x}Gd_xPO_4·0.667$ composition (**Figure 30**). A linear trend of the Raman band positions as a function of Gd^{3+} content (x_{Gd}) is observed for all vibrational normal modes.

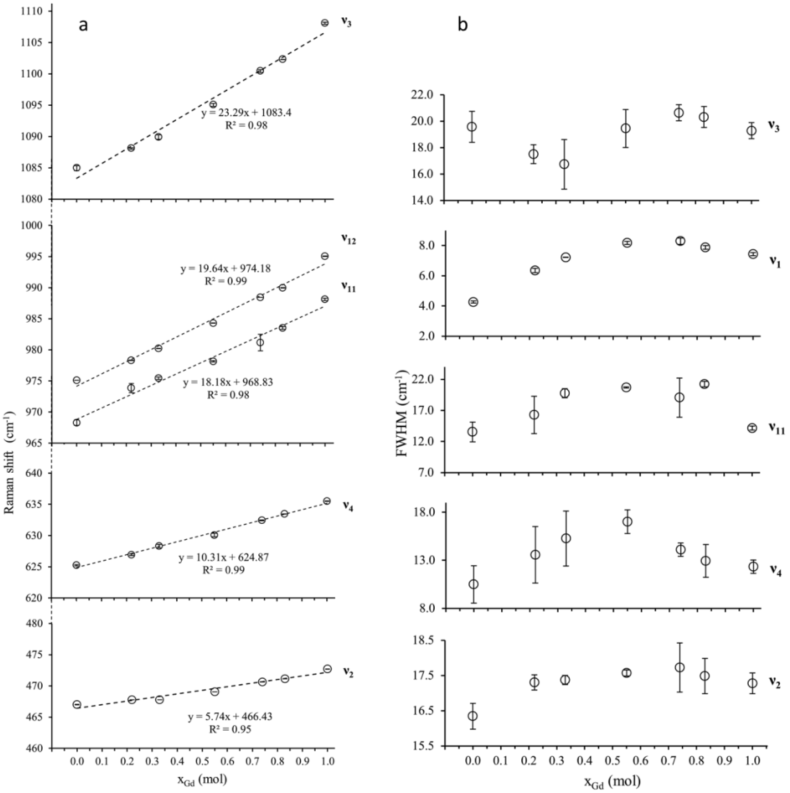

Figure 30. Raman band positions as a function of $La_{1-x}Gd_xPO_4\cdot0.667$ composition for the vibrations of the phosphate tetrahedra (ν_1 – ν_4) (left, a) with the corresponding band widths (FWHM) (right, b).

Analysis of the Raman spectra revealed broadening of the Raman bands (ν_1, ν_2, ν_4) when going form the endmembers towards the solid solutions, with the highest FWHM for $x_{Gd} = 0.5 – 0.7$. These results seem to correlate with the lattice strain determined from the Rietveld analysis of the XRD data (**Figure 27**). Similar broadening of the FWHM of Raman bands has been also observed for (La,Gd)PO_4 and (La,Eu)PO_4 monazite solid solutions [110, 136, 248]. The monazite solid solutions were highly crystalline and lattice strain was absent. The broadening was attributed to the increasing bond length distribution around the cation causing the distortion of the phosphate tetrahedra when going from the pure endmembers towards the equimolar composition [136]. In case of the hydrated rhabdophane compounds, the broader band widths might be caused by the combination of the strain and bond length distribution effects. Additionally, decreasing bond lengths and thus the size of the channels accommodating crystalline water with increasing Gd-content could cause the distortions of the phosphate terahedra.

Time resolved laser fluorescence spectroscopy

In order to study the local environment of the cation site in the hydrated rhabdophane solid solutions, the TRLFS method was applied. The ionic radius of Eu is close to that of Gd (difference of approximately 1 %), thus, the local environment of Eu is expected to resemble the local environment of Gd in the $La_{1-x}Gd_xPO_4{\cdot}0.667H_2O$ solid solutions. The excitation spectra of the synthesised $La_{1-x}Gd_xPO_4{\cdot}0.667H_2O$ ($x = 0, 0.55, 1$) solid solution compositions doped with 500 ppm Eu^{3+} as luminescent probe are presented in **Figure 31**.

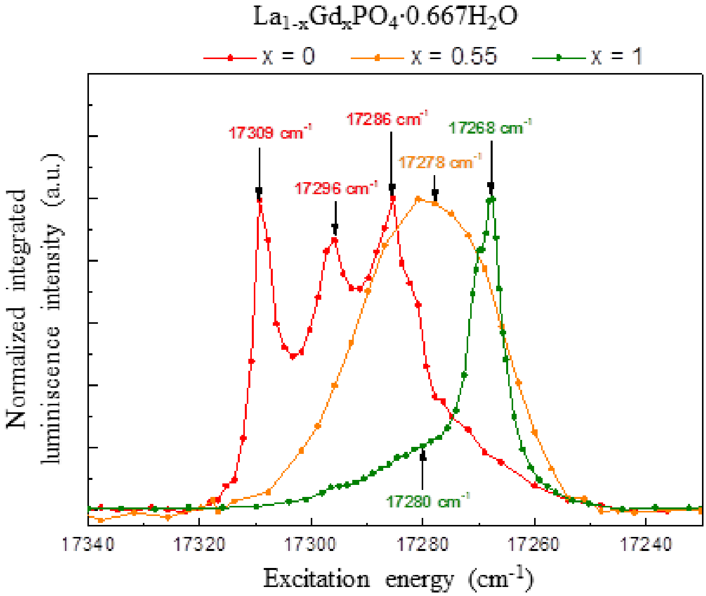

Figure 31. Excitation spectra of the synthetic $La_{1-x}Gd_xPO_4{\cdot}0.667H_2O$ rhabdophane solid solutions doped with 500 ppm Eu^{3+}. Excitation energies used for the collection of high-resolution emission spectra and lifetimes are indicated with arrows.

The investigated compounds show relatively broad excitation peaks compared to Eu^{3+} doped $La_{1-x}Gd_xPO_4$ monazites [136], due to the lower crystallinity of the hydrated rhabdophane samples confirmed by the Rietveld refinement of the XRD data and multiple Eu^{3+} sites in the crystal structure. There are three major excitation peak maxima for $LaPO_4 \cdot 0.667H_2O$ found at 17309, 17296, and 17286 cm^{-1}. This indicates the presence of three distinct Eu^{3+} species in the sample. The $La_{0.45}Gd_{0.55}PO_4 \cdot 0.667H_2O$ composition shows one, broad excitation peak with a peak maximum at 17279 cm^{-1} and a half width of 24 cm^{-1} assuming a Gaussian peak shape. Whether this broad peak is composed of multiple Eu^{3+} species or rather one Eu^{3+} species in a disordered environment causing the observed broad excitation signal, cannot be deduced from the excitation spectrum alone. The excitation spectrum of $GdPO_4 \cdot 0.667H_2O$ yields one narrower excitation peak with a maximum at 17268 cm^{-1} and a "tail" stretching from 17300 cm^{-1}, indicating the presence of two Eu^{3+} species in this sample. The shift of the excitation peak maximum to lower excitation energies with increasing x_{Gd} can be attributed to the shorter average *Ln*-O bond distance and consequently stronger ligand field in $GdPO_4 \cdot 0.667H_2O$ in comparison to that in $LaPO_4 \cdot 0.667H_2O$, as it was also shown for $La_{1-x}Gd_xPO_4$ monazite solid solutions and *Ln*PO_4 monazite endmembers series (*Ln* = La to Gd) [108, 136]. A similar linear relationship between the excitation peak position and the Gd substitution (x), as derived for the monazite solid solution series [136], cannot be obtained in the present study due to the presence of varying numbers of Eu^{3+} species in the rhabdophane solid solutions.

High resolution emission spectra and luminescence lifetimes were collected for the rhabdophane solid solutions after excitation at the local excitation energy maxima of the different Eu^{3+} species, indicated with arrows in **Figure 31**. The resulting spectra and lifetimes are shown exemplarily for the endmember compositions in **Figure 32** and **Figure 33**, respectively.

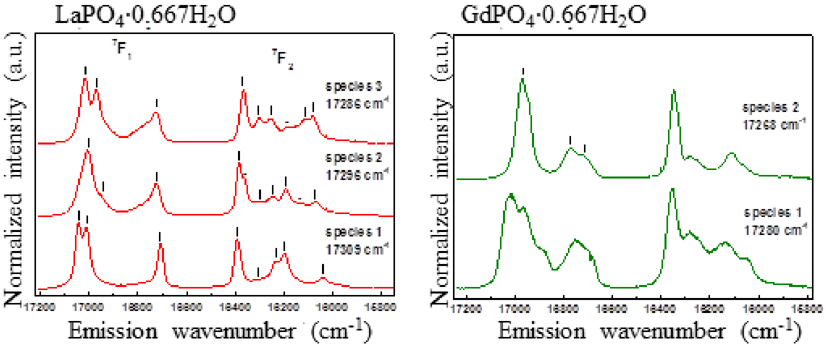

Figure 32. Emission spectra collected for the different Eu^{3+} species in the rhabdophane endmembers. Lines indicate the peak positions of the $^7F_1$ and $^7F_2$ multiplets.

In general, the emission spectra collected for $LaPO_4 \cdot 0.667H_2O$ rhabdophane are better resolved than the corresponding spectra for $GdPO_4 \cdot 0.667H_2O$. This is partly due to the large overlap between the two coexisting species in the gadolinium endmemberwhich does not allow for selective excitation of one species at a time. However, the degree of crystallinity of the samples might be slightly different (with a higher crystallinity of the La endmember), implying that the short-range order around the Eu^{3+} dopant in the samples varies causing a broadening of the emission peaks in the less ordered $GdPO_4 \cdot 0.667H_2O$ environment. Nevertheless, in both rhabdophane compositions a fully lifted degeneracy, resulting in a three-fold spitting of the $^7F_1$ band and a five-fold splitting of the $^7F_2$ band, can be seen. This is consistent with a low symmetry lattice site for all observed Eu^{3+} species, which is in concordance with the refined monoclinic rhabdophane structure [59] with a monoclinic (C_1, C_2) symmetry.

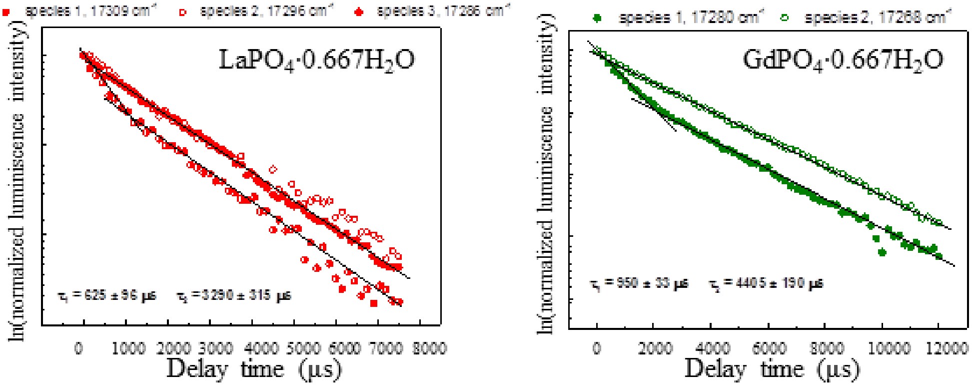

Figure 33. Lifetimes corresponding to the emission spectra of the synthetic $La_{1-x}Gd_xPO_4 \cdot 0.667H_2O$ rhabdophane solid solutions doped with 500 ppm Eu^{3+}, shown in Figure 32.

Multiexponential luminescence decay curves for Eu^{3+} doped hydrated rhabdophane compounds confirm the presence of at least two Eu^{3+} species in the structure. The longer component is approximately 3290±315 µs for Eu^{3+} incorporation in $LaPO_4 \cdot 0.667H_2O$ rhabdophane and 4405±190 µs in $GdPO_4 \cdot 0.667H_2O$. Such long lifetimes speak for a full loss of the hydration sphere as well as the absence of water of hydration on the lattice site where the dopant is incorporated. The shorter lifetimes of 625±96 μs and 950±33 μs for Eu^{3+} incorporation in lanthanum and gadolinium rhabdophane, respectively, indicate partial quenching of the lifetime, most probably due to water of hydration in the rhabdophane crystal structure. Estimating the number of water molecules ($n(H_2O)$) in the first coordination sphere of europium ions with the Horrocks equation presented above (**Section 2.4.4.3**), values of 1.1 (La phase) and 0.51 (Gd phase) are obtained. However, it has to be noted that the Horrocks equation is valid for aqueous Eu^{3+} species and definite conclusions about the number of crystal water molecules in the lattice cannot be drawn from the recorded lifetimes in the present study. Nevertheless, according to the analysis of the lifetimes, Eu^{3+} is incorporated in the rhabdophane matrix on a minimum of two different site types, one of which is completely dehydrated and one which is associated with water of hydration.

5.3.3 Structural incorporation of Cm^{3+} in lanthanide orthophosphates with rhabdophane and monazite structures

Within this work the incorporation of the minor actinide curium (Cm^{3+}) in a series of synthetic $La_{1-x}Gd_xPO_4$ ($x = 0, 0.24, 0.54, 0.83, 1$) monazite and rhabdophane solid solutions was studied by combined spectroscopic and computational methods. To obtain information of the incorporation process on the molecular scale and to understand the distribution of the dopant in the synthetic phosphate phases, combined time-resolved laser fluorescence spectroscopy (TRLFS) and X-ray absorption fine structure (XAFS) spectroscopy investigations have been conducted and complemented with *ab initio* atomistic simulations.

Although especially the monazite phases have been subject to numerous studies ranging from investigations of material properties to synthesis of various solid solution compositions to detailed spectroscopic studies of the dopant incorporation behavior, the vast majority of them have been conducted with inactive elements (mainly lanthanides) as surrogates for the actinides. Although 4*f* elements are similar to 5*f* ones, there are some substantial differences in their chemical and physical behavior (see **Chapter 2.4.1**). For rhabdophane matrices, there are no studies addressing actinide incorporation within the solid structure from the dopant point of view. Thus, the present study aims at generating new data on actinide incorporation in rhabdophane solid solutions and to complement already existing data for lanthanide-doped monazite phases (see **Chapters 5.3.1, 5.3.2** and [108, 119, 136]) with data obtained for an actual actinide element.

Here, the use of Cm^{3+}, with outstanding luminescence properties, can provide new insights into the number of species in the studied solid solutions, and strong indications for the order or crystallinity of the solid phase under investigation, which are properties that are not accessible to the same extent with the more commonly used luminescent lanthanide, Eu^{3+} (see **Chapters 5.3.1**, **5.3.2** and [108, 119, 136]).

For this purpose, the incorporation of the minor actinide Cm^{3+} in a series of $La_{1-x}Gd_xPO_4 \cdot 0.667H_2O$ (hydrated rhabdophane) and $La_{1-x}Gd_xPO_4$ (monazite) solid solutions has been investigated with the combined spectroscopic and computational methods discussed above.

The Cm^{3+}-doped (La,Gd)PO_4 compounds represent an excellent ternary model system for investigating the flexibility of the monazite and rhabdophane structures towards incorporation of differently sized actinide cations, and the homogeneity of the synthesised solid solutions. The system is composed of lanthanum ($r_{La(III)}^{IX}$ = 1.216 Å [247]) serving as a matrix element, gadolinium ($r_{Gd(III)}^{IX}$ = 1.107 Å [247]) as a neutron capturer, and an actinide, curium ($r_{Cm(III)}^{IX}$ = 1.146 Å [249]). Lanthanum and gadolinium poses the largest difference in cationic radii within the stability region of the monazite phase for the lanthanide series. Thus, any possible structural effects occurring in the solid solutions due to the difference in the cationic radii should be most pronounced for the (La,Gd)-solution. Furthermore, neither lanthanum nor gadolinium interfere with the luminescence emission of curium monitored in the laser spectroscopic investigations in the present study. To explain the spectroscopically observed substitution of Cm^{3+} for the various site types in the investigated $La_{1-x}Gd_xPO_4$ monazite and rhabdophane solid solution matrices, the structural arrangements, energetics, and MPO_4 formula unit volumes of Cm^{3+}-doped phosphates were computed using *ab initio* calculations. Due to slightly different experimental and computational approaches used in the investigations of monazites vs. rhabdophane solids, results and discussion on Cm^{3+} incorporation in these two different phases will be presented separately in the following text.

5.3.3.1 Materials characterization

SEM-EDX analysis was performed for the $La_{1-x}Gd_xPO_4$ monazite solid solutions to determine the actual compositions of the synthesised compounds. As the monazites were obtained by direct calcination and sintering of the rhabdophane precursor phases, identical La^{3+} and Gd^{3+} contents are expected in both materials. The compositions are compiled in **Table A 6** in the **Appendix**.

PXRD-patterns of $La_{1-x}Gd_xPO_4 \cdot 0.667H_2O$ rhabdophane and $La_{1-x}Gd_xPO_4$ monazites are presented in **Figure 34**. Pure-phase $La_{1-x}Gd_xPO_4 \cdot 0.667H_2O$ solid solutions with rhabdophane structure were successfully obtained after synthesis for all the investigated compositions.

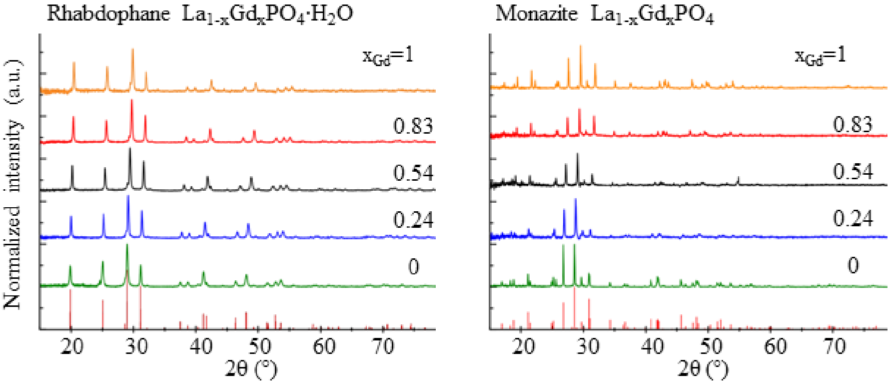

Figure 34. Experimental XRD patterns obtained for the synthetic Cm^{3+}-doped $La_{1-x}Gd_xPO_4$ rhabdophane (left) and monazite (right) phases with the theoretical XRD patterns of the hydrated monoclinic rhabdophane [59] and monazite [42] structures for the La-endmember.

Lattice parameters for the monazite and rhabdophane solids were derived using Rietveld refinement of collected XRD-data. Lattice parameters and cell volumes, derived both from experimental PXRD data and *ab initio* calculations, of the rhabdophane and monazite compounds, except for the lattice parameter β of the rhabdophanes, show a linear compositional trend in agreement with Vegard's law, **Figure 35**. The experimental and computed lattice parameters are in very good agreement with one another. Slightly larger unit cell volumes are obtained computationally for the La-rich rhabdophane and monazite solid solution compositions in comparison to the Rietveld-derived parameters, while the opposite is true for the Gd-rich solids. The largest difference between experimental and computed data (< 1%) can be seen for the lattice parameter β. For the rhabdophane solid solutions, it deviates from the expected linear behavior according to both DFT calculations and experiment. In the experimental case, this deviation may result from the Rietveld refinement. Here, the reflex broadening due to the relatively low crystallinity of the rhabdophane compounds as well as rather high background due to the contribution of the domed sample holder for radioactive materials could influence the accuracy of the Rietveld refinement results. Another possibility for the non-linear compositional trend for the lattice parameter β, could be small variations in the hydration state of the hydrated rhabdophane compounds, i.e. water of hydration is slightly lower than the expected 0.667 for fully hydrated, monoclinic rhabdophane. According to literature, a first dehydration step for hydrated rhabdophane has been observed above approximately 353 K [60, 250]. In this work, the precipitation of rhabdophane was performed at 363 K for a total duration of 1 week, followed by drying of the solid phase at this temperature for 12 h. Thus, a small amount of dehydration could be expected, leading to a small deviation of the beta angle. The dehydration reaction should be reversible [59, 60], but incomplete rehydration of the compounds cannot be excluded. This is discussed further in connection to the spectroscopic data obtained for the rhabdophane compounds.

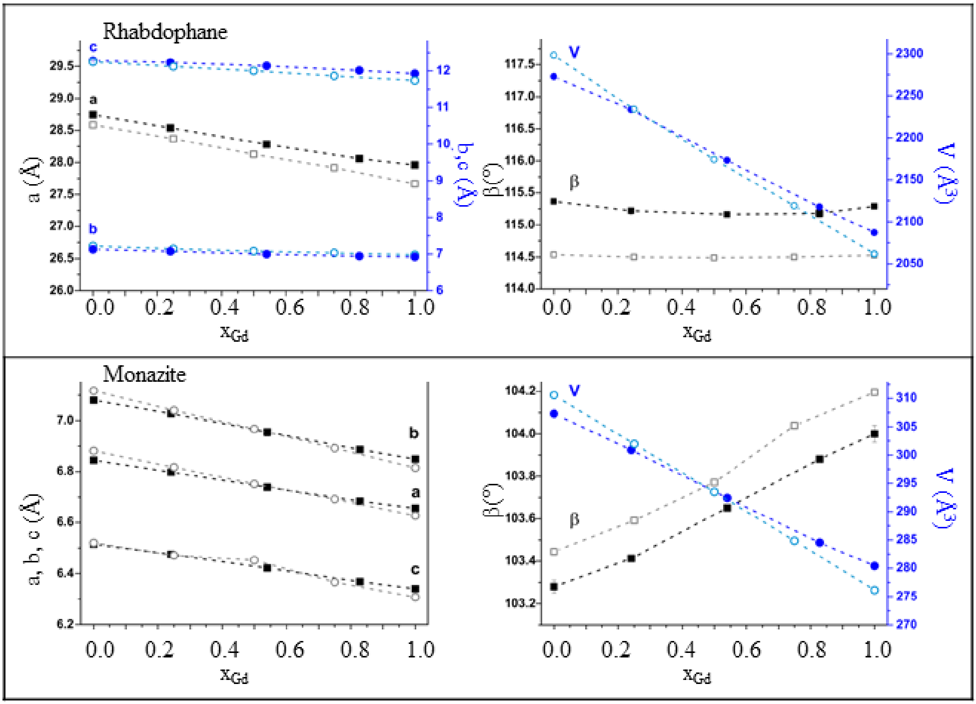

Figure 35. Derived lattice parameters for the synthetic rhabdophane (top) and monazite (bottom) solid solutions. Computed parameters are represented by open symbols and lighter dashed lines than the corresponding experimentally derived data represented by closed symbols.

5.3.3.2 *Spectroscopic investigations of Cm^{3+}-doped monazites*

Time-resolved laser fluorescence spectroscopy

The Cm^{3+} excitation spectra obtained with the TRLFS method of the pure $LaPO_4$ and $GdPO_4$ endmembers (**Figure 36**, left) show four well-resolved peaks corresponding to the four-fold splitting of the Cm^{3+} ground state. The highly resolved ground-state splitting and the absence of additional excitation peaks, indicate the presence of only one, very well-defined, crystalline environment for the incorporated Cm^{3+} cation in the La and Gd monazite endmembers. The resolved magnitude of the ground-state splitting is approximately 24 cm^{-1} for $GdPO_4$ and 27 cm^{-1} for $LaPO_4$.

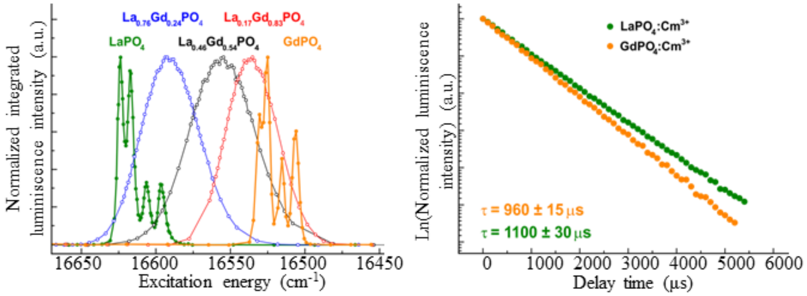

Figure 36. Excitation spectra (left) and selected luminescence lifetimes (right) of the synthetic $La_{1-x}Gd_xPO_4$ monazite solid solutions doped with 50 ppm Cm^{3+}.

The presence of only one Cm^{3+} species in the monazite endmember compositions can further be seen in the recorded luminescence lifetimes (**Figure 36**, right), which decay monoexponentially with lifetimes of 1100 ± 30 μs ($LaPO_4$) and 960 ± 15 μs ($GdPO_4$). The long lifetimes speak for a full loss of the Cm^{3+} hydration sphere upon incorporation in the monazite lattice on the Ln^{3+} site, as can be expected after sintering of the samples at 1723 K.

When examining the Cm^{3+} excitation spectra obtained for the solid solution compositions ($La_{0.76}Gd_{0.24}PO_4$, $La_{0.46}Gd_{0.54}PO_4$, and $La_{0.17}Gd_{0.83}PO_4$), a complete loss of the splitting fine-structure and a broadening of the excitation peaks can be seen (**Figure 36**), indicating a decrease of local structural order and formation of randomized solid solutions. When exciting the incorporated Cm^{3+} in the solid solution matrix using varying excitation energies, a manifold of narrow emission spectra are obtained, exemplarily shown for the $La_{0.46}Gd_{0.54}PO_4$ composition in **Figure 37**.

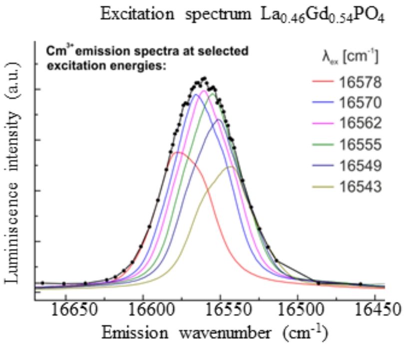

Figure 37. Excitation spectrum of Cm^{3+}-doped $La_{0.46}Gd_{0.54}O_4$ (black spectrum) and emission spectra showing emission line narrowing collected at various excitation energies, λ_{ex} (colored spectra).

Such luminescence line narrowing has previously been reported for Cm^{3+} adsorption species on the clay mineral kaolinite [251] and for Cm^{3+} incorporation into amorphous grain boundaries in bioapatite [252]. In both studies, the observed line narrowing was explained by a continuum of related environments arising from e.g. imperfections on a solid surface or from the decrease of the long-range order in a solid structure. Thus, in concordance with these studies, the line-narrowing behavior observed in the present study, is attributed to the presence of multiple, very similar local Cm^{3+} environments within the monazite solid solution matrix. The origin of this disordering of the solid solution structure will be discussed later in the text.

When plotting the excitation peak position, i.e. the center value of the excitation energy at the full width at tenth maximum (FWTM), for all monazite compositions as a function of Gd^{3+} doping (x), a linear trend can be observed (**Figure 38**). The linear fit of the experimental data yields an expression for the excitation peak maximum given by **Equation 26**. This allows to predict the excitation peak maximum for known solid solution compositions or conversely, to calculate the composition of a Cm^{3+}-doped $La_{1-x}Gd_xPO_4$ solid solution from a measured Cm^{3+} excitation peak maximum.

Equation 26

$$x_c(^5D_0 \rightarrow {}^7F_0)[cm^{-1}] = 16610.7 \pm 3.5 - 92.6 \pm 5.6 \cdot x\ (La_{1-x}Gd_xPO_4)$$

Furthermore, the linear shift of the excitation spectra when going from a larger $LaPO_4$ host towards the smaller $GdPO_4$ solid implies that the ligand-field exerted on the Cm^{3+} cation by the surrounding oxygen ligands becomes systematically stronger, resulting in a bathochromic shift of the excitation spectra. This behaviour is in agreement with the decreasing size of the monazite unit cell when going from the larger $LaPO_4$ host toward $GdPO_4$ and the subsequent contraction of the average Cm-O distance in the solid solutions.

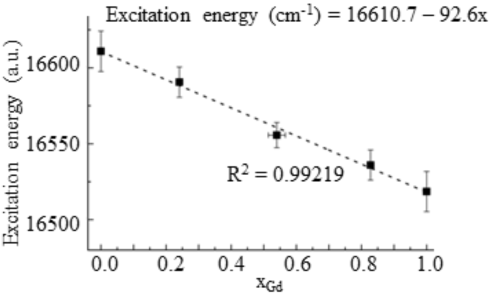

Figure 38. The Cm^{3+} excitation peak maxima derived from the excitation spectra in **Figure 36** plotted as a function of Gd^{3+} substitution (x).

Extended X-ray absorption spectroscopy

The laser-spectroscopic investigations of the Cm-doped monazite solid solutions were complemented with Cm^{3+} L_{III}-edge XAFS investigations of the two endmembers and the intermediate solid solution ($x = 0.54$). The k^3-weighted EXAFS spectra with corresponding Fourier transform magnitudes (FTs) are presented in **Figure 39**. The EXAFS signal is dampened by self-absorption effects, and the noise level is high due to the low Cm concentration (50 ppm). Nevertheless, the FTs of all three samples show a backscattering peak at about 2 Å (uncorrected for phase shift), which can be assigned to the Cm-O coordination shell. The fitting of the EXAFS data shows a contraction of the Cm-O distance from 2.46 to 2.43 Å with increasing Gd substitution (x) within the $La_{1-x}Gd_xPO_4$ solid solution series, **Table 9**. This is consistent with the laser spectroscopic data presented above and can be explained by the decreasing unit cell and the shortening of *Ln*-O bond distance, and consequently shorter Cm-O distances, when going from the larger $LaPO_4$ monazite toward $GdPO_4$. Furthermore, the Debye-Waller factor (DW, σ^2) is smaller for the Cm-O coordination shell of the two endmembers as compared to the solid solution sample, suggesting a higher structural disorder of the latter one.

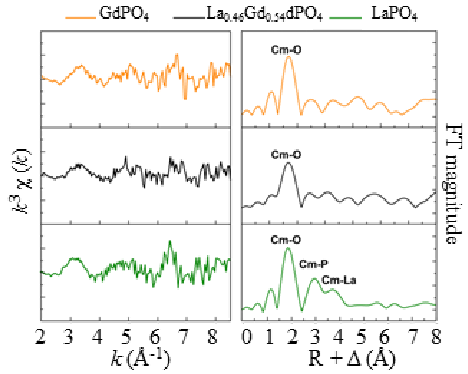

Figure 39. Cm L_{III}-edge k^3-weighted EXAFS spectra (left) and their Fourier transform magnitude (right). Fitted coordination shells are indicated in the figure.

Due to a better signal-to-noise ratio in comparison to the other samples, further details of the monazite local structure could be derived for the $LaPO_4$ sample (**Table 9**). The FTs of this sample show distinct backscattering peaks that can be assigned to Cm-P and Cm-La interactions. In the $LaPO_4$ structure, the seven P atoms from the phosphate units directly linked to the LaO_9 polyhedron have distances ranging from 3.20 to 3.79 Å, followed by 3 La neighbors from 4.08 to 4.15 Å and another three La neighbors from 4.30 to 4.36 Å. By dividing the individual interatomic distances into sub-shells for EXAFS fitting, the Cm-P and Cm-La peaks in the FTs could be described by 3 shorter and 4 longer Cm-P distances and 3 shorter and 3 longer Cm-La distances, respectively. The two Cm-P paths yielded distances at 3.25 and 3.69 Å, in line with the $LaPO_4$ structure determining the long-range order around Cm^{3+}. The two Cm-La shells were fitted with average distances of 4.08 and 4.42 Å, again largely in line with the monazite structural model.

Table 9. Fitting results of Cm-L_{III} EXAFS data of the Cm-doped monazite solid solutions (fit range 1.5 – 8.5 $Å^{-1}$). Computed bond lengths, R (cal.), obtained for the DFT optimized monazite structures are included in the table.

Sample	Path	CN	R [Å] (exp.)	R [Å] (cal.)	σ^2 [$Å^2$]	ΔE_0 [eV]	S_0^2	χ_{res} [%]
$LaPO_4$	Cm-O	9	2.46	2.50	0.0090	7.3	0.80	19.2
	Cm-P	3	3.25	3.33	0.0068^c			
	Cm-P	4	3.69	3.72	0.0068^c			
	Cm-La	3	4.08	4.14	0.0030^c			
	Cm-La	3	4.42	4.36	0.0030^c			
$La_{0.46}Gd_{0.54}PO_4$	Cm-O	9	2.43	2.47	0.0120	8.8	0.57	12.6
$GdPO_4$	Cm-O	9	2.43	2.46	0.0063	8.8	0.50	16.5

CN: coordination number, error ± 25 %, R: Radial distance, error ±0.01 Å, σ^2: Debye-Waller factor, error ±0.0005 $Å^2$, ΔE_0: phase shift, S_0^2: amplitude reduction factor, χ_{res}: residual error, c: parameters were correlated during the EXAFS fit.

Atomistic simulations of Cm^{3+} incorporation in monazites

By investigating the incorporation of Eu^{3+} in $La_{1-x}Gd_xPO_4$ monazite solid solutions it was shown that the broadening of experimental TRLFS excitation profiles could be explained by a different distribution of Eu-O bond lengths in these solid matrices (cf. section 5.2.1). Corresponding atomistic simulations for Cm^{3+} were performed in order to validate such behavior for actinide-doped monazite solids. The average Cm-O bond length simulated for different $La_{1-x}Gd_xPO_4$ monazite compositions (x = 0, 0.25, 0.5, 0.75, 1) is shown in **Figure 40**. A linear trend described by **Equation 27** is obtained as a function of Gd^{3+} substitution (x).

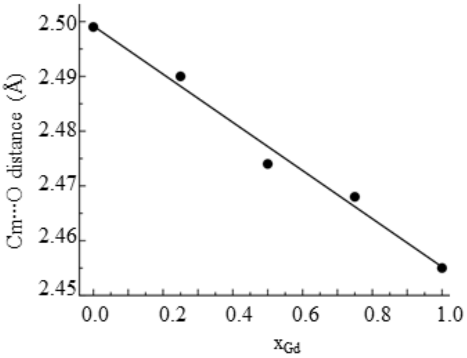

Figure 40. Computed average Cm-O bond lengths in the monazite solid solutions as a function of Gd^{3+} fraction, x.

Equation 27

$$\mathbf{Cm-O}[\text{Å}] = \mathbf{2.50 \pm 0.01 - 0.044 \pm 0.003 \cdot x\ (La_{1-x}Gd_xPO_4)}$$

In order to convert the simulated distribution of Cm-O bond lengths in the monazite solid solutions into excitation energies, as done for Eu^{3+} (Section 5.3.1,[136]), **Equation 26** and **Equation 27** were combined, resulting in a linear expression relating the excitation energy to the Cm-O bond length.

Equation 28

$$\mathbf{E(\,^5D_0 \rightarrow\,^7F_0)[cm^{-1}] = 11351.0 \pm 479.98 + 2104.5 \pm 191.8 \cdot Cm - O}\ [\text{Å}]$$

To allow for direct comparison with the experimental TRLFS data, the computed excitation energy profile for the $La_{0.5}Gd_{0.5}PO_4$ composition was fitted by Gaussian distribution using the Gaussian normal distribution given by:

Equation 29

$$\mathbf{f(x) = e^{-\frac{(x-x_c)^2}{2\sigma^2}}},$$

where x_c is the excitation peak position and σ is the broadening. As shown in **Figure 41**, the obtained profile is comparable to the experimental TRLFS spectrum for $La_{0.46}Gd_{0.54}PO_4$. The slight blue-shift of the computed profile in comparison to the experimental one may arise from the slightly different solid solution composition with a larger La^{3+} content used in the simulations (i.e. $La_{0.5}Gd_{0.5}PO_4$ instead of $La_{0.46}Gd_{0.54}PO_4$). Similar, broad distributions were obtained for other solid solutions compositions, which indicates that the large broadening of TRLFS profiles for the considered solid solutions is caused by the increasing distribution of Cm-O bond lengths.

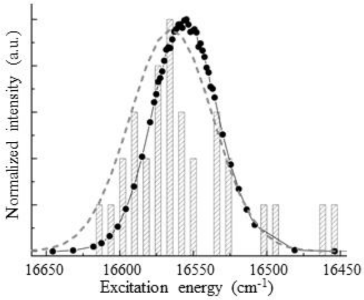

Figure 41. Experimental (solid line) excitation spectrum of the $La_{0.46}Gd_{0.54}PO_4$ solid solution doped with Cm^{3+} and the corresponding Gaussian fitting (dashed line) of the computed distribution (black bars).

Finally, all computed Cm-O bond lengths for the monazite solid solution compositions have been summarised in **Table 9**, together with the computed Cm-P and Cm-La distances in Cm-doped $LaPO_4$, to allow for comparison between experimentally derived (EXAFS) bond lengths. In general, the computed bond lengths are slightly overestimated in comparison to the experimental data. However, the largest difference is below 2.5 % of the experimentally determined value, and the Cm-O bond contraction of 0.04 Å from $LaPO_4$ to $GdPO_4$ is in excellent agreement with the experimental value of 0.03 Å. Such small differences between observed and computed bond-lengths are common for application of the DFT method.

Discussion

The combined data obtained in the laser- and X-ray absorption spectroscopic investigations of the Cm^{3+}-doped $La_{1-x}Gd_xPO_4$ monazite solid solutions clearly show that Cm^{3+} is incorporated on the crystallographic lattice sites within the ceramic structure. The resolved ground-state splitting obtained with the TRLFS method for Cm^{3+} incorporated in the $LaPO_4$ and $GdPO_4$ endmembers (**Figure 36**) is a clear indication for a single, very well defined (crystalline) environment in the monazite hosts. For the solid solution compositions ($La_{0.76}Gd_{0.24}PO_4$, $La_{0.46}Gd_{0.54}PO_4$, and $La_{0.17}Gd_{0.83}PO_4$), a complete loss of this splitting fine-structure and a broadening of the excitation peaks could be seen, implying a decrease of order in the solids. This is also visible in the XAFS investigations when examining the Debye-Waller factors obtained in the fitting of the EXAFS data, see **Table 9**. The DW factor is an indicator for thermal and structural disorder and it can be seen to decrease from 0.0090 Å^2 in $LaPO_4$ to 0.0063 Å^2 in $GdPO_4$, while it is substantially larger for the $La_{0.46}Gd_{0.54}PO_4$ solid solution composition (0.0120 Å^2). The higher structural disorder in the $LaPO_4$ endmember in comparison to $GdPO_4$ can be understood when examining the cation radii of La^{3+}, Cm^{3+}, and Gd^{3+}. The dopant vs. host cation radii show a difference of approximately 6% and 3.5% for Cm^{3+} vs. La^{3+} and Cm^{3+} vs. Gd^{3+}, respectively, i.e. a larger mismatch in the larger $LaPO_4$ host. This mismatch causes a slightly larger distortion around the Cm^{3+} dopant site, which is the probable the reason for the larger DW factor obtained for the larger $LaPO_4$ host. Such behavior, i.e. a larger disorder in $LaPO_4$ than $GdPO_4$ monazite, has previously been observed for Eu^{3+} incorporation into monazite endmembers [108], where the $^7F_1$ and $^7F_2$ emission transitions of the incorporated Eu^{3+} cation were used as an indicator for the relative increase or decrease of the site symmetry in the various monazites. The largest $^7F_2/^7F_1$ ratio (0.50), i.e. the lowest relative site-symmetry was obtained for Eu^{3+} incorporation into the large $LaPO_4$ host, while Eu^{3+} incorporation in $GdPO_4$ monazite yielded the lowest $^7F_2/^7F_1$ ratio (0.37). In concordance with the present study, this phenomenon was explained by the slight distortion of the crystal lattice accommodating a dopant with a dissimilar cation radius and the subsequent lowering of the site symmetry.

The substantially larger DW factor obtained in the present work for $La_{0.46}Gd_{0.54}PO_4$ in comparison to the monazite endmembers implies a further loss of structural order around the dopant in comparison to the monazite endmembers. This is consistent with the observed line-broadening for the solid solution excitation spectra in the TRLFS investigations, **Figure 36**. In atomistic simulations the line width of the excitation peaks were reproduced by calculating the Cm-O bond length distribution in the solid solutions and correlating the bond lengths to excitation energies using **Equation 28**. Thus, both the high DW factor obtained in the XAFS fitting, and the spectral broadening observed with the TRLFS method can be explained by the increasingly broad distribution of possible Cm-O bond lengths in the solid solution compositions in comparison to the endmembers with very well-defined Cm-O distances. The different Cm-O distances are also the cause of the emission line narrowing presented in **Figure 37**, where the presence of multiple Cm^{3+} species differing only in the Cm-O distance, experiencing slightly different ligand field strengths, will give rise to the observed "continuum" of emission peaks for the solid solution compositions.

The systematic bathochromic shift of the Cm^{3+} excitation spectra when going from the larger $LaPO_4$ host toward the smaller $GdPO_4$ monazite has already been explained to occur due to the stronger ligand-field exerted on the Cm^{3+} cation by the surrounding oxygen ligands as a function of decreasing size of the monazite unit cell. This is further confirmed by the XAFS fits showing a contraction of the Cm-O distances (**Table 9**) from $LaPO_4$ to $GdPO_4$, corroborating the interpretation of the laser spectroscopic data. The bond distances derived in the *ab initio* calculations show a similar trend, however, the overall bond-lengths tend to be slightly longer than the experimentally derived ones (**Table 9**). Interestingly, the Cm-O bond contraction is much smaller than the overall *Ln*-O bond contraction derived from the refined monazite structures published in Ni et al. [42]. A decrease of only 0.03 Å (experimental) or 0.04 Å (computed) for Cm-O in $LaPO_4$ vs. $GdPO_4$ is observed, while the La-O and Gd-O bonds display a difference of 0.1 Å in the monazite endmembers. A similar behavior was obtained in the recent study on plutonium incorporation into $LaPO_4$ monazite (**Section 5.3.3.1**, [253]). Here, the Pu-O distance in $LaPO_4$ remained unchanged at 2.48 Å for doping levels between 1-15%, whereas a decrease of a mere 0.01 Å in pure $PuPO_4$ (2.47 Å) was observed. This behavior obtained for both Pu and Cm in the monazite hosts implies that the local environments of La and Gd in the host structures are adjusting to accommodate the incorporated actinide cations, rather than the actinide environments adjusting to the size of the LnO_9 polyhedron in the host crystal lattice.

Finally, the systematic trend in the Cm^{3+} luminescence behavior as a function of Gd^{3+} substitution (x), allows us to exclude Cm^{3+} clustering within the solid solutions, as Cm-rich monazite clusters within the solid structure would result in distinctly different excitation peak maxima and a disruption of the linear trend observed for the solid solution compositions. This is again in concordance with the XAFS results, where no Cm-Cm backscatter was detected in the recorded EXAFS spectra. The absence of clustering is of great importance when considering the performance of monazite materials as immobilisation matrices for highly radioactive actinide compounds, as a preferential clustering of dopants around matching lattice sites could lead to incongruent leaching rates and further to an inadequate retention of the radionuclides in a deep geological repository environment.

5.3.3.3 Laser spectroscopic investigations of Cm^{3+}-doped rhabdophane

The recorded excitation spectra for Cm^{3+}-doped $LaPO_4$ and $GdPO_4$ rhabdophane compounds are shown in **Figure 42**, left. Here, also hot-band transitions are shown (denoted with asterisks) as they have been included in the calculations of the relative amounts of various Cm^{3+} species in the rhabdophane solids, see discussion later in the text. Two distinct curium species with corresponding hot-bands can be seen for $LaPO_4$ rhabdophane, while three species exists in $GdPO_4{\cdot}0.667H_2O$. Especially, the curium species found in $GdPO_4{\cdot}0.667H_2O$ are rather ill-defined, yielding asymmetric emission spectra (**Figure 42**, right) that seem to have two local maxima rather than one clear emission peak. This asymmetry may to some extent arise from the non-resolved ground state splitting of the incorporated Cm^{3+} species, but local imperfections around the Cm^{3+} cation site or slightly different host lattice environments (see analogy to the monazite solid solutions discussed above) certainly play a role as well. This implies, that even the rhabdophane endmember compositions are substantially less ordered, most likely due to crystallinity reasons, than the monazites, which show a clearly resolved ground-state splitting for both $LaPO_4$ and $GdPO_4$ (**Figure 36**). Despite this asymmetry, three clearly distinguishable Cm^{3+} species are present in $GdPO_4$ rhabdophane, two of which are also found in $LaPO_4$ rhabdophane. For the solid solution compositions ($La_{0.76}Gd_{0.24}PO_4{\cdot}0.667H_2O$, $La_{0.46}Gd_{0.54}PO_4{\cdot}0.667H_2O$, and $La_{0.17}Gd_{0.83}PO_4{\cdot}0.667H_2O$), two species are found, in agreement with the $LaPO_4$ rhabdophane solid, i.e. only $GdPO_4$ rhabdophane shows the presence of three curium species.

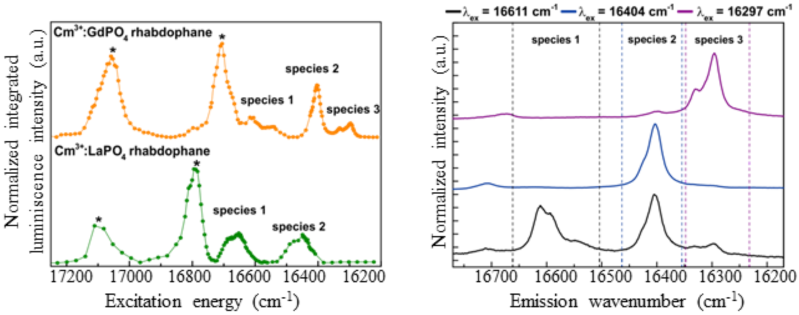

Figure 42. Left – measured excitation spectra of Cm^{3+}-doped $LaPO_4$ and $GdPO_4$ rhabdophane. Hot-band transitions ($Z_1 \rightarrow A_2/A_3$) are denoted with asterisks. Right – emission spectra of the three different Cm^{3+} species found in $GdPO_4$ rhabdophane. The excitation energies used for the collection of the respective emission spectra are denoted on top of the figure.

By carefully selecting the excitation energy, the various species can be individually excited and both emission spectra and lifetimes can be recorded for the respective species. However, especially for $GdPO_4 \cdot 0.667H_2O$ with three Cm^{3+} species present within the solid structure, hot-band transitions (typically $Z_1 \rightarrow A_2$) of energetically lower lying species overlap with the main transition ($Z_1 \rightarrow A_1$) of higher-lying species, i.e. a perfect separation of the three species could not be achieved. This is visible in e.g. the emission spectra **Figure 42**, right, where the bottom (black) spectrum shows the presence of all three species despite "selective" excitation at 16611 cm^{-1}, i.e. at the excitation energy maximum of the first Cm^{3+} species (species 1). Due to this overlap, the recorded lifetime of this species 1 in $GdPO_4$ rhabdophane shows multi-exponential decay behavior (**Figure 43**), while monoexponential decay curves, corresponding to the lifetimes of individual Cm^{3+} species, are obtained in all other cases for the $LaPO_4$ and $GdPO_4$ rhabdophane solids.

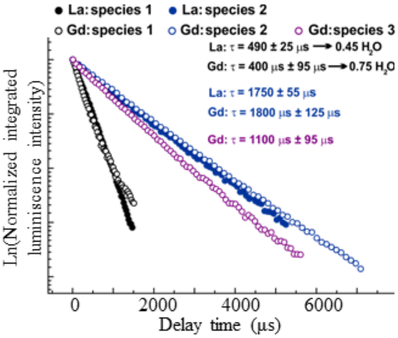

Figure 43. Recorded lifetimes for the individual Cm^{3+} species present in $LaPO_4 \cdot 0.667H_2O$ (closed symbols) and $GdPO_4 \cdot 0.667H_2O$ (open symbols).

The lifetimes obtained for species 1 and species 2 are comparable for Cm^{3+} incorporated in $LaPO_4 \cdot 0.667H_2O$ and $GdPO_4 \cdot 0.667H_2O$. Species 1 in these solids is characterized by a short lifetime of 400 – 490 µs, while species 2 is substantially longer, 1750 – 1800 µs. The third species which is present in $GdPO_4 \cdot 0.667H_2O$ only, has a lifetime of 1100 ± 95 µs. By using **Equation 26** to correlate the recorded lifetimes to the number of hydration water molecules around the Cm^{3+} cation, $n(H_2O)$ values below zero are obtained for species 2 and species 3, implying that these Cm^{3+} species are incorporated within the rhabdophane solids on lattice sites which are not associated with water of hydration or other luminescence quenchers. Species 1 on the other hand yields approximately 0.45 ± 0.07 H_2O entities for Cm^{3+} in $LaPO_4·0.667H_2O$ and 0.75 ± 0.32 H_2O for Cm^{3+} in $GdPO_4·0.667H_2O$ when using **Equation 3**. This would imply that Cm^{3+} incorporation has occurred on a lattice site in rhabdophane that is in direct contact with water of hydration. As previously stated, **Equation 3** cannot be used to predict the exact number of hydration water molecules associated with the Cm^{3+} lattice site, as the quenching behavior of such water molecules is not fully understood. Based on the refined structure of rhabdophane, however, the lattice site should contain one water of hydration [59]. Further discussion of the various lattice sites in the rhabdophane solids is given in the following section.

Determination of the site occupancy in Cm^{3+}-doped rhabdophane compounds

The site occupancy of Cm^{3+} in the rhabdophane solid solutions has been derived from the experimental TRLFS data presented above, and *ab initio*-based calculations of the lattice site energetics as given by **Equation 7**.

The experimental Cm^{3+} site occupancy in the rhabdophane solid solutions was calculated by relating the magnitude of the TRLFS excitation peak intensities of individual curium species to the total excitation peak intensity of all curium species in the system. Due to the overlap of hot-band transitions (typically $Z_1 \rightarrow A_2$) and main transition ($Z_1 \rightarrow A_1$), as explained above, only the integrated intensity of the lowest-lying species with the largest crystal field splitting could be determined without interference from other species. Thus, in those rhabdophane compositions with only two Cm^{3+}-species present, i.e. all solids except $GdPO_4·0.667H_2O$, the percentages of the individual species were obtained by integrating the total excitation peak intensity including the hot-bands, and thereafter integrating the total excitation energy of species 2 (without interference of species 1). The presence of three curium species in the $GdPO_4$ rhabdophane solid clearly hampered the accurate determination of the site occupancies, where the absolute integrals of especially the minor species (species 1 and species 3, see **Figure 42**, left) could not be properly separated from the rather dominant signal originating form species 2. Thus, these site occupancies are connected to rather high uncertainties as seen in **Figure 44**, left, where the experimentally derived site occupancies are presented as a function of Gd^{3+} substitution (x).

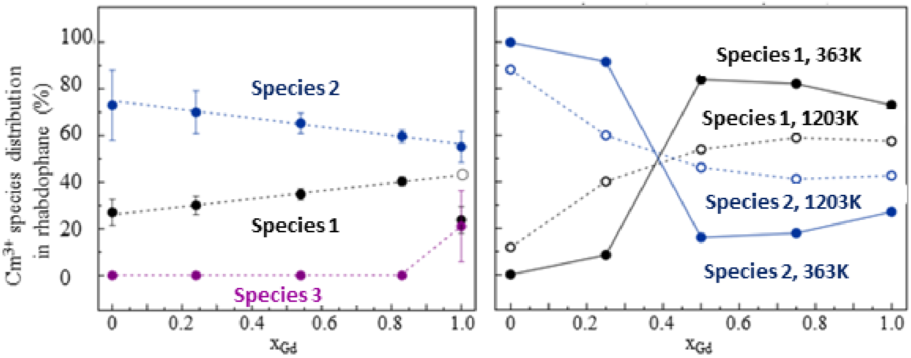

Figure 44. Derived experimental (left) and computational (right) Cm^{3+} site occupancies as a function of Gd^{3+} substitution (x) in rhabdophane solid solutions. Species 3 in the derived experimental distribution was only encountered in GdPO$_4$·0.667H$_2$O. The open blue symbol for the GdPO$_4$ rhabdophane composition (left), illustrates the expected percentage of species 1, assuming a linear compositional trend with increasing x, in the absence of species 3.

The distribution of Cm^{3+} between hydrated and non-hydrated cation sites at two different temperatures derived from atomistic simulations is shown in **Figure 44**, right. The *ab initio* energies show that for La-rhabdophane the non-hydrated site is preferred by 20 kJ·mol^{-1}, while for Gd-rhabdophane the hydrated site is preferred, but only by 3 kJ·mol^{-1}. Although such small energy differences are difficult to be accurately captured by DFT [168], the resulting trend indicates preference for non-hydrated sites in La-rich solid solutions and approximately equal distribution in Gd-rich compositions, which is consistent with the experiments. Furthermore, the results imply that higher temperatures promote incorporation of Cm^{3+} on non-hydrated sites. We are fully aware that the high temperature (1203 K) used in the simulations, would cause complete dehydration of rhabdophane under experimental conditions. However, as the purpose of the simulations was to illustrate the influence of temperature on the Cm^{3+} site occupancy, chemical changes of the rhabdophane phase itself were not considered.

To understand the incorporation behavior of Cm^{3+} in the rhabdophane matrices, we complemented the computational results with calculated volumes per MPO$_4$ formula unit (M = La, Gd or Cm) for pure rhabdophane phases and for Cm-doped rhabdophane on hydrated (hyd) and non-hydrated (non-hyd) lattice sites in Cm^{3+}:LaPO$_4$·0.667H$_2$O, Cm^{3+}:GdPO$_4$·0.667H$_2$O and

$CmPO_4{\cdot}0.667H_2O$. The volumes of hydrated and non-hydrated Cm species in $CmPO_4{\cdot}0.667H_2O$ are derived by comparing the volumes of $CmPO_4{\cdot}0.667H_2O$ and $CmPO_4$ (rhabdophane supercell with all waters removed). The results are compiled in **Table 10**. When looking at the obtained values, it is clear that non-hydrated Cm species are larger than the hydrated ones and, thus, can be expected to prefer larger host lattice sites. A comprehensive discussion of the site occupancy will be given later in the text.

Table 10. Computed volumes per MPO_4 formula unit (M = La, Gd, Cm) for pure rhabdophane phases and for Cm^{3+} incorporated on hydrated (hyd) and non-hydrated (non-hyd) lattice sites in $LaPO_4{\cdot}0.667H_2O$, $GdPO_4{\cdot}0.667H_2O$, and $CmPO_4{\cdot}0.667H_2O$.

Rhabdophane composition (site type)	Vol/MPO_4 (Å^3)
$LaPO_4{\cdot}0.667H_2O$	95.761
$GdPO_4{\cdot}0.667H_2O$	85.910
$CmPO_4{\cdot}0.667H_2O$	89.986
$CmPO_4{\cdot}0.667H_2O$ (hyd)	89.031
$CmPO_4{\cdot}0.667H_2O$ (non-hyd)	91.897
Cm^{3+}:$LaPO_4{\cdot}0.667H_2O$ (hyd)	89.849
Cm^{3+}:$LaPO_4{\cdot}0.667H_2O$ (non-hyd)	94.503
Cm^{3+}:$GdPO_4{\cdot}0.667H_2O$ (hyd)	90.389
Cm^{3+}:$GdPO_4{\cdot}0.667H_2O$ (non-hyd)	89.319

Discussion

The incorporation of actinides into rhabdophane has been studied for the first time from the perspective of the dopant itself. As expected, the presence of two cation sites (hydrated and non-hydrated) within the hydrated rhabdophane matrix influences the incorporation behavior of the actinide. In contrast to the monazites where only one host cation site is available for Cm^{3+} incorporation, this study shows that two or three different actinide species are present in the synthesised rhabdophane solids, depending on composition. Interestingly, the site occupancy derived both experimentally from the TRLFS investigations and computationally by calculating the energy of Cm incorporation into the hydrated and non-hydrated configurations, is not in agreement with the fully hydrated rhabdophane structure. As previously described, two thirds of the sites in hydrated rhabdophane are associated with water of hydration, leaving only one third of the sites non-hydrated. According to experimental data, all rhabdophane compositions show preferential incorporation of Cm^{3+} on the non-hydrated site, while *ab initio* calculations result in slightly higher hydrated site occupancies in comparison to the non-hydrated sites for high Gd^{3+} substitutions, depending on temperature, Figure 44. However, a 67 % vs. 33% hydrated vs. non-hydrated site occupancy is not obtained in any case. Thus, the present study emphasizes the importance of spectroscopic methods to accurately determine site occupancies, which clearly cannot be predicted based on the structure of the host matrix only.

The underlying reason for the site occupancy can be understood when looking at the calculated MPO_4 formula unit volumes for Cm^{3+} incorporation on hydrated and non-hydrated lattice sites in $LaPO_4 \cdot 0.667H_2O$ and $GdPO_4 \cdot 0.667H_2O$ (**Table 10**). In $LaPO_4$-rhabdophane, the non-hydrated site is significantly larger than the hydrated one. When comparing the formula unit volume for pure $CmPO_4$ rhabdophane for both hydrated and non-hydrated positions, only the larger non-hydrated site in the La-rhabdophane solids can accommodate both Cm^{3+} species without inducing local strain around the dopant cation. This is the likely explanation for the preferential incorporation of Cm^{3+} on non-hydrated lattice sites in La-rich rhabdophane compositions. In $GdPO_4$ rhabdophane, the situation is different. Here, both sites are too small in comparison to pure $CmPO_4$ rhabdophane, implying that a distortion of the lattice is required upon incorporation of Cm^{3+}. The resulting $CmPO_4$ formula unit volumes in Gd-rich rhabdophane solids are very similar in size, with a slightly larger volume for the hydrated sites, resulting in a small preference for Cm^{3+} incorporation on these site types according to the *ab initio* calculations. The experimental data deviates slightly from this behavior for the Gd-rich rhabdophane compositions. In neither of the samples, a preferential incorporation on the hydrated sites is obtained. Instead, the formation of a third species in the pure $GdPO_4 \cdot 0.667H_2O$ solid is observed, which is not accounted for in the other synthesised rhabdophane solids. Based on the luminescence lifetime of this species (1100 ± 95 µs), there are no quenching entities, such as water of hydration, directly associated with the incorporated curium cation. This would exclude the presence of small amounts of other low temperature phosphate phases with more water of hydration in the structure, such as churchite/weinschenkite ($LnPO_4 \cdot 2H_2O$), which under certain experimental conditions could coexist with rhabdophane for Gd to Dy, but not for the larger lanthanides like La [64]. In contrast, it is more likely that slight dehydration of the hydrated rhabdophane structure has occurred for the $GdPO_4 \cdot 0.667H_2O$ solid, leading to the presence of another dehydrated site for curium incorporation. In a recent publication by Mesbah et al. (2017) [60], investigating the stepwise dehydration of rhabdophane, the authors could confirm a first dehydration step with a loss of 0.167 water molecules between 333 K and 413 K, depending on the size of the host lanthanide, leading to the formation of hemihydrated rhabdophane, $LnPO_4 \cdot 0.5H_2O$. This hemihydrated rhabdophane structure has two cation sites associated with water of hydration and two cation sites that do not coordinate with water. The dehydration temperature was shown to decrease linearly with decreasing cation radius. For La and Gd-rhabdophanes, dehydration temperatures of around 413 K and 333 K, respectively, were found. Thus, bearing in mind that the rhabdophane synthesis was carried out at 363 K, it is indeed likely that dehydration, followed by incomplete rehydration of the Gd-rhabdophane solid has occurred, leading to the presence of additional cation sites for curium incorporation in the examined solid. In addition, when examining the published values for lattice parameters of the fully hydrated and hemihydrated rhabdophane solids, a very small increase (< 0.2 %) of the unit cell volume is observed in the dehydration process, while the β angle increases from 115.23° ($SmPO_4 \cdot 0.667H_2O$) [59] to 133.73° ($SmPO_4 \cdot 0.5H_2O$) [60]. This rather large increase of the β angle could indeed explain the non-linear behavior of this lattice parameter obtained in the Rietveld refinements of the rhabdophane PXRD data and serves as a further indication of a slight dehydration of the $GdPO_4 \cdot 0.667H_2O$ composition during synthesis.

5.3.4 Structural incorporation of Pu^{+3} in lanthanide orthophosphates with rhabdophane and monazite structures

Solid state chemistry methods play an important role regarding the immobilisation of existing separated inventories of Pu as it is stored intermediately as PuO_2. Wet chemistry methods such as precipitation may offer some advantages over the solid state route with respect to the safe handling of radionuclides and minimization of contamination risk due to dust formation. But the merits vanish taking into account the criticality risks, and thus much smaller industrial batches, as well as the efforts needed to dissolve the hardly soluble PuO_2 in glove boxes. Hence, within this work the structural incorporation and loading limitations of Pu^{III} in monazite-type phosphate ceramics by solid state synthesis using PuO_2 as starting material has been investigated systematically for the first time. The refined crystal structure of the $(La,Pu)PO_4$-monazite solid solutions has been studied by a combination of XRD and EXAFS. Particular attention has been paid to the determination of the valence state of plutonium in the solid solution using XANES since $Pu^{IV}O_2$ has been used as precursor material for the solid solution preparation under inert atmosphere. $PuPO_4$ was additionally synthesised over wet chemical method by precipitation from the Pu^{4+} nitrate stock solution reduced to Pu^{3+} by hydrazine with an excess of concentrated phosphoric acid and subsequent thermal treatment.

Powder X-ray diffraction

The conventional solid state method, reported previously for synthesis of $Pu^{III}PO_4$ with monazite structure [117, 124], was applied in this work to obtain $La_{1-x}Pu_xPO_4$ monazite solid solutions according to **Equation 30**:

Equation 30

$$(1-x)\ La_2O_3 + 2x\ Pu^{IV}O_2 + 2\ (NH_4)_2HPO_4 \rightarrow 2\ La_{1-x}Pu_x{}^{III}PO_4 + 4\ NH_3{}^{\uparrow} + 3\ H_2O + 0.5x\ O_2{}^{\uparrow}$$

PXRD patterns of the resulting compounds with the corresponding references from COD (Crystallography Open Database) for the endmembers are shown in **Figure 45**.

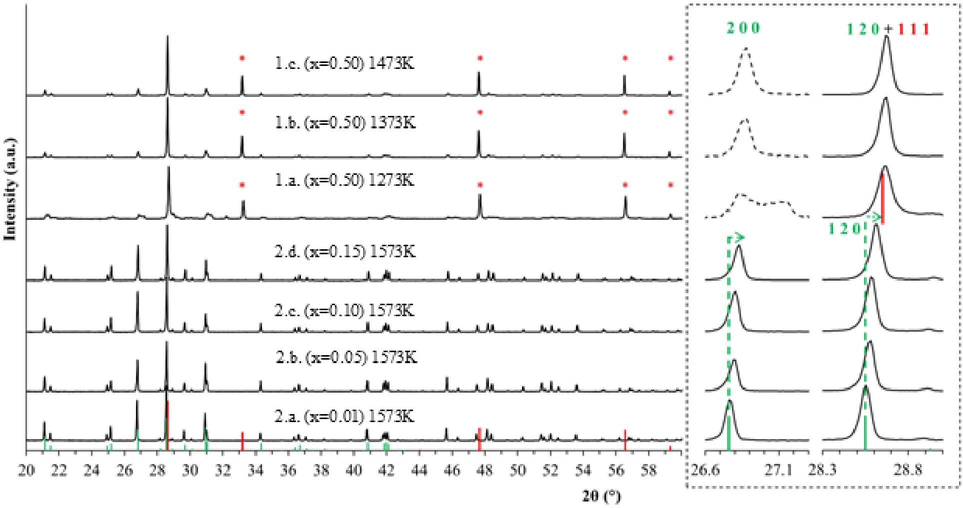

Figure 45. Diffraction patterns of the synthesised $La_{1-x}Pu_xPO_4$ compounds with x = 0.01, 0.05, 0.1, 0.15, (0.50) with the corresponding references from COD (Crystallography Open Database) for $LaPO_4$-monazite (green) and PuO_2 (red). Red stars highlight the characteristic Bragg reflections of the PuO_2 phase. The 200 and 120 reflections of the monazite phase are shown in the insert. The 200 Bragg reflections marked with the dashed line are magnified by factor 7 relatively to the corresponding diffraction patterns.

According to the XRD data, the first attempt to synthesize $La_{0.50}Pu_{0.50}PO_4$ solid solution by the conventional solid state method at 1273 K, led to the formation of several phases: $(La,Pu)PO_4$ monazite solid solutions with varying Pu-loadings and a cubic PuO_2 phase. The corresponding diffraction pattern (1.a) is shown in **Figure 45**, red stars highlight the characteristic Bragg reflections of the PuO_2 phase. The splitting of the 200 Bragg reflections of the monazite phase (insert of **Figure 45**) indicates the formation of at least two monazite phases with different molar fractions of Pu. A similar effect was already observed by Bregiroux et al. [254] for mixed lanthanide orthophosphates. It seems to be challenging to obtain a pure and homogeneous monazite phase of orthophosphate solid solutions by a solid state method due to the differences in reaction kinetics for different cations. In the case of lanthanum and plutonium oxides the differences in reaction kinetics are apparently caused by the reduction step of Pu^{IV} during the solid state synthesis. By increasing the synthesis temperature up to 1373 and 1473 K, a single solid solution with monazite structure was obtained, but the PuO_2 Bragg reflections remained evident too (**Figure 45**, diffraction patterns 1.b and 1.c). The phase ratio and lattice parameters of the monazite phase were determined using Rietveld refinement of the XRD data. The increase of temperature from 1373 to 1473 K led to an increase of the monazite phase fraction by 5% reaching 86±1%. However the molar fraction of Pu remained constant within the uncertainties of the refinement (0.15±0.03 and 0.22±0.05, respectively). No further heating has been applied, bearing in mind the thermal decomposition of the $PuPO_4$ endmember.

The Pu^{IV} to Pu^{III} redox-reaction may inhibit the formation of a pure single phase monazite-type $La_{1-x}Pu_xPO_4$ solid solution by the solid state reaction, especially at higher Pu-content. Moreover it explains the presence of residual PuO_2 after the solid state reaction. A thermal decomposition of $PuPO_4$ at 1473 K in inert atmosphere according to Jardin et al. [125] (**Equation 31**) can definitely be excluded because in detailed evaluation of the XRD patterns no Pu_2O_3 was found.

Equation 31

$4\ PuPO_4 \rightarrow 2\ Pu_2O_3 + P_4O_{10}{}^{\uparrow}$

Therefore, the residual PuO_2 appears to be unreacted and not-reduced precursor material of the synthesis. The formation of a single phase solid solution bearing a higher Pu content can be expected by optimizing the synthesis parameters in terms of the excess of $(NH_4)_2HPO_4$. Additionally, $La_{1-x}Pu_xPO_4$ solid solutions with relatively low molar fraction of Pu might be stabilized by the high thermal stability of the $LaPO_4$ matrix (melting temperature 2345 K) [255] that would allow for solid state reactions at a temperature above the decomposition temperature of pure $PuPO_4$.

Based on these considerations the target molar fraction of Pu was reduced and pure-phase $La_{1-x}Pu_xPO_4$ solid solutions with monazite structure were successfully obtained at 1573 K for the compositions with x = 0.01, 0.05, 0.10, 0.15 according to the PXRD data (**Figure 45**, diffraction patterns 3.a – d). No characteristic Bragg reflections for PuO_2 are evident in the PXRD patterns. The insert of **Figure 45** demonstrates exemplarily the linear shift of the 200 and 120 Bragg reflections towards higher 2θ values on increasing the Pu-loading. This effect is caused by the lattice contraction due to the incorporation of the slightly smaller Pu^{3+} ions compared to La^{3+} (1.187 Å [124], estimated from David [249], and 1.215 Å [43], respectively (radii are given for a nine-fold coordinated environment)). As a consequence the lattice parameters decrease linearly as a function of Pu-content confirming solid solution formation according to the Vegard's law

(**Figure 46**). The corresponding refined cell constants are summarised in **Table A 7** in the **Appendix**.

The reaction to form a solid solution appears to be more favourable from a kinetic point of view compared to the plutonium phosphate decomposition, which possibly starts from 1473 K $PuPO_4$ seems to be stabilized at this temperature due to the incorporation into the lattice of the $LaPO_4$ host matrix forming a solid solution.

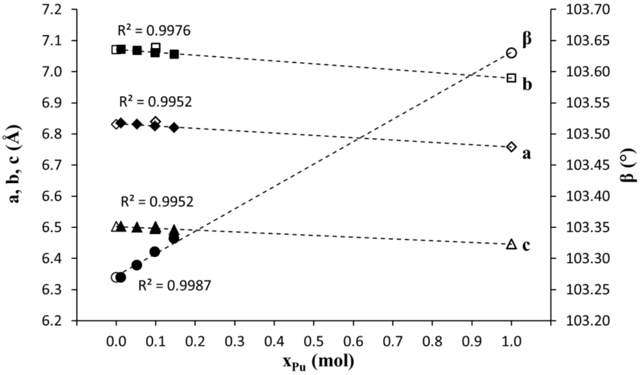

Figure 46. Evolution of the lattice parameters of the $La_{1-x}Pu_xPO_4$ solid solutions with monazite structure (x = 0 – 1). Lattice parameters for $LaPO_4$ [42], $PuPO_4$ [25] as well as for $La_{0.9}Pu_{0.1}PO_4$ [126] are marked with open symbols.

Scanning electron microscopy with energy dispersive spectroscopy

The chemical composition and the microstructure of the single phase solid solutions have been investigated using SEM-EDS. The EDS analysis confirmed the homogeneity of the samples as well as the actual compositions of the synthesised solid solutions. The resulting molar fraction of Pu is given in **Table A 7**.

The SEM-micrographs in **Figure 47**, left, a show the microstructures of selected compounds with x = 0.01 and x = 0.15 at different magnifications. The sponge-like microstructure of the samples indicates a vigorous reaction during the heat treatment accompanied by active gas release. These observations confirmed self-homogenization of the reaction mixture during heat treatment. The average grain diameter for each composition determined from the corresponding SEM micrographs is presented in **Figure 47**, right, as a function of composition. It is noticeable, that the grains for the composition with the molar fraction of plutonium x = 0.15 are larger whereas its porosity is smaller in comparison to those for x = 0.01 (**Figure 47**, a). A linear increase in the average grain diameter with increasing molar fraction of plutonium was observed. It suggests that the Pu content increases the grain growth rate of the solid solutions at a given temperature.

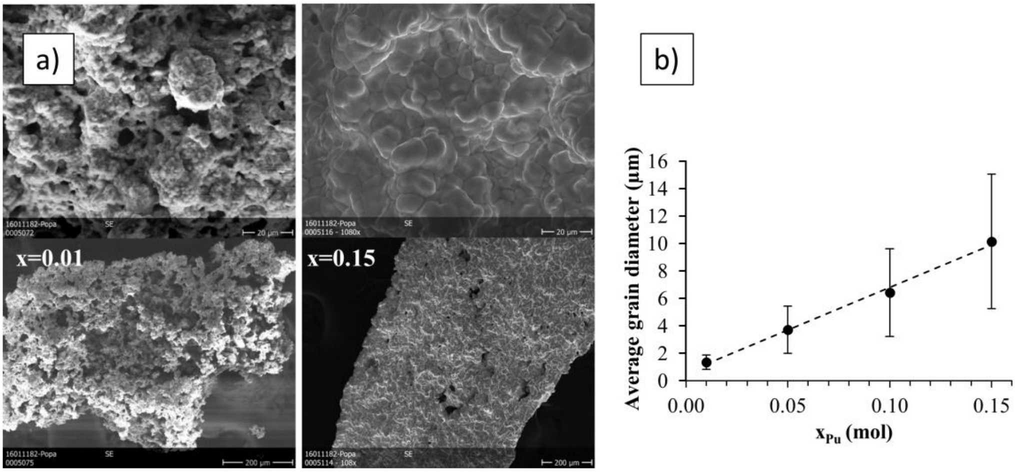

Figure 47. SEM images of microstructure (a) and average grain diameters (b) of the $La_{1-x}Pu_xPO_4$ solid solutions with monazite structure in dependence on composition. The apparent increasing error bars with increasing Pu content represent the grain size distribution.

X-ray absorption spectroscopy

The Pu-L_{III} edge X-ray absorption near-edge structure (XANES) spectra of the synthesised solid solutions (x = 0.01, 0.05, 0.10, 0.15) are presented in **Figure 48**. The line position of the solid solutions matches that of the purely trivalent Pu-monazite endmember (x = 1.00), and is about 5 eV lower than that of the Pu^{IV} reference PuO_2. A subsequent analysis of the spectral series by iterative transformation factor analysis (ITFA) [256, 257] confirmed that all samples contain at least 95% of Pu^{III}, as expected for the synthesis under inert atmosphere [125].

The atomic environment of the incorporated Pu atoms in the crystal structure has been studied as a function of composition of the synthesised solid solutions (x = 0.01, 0.05, 0.10, 0.15) by extended X-ray absorption fine-structure (EXAFS) spectroscopy.

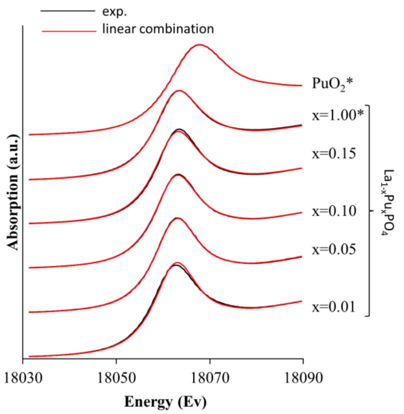

Figure 48. Experimental Pu-L$_{III}$ XANES spectra (black) and their reproduction (red) by the two reference spectra show on top (Pu^{III} and Pu^{IV}).

Figure 49 shows from top to bottom the Pu-L$_{III}$ edge Fourier transform magnitudes (FTM) of the pure Pu-monazite endmember, of the Pu-doped La-monazite samples sorted along decreasing Pu molar fraction, and finally the La-L$_{III}$ spectrum of the pure La-monazite endmember. The FTM of the Pu-La solid solution series are almost identical, independent of Pu-doping; while the FTM of pure Pu-monazite has distinct features in the regions of the next P neighbors (marked in orange) and of the next Pu/La neighbors (marked in purple). In contrast, the spectrum of LaPO$_4$ shows a longer distance of the oxygen coordination shell (red), in addition to different peak shapes in the P and Pu/La regions.

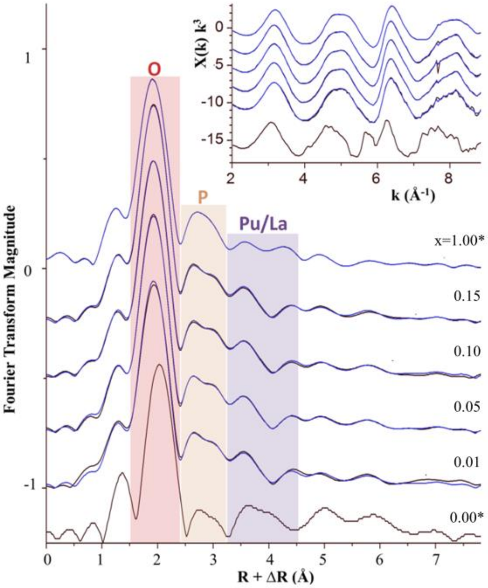

Figure 49. Pu-L_{III} EXAFS spectra of Pu monazite and Pu-La monazite solid solutions in comparison to the La-L_{III} EXAFS spectrum of La monazite. Experimental data are given as black lines, blue lines are the reconstruction of the Pu-L_{III} spectra by two principal components. The large figure gives the k^3-weighted Fourier transform magnitudes (FTM), the insert the k^3-weighted chi-spectra. Major contributions from the nine coordinating oxygen atoms are within the red area, those of the seven nearest phosphorous atoms are within the orange area, and those of the six nearest Pu/La atoms are within the purple area.

With space group P 1 21/n 1(14), the monazite structure shows poor radial distribution ordering of the atoms around the cation centers. In $LaPO_4$, for instance, the coordination shell of nine oxygen atoms has La-O distances (R_{La-O}) ranging from 2.45 to 2.78 Å; the seven P atoms from the phosphate units directly linked to this LaO_9 polyhedron have distances ranging from 3.20 to 3.79 Å, followed by 3 La neighbors from 4.08 to 4.15 Å and another three La neighbors from 4.30 to 4.36 Å. Since the distal resolution of EXAFS is limited by $\pi/(2*\Delta\chi)$, shells have to be separated by at least 0.21 Å, given the limited k-range available (2.0 to 9.5 Å). Therefore, the different individual interatomic distances had to be grouped into shells for EXAFS fitting. The most stable fits were obtained with the following grouping: a coordination shell of 9 oxygen atoms, 3 shorter and 4 longer cation-P distances, as well as 3 shorter and 3 longer cation-cation distances. The results derived from the corresponding fits are shown in **Table 11**.

Table 11. EXAFS shell fit results of Pu-doped La-monazites in comparison to $PuPO_4$ and $LaPO_4$ (Pu-L_{III} and La-L_{III} spectra, respectively).

Sample	Path	CN	R (Å)	σ^2 (Å^2)	ΔE_0 (eV)	S_0^2	χ_{res} (%)
$PuPO_4$ (T)	Pu-O	9	2.47	0.0103	9.9	0.70	7.4
	Pu-P	3	3.21	0.0117			
	Pu-P	4	3.74	0.0105			
	Pu-Pu	3	4.07	0.0061			
	Pu-Pu	3	4.24	0.0057			
$La_{0.85}Pu_{0.15}PO_4$ (T)	Pu-O	9	2.48	0.0094	9.2	0.77	6.3
	Pu-P	3	3.20	0.0122			
	Pu-P	4	3.75	0.0083			
	Pu-Pu	3	4.10	0.0014			
	Pu-La	3	4.33	0.0010			
$La_{0.90}Pu_{0.10}PO_4$ (T)	Pu-O	9	2.48	0.0098	8.9	0.79	6.3
	Pu-P	3	3.20	0.0125			
	Pu-P	4	3.74	0.0085			
	Pu-Pu	3	4.05	0.0016			
	Pu-La	3	4.32	0.0010			
$La_{0.95}Pu_{0.05}PO_4$ (T)	Pu-O	9	2.48	0.0094	8.8	0.78	6.6
	Pu-P	3	3.20	0.0130			
	Pu-P	4	3.74	0.0082			
	Pu-Pu	3	4.06	0.0014			
	Pu-La	3	4.33	0.0010			
$La_{0.99}Pu_{0.01}PO_4$ (F)	Pu-O	9	2.48	0.0100	9.2	0.74	7.6
	Pu-P	3	3.20	0.0112			
	Pu-P	4	3.74	0.0083			
	Pu-Pu	3	4.06	0.0012			
	Pu-La	3	4.33	0.0010			
$LaPO_4$ (F)	La-O	9	2.53	0.0106	10.2	0.63	13.8
	La-P	3	3.31	0.0205^c			
	La-P	4	3.73	0.0205^c			
	La-La	3	4.08	0.0082^c			
	La-La	3	4.38	0.0082^c			
$LaPO_4$ (XRD)[42]	La-O	9	2.56				
	La-P	3	3.32				
	La-P	4	3.76				
	La-La	3	4.11				
	La-La	3	4.32				

CN: coordination number, R: radial distance, σ^2: Debye-Waller term, ΔE_0: phase shift, S_0^2: amplitude reduction factor, χ_{res}: residual error, c: parameters were correlated during the EXAFS fit, T, F: EXAFS data collected in transmission or fluorescence mode, respectively.

In all Pu-containing monazites, the coordination shell could be fitted with 9 Pu-O paths, giving average distances of 2.47 to 2.48 Å and a relatively high local disorder expressed by Debye-Waller factors of ~0.01 Å^2 in line with the expected distorted tricapped prism structure (**Table 11**). For $LaPO_4$, this distance is significantly larger (2.53 Å), owing to the larger ionic radius of La^{3+} versus Pu^{3+}. Furthermore, the two Pu-P paths provided distances at 3.20 and 3.74 Å, with no significant change of distances or disorder from 100% to 1% Pu.

For $PuPO_4$, the following two Pu-Pu shells were fitted with average distances of 4.07 and 4.24 Å, well in line with the monazite structural model. For the Pu-La solid solution series, however, the backscattering elements of the shorter and longer cation-cation interactions may be La or Pu, with a prevalence of Pu-Pu for high Pu content, and a prevalence of Pu-La for lower Pu content. Identification of the prevalent backscattering element by wavelet analysis [258] could not distinguish contributions from La and Pu due to the k range (2.0 to 9.5 Å) limited by the presence of the Am daughter nuclide. Therefore different combinations of Pu-Pu and Pu-La paths were applied. For all samples, with the molar fraction of Pu ranging from 1 to 15, the best fit was obtained with Pu-Pu paths for the shorter, and Pu-La paths for the longer distance. This may be an indication for an inhomogeneous distribution of Pu in the La-Pu-monazite lattice, i.e. a certain clustering of Pu cations, which changes little as revealed by the invariant FTM pattern in the La/Pu region. With $R_{Pu\text{-}Pu}$ between 4.05 and 4.10 Å, the solid solution samples do not vary significantly from the distance of 4.07 Å found for the pure $PuPO_4$ endmember, further supporting a clustering of Pu atoms. In contrast, the Pu-La distances at 4.33 Å are significantly longer than the corresponding Pu-Pu distance of 4.24 Å in $PuPO_4$, and similar to the La-La distance in $LaPO_4$.

In conclusion, the local environment of Pu remains $PuPO_4$-like along the solid solution series, except for the longest fitted cation-cation distance, which is always $LaPO_4$-like. Such an effect is most consistently explained by clustering, i.e. a heterogeneous distribution of cations in solid solutions at the molecular scale, which is observable by short-range order probes like EXAFS, but not by long-range order probes like XRD, as was observed for instance for metal oxides, silicates and phosphates [259-266]. Even more relevant, a similar effect was recently observed by EXAFS for $(La,Eu)PO_4$ and Cm-doped $(La,Gd)PO_4$ monazite solid solutions, where Eu or Gd served as inactive surrogates for trivalent actinides [135, 267]. For both solid solution series bond lengths in the local environment of Eu and Cm, respectively were significantly shorter in comparison to those in the local environment of La. This indicates that the local environment of La with relatively longer and therefore weaker bonds is adjusting by the incorporation of smaller cations in the $LaPO_4$ monazite matrix.

Wet-chemical synthesis of $PuPO_4$

$PuPO_4$ was additionally synthesised over wet chemical method by precipitation from a Pu^{4+} nitrate stock solution reduced to Pu^{3+} by hydrazine with an excess of concentrated phosphoric acid. XRD measurements revealed formation of hydrated plutonium hypophosphite contaminated by a minor fraction of an unidentified phase (**Figure 50**, 303 K). The formation of hypophosphite is caused by the excess of phosphoric acid. *In situ* high temperature XRD has revealed vanishing of reflexes at about 12° 2θ after 373 K presumably caused by dehydration of hydrated plutonium hypophosphite (**Figure 50**). Formation of a pure monazite phase from the precursor was detected by HT-XRD at 1073 K. Thermal expansion of $PuPO_4$ was observed from 1073 K up to 1273 K. It is important to notice that a crystal structure of Pu-rhabdophane refined by XRD as well as its XRD pattern have not been reported so far. Therefore, it can be assumed, that the "rhabdophane" phase for the precipitation product was suggested in the literature solely analogously to the *Ln*-rhabdophane (**Figure 50**). Formation of pure monazite phase was detected by HT-XRD at 1073 K. Thermal expansion of $PuPO_4$ monazite was observed from 1073 up to 1273 K (**Figure 50**).

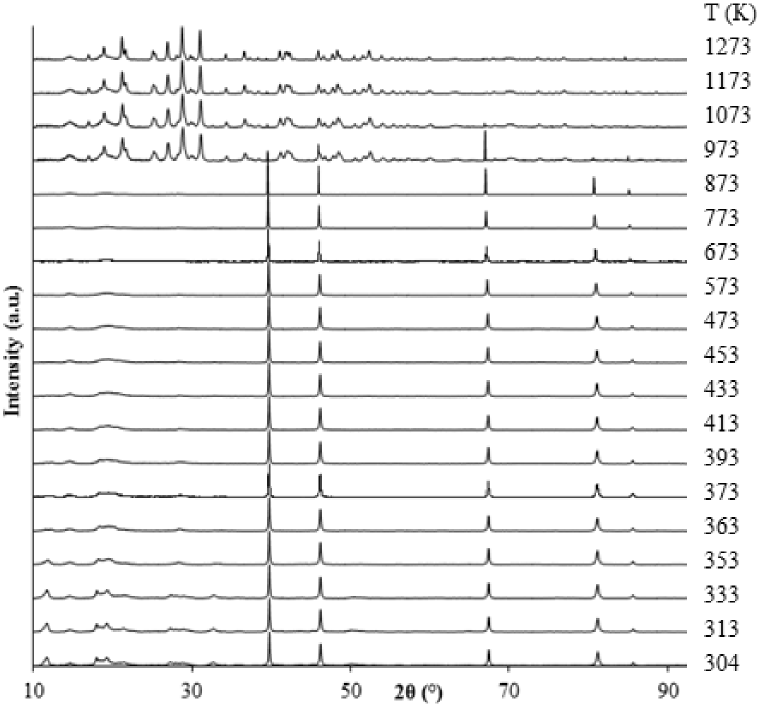

Figure 50. *In situ* high temperature XRD of the precipitate from the wet chemical synthesis of $PuPO_4$.

5.3.5 Résumé of Chapter 5.3

Formation of monazite-type of $La_{1-x}Ln_xPO_4$-monazite solid solutions (Ln = Gd, Eu)

Synthetic $La_{1-x}(Gd/Eu)_xPO_4$ monazite-type solid solutions were studied by combined X-ray diffraction, Raman and TRLFS spectroscopic techniques and atomistic modelling in order to evaluate the homogeneity of the solid solution. The Gd^{3+} and Eu^{3+} cations were taken as analogues for the trivalent actinides (e.g. Am, Cm, Pu(III)) to gain insight into the flexibility of the monazite host structure and potential changes therein in the presence of varying substituent concentrations. The Eu^{3+} cation also served as luminescent probe to provide specific information on the dopant environment within the mixed $La_{1-x}Gd_xPO_4$ monazite solid solution series. The Raman spectra show a clear linear trend when plotting both the vibrational normal modes (ν_1-ν_4) and various lattice vibrations as a function of Gd^{3+} or Eu^{3+} substitution (x) in the $La_{1-x}(Gd/Eu)_xPO_4$ monazites. This linear relationship arises from the large contraction of the LnO_9 polyhedron accompanied by a slight compression of the PO_4 tetrahedron in the monazite structure. The half-width (FWHM) of the Raman peaks corresponding to the ν_1, ν_3, ν_4 and the lattice vibrations show a broadening when going from the pure endmembers $LaPO_4$ and $GdPO_4$ /$EuPO_4$ toward the $La_{0.5}(Gd/Eu)_{0.5}PO_4$ composition, indicating a loss of short-range order within the solid structure. This broadening is much more pronounced for lattice vibrations assigned to the LnO_9 polyhedon than for the PO_4 tetrahedron, implying that the $La_{1-x}Gd/Eu_xPO_4$ solid solutions show a stronger distortion around the lanthanide cation site than around the phosphate anion. The decreasing order around the *Ln* cation site becomes evident when studying the luminescence behavior of the co-doped Eu^{3+}cation. The excitation peak position shows a linear shift to lower energies as a function of Gd^{3+} substitution (x) due to a systematic contraction of the average Eu-O distance in the solid solutions, as illustrated by the atomistic simulations. Analogous to the Raman results, both the FWHM of the excitation peak and the $^7F_2/^7F_1$ ratio derived from the emission spectra show an increase when going from the pure endmembers toward the equimolar composition. This increase is slightly more pronounced for the $x > 0.5$ composition than for $x < 0.5$, implying that monazite compositions with higher Gd^{3+}concentrations result in a slightly higher order around the Eu^{3+} luminescent center than the corresponding compositions with the larger La^{3+} concentration. This asymmetry can be understood when considering the size differences between the dopant and host cation radii, being around 1% for the Eu^{3+}/Gd^{3+} couple and more than 8% for Eu^{3+}/La^{3+}. Finally, the atomistic simulations of the Eu-O distances in Eu-doped $La_{1-x}Gd_xPO_4$ show that the experimental Eu^{3+} excitation peak broadening in the synthetic solid solution series can be attributed to a broadened distribution of Eu-O bond lengths when going from the pure endmembers toward the equimolar solid solution composition. The broadening of the experimental excitation spectra can be correlated with the simulated distribution of the Eu-O bond lengths.

Formation of $La_{1-x}Ln_xPO_4{\cdot}0.667H_2O$-rhabdophane-type solid solutions

The crystal structure of pure-phase $La_{1-x}Gd_xPO_4{\cdot}0.667H_2O$ (x = 0 – 1) solid solutions with rhabdophane structure was systematically studied by the combination of X-ray diffraction and spectroscopic techniques. TRLFS-measurements of the Eu-doped $La_{1-x}Gd_xPO_4{\cdot}0.667H_2O$ compounds with hydrated rhabdophane structure yield fully split emission spectra and biexponential decay curves of the luminescence lifetimes indicating the presence of at least two Eu^{3+} species with low site symmetry. Raman analysis revealed higher distortion of the phosphate tetrahedra for the solid solutions when compared to pure endmembers.

Structural incorporation of Cm^{3+} in lanthanide orthophosphates with rhabdophane and monazite structures

The incorporation of curium in monazite and rhabdophane solid solutions was investigated using combined spectroscopic and computational techniques. The results obtained for Cm^{3+} incorporation in the synthetic $La_{1-x}Gd_xPO_4$ monazite ceramics confirm structural incorporation of the actinide dopant on host lattice sites and the formation of homogenous solid solutions without dopant clusters. Slight structural disorder around the Cm^{3+} dopant cation is observed for the intermediate solid solution compositions due to variations of Cm-O bond lengths in these solid matrices. These results are in perfect agreement with the data for monazites doped with inactive lanthanide elements and corroborate the extrapolation of results obtained in analogue studies to actinide-bearing monazite host phases. This is imperative for accurate predictions of the long-term performance of monazite ceramics containing actinide elements. Despite similarities between the incorporated Ln^{3+} and An^{3+} cations in monazite ceramics, differences between the host (*Ln*) and dopant (*An*) elements seem to exist based on the *An*-O bond lengths determined in

XAFS and *ab initio* investigations and in the work for plutonium incorporation in $LaPO_4$ monazite (**Section 5.3.3.1**, [253]). While a contraction of 0.1 Å is expected for the *Ln*-O bond length when going from $LaPO_4$ to $GdPO_4$, the Cm-O distance is seen to decrease by only 0.03 Å, while no changes were found for the Pu-O bond length. The underlying reasons for these observations cannot be provided based on the spectroscopic data. A better understanding of such fundamental phenomena and apparent differences between the 4*f* and 5*f* elements in the monazite ceramics, however, would be worthy to pursue in future studies.

The rhabdophane solid solutions exhibit a more complex incorporation behavior of the trivalent actinide in comparison to the monazite solid phases, due to the presence of several non-equivalent lattice sites in the host structure. Especially the La-rich solid solutions show a preferential incorporation of Cm^{3+} on lattice sites which are not associated with water of hydration. This perceived site occupancy is not in agreement with the rhabdophane crystal structure where 2/3 of the lattice sites are associated with water of hydration. This shows that the site occupancy cannot be predicted based on the host crystal structure alone, but that factors such as the size of the host lattice site may influence the incorporation behavior. Slight dehydration of the $GdPO_4 \cdot 0.667H_2O$ solid phase is further shown to result in the formation of a third, non-equivalent Cm^{3+} species in the crystal lattice, which is not accounted for in the other rhabdophane compositions. According to published data [60] two rhabdophane dehydration steps are expected to occur, leading to the formation of hemihydrated $LnPO_4 \cdot 0.5H_2O$ and hexagonal anhydrous $LnPO_4$ rhabdophane phases, before phase transformation to monazite at temperatures around 773 – 1173 K takes place [189]. Thus, multiple coexisting rhabdophane phases, deviating in their degree of hydration, are likely to form under repository conditions in the proximity of a heat-generating waste matrix, further influencing or complicating the actinide incorporation behavior within this mixed “low-temperature” phase.

Structural incorporation of Pu^{+3} in lanthanide orthophosphates with rhabdophane and monazite structures

Single-phase $La_{1-x}Pu^{III}_xPO_4$-monazite solid solutions with molar fraction of Pu up to x = 0.15were synthesised by a solid state method at 1573 K. At a higher Pu content (x = 0.50) residues of unreacted PuO_2 were detected. Due to the absence of Pu_2O_3, however, decomposition of formed $PuPO_4$ or associate solid solution can be excluded. Moreover, the formation of single phase solid solutions with high Pu content can be expected after optimization of synthesis method. XRD and SEM analysis the solid solutions are found to be single phase and homogeneous. X-ray absorption spectroscopy (XAS) analysis of the single phase (La,Pu)PO_4 solid solutions at the Pu-L_{III} and La-L_{III} edges proves the incorporation of Pu^{III} into defined lattice sites of the monazite structure and indicates clustering of few Pu atoms in the La-Pu-monazite lattice. Comparison of XRD and EXAFS data reveals adjusting of the $LaPO_4$ local environment by incorporation of Pu, whereas the local environment of Pu remains $PuPO_4$-like for the entire solid solution range. Additionally, pure phase $PuPO_4$ was synthesised wet chemically after heating the precipitate at 1073 K. This work demonstrates that monazite-type ceramics with a reasonable amount of Pu (10 – 15%) for nuclear waste applications can be fabricated by conventional solid state reaction at 1573 K, and an even higher fraction of Pu might be immobilized by optimisation of the solid state synthesis method or by using the wet chemical synthesis. An attempt to synthesize a $PuPO_4$-rhabdophane compound by precipitation from a Pu^{4+} nitrate stock solution reduced to Pu^{3+} by hydrazine with an excess of concentrated phosphoric acid led to the formation of hydrated plutonium hypophosphite contaminated by a minor fraction of an unidentified phase.

5.4 Properties of monazite-type ceramics

5.4.1 Thermodynamic properties of $La_{1-x}Ln_xPO_4$ (Ln = Gd, Eu)

In this Subchapter the thermodynamic properties of $La_{1-x}Ln_xPO_4$ compounds with monazite structure will be discussed. Thermodynamics of monazite-type solid solutions were investigated by calorimetric measurements allowing for the determination of heat capacity (microcalorimetry) as well as enthalpy of formation (drop solution calorimetry).

Enthalpy of formation and enthalpy of mixing

The enthalpy of formation ($\Delta H°_f$) of single phase orthophosphate solid solutions $La_{1-x}Ln_xPO_4$ (Ln = Eu, Gd; $0 < x < 1$) with monazite structure synthesised by a precipitation method ((**Section 4.1.1.1**) and structurally characterized by XRD, Raman and TRLFS analysis (**Section 5.3.1**) was determined by high temperature oxide melt solution calorimetry.

To determine the enthalpy of formation ($\Delta H°_f$) of a given compound one takes the difference between the heat effect from dissolving its oxide components and the heat effect of dissolving its oxide components under equivalent conditions (here dissolved in the high temperature solvent $3Na_2O{\cdot}4MoO_3$ at 973 K). Similarly, the heat of mixing can be calculated from the difference in enthalpy of solution of a weighted average of endmembers and of the solid solution. Drop-solution calorimetry yields the enthalpy of formation or mixing at room temperature. The results for $La_{1-x}Gd_xPO_4$ and $La_{1-x}Eu_xPO_4$-monazite solid solutions are listed in **Table 12** and **Table 13**. **Table 14** shows the thermochemical cycle for the calculation of the enthalpy of formation from oxides and elements at 298 K for $La_{1-x}Ln_xPO_4$ (Ln = Eu, Gd). **Figure 51** depicts the enthalpy of drop solution ($\Delta H°_{ds,\ 973\ K}$) versus the mole fraction of Eu in the $La_{1-x}Eu_xPO_4$ solid solution. The dotted line in **Figure 51** represents the trend of ideal mixing. Within the frame of uncertainties the solid solution of $La_{1-x}Eu_xPO_4$ follows the trend of an ideal solid solution with a possible excess, which will be discussed later. It is noticeable that the value for $\Delta H°_{ds,973\ K}$ determined by [107] is approx. 7.5 $kJ{\cdot}mol^{-1}$ less endothermic (grey triangle) than the value determined in this work (black circles).

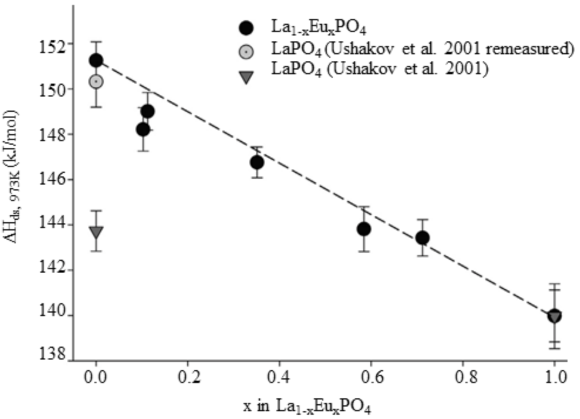

Figure 51. $\Delta H°_{ds,973\ K}$ of $La_{1-x}Eu_xPO_4$ solid solutions vs. molar fraction of Eu, x. The dotted line represents the trend of ideal mixing.

Table 12. Enthalpies of drop solution ($\Delta H_{(ds,\ 973\ K)}$) in $3Na_2O{\cdot}4MoO_3$ at 973 K, enthalpies of formation from oxides ($\Delta H°_{(f,\ ox)}$) and elements ($\Delta H°_{(f,\ el)}$), as well as enthalpies of mixing (ΔH_{mix}) of $La_{1-x}Eu_xPO_4$ solid solutions at temperature T = 298 K and pressure p = 0.1 MPa.[a]

x_{Eu}	Number of experiments	$\Delta H°_{(ds.\ 973\ K)}$ $La_{1-x}Eu_xPO_4$ ($kJ{\cdot}mol^{-1}$)	$\Delta H°_{(f,\ ox)}$ $La_{1-x}Eu_xPO_4$ ($kJ{\cdot}mol^{-1}$)	$\Delta H°_{(f,\ el)}$ $La_{1-x}Eu_xPO_4$ ($kJ{\cdot}mol^{-1}$)	$\Delta H°_{mix}$ $La_{1-x}Eu_xPO_4$ ($kJ{\cdot}mol^{-1}$)
1.0	11	138.98 ± 1.15	-286.90 ± 1.92	-1870.70 ± 3.32	–
0.71	9	143.43 ± 0.81	-304.15 ± 1.95	-1906.51 ± 3.07	0.20 ± 1.15
0.58	8	143.82 ± 0.99	-310.66 ± 2.12	-1921.25 ± 3.06	0.85 ± 1.36
0.34	11	146.76 ± 0.68	-324.78 ± 2.15	-1950.40 ± 2.85	0.54 ± 1.31
0.11	6	149.01 ± 0.83	-338.47 ± 2.35	-1979.47 ± 2.75	0.98 ± 1.55
0.10	16	148.21 ± 0.96	-338.15 ± 2.40	-1979.79 ± 2.79	1.89 ± 1.63
0.0	11	151.26 ± 0.82	-346.11 ± 2.41	-1994.36 ± 2.68	–

[a] The standard uncertainties *u* are *u*(p) = 5 kPa, *u*(T) ≤ 0.001 K for the calorimeter temperature and the expanded uncertainties for ΔH with 0.95 level of confidence (k ≈ 2).

Table 13. Enthalpies of drop solution ($\Delta H_{(ds,\ 973\ K)}$) in $3Na_2O{\cdot}4MoO_3$ at 973 K, enthalpies of formation from oxides ($\Delta H^\circ_{(f,\ ox)}$) and elements ($\Delta H^\circ_{(f,\ el)}$), as well as enthalpies of mixing (ΔH_{mix}) of $La_{1-x}Eu_xPO_4$ solid solutions at temperature T = 298 K and pressure p = 0.1 MPa.[a]

X_{Gd}	Number of experiments	$\Delta H^\circ_{(ds.\ 973\ K)}$ $La_{1-x}Gd_xPO_4$ ($kJ{\cdot}mol^{-1}$)	$\Delta H^\circ_{(f,\ ox)}$ $La_{1-x}Gd_xPO_4$ ($kJ{\cdot}mol^{-1}$)	$\Delta H^\circ_{(f,\ el)}$ $La_{1-x}Gd_xPO_4$ ($kJ{\cdot}mol^{-1}$)	ΔH°_{mix} $La_{1-x}Gd_xPO_4$ ($kJ{\cdot}mol^{-1}$)
1.0	8	139.33 ± 0.96	-293.80 ± 1.40	-1959.75 ± 6.11	–
0.76	8	140.19 ± 0.71	-304.94 ± 1.61	-1966.38 ± 5.42	2.18 ± 1.00
0.55	9	141.80 ± 0.96	-314.60 ± 1.95	-1972.52 ± 4.88	2.95 ± 1.28
0.44	8	142.92 ± 0.66	-320.55 ± 1.95	-1976.35 ± 4.44	3.25 ± 1.15
0.24	8	147.48 ± 0.40	-333.41 ± 2.09	-1985.57 ± 3.65	1.15 ± 1.16
0.0	11	151.26 ± 0.82	-346.11 ± 2.41	-1994.36 ± 2.68	–

[a]The standard uncertainties u are u(p) = 5 kPa, u(T) ≤ 0.001 K for the calorimeter temperature and the expanded uncertainties for ΔH with 0.95 level of confidence ($k \approx 2$).

Table 14. Thermochemical cycle for the determination of the enthalpy of formation of $La_{1-x}Eu_xPO_4$ solid solution from oxides ($\Delta H^\circ_{f,ox}$) and elements ($\Delta H^\circ_{f,el}$). The thermochemical cycle for the determination of enthalpy of formation of $La_{1-x}Eu_xPO_4$ solid solution from oxides ($\Delta H^\circ_{f,ox}$) and elements ($\Delta H^\circ_{f,el}$) is equal with -144.34 ± 1.35[c] $kJ{\cdot}mol^{-1}$ for (3) and -1827.0 ± 8.4[d] $kJ{\cdot}mol^{-1}$ for (5).

Reaction		ΔH ($kJ{\cdot}mol^{-1}$)[a]
$La_{1-x}Eu_xPO_{4(s,\ 298)} \rightarrow \frac{1}{2}(1-x)La_2O_{3(sln,\ 973)} + \frac{1}{2}xEu_2O_{3(sln,\ 973)} + \frac{1}{2}P_2O_{5(sln,\ 973)}$	(1) ΔH_{ds} $La_{1-x}Eu_xPO_4$	See **Table 12**
$La_2O_{3(cr,\ 298)} \rightarrow La_2O_{3(sln,\ 973)}$	(2) ΔH_{ds} La_2O_3	- 225.1 ± 3.2 [b]
$Eu_2O_{3(cr,\ 298)} \rightarrow Eu_2O_{3(sln,\ 973)}$	(3) ΔH_{ds} Eu_2O_3	- 129.2 ± 2.2 [c]
$P_2O_{5(cr,\ 298)} \rightarrow P_2O_{5(sln,\ 973)}$	(4) ΔH_{ds} P_2O_5	- 164.6 ± 0.5 [c]
$2Eu_{(s.\ 298)} + 3/2\ O_{2(g.\ 298)} \rightarrow Eu_2O_{3(s.\ 298)}$	(5) ΔH°_f Eu_2O_3	- 1662.7 ± 3.8 [d]
$2La_{(s.\ 298)} + 3/2\ O_{2(g.\ 298)} \rightarrow La_2O_{3(s.\ 298)}$	(6) ΔH°_f La_2O_3	- 1791.6 ± 1.6 [d]
$2P_{(s.\ 298)} + 5/2\ O_{2(g.\ 298)} \rightarrow P_2O_{5(s.\ 298)}$	(7) ΔH°_f P_2O_5	- 1504 ± 0.5 [d]
$\frac{1}{2}(1-x)La_2O_{3(s.\ 298)} + \frac{1}{2}xEu_2O_{3(s.\ 298)} + \frac{1}{2}P_2O_{5(s.298)} \rightarrow La_{1-x}Eu_xPO4_{(s,\ 298)}$	(8) $\Delta H^\circ_{f,\ ox}$ $La_{1-x}Eu_xPO_4$	See **Table 12**
$\Delta H(8) = -\Delta H(1) + (1-x)\ \frac{1}{2}\ \Delta H(2) + x\ \frac{1}{2}\ \Delta H(3) + \frac{1}{2}\ \Delta H(4)$		
$(1-x)La_{(s.\ 298)} + xEu_{(s.\ 298)} + P_{(s.\ 298)} + 2O_{2(g.\ 298)} \rightarrow La_{1-x}Eu_xPO4_{(s,\ 298)}$	(8) $\Delta H^\circ_{f,\ el}$ $La_{1-x}Eu_xPO_4$	See **Table 12**
$\Delta H(9) = \frac{1}{2}\ x\ \Delta H(5) + \frac{1}{2}\ (1-x)\ \Delta H(6) + \frac{1}{2}\ \Delta H(7) + \Delta H(8)$		

[a] The expanded uncertainties for ΔH are given with 0.95 level of confidence (k ≈ 2).

[b] [268]

[c] [107]

[d] [152]

Fortunately a re-measurement of the $LaPO_4$ material of Ushakov [107] could be realized using the same conditions applied in this work. The source of the difference in the older value could not be readily identified. The remeasured value (light grey circle) for this sample is in very good agreement with the pure $LaPO_4$ of this work. The earlier value for pure $EuPO_4$ [107] and this work are in very good agreement.

Figure 52 shows the $\Delta H^{\circ}_{ds,973\ K}$ of $La_{1-x}Gd_xPO_4$ solid solution vs. molar fraction of Gd. The value of this work (black circles) for pure $GdPO_4$ compared to the earlier measurements of the $GdPO_4$ endmember [107] (light grey circle) is in very good agreement. The dotted line represents ideal mixing. It is evident that the $La_{1-x}Gd_xPO_4$ solid solution shows a significant deviation towards less endothermic enthalpies of drop solution, consistent with a positive heat of mixing. The drop solution enthalpies can be fitted to a quadratic equation, implying regular solution behaviour. **Table 15** the determined data for the enthalpies of formation from elements ($\Delta H^{\circ}_{(f,el)}$) of the endmembers of this work ($\Delta H^{\circ}_{(f,el)}$ values of **Table 12** and **Table 13** for x = 0 and 1) are listed together with data from literature. The data are in very good agreement to those presented by Ushakov taking into account the re-measurement of the $LaPO_4$ sample from Ushakov in this study as discussed before. In contrary a difference of ~80 $kJ \cdot mol^{-1}$ to data referred to in Yungman et al. [153] is evident. Since these measurements were performed in 1970s this observation is attributed to the enormous progress in development and advancement of high temperature calorimetry measurements as reported by Navrotsky [154, 156, 208]. It is underlined by the fact that the data compared in **Table 15** show the same trend. The values of $\Delta H^{\circ}_{(f,el)}$ of $LaPO_4$ and $GdPO_4$ are very similar, while $EuPO_4$ exhibit the same unexpected less exothermic enthalpy of formation discussed by Ushakov et al. [107].

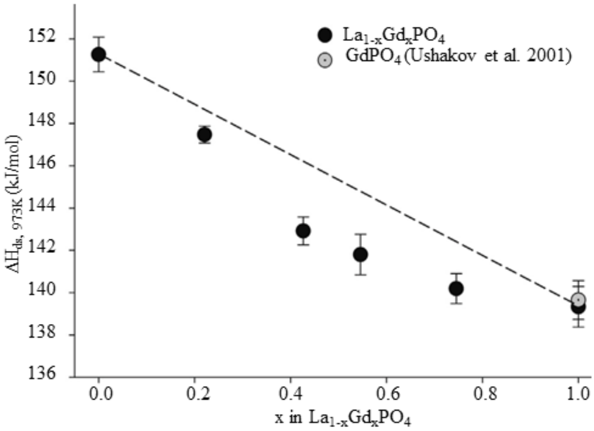

Figure 52. $\Delta H^\circ_{ds,973\ K}$ of $La_{1-x}Gd_xPO_4$ solid solutions as a function of the molar fraction of Gd. The value of this work (black circle) for pure $GdPO_4$ compared to the measurements of the $GdPO_4$ endmember by Ushakov et al. [107] (light grey circle) is in very good agreement. The dotted line represents the trend of ideal mixing.

Table 15. Compilation of enthalpies of formation from elements ($\Delta H^\circ_{f,\ el}$.) of the endmembers derived from this work and from literature.

$\Delta H^\circ_{f,\ el}$ (kJ·mol^{-1})			References
$LaPO_4$	$EuPO_4$	$GdPO_4$	
1994.36 ± 2.68	1870.70 ± 3.32	1959.75 ± 6.11	This work
1913.8^a	1787.8^a	1888.2^a	Yungman et al. [153]
1970.7 ± 1.8	1870.6 ± 2.6	1962.2 ± 4.4	Ushakov et al. [107]

^{a} Data are taken from [153] and literature is cited therein.

To determine the enthalpy of mixing, the values of enthalpy of drop solution were fitted by a second order polynomial. This procedure is equivalent to the application of a regular model for the excess enthalpy of mixing, $H^E = Wx(1-x)$, where W is the Margules interaction parameter [269, 270]. The fit gives a relationship $H = A + (B-W)x + Wx^2$ where A and B are the parameters of ideal mixing, with the ideal mixing enthalpy $H_{id} = A + Bx$, representing the enthalpies of the endmembers, $A = H_{La}$ and $B = H_{Ln\ =\ Eu,Gd} - H_{La}$. The measured excess enthalpies are plotted in **Figure 53** together with the results of recent *ab initio* calculations and the subsequent modelling [171, 172].

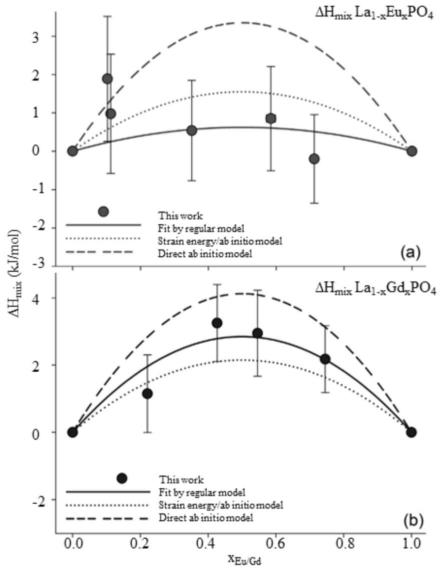

Figure 53. Measured excess enthalpy of mixing (ΔH_{mix}) for $La_{1-x}Eu_xPO_4$ (a) and $La_{1-x}Gd_xPO_4$ (b) solid solution series. Besides the experimental data for modelling results are added: Solid line: fit to the data by regular solid solution model; dashed line: direct *ab initio* prediction after [171]; dotted line: *ab initio*/strain energy based model after [172].

The fitted Margules interaction parameters are reported in **Table 16**. The measurements resulted in W = 2.5 ± 2.6 $kJ \cdot mol^{-1}$ and W = 11.4 ± 3.1 $kJ \cdot mol^{-1}$ for (La,Eu) and (La,Gd) solid solutions, respectively. The errors are at 1σ level (confidence of 0.68) and are estimated using reduced χ^2 analysis corrected for statistical sample size by applying t-student's distribution. The current and previously reported experimental and modelling data are qualitatively consistent showing a positive excess enthalpy of mixing. This study indicates a larger mixing enthalpy in case of (La,Gd) than (La,Eu) which is consistent with all previous studies and expected because of larger mismatch between sizes of La and Gd than La and Eu. However, the current data indicate that the excess properties of Eu are by a factor of ~ 2 – 3 smaller than Gd, possibly even zero within experimental uncertainties, which is rather unexpected having Eu and Gd as neighbours in the periodic table. However, this potential discrepancy could be understood taking into account the still significant experimental uncertainties and the limited size of the statistical sample (see **Table 16**). Recently Kowalski and Li [172] have shown that the Margules interaction parameters derived *ab initio* can be well described as a function of Young's modulus and mismatch in volumes of endmembers, by a simple expression, which shows that strain energy is the main contributor to the excess mixing enthalpy. The Margules interaction parameter (*W*) was derived using the formula (**Equation 32**) is

Equation 32

$$W = \frac{E}{6}\frac{\Delta V^2}{V^3}$$

where *E* is the Young's modulus, *V* is the host phase volume and ΔV is the difference in endmembers volumes. The computed *W* values derived from experimental data of volumes and Young's moduli [180, 213] are also reported in **Table 16**. These values are consistent with the drop solution calorimetry data. We note that the significant difference between the *ab initio* and the estimated values are due to the overestimation of the volume of $LaPO_4$ and an underestimation of the volume of $EuPO_4$ and $GdPO_4$ by the *ab initio* method [166, 168].

Table 16. Margules interaction parameters (*W*) derived from this study and in previous experimental and modelling studies.[a]

W ($kJ \cdot mol^{-1}$)			References
Eu	Gd	Method	
13.4	16.5	*Ab initio*	[171]
5.2	6.77	Strain energy	[170]
14 ± 8	24 ± 9	Drop calorimetry	[109]
6.2	8.6	*Ab initio*/strain energy	[172]
2.5 ± 2.6	11.4 ± 3.1	Drop solution	This work

[a] The uncertainties on the values measured here are computed using χ^2 analysis taking one sigma as the error.

To investigate possible differences in structure and bonding of the two solid solutions that could affect the excess enthalpies of mixing, the evolution of the shape of Raman peak along the solutions was determined (see **Section 5.3.1**).

The broadening of the Raman band points to a local distortion within the lattice due to bond length distribution. The maximum band width is reached at the composition that contains an equimolar mixture of lanthanides ($La_{0.5}Ln_{0.5}PO_4$) which indicates the largest bond length distribution as has been shown previously (cf. **Sections 5.3.1** and **5.3.3**). The structure and bond lengths of the pure endmembers $LaPO_4$ and $GdPO_4$ are well defined due to the complete ordering of atoms. In the solid solutions the lanthanides of two different sizes are probably distributed close to randomly since the heats of mixing are small. The number of different bonding environments is presumably maximized at a mole fraction of 0.5.

Moreover, a different behaviour of Eu and Gd during precipitation for instance from a kinetic point of view cannot be excluded. In very recent studies La was found to precipitate faster compared to Gd and Eu [65] which may induce a deviation of the homogeneity of lanthanide distribution within the samples. Finally, the band widths are larger for the Gd compared to Eu substituted compounds, which reflects the larger mismatch of ionic radii within the (La,Gd) solid solution than in the (La,Eu) system (**Figure 19**). These results are in a good correlation with TRLFS data, providing information about the local distortions on the cation site (see **Section 5.3.1**). The overall results for both solid solutions are very similar with only slightly larger distortions in the case of $La_{1-x}Gd_xPO_4$. The mixing enthalpies can be used for assessment of the thermodynamic stability of solid solutions. A solid solution becomes immiscible when $W/K_BT>2$ [271]. The Margules interaction parameters obtained by drop solution calorimetric measurements indicate that the temperature below which a miscibility gap occurs is T = 310 K for the (La,Eu) solid solution system. For the (La,Gd) system, this critical temperature is 690 ± 190 K. These results underline the thermodynamic stability of the investigated monazite solid solutions.

Heat capacity

The measurements of the temperature-dependence of the heat capacities of the monazite-type $La_{1-x}Eu_xPO_4$ ceramics were complemented by an additional measurement of a $La_{0.5}Eu_{0.5}PO_4$ single crystal. The temperature dependency of the heat capacity is depicted in **Figure 55** for selected solid solution compositions, since the heat capacities of the solid solutions are very similar **Figure 54**. The calculated values for the standard entropy and the enthalpy at 298.15 K are listed in **Table 17**.

Table 17. Calculated values for the standard entropy and the enthalpy at 298.15 K of $La_{1-x}Eu_xPO_4$ monazite from heat capacity measurements.

x_{Eu}	$S_{298.15\ K}$ $(J{\cdot}(K{\cdot}mol)^{-1})$	$H_{298.15\ K}$$(J{\cdot}mol^{-1})$
0.0	107(1)	17282(138)
0.0	108(1)	17345(139)
0.10	109(1)	17531(140)
0.35	111(1)	17823(143)
0.50	112(1)	18013(144)
0.65	111(1)	18068(145)
0.90	113(1)	18450(148)
1.0	114(1)	18668(149)

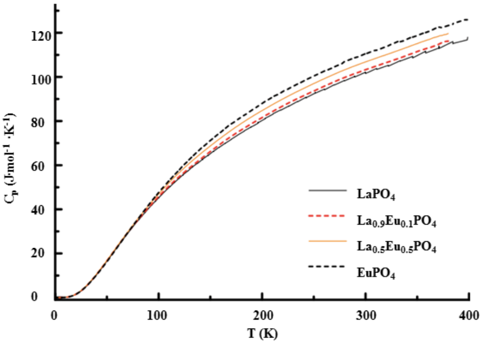

Figure 54. Temperature dependence of the heat capacities of $La_{1-x}Eu_xPO_4$ solid solutions.

A continuous decrease in the heat capacity with decreasing temperature was observed; hence, there is no anomaly due to a structural phase transition at low temperatures. The compositional dependence of the heat capacity at 298 K is shown in **Figure 55**.

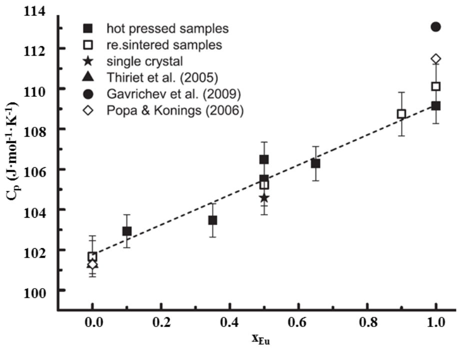

Figure 55. Heat capacities at 298.15 K of $La_{1-x}Eu_xPO_4$ solid solutions compared to previously published data [106, 164, 272].

There is a significant increase in the heat capacity of the solid solutions with increasing Eu content. The result for the $LaPO_4$ endmember from this work is in excellent agreement with the data from Thiriet et al. [272] derived from low temperature heat capacity measurements ($C_p(LaPO_4) = 101.28$ J·mol^{-1}·K^{-1}) and with the data from Popa and Konings [106], who obtained the same value from high-temperature drop calorimetry **Figure 55**. Thus, the value of $C_p(LaPO_4) = 101.6(8)$ J·mol^{-1}·K^{-1} is now very well established. This is in contrast to the heat capacity of the $EuPO_4$ endmember, where the value published by Gavrichev et al. [164] is significantly larger than a value published by Popa and Konings [106], which in turn is slightly larger than the value obtained in this work. This might be due to the use of different starting materials and the different technique. Hence, the value obtained in this work should be more accurate than the older data, as an extrapolation of the heat capacities of the solid solutions coincides very well with the value obtained from measurements with two samples. Also a direct determination, such as performed in this work, is more accurate than data calculated from the heat capacity of $LaPO_4$ and $GdPO_4$, as has been done by Popa and Konings [106]. Hence, the most accurate value $C_p(EuPO_4)$ is 110.1(8) J·mol^{-1}·K^{-1}. The data obtained in this work for the solid solutions strongly imply that the heat capacity increases linearly with increasing Eu content. The data obtained in this work can be compared to a Pu-bearing monazite analysed by Popa et al. [126] with a value of 110 J·mol^{-1}·K^{-1} and the value published earlier by Thiriet et al. [173] for $PuPO_4$ of 114.5 J·mol^{-1}·K^{-1} at ambient temperature. These data are similar to the values from this work.

The heat capacities of the endmember can be used to evaluate the Schottky contribution to heat capacity of the solid solution [164], where the total heat capacity is described as the sum of a lattice component (lattice vibrations, C_{lat}) and an electronic contribution due to the thermal excitation of *4f*-electrons, C_{elec}):

Equation 33

$$C_p = C_{lat} + C_{elec}$$

As $LaPO_4$ has no *4f*-electrons, there is no electronic contribution. Hence, if the mass difference between La and Eu is neglected, the contribution due to the *4f*-excitations can be obtained by subtracting the heat capacity of $LaPO_4$ from those of the solid solutions, to yield ΔC_p:

Equation 34

$$\Delta C_p = C_p(La_{1-x}Eu_xPO_4) + C_p(LaPO_4)$$

The temperature dependence of ΔC_p is shown in **Figure 56**. For pure $EuPO_4$ the maximum ΔC_p = 8.25(6) $J \cdot mol^{-1} \cdot K^{-1}$ is in a very good agreement with the data calculated by Popa and Konings [106] where ΔC_p = 9.41 $J \cdot mol^{-1} \cdot K^{-1}$ and with a value computed recently by Kowalski et al. [273] where ΔC_p = 9.7 $J \cdot mol^{-1} \cdot K^{-1}$. At temperatures $T < 75$ K, the heat capacities of the solid solutions are very similar as at these temperatures the 4f-transitions cannot thermally be excited to any significant extent. By temperature increase with > 75 K, the *4f*-electrons can be excited, and hence cause a strong increase in ΔC_p of the Eu-containing solid. At around 200 K the low-lying levels are all populated, and ΔC_p remains essentially constant.

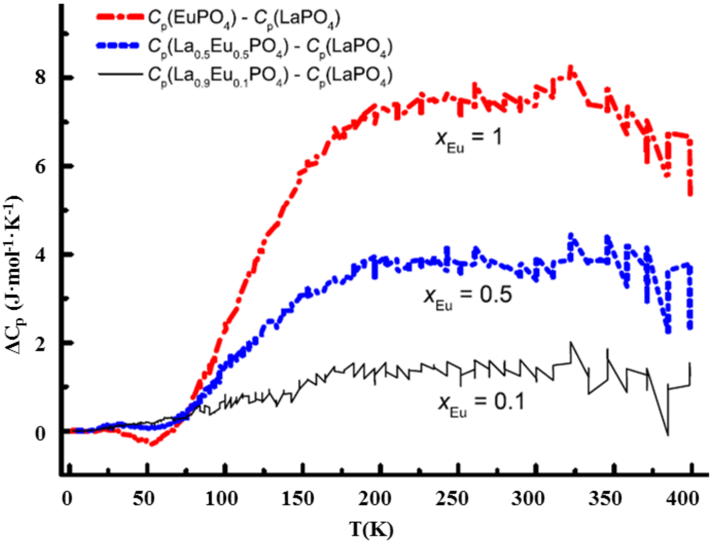

Figure 56. Comparison of ΔC_p of pure $EuPO_4$ monazite (x_{Eu} = 1) and two $La_{1-x}Eu_xPO_4$ solid solutions (x_{Eu} = 0.5 and x_{Eu} = 0.1).

5.4.2 Physical properties

5.4.2.1 Thermal expansion

Figure 57 shows the thermal expansion of hot-pressed $La_{1-x}Eu_xPO_4$ ceramics. These data were used to calculate the linear CTEs using **Equation 10**. The linear CTEs are shown for two different reference temperatures, T_{ref} = 473 K and T_{ref} = 1273 K, in **Figure 58**. The data obtained in this work for the endmembers at 1273 K are in very good agreement with published data for $LaPO_4$ and $EuPO_4$ respectively [73, 179].

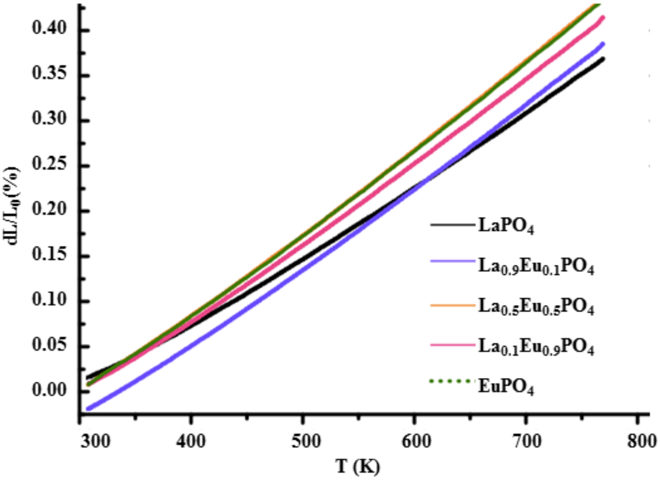

Figure 57. Thermal induced strains of $La_{1-x}Eu_xPO_4$ ceramics from ambient temperature to 773 K.

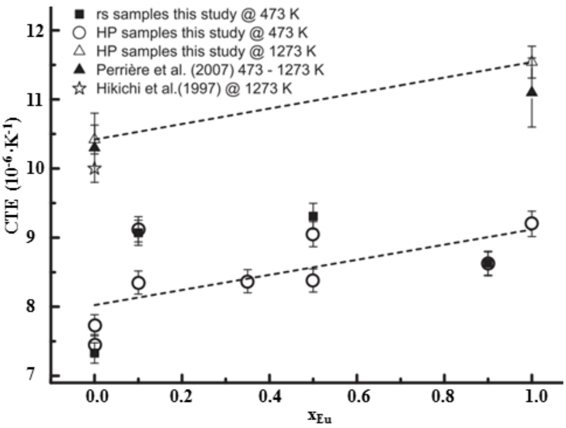

Figure 58. Linear thermal expansion coefficients CTEs of solid solutions $La_{1-x}Eu_xPO_4$ including previously published data [73, 179]. Filled squares report data for re-sintered samples at T_{ref} = 473 K, open circles (T_{ref} = 473 K) and triangles (T_{ref} =1273 K) are data for HP samples, the filled triangle (T_{ref} = 473 – 1273 K) and the star (T_{ref} = 1273 K) are the previously published data [73, 179].

There is a slight increase in the CTEs with increasing Eu-content (**Figure 58**), which is more obvious if only the hot-pressed samples are considered, as the scatter of the data increases for the re-sintered samples. During re-sintering, the sample density decreases slightly and samples can crack, and this is thought to be the origin of the data scatter. However, re-sintering does not seem to affect the value of the thermal expansion coefficients for these ceramics significantly.

The CTE increases with increasing temperature by about 10% when the temperature is increased by 300 K. This increase is independent on the composition. There was no persistent change in the sample geometry due to the heating during the measurements. For one of the samples the thermal expansion was measured twice, once perpendicular to the compression axis and once parallel to the compression axis. No significant difference in thermal expansion up to 773 K was observed between the two orientations. This is consistent with the previous observations indicating that the samples are isotropic, despite the application of uniaxial pressure during the pelletization procedure (see **Section 5.2.2.2**). From an analysis of all the obtained data, the thermal expansion coefficients at 473 K vary between $7.8(3)\cdot10^{-6}$ (K^{-1}) for $LaPO_4$ and $9.1\ (3)\cdot10^{-6}$ (K^{-1}) for $EuPO_4$. For T_{ref} = 1273 K the corresponding values are $10.4(3)\cdot10^{-6}$ (K^{-1}) for $LaPO_4$ and $11.5(3)\cdot10^{-6}$ (K^{-1}) for $EuPO_4$. These coefficients are slightly lower in comparison to other materials considered as nuclear waste forms. For example Shih [274] analysed lead phosphate glasses doped with mixed metal oxides. These glasses yield CTEs between $13.5 \cdot 10^{-6}$ (K^{-1}) and $15.0 \cdot 10^{-6}$ (K^{-1}). Day et al. [275] measured iron phosphate glass waste forms and calculated a thermal expansion coefficient of $12.8 \cdot 10^{-6}$ (K^{-1}) for 573 K. The mean CTE of borosilicate glasses [276] are close to $8.2 \cdot 10^{-6}$ (K^{-1}) measured between 298 – 573 K, and hence, they are in the same range as the values determined in this work. The CTEs of the ceramics measured in this work are similar to those of other potential ceramic waste forms such as SYNROC (a titanate ceramic waste) [10, 45], which have a CTE of $9.6 \cdot 10^{-6}$ (K^{-1}) in the temperature range of 295 – 698 K [277] or zirconates such as $La_2Zr_2O_7$ with a CTE of $9.1 \cdot 10^{-6}$ (K^{-1}) between 303 – 1273 K [278].

5.4.2.2 Elastic properties from ultrasound spectroscopy

The elastic stiffness coefficients of the hot-pressed $La_{1-x}E_xPO_4$ samples are listed in **Table 18**. While there is some scatter in the data, a significant increase in the elastic stiffness coefficients with increasing Eu content is obvious. In **Figure 59**, the corresponding Young's moduli, calculated from c_{ij} according to **Equation 16**, are presented and compared to data of the endmembercompositions published earlier [73, 178, 180]. The value for the $LaPO_4$ endmember obtained in this work is intermediate between the values published in the literature [73, 178, 180]. For the $EuPO_4$ endmember, the data obtained in this work are in excellent agreement with the value published by Du et al. [180], which differs significantly from the much larger value published by Perrière et al. [73]. As an extrapolation of the values obtained for the solid solutions also yields a value of E = 155 GPa, this should be the preferred value. The wave velocities and consequently the elastic properties strongly depend on the sample density. As can be seen in **Figure 60**, the velocity of longitudinal acoustic waves and c_{11} decrease with decreasing density. A density increase of ≈3% leads to a ≈8% change of c_{11}. The values of Young's moduli calculated form c_{11} and c_{44} were used for the calculation of fracture toughness (**Section 5.4.3**).

Table 18. Elastic stiffness coefficients of the hot-pressed $La_{1-x}Eu_xPO_4$ samples.

x_{Eu}	ρ ($g \cdot cm^{-3}$)	c_{11} (GPa)	c_{44} (GPa)
0.00	4.796(6)	182(1)	53.8(7)
0.10	5.117(6)	186(1)	54.8(4)
0.50	5.366(1)	194(1)	56.9(3)
0.50	5.415(7)	198(1)	57.7(7)
0.50	5.413(7)	198(1)	58.2(5)
0.50	5.294(6)	185(1)	54.8(3)
0.90	5.726(7)	202(1)	61.1(4)
1.00	5.736(5)	202(1)	58.4(3)

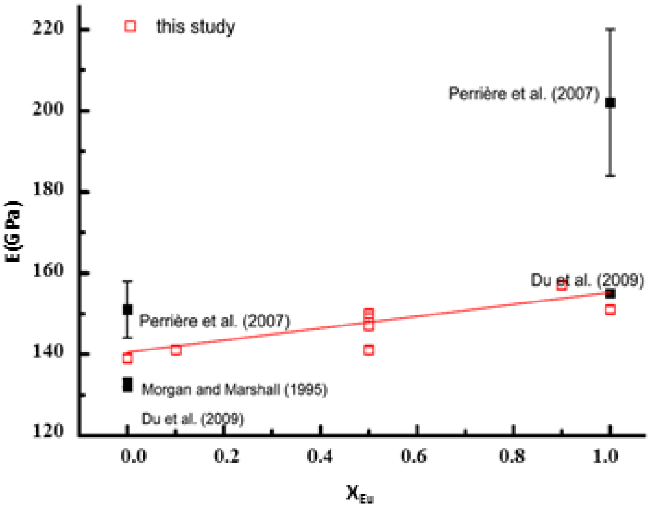

Figure 59. Young's moduli calculated form c_{11} and c_{44} compared to previously published data [73, 178, 180] of $La_{1-x}Eu_xPO_4$.

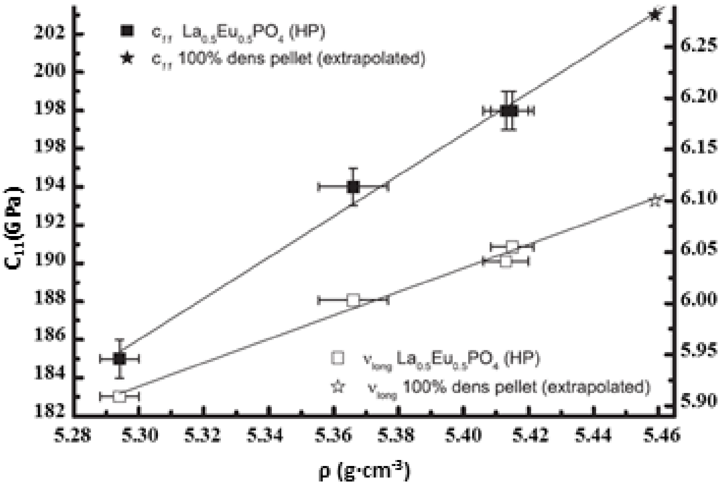

Figure 60. Dependence of the elastic stiffness coefficient c_{11} (filled symbols) and longitudinal acoustic wave velocity (open symbols) of $La_{0.5}Eu_{0.5}PO_4$ on sample density. The stars refer to extrapolations to 100% theoretical density.

5.4.3 Mechanical properties

5.4.3.1 Influence of microstructure and texture on mechanical properties of $La_{0.5}Eu_{0.5}PO_4$ monazite ceramics

The microhardness and fracture toughness of the hot-pressed HTS-1 and HTS-10 specimens with different grain sizes, with and without any preferential grain orientations (100), respectively, as well as of the (100) plane of $La_{0.5}Eu_{0.5}PO_4$ single crystal were measured. Fabrication and characterisation of the HTS-1 HP and HTS-10 HP pellets is discussed in detail in **Section 5.2.2**. The typical optical micrographs of the indenter are presented exemplarily for the single crystal and the hot-pressed HTS-10 pellet in **Figure A 1** in the **Appendix**.

According to the literature, elastic moduli [73, 213] and flexural strength of polycrystalline isotropic synthetic monazites are strongly dependent on porosity whereas no significant influence of the grain size considering equal density of the material on mechanical properties have been revealed [73]. The crystal structure of monazite compounds is anisotropic as it is represented by LnO_9-polyhedra (*Ln* = La – Gd) interpenetrated by phosphate tetrahedra building edge-connected chains along the c-direction [23, 42]. Given the low symmetry of the monazite structure and its pseudo-one-dimensional character, the bond strength along different crystallographic directions differs and an anisotropy of the physical properties can be expected [56]. Effects of texture on the thermal conductivity [56] and on the anisotropic Young's moduli [58] has also been demonstrated. In this work, the single crystal and the high density hot-pressed pellets allowed for porosity-independent measurement of the impact of microstructure and texture on the mechanical strength. The determined microhardness and fracture toughness values are presented in **Table 19**.

Table 19. Microhardness (H_v) and fracture toughness (K_{1c}) of $La_{0.5}Eu_{0.5}PO_4$ materials with monazite structure.

	H_v (GPa)	K_{1c} (MPa·m$^{0.5}$)
HTS-1 HP	5.3(4)	0.90(10)
HTS-10 HP	4.6(3)	1.00(10)
HTS-10 [67]	4.3(2)	1.04(08)
Single crystal, (100) face	5.4(2)	0.87(07)

As mentioned previously, calculations have shown that the Young's moduli of synthetic $LaPO_4$-monazite are highly anisotropic with the lowest value in the a-axis direction (two times lower than in the c-axis direction) [58]. At a fundamental level, Young's modulus is a measure of the bond strength between atoms. Therefore, it was concluded that the bond strength in the a-axis direction (the direction perpendicular to the (100) plane) is the weakest among the three directions of the monazite unit cell [56, 58].

Hardness is governed by both intrinsic properties (i.e. bond strength, cohesive energy and crystal structure), and extrinsic properties, such as stress fields, defects and morphology [279]. The experimental data from this work have shown the highest microhardness (5.3(4) GPa) for the (100) plane of the single crystal when compared to the values for the high density polycrystalline monazite material. However, grain boundaries of the HP pellets deflect crack propagation and prohibit crack growth. The cracking energy dissipates on the grain boundaries resulting in higher fracture toughness for polycrystalline specimens than for the single crystal. Due to the texturing effect in the HTS-1 specimen its fracture toughness as well as microhardness values (0.90(10) MPa·m$^{0.5}$ and 5.3(4) GPa, respectively) are very close to those measured in this work for the (100) plane of the single crystal. Microhardness of the HTS-10 HP pellet with smaller grains and apparently random crystal orientation is similar to that reported previously for the hot-pressed pellet from the powder synthesised analogously to HTS-10 (4.6(3) GPa and 4.3(2) GPa, respectively) [67].

5.4.4 Dissolution: Influence of temperature on dissolution kinetics of synthetic $LaPO_4$-monazite in acidic media

5.4.4.1 Sample characterization

The $LaPO_4$ powders were synthesised by HTS-1 method. The X-ray diffraction (XRD) pattern of the synthesised and sintered $LaPO_4$ powder is depicted in **Figure 61**. According to XRD, single-phase $LaPO_4$-monazite of high crystallinity was obtained after the sintering step. The EDX analyses performed on sintered pellets revealed that, within the error of the applied analytical method, the synthesised La-monazite is chemically homogeneous and lacking any zonation. The density of the sintered pellets reached about 96% of the theoretical density of $LaPO_4$. SEM observations on powders used in the dissolution experiments (100 – 180 µm fraction) indicated that the particles are made up of well sintered grains up to 30 µm in size with trapped intragranular pores of sub-micrometric size with minor intergranular porosity in the grain interstices (**Figure 62**). The N_2-BET surface area of the powder used in the dissolution experiments was 0.4 ± 0.1 m^2 g^{-1}.

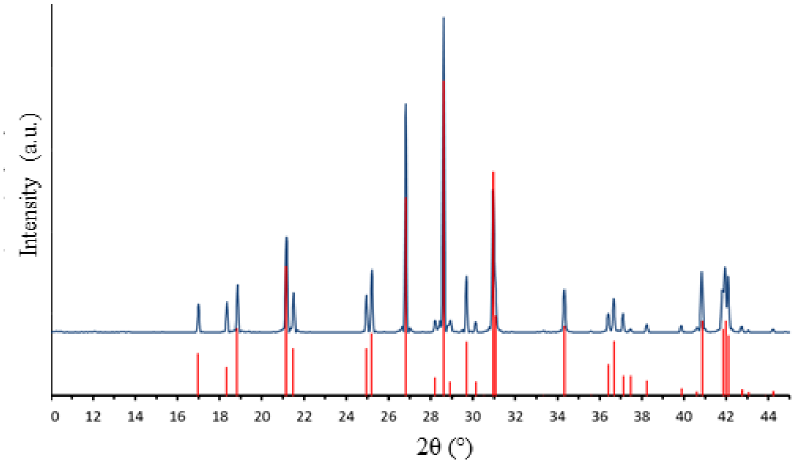

Figure 61. XRD-pattern of sintered $LaPO_4$ powder showing the presence of single-phase La-monazite (Reference data monoclinic $LaPO_4$, COD ID 9001647).

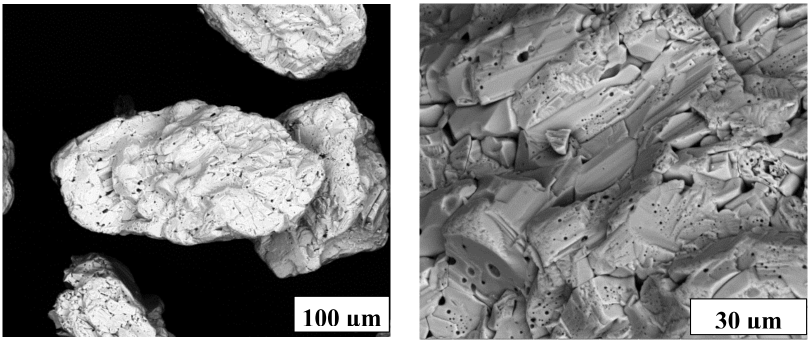

Figure 62. SEM micrographs of the sieved $LaPO_4$-powder used in the dissolution experiments.

5.4.4.2 Dissolution kinetics

The La-concentrations, obtained in the dynamic dissolution experiments at temperatures between 323 and 403 K, are provided in **Table A 8** and **Table A 9** in **Appendix**. In particular in experiments performed at temperatures below 363 K, the dissolution experiments followed the typical trend of dynamic dissolution experiments as frequently described in the literature (e.g.

[47, 216, 280, 281]). In the initial stages of the experiments, higher dissolution rates were observed that decrease with time until a steady state, i.e. a constant rate with time, was reached. Steady state dissolution rates were approached within one week for all temperatures. The higher initial dissolution rates are generally thought to be due to dissolution of fine particles adhering to the materials surface and/or dissolution at highly reactive surface sites created during the crushing of the pellets (e.g. [47, 281-285]). An alternative explanation for the enhanced initial dissolution rates proposed by Luettge et al. [286] is related to changes of the dominating dissolution mechanism e.g., from dissolution at grain boundaries to the dissolution on steps, kinks and etch pits on grain surfaces.

The steady state dissolution rates of the $LaPO_4$ monazite powders are summarised in **Table 20**. Within the temperature interval from 323 to 403 K, the normalised dissolution rates increased by roughly one order of magnitude from $3.2 \cdot 10^{-5}$ to $2.5 \cdot 10^{-4}$ $g \cdot m^{-2} \cdot d^{-1}$. The dissolution rates obtained using the two different experimental setups at the same temperatures are in a good agreement.

Table 20. Normalised dissolution rates of $LaPO_4$ in 0.01M HNO_3 at different temperatures using two different experimental setups.

T (K)	r_{mon} ($g \cdot m^{-2} \cdot d^{-1}$) PFA-reactor / SPFT	r_{mon} ($g \cdot m^{-2} \cdot d^{-1}$) Ti-reactor / mixed flow
323	$3.2 \cdot 10^{-5} \pm 2 \cdot 10^{-7}$	
333	$4.6 \cdot 10^{-5} \pm 3 \cdot 10^{-7}$	$3.6 \cdot 10^{-5} \pm 3 \cdot 10^{-6}$
353	$8.5 \cdot 10^{-5} \pm 9 \cdot 10^{-6}$	$1.2 \cdot 10^{-4} \pm 2 \cdot 10^{-7}$
363	$1.8 \cdot 10^{-4} \pm 5 \cdot 10^{-5}$ [a]	$2.2 \cdot 10^{-4} \pm 4 \cdot 10^{-6}$
383		$2.0 \cdot 10^{-4} \pm 2 \cdot 10^{-5}$
403		$2.5 \cdot 10^{-4} \pm 1 \cdot 10^{-5}$

[a] data from Brandt et al. 2014

The normalised dissolution rates of $LaPO_4$ obtained in this study correspond rather well to data derived for various other natural or synthetic monazites. Oelkers and Poitrasson [47] determined dissolution rates of $9.3 \cdot 10^{-6}$ and ~$2.2 \cdot 10^{-5}$ g m^{-2} d^{-1} for natural Ce-monazite from Manangotry, Madagascar, under dynamic conditions at 323 and 343 K, respectively. Terra et al. measured dissolution rates of synthetic $GdPO_4$ with monazite structure of $3.8 \cdot 10^{-4}$ to $5.9 \cdot 10^{-4}$ g m^{-2} d^{-1} at 363 K at pH 1. Slightly higher dissolution rates of $1.7 \cdot 10^{-3}$ g m^{-2} d^{-1} were obtained by Brandt et al. [44] for synthetic Eu-monazite at 363 K and pH 2 in SPFT experiments. In this study, within the solid solution series $LaPO_4$ – $EuPO_4$, a minimum of the dissolution rate ($5.8 \cdot 10^{-5}$ g m^{-2} d^{-1}) was observed at an $EuPO_4$ mole fraction of 0.2. Teng et al. [187] investigated the dissolution behaviour of synthetic $Ce_{0.5}Eu_{0.5}PO_4$ with monazite structure at 363 K in deionised water. They found normalised elementary release rates of Ce and Eu below $4 \cdot 10^{-5}$ and $2 \cdot 10^{-4}$ $g \cdot m^{-2} \cdot d^{-1}$, respectively, after 21 d. Veilly [287] determined the dissolution kinetics of Th-cheralite ($CaTh(PO_4)_2$), a monoclinic monazite type phase with similar lattice parameters compared to $LaPO_4$, in dynamic dissolution experiments at 363 K and pH 1, reporting a Th-based dissolution rate of $2.2 \cdot 10^{-5}$ g m^{-2} d^{-1}.

Based on the dissolution rates obtained at constant pH and at far from equilibrium conditions, the apparent activation energy of the dissolution process can be determined according to the Arrhenius' law (**Equation 35**), where:

Equation 35

$$r_{mon} \propto e^{-E_a/RT} ,$$

with the activation energy E_a, the gas constant R, and the absolute temperature T. Using a simple mathematical transformation **Equation 35** takes the form:

Equation 36

$$\ln(r_{mon}) = -(E_a/R)(1/T) + lnA \quad ,$$

where A is the pre-exponential factor of the Arrhenius equation. In the Arrhenius plot (**Figure 63**) two different linear trends can be observed for the temperature dependence of the dissolution rates of $LaPO_4$ under acidic conditions, suggesting changes in the rate limiting step in the overall dissolution mechanism. From the slopes of the regression lines, apparent activation energies of 44 ± 5 and 7.5 ± 4.3 kJ mol^{-1} were determined for the temperature ranges 323 K to 363 K and 363 K to 403 K, respectively.

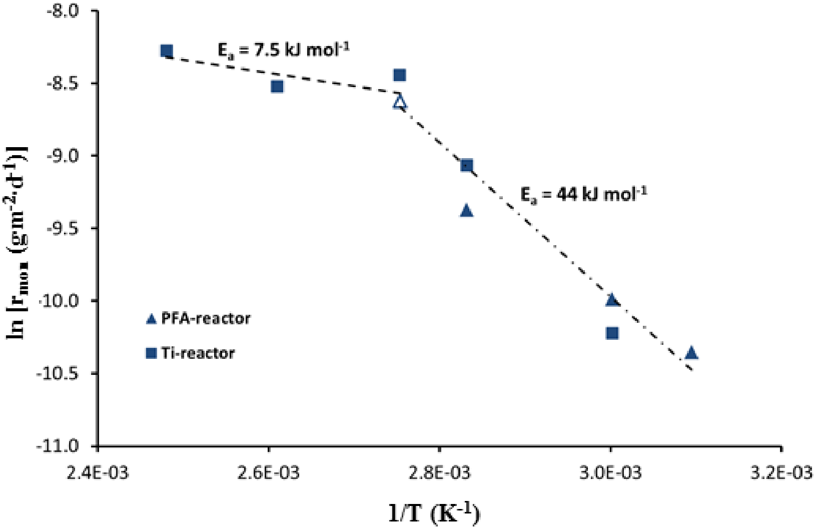

Figure 63. Arrhenius plot of the dissolution rates of $LaPO_4$ as function of reciprocal temperature. The open triangle corresponds to the dissolution rate from Brandt et al. (2014) [44].

These values of apparent activation energies allow for an evaluation of the mechanisms of the overall dissolution reactions. According to literature, the apparent activation energy of surface-reaction controlled dissolution (E_a from ~40 to 140 kJ mol^{-1}) is distinctively higher than for transport-controlled dissolution (E_a less than ~20 kJ mol^{-1}) (cf. [186, 288-291]). This suggests that the dissolution of the $LaPO_4$ ceramics proceeds via a surface-reaction controlled mechanism at temperatures below 363 K and via a transport-controlled dissolution mechanism at higher temperatures. Similar results revealing two different mechanisms for the dissolution of *Ln*-orthophosphate ceramics depending on temperature were obtained by Gausse (2016) [246] in dynamic dissolution experiments. In this study apparent activation energies of 79 ± 8 kJ mol^{-1} (T: 298 K to 313 K) and 13 ± 1 kJ mol^{-1} (T: 313 K to 363 K) for the dissolution of $LaPO_4$ were determined (Gausse, 2016) [246], suggesting similarly a surface-reaction controlled dissolution mechanism at lower temperatures and a transport controlled dissolution mechanism at elevated temperature. The higher apparent E_a determined in the temperature range 298 K to 313 K by Gausse (2016) [246] might be due to the fact that only two data points were used for the determination of E_a.

Different dissolution mechanisms as function of temperature have been also reported previously with respect to the leaching kinetics of brannerite (nominally UTi_2O_6) ores ([292, 293]). In the low temperature range from 288 to 308 K, an apparent activation energy of 50.5 $kJ \cdot mol^{-1}$ was determined, typically for surface-reaction controlled dissolution mechanisms. Between 308 and 363 K, a decrease of the apparent activation energy down to 30.3 $kJ \cdot mol^{-1}$ was reported. Gogoleva (2012) [293] assigned this value to a mix of two mechanisms, i.e. surface-reaction and product layer diffusion.

Terra et al. (2003) [69] evaluated an apparent activation energy of 39 to 45 kJ mol^{-1} for the dissolution of synthetic $GdPO_4$ with monazite structure from the values of the normalised dissolution rates at 363 K and room temperature, in line with the value for $LaPO_4$, obtained in this work, below 363 K. In contrast, Oelkers and Poitrasson (2002) [47] determined the apparent activation energy associated with the dissolution of natural Ce-monazite from Manangotry, Madagaskar, to be 41.8 ± 12.6 kJ mol^{-1} in the entire temperature range from 323 to 503 K at pH = 2, without observing any change in the E_a value. However, Oelkers and Poitrasson (2002) [47] studied natural monazite samples with very complex elemental composition, containing both, various lanthanide (Ce, La, Nd) and actinide (Th, U) cations, as well as SiO_4^{3-} and PO_4^{3-} anions. Du Fou de Kerdaniel et al. (2007) [53] demonstrated the influence of the chemical composition of the *Ln*-orthophosphates on the temperature range of stability of rhabdophane-type compounds phases, which might explain the absence of two different dissolution mechanisms in the experiments of Oelkers and Poitrasson (2002) [47].

5.4.4.3 Thermodynamic modelling of the dissolution of $LaPO_4$-monazite in an acidic aqueous solution

In **Figure 64**, the results of the thermodynamic modelling of the dissolution of $LaPO_4$-monazite in an acidic aqueous solution (0.01M HNO_3) at various temperatures are shown. The calculated La concentrations in solution depict the retrograde solubility of *Ln*-orthophosphates (cf. [24, 294]) with La-concentrations decreasing from about $3.7\cdot10^{-5}$ mol L^{-1} to about $1.5\cdot10^{-5}$ mol L^{-1} in the temperature interval from 303 K to 370 K. Moreover, the thermodynamic calculations with GEM-Selektor revealed that La-rhabdophane is the thermodynamically stable phase in this temperature range. Scoping calculations at higher temperatures indicate that above about 375 K La-monazite is the thermodynamically favoured La-orthophosphate phase (cf. **Figure 64**). This is consistent with the experimental findings of du Fou de Kerdaniel et al. (2007) [53], who observed in synthesis from oversaturation conditions, the formation of La-monazite at and above 373 K, whereas at temperatures below 363 K, La-rhabdophane occurred. In contrast, Cetiner et al. (2005) [294] concluded from PXRD data that the solid phase used in experiments to determine the solubility product of $LaPO_4$ from under-saturation at 296 K and 323 K had the monazite structure before and after the experiment. However, this can probably be explained by the very low amount of neoformed rhabdophane during the dissolution experiment, which cannot be evidenced by PXRD (cf. [246]).

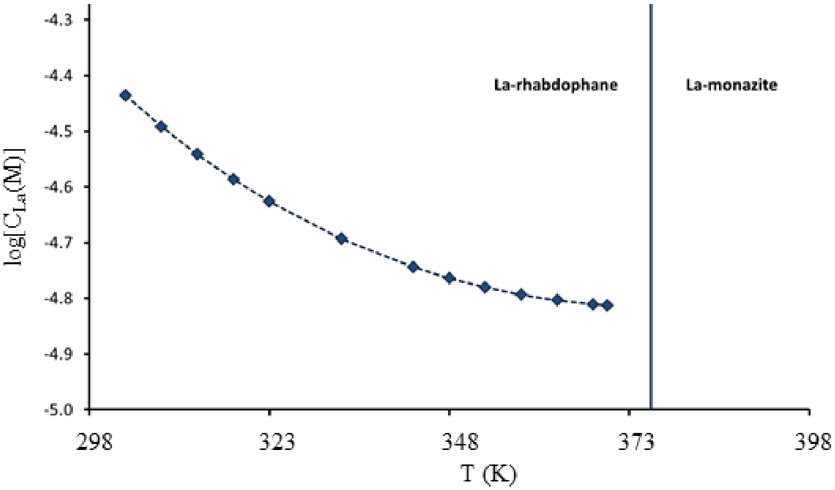

Figure 64. La-concentrations in equilibrium with a solid La-orthophosphate phase in 0.01M HNO_3 calculated with GEM-Selektor and estimated predominance fields of La-rhabdophane and La-monazite as function of temperature.

The estimated border between the predominance fields of the different La-orthophosphates is thus in the same temperature range as the observed change in the dissolution mechanism. This coincidence suggests that the different dissolution mechanisms might be caused by the hydration of monazite and the formation of a thin rhabdophane layer on the sample surface as an intermediate step controlling the dissolution in the temperature range below about 373 K, whereas the dissolution behaviour at elevated temperatures is controlled by direct dissolution of La-monazite.

5.4.5 Résumé of Chapter 5.4

Thermodynamic properties

The thermodynamic properties of $La_{1-x}Ln_xPO_4$ solid solutions (*Ln* = Eu, Gd) with monazite structure have been investigated by measuring the formation enthalpies utilizing high temperature oxide melt solution calorimetry. The Eu system shows a possible small excess enthalpy of mixing while the Gd system clearly shows regular solid solution behavior with an interaction parameter of 11.4 ± 3.1 $kJ\cdot mol^{-1}$. The experimentally derived enthalpies of mixing are in reasonable agreement with previous modelling studies. The obtained Margules interaction parameters underline the thermodynamic stability of continuous (La,Eu)PO_4 and (La,Gd)PO_4 solid solutions. The heat capacity of the (La,Eu)PO_4 solid solutions shows a linear compositional trend significantly increasing with increasing Eu content.

Physical properties

In this study, new data for the physical properties of monazite-type solid solutions ceramics were presented. The obtained thermal expansion data are compared to those of other potential waste forms. The temperature induced dilatations of the investigated samples are isotropic and showed that there is a slight linear dependency on the composition of about 10%. The elastic behavior of the solid solutions strongly depends on the mechanical integrity of the samples. An increasing Eu-content leads to an increase in all elastic parameters (9% for E).

Mechanical properties

Mechanical properties of the hot-pressed pellets with different microstructure as well as of a single crystal were studied by the Vickers indentation method. The dependence of microhardness and fracture toughness on microstructure and texture was demonstrated. The polycrystalline high-density monazite material, larger grains and preferential orientation of the grains along the (100) plane were found to increase the microhardness.

Dissolution kinetics of synthetic $LaPO_4$-monazite in acidic media

The temperature dependence of the dissolution kinetics of sintered La-phosphate ceramics with monazite structure was studied, to gain a more detailed insight into the mechanisms governing the dissolution of monazite-type ceramics proposed as nuclear waste forms for actinide immobilisation. Pure single-phase La-monazite was obtained from precursors synthesised via a hydrothermal route after calcination and sintering. The dissolution kinetics of sintered La-phosphate powders were studied in dynamic dissolution experiments in the temperature range from 323 to 403 K under acidic conditions (0.01M HNO_3). The overall dissolution rates at far from equilibrium conditions increased by roughly one order of magnitude from $3.2\cdot10^{-5}$ to $2.5\cdot10^{-4}$ g m^{-2} d^{-1} in this temperature interval. The dissolution rates are in a similar range as those reported from dynamic experiments with natural and synthetic monazite in the literature. In the Arrhenius plot, two different temperature regions were observed, in which the normalised dissolution rates of $LaPO_4$ show a distinctively different dependence on temperature, indicating two different mechanisms of dissolution: surface-controlled dissolution at lower temperature (T = 323 K – 363 K; $E_a = 44$ kJ·mol^{-1}) and transport-controlled dissolution at higher temperature (T = 363 K – 403 K; $E_a = 7.5$ kJ·mol^{-1}). Complementary thermodynamic modelling reflecting the experimental conditions in the dissolution experiments demonstrated that La-rhabdophane ($LaPO_4 \cdot 0.667H_2O$) is the thermodynamically favoured phosphate phase in aqueous environments below about 373 K, whereas at higher temperatures La-monazite is the thermodynamically stable La-orthophosphate. Based on these results, it is proposed that the dissolution rates and activation energy reported here for temperatures below 363 K refer not directly to the dissolution of La-monazite but to the formation and dissolution of a thin layer of La-rhabdophane formed at the monazite surface, including potentially a hydration step. Hence, rhabdophane-type phases might control the dissolution kinetics of *Ln*-orthophosphate-based ceramic waste forms under conditions relevant to geological disposal. Taking into account the dependency of the temperature of the rhabdophane-monazite transition on the cation radius described by du Fou de Kerdaniel et al. (2007), the transition temperature for An^{III}-bearing La-monazite waste forms (An^{III} = Pu^{III}, Am^{III}, Cm^{III}) would be higher than the temperature calculated here for the pure La-phosphate-system. Thus for an *An*-bearing La-monazite waste form generally the dissolution behaviour of the rhabdophane phase is the relevant issue under repository conditions.

6 Conclusions and outlook

Within the present work systematic fundamental studies on monazite-type waste forms were performed covering several aspects: synthesis and sintering of monazite-type ceramics, structural characterisation of monazite- and rhabdophane-type solid solutions and properties (thermodynamic, thermal, physical and mechanical properties, as well as dissolution behaviour) of monazite-type ceramics. The results of these studies contribute to the development of a refined fundamental understanding of the stability of potential monazite-type waste forms for actinides under repository relevant conditions thus allowing for reliable predictions of the long-term behaviour of these materials. The main conclusions are summarised in **Subchapter 6.1**; an outlook regarding future research needs is presented in **Subchapter 6.2**.

6.1. Conclusions

The synthesis and detailed structural characterisation of monazite- and rhabdophane-type solid solutions doped with actinides (Cm^{3+}, Pu^{3+}) and/or their surrogates using advanced analytical methods led to a refined understanding of the incorporation mechanism and speciation of actinides in the investigated materials on the molecular level. Although the experimental and computational data suggest a structural disordering due to a broader distribution of *Ln*(*An*)-O bond distances in the monazite solid solutions, the results of the present work also prove the homogeneity of the solid solutions since no preferential incorporation of dopants on host cation sites with similarly sized cationic radii occurs. This is of great importance when considering the performance of monazite materials as immobilisation matrices for actinide compounds. A preferential clustering of dopants around matching lattice sites could lead to incongruent dissolution and further to an inadequate retention of the radionuclides in a deep geological repository environment. Furthermore, the flexibility of the monazite structure toward dopants with varying cationic radii allows for the co-doping of multiple different actinides and deliberately added lanthanides, such as Eu^{3+} and Gd^{3+}, serving as e.g. neutron poisons to prevent criticality in the nuclear waste forms. This work demonstrates also that monazite-type ceramics with a reasonable amount of Pu (10–15%) for nuclear waste applications can be fabricated by conventional solid state reaction. Thereby Pu is incorporated into monazite structure in the oxidation state +III, thus no coupled substitution with divalent cations is required.

The low temperature rhabdophane phases exhibit more complex incorporation behaviour of the trivalent actinide in comparison to the monazite phases, due to the presence of multiple coexisting rhabdophane phases, deviating in their degree of hydration as well as several non-equivalent lattice sites in the host structures. However the investigated synthesis routes do not influence the formation of single phase monazite solid solutions after sintering due to the incorporation of trivalent actinides or their inactive surrogates on defined lattice sites.

It can be concluded that homogeneous monazite waste forms can be prepared via different synthesis routes. This indicates robust process control for various types of waste (e.g., precipitation processes can be used with liquid waste streams, and PuO_2 can be directly incorporated into monazite without any additional dissolution step).

From systematic comprehensive investigations of the physical properties of the monazite solid solution series a linear relationship between the structural chemistry and the properties was observed. The microhardness, fracture toughness, Young's modulus, thermal expansion as well as the heat capacity were found to be linearly dependent on the composition of the solid solutions, providing a predictability of the properties of monazite-type waste forms. The formation enthalpies derived from calorimetric measurements indicate the formation of regular monazite solid solutions with relatively small heat of mixing. Kinetic dissolution experiments of monazite-type ceramics in aqueous media and complementary performed thermodynamic modelling studies indicate that the dissolution at the temperatures expected in the final repository is controlled by the formation of a thin layer of rhabdophane phase leading to higher activation energy of dissolution, thus inhibiting the dissolution.

These results underline the chemical homogeneity and thermodynamic stability of the investigated monazite-type solid solutions and provide key input parameters for calculation of stability and solubility of the monazite solid solutions as a function of temperature, contributing to the long-term stability prediction of monazite nuclear waste forms. These results finally make the behaviour of monazite-type ceramics predictable in dependence on crystal structure, microstructure and temperature with respect to these properties.

6.2. Outlook

The results presented in this thesis provide a solid basis for several still unresolved research lines for prospective studies.

One of the points, which should be addressed in the future, includes structure, thermodynamic properties of and actinide incorporation in rhabdophane-type phases, since rhabdophane seems to control the dissolution behaviour of monazite waste forms under repository conditions. The structural studies of rhabdophane-type compounds doped with Cm and inactive surrogates for minor actinides and Pu, performed in this work, demonstrate the complexity of the actinide incorporation behaviour in the mixed "low-temperature" rhabdophane phases and suggest coexistence of multiple rhabdophane phases, deviating in their degree of hydration, in the proximity of the waste matrix. The existing data on rhabdophane phases containing trivalent actinides and in particular for plutonium is rare, and a refined crystal structure of the hydrated actinide bearing phosphate compounds as well its XRD patterns have not been reported so far. Thus the crystal structure of the low-temperature actinide bearing orthophosphate compounds and if and how actinides are incorporated into these compounds upon slow dissolution of a monazite waste form under repository conditions, should be investigated in future studies to gain further understanding on the performance of monazite host phases for actinide-bearing waste streams. Thus, detailed structural studies both on pure hydrated actinide phosphates and actinide-bearing lanthanide phosphate solid solutions with higher actinide content as well as thermodynamic data for the hydrated rhabdophane solid solutions and anhydrous rhabdophanes, as well as actinide-bearing monazites, are needed for computational predictions of the long-term behaviour of monazite waste forms under repository conditions.

The dissolution experiments should then be verified in connection with a particular repository case to elucidate to which extent the groundwater chemistry in the near field conditions in the contact with the materials of an engineered barrier system, such as buffer and backfill materials, has an impact on thermodynamic stability of monazite waste forms and on the formation of secondary phases.

Another aspect, interesting from a fundamental point of view, is the mechanism and kinetics of self-healing of the monazite crystal lattice after exposure to radiation damages due to self-irradiation. Monazite-type phosphates are known for their radiation resilience because natural monazite minerals do not exist in the metamict state although they can contain significant amount of α-decaying actinides since several hundred millions of years. This indicates that the rate of annealing even in low temperature environments is faster than the accumulation of radiation damage. The results reported in the literature have demonstrated the ability of the crystal structure also of synthetic plutonium-doped monazite to maintain a crystalline state despite high radiation damage levels. Self-irradiation studies based on doping with short-lived radionuclides (volumic irradiation) are still required as they do not always induce the same damages and consequences in comparison to the more localised irradiation at the surface of the material due to external irradiation with heavy ions.

7 Appendix

Table A 1 Mol fraction of Gd and Eu measured by EDX and XRF have been listed together with the resulting actual composition of the solid solution

x(Gd)		actual composition	x(Eu)		actual composition
EDX	XRF		EDX	XRF	
-	-	$GdPO_4$	-	-	$EuPO_4$
0.92	0.92	$La_{0.08}Gd_{0.92}PO_4$	0.91	0.91	$La_{0.09}Eu_{0.91}PO_4$
0.83	0.84	$La_{0.16}Gd_{0.84}PO_4$	0.81	0.82	$La_{0.18}Eu_{0.82}PO_4$
0.75		$La_{0.25}Gd_{0.75}PO_4$	0.70	0.72	$La_{0.29}Eu_{0.71}PO_4$
0.63	0.64	$La_{0.36}Gd_{0.64}PO_4$	0.65	-	$La_{0.35}Eu_{0.65}PO_4$
0.55		$La_{0.45}Gd_{0.55}PO_4$	0.57	0.58	$La_{0.58}Eu_{0.42}PO_4$
0.43	0.44	$La_{0.57}Gd_{0.43}PO_4$	0.40	-	$La_{0.60}Eu_{0.40}PO_4$
0.33	0.34	$La_{0.66}Gd_{0.34}PO_4$	0.34	0.36	$La_{0.65}Eu_{0.35}PO_4$
0.22	0.26	$La_{0.75}Gd_{0.25}PO_4$	0.22	0.23	$La_{0.78}Eu_{0.22}PO_4$
0.11	0.11	$La_{0.89}Gd_{0.11}PO_4$	0.11	-	$La_{0.89}Eu_{0.11}PO_4$
-	-	-	0.10	-	$La_{0.90}Eu_{0.10}PO_4$
-	-	$LaPO_4$	-	-	$LaPO_4$

Table A 2 The lattice parameter of $La_{1-x}Ln_xPO_4$ monazite solid solutions (Ln = Eu, Gd, x = 0 – 1)

x(Eu)	a/Å	b/Å	c/Å	β/°
1.00	6.6698(3)	6.8665(3)	6.3561(3)	103.94(1)
0.91	6.6864(3)	6.8861(3)	6.3720(3)	103.89(1)
0.81	6.7034(4)	6.9072(4)	6.3879(4)	103.83(1)
0.70	6.7224(4)	6.9319(5)	6.4053(4)	103.76(1)
0.57	6.7475(5)	6.9615(5)	6.4292(5)	103.67(1)
0.40	6.7766(5)	6.9968(5)	6.4556(5)	103.56(1)
0.22	6.8079(3)	7.0347(3)	6.4835(3)	103.44(1)
0.11	6.8258(4)	7.0567(4)	6.4993(4)	103.37(1)
x(Gd)	a/Å	b/Å	c/Å	β/°
1.00	6.6533(1)	6.8464(1)	6.3366(1)	104.00(1)
0.92	6.6694(1)	6.8663(1)	6.3527(1)	103.94(1)
0.83	6.6841(2)	6.8845(2)	6.3678(2)	103.88(1)
0.75	6.7009(1)	6.9047(1)	6.3838(1)	103.83(1)
0.63	6.7206(3)	6.9296(3)	6.4029(3)	103.75(1)
0.55	6.7393(1)	6.9553(1)	6.4204(1)	103.68(1)
0.43	6.7635(1)	6.9802(1)	6.4431(1)	103.60(1)
0.33	6.7833(4)	7.0050(4)	6.4606(4)	103.52(1)
0.22	6.8017(5)	7.0274(5)	6.4780(4)	103.45(1)
0.11	6.8203(4)	7.0515(4)	6.4930(4)	103.36(1)
0.00	6.8421(1)	7.0782(1)	6.512(1)	103.28(1)

Table A 3 Experimental Raman wavenumbers (cm^{-1}) of normal modes exemplarily for $La_{1-x}(Eu,Gd)_xPO_4$; x = 0, 0.5, 1 samples after sintering at 1723 K for 5 hours derived from peak maximum of fitted spectra using Fityk software.

Normal modes	Vibration	$GdPO_4$	$La_{0.5}Gd_{0.5}PO_4$	$LaPO_4$	$La_{0.5}Eu_{0.5}PO_4$	$EuPO_4$
v_2	sym. bending (δ_S)	477.6	470.1	465.7	468.4	472.8
v_4	asym. bending (δ_{AS})	633.1	623.9	619.5	623.6	629.3
v_1	sym. stretching (v_S)	987.9	978.8	967.9	979.8	987.9
v_3	asym. stretching (v_{AS})	1072.6	1062.6	1056.1	1062.4	1068.1

Table A 4. Compiled values obtained after Gaussian fitting of the experimental and computed Eu^{3+} excitation spectra and Eu-O bond length distributions.

Experimental profile				Calculated distribution			
x	Excitation energy x_c (cm^{-1})	FWHM (cm^{-1})	σ	x	Excitation energy x_c (cm^{-1})	FWHM (cm^{-1})	σ
0.0	17289	1.03(24)	0.44(11)	-	-	-	-
0.11	17288	8.1(1.3)	3.5(5)	0.1	17286	5.6(8)	2.4(4)
0.33	17282	16.3(1.1)	6.9(5)	0.3	17282	9.2(1.2)	3.9(5)
0.55	17278	18.3(1.1)	7.8(5)	0.5	17279	10.6(1.1)	4.5(5)
				0.5 (*ab initio*)	17280	8.6(9)	3.6(4)
0.75	17273	15.3(1.1)	6.5(5)	0.7	17274	8.7(1.1)	3.7(5)
0.92	17270	7.6(9)	3.2(4)	0.9	17270	5.3(9)	2.2(4)
1.0	17268	0.92(19)	0.39(8)	-	-	-	-

Table A 5. Actual compositions of the synthesized $La_{1-x}Gd_xPO_4\cdot0.667H_2O$ solid solutions derived from EDS and XRF measurements with the corresponding refined unit cell parameters.

x_{Gd}		**Actual composition**	**a (Å)**	**b (Å)**	**c (Å)**	**2θ (°)**
EDX	XRF					
-	-	$GdPO_4\cdot0.667H_2O$	27.960(4)	6.924(8)	11.928(1)	115.28(1)
0.83	0.84	$La_{0.16}Gd_{0.84}PO_4\cdot0.667H_2O$	28.080(4)	6.940(8)	12.018(2)	115.30(1)
0.75		$La_{0.25}Gd_{0.75}PO_4\cdot0.667H_2O$	28.161(6)	6.960(1)	12.054(2)	115.31(1)
0.63	0.64	$La_{0.36}Gd_{0.64}PO_4\cdot0.667H_2O$	28.219(3)	6.979(7)	12.083(9)	115.33(1)
0.55		$La_{0.45}Gd_{0.55}PO_4\cdot0.667H_2O$	28.312(4)	6.999(9)	12.124(2)	115.32(1)
0.33	0.34	$La_{0.66}Gd_{0.34}PO_4\cdot0.667H_2O$	28.482(8)	7.048(2)	12.204(3)	115.34(1)
0.22	0.26	$La_{0.75}Gd_{0.25}PO_4\cdot0.667H_2O$	28.570(4)	7.070(8)	12.240(1)	115.33(1)
-	-	$LaPO_4\cdot0.667H_2O$	28.741(3)	7.124(5)	12.285(9)	115.34(1)

Table A 6 Obtained compositions of the synthetic Cm^{3+}-doped $La_{1-x}Gd_x$-phosphates.

x (Gd^{3+})	Actual composition
1	$GdPO_4$
0.83±0.01	$La_{0.17}Gd_{0.83}PO_4$
0.54±0.03	$La_{0.46}Gd_{0.54}PO_4$
0.24±0.01	$La_{0.76}Gd_{0.24}PO_4$
0	$LaPO_4$

Table A 7. Refined unit cell parameters of the synthesised $La_{1-x}Pu_xPO_4$ solid solutions.

x_{Pu}	a (Å)	b (Å)	c (Å)	β (°)	V ($Å^3$)
0.01(1)[a]	6.83530(20)	7.07295(20)	6.50377(17)	103.2694(19)	306.035(15)
0.05(0)[b]	6.83161(16)	7.06925(17)	6.50172(16)	103.2890(17)	305.588(13)
0.10(0)[a]	6.82551(20)	7.06221(21)	6.49611(17)	103.3110(20)	304.722(15)
0.15(0)[b]	6.82067(15)	7.05651(16)	6.49266(17)	103.3322(19)	304.071(15)
1 **[124]**	6.759(1)	6.980(1)	6.447(1)	103.63(1)	295.59
0.1 **[126]**	6.8396(8)	7.0777(1)	6.5008(2)	103.2(7)	306.38

Mean value of the molar fraction of Pu derived from [a]3 and [b]2 EDS measurements.

Table A 8. Pump rates and La-concentrations (C_{La}) during dissolution of $LaPO_4$ powder (100 – 180 µm) in 0.01M HNO_3 in single path flow through (SPFT) experiments at temperatures between 323 K and 353 K using perfluoroalkoxy polymer (PFA) reactors.

T	323 K		333 K		353 K	
day	pump rate ml min^{-1}	C_{La} mol L^{-1}	pump rate ml min^{-1}	C_{La} mol L^{-1}	pump rate ml min^{-1}	C_{La} mol L^{-1}
1	0.184	$2.88\cdot10^{-7}$	0.183	$4.32\cdot10^{-7}$	0.195	$6.48\cdot10^{-7}$
2	0.181	$2.16\cdot10^{-7}$	0.183	$3.60\cdot10^{-7}$	0.192	$5.76\cdot10^{-7}$
5	0.180	$1.44\cdot10^{-7}$	0.182	$2.16\cdot10^{-7}$	0.193	$4.32\cdot10^{-7}$
6	0.180	$1.44\cdot10^{-7}$	0.182	$2.16\cdot10^{-7}$	0.192	$3.60\cdot10^{-7}$
7	0.171	$1.44\cdot10^{-7}$	0.175	$2.16\cdot10^{-7}$	0.183	$3.60\cdot10^{-7}$
8	0.170	$1.44\cdot10^{-7}$	0.174	$2.16\cdot10^{-7}$	0.181	$3.60\cdot10^{-7}$
9	0.178	$1.44\cdot10^{-7}$	0.181	$2.16\cdot10^{-7}$	0.190	$3.60\cdot10^{-7}$
12	0.178	$1.44\cdot10^{-7}$	0.182	$2.16\cdot10^{-7}$	0.191	$3.60\cdot10^{-7}$
13	0.179	$1.44\cdot10^{-7}$	0.180	$2.16\cdot10^{-7}$	0.191	$3.60\cdot10^{-7}$
14	0.179	$1.44\cdot10^{-7}$	0.182	$2.16\cdot10^{-7}$	0.191	$4.32\cdot10^{-7}$
16	0.179	$1.44\cdot10^{-7}$	0.183	$2.16\cdot10^{-7}$	0.191	$4.32\cdot10^{-7}$

Table A 9. Pump rates and La-concentrations (C_{La}) during dissolution of $LaPO_4$ powder (100 – 180 µm) in 0.01M HNO_3 using mixed flow titanium reactors at temperatures between 333 K and 403 K.

T	333 K		353 K		363 K		383 K		430 K	
day	pump rate ml min^{-1}	C_{La} mol L^{-1}	pump rate ml min^{-1}	C_{La} mol L^{-1}	pump rate ml min^{-1}	C_{La} mol L^{-1}	pump rate ml min^{-1}	C_{La} mol L^{-1}	pump rate ml min^{-1}	C_{La} mol L^{-1}
0							0.434	$4.32\cdot10^{-7}$	0.538	$9.36\cdot10^{-7}$
1	0.696	$7.92\cdot10^{-8}$	0.647	$2.30\cdot10^{-7}$	0.647	$7.41\cdot10^{-7}$	0.447	$4.32\cdot10^{-7}$	0.447	$7.63\cdot10^{-7}$
2			0.659	$2.02\cdot10^{-7}$	0.645	$7.56\cdot10^{-7}$			0.449	$7.99\cdot10^{-7}$
3					0.640	$7.05\cdot10^{-7}$	0.447	$4.18\cdot10^{-7}$		
4	0.650	$1.01\cdot10^{-7}$					0.446	$4.32\cdot10^{-7}$		
5									0.450	$7.34\cdot10^{-7}$
6	0.667	$8.64\cdot10^{-8}$	0.644	$2.16\cdot10^{-7}$					0.448	$6.62\cdot10^{-7}$
7	0.644	$6.48\cdot10^{-8}$			0.640	$6.55\cdot10^{-7}$	0.445	$4.10\cdot10^{-7}$	0.450	$6.19\cdot10^{-7}$
8									0.450	$5.98\cdot10^{-7}$
9			0.647	$2.16\cdot10^{-7}$					0.448	$5.47\cdot10^{-7}$
10							0.448	$3.53\cdot10^{-7}$		
12	0.515	$6.48\cdot10^{-8}$	0.644	$2.02\cdot10^{-7}$	0.642	$5.18\cdot10^{-7}$			0.461	$5.40\cdot10^{-7}$
14					0.645	$4.18\cdot10^{-7}$			0.442	$5.83\cdot10^{-7}$
15	0.645	$6.48\cdot10^{-8}$	0.644	$1.80\cdot10^{-7}$	0.644	$3.96\cdot10^{-7}$			0.443	$5.62\cdot10^{-7}$
16									0.443	$5.04\cdot10^{-7}$
17							0.448	$4.32\cdot10^{-7}$		
18	0.648	$5.04\cdot10^{-8}$					0.448	$4.03\cdot10^{-7}$		
20					0.644	$2.81\cdot10^{-7}$			0.441	$5.18\cdot10^{-7}$
21			0.629	$1.73\cdot10^{-7}$			0.461	$3.31\cdot10^{-7}$		
22					0.645	$2.81\cdot10^{-7}$	0.442	$3.60\cdot10^{-7}$	0.440	$4.97\cdot10^{-7}$
23			0.643	$1.80\cdot10^{-7}$					0.440	$4.75\cdot10^{-7}$
26					0.649	$2.88\cdot10^{-7}$				
27			0.649	$1.51\cdot10^{-7}$						
29	0.646	$5.04\cdot10^{-8}$	0.647	$1.51\cdot10^{-7}$						
32	0.645	$4.32\cdot10^{-8}$								
36	0.646	$5.04\cdot10^{-8}$								
41	0.645	$5.04\cdot10^{-8}$								
49	0.653	$4.32\cdot10^{-8}$								

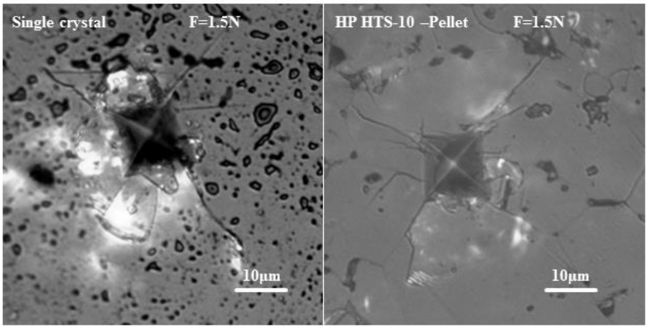

Figure A 1. Typical optical micrographs of the indenter on the surface of the single crystal and the hot-pressed HTS-10 pellet.

8 References

1. Brendebach, B. *Decommissioning of nuclear facilities: Germany's experience.* IAEA Bulletin, **2016**, 24.
2. Baldev, R.; Busurin, Y.; Depisch, F.; Ganguly, C.; Ghosh, S.; Koganti, S.B.; Kormilitsyn, M.; Koyama, T.; Kudryavtsev, Y.; Kutty, K.V.G.; Masson, M.; Nagarajan, K.; Natarajan, R.; Nawada, H.P.; Prabhakara Reddy, B.; Rao, P.R.V.; Srinivasan, T.G.; Swaminathan, P.; Wattal, P.K. *Status of developments in the back end of the fast reactor fuel cycle*. IAEA Nuclear Energy Series, **2011**, NF-T-4.2.
3. Bergmans, A.; Boe, T.; Bragg, K.; Burcl, R.; Chandraker, K.; Crossland, I.; Damette, G.; Delligatti, M.; Doneux, J.; Egan, M.; Garamszeghy, M.; Hedberg, B.; Hutchison, S.; Jack, G.; Janssen, L.; Koudriavtsev, E.; Kröger, H.; Lee, J.S.; Linsley, G.; Lo Giudice, F.; Mele, I.; Metcalf, P.; Müller, W.; Ntuane, B.; Pino, G.; Rabotnov, N.; Rowat, J.; Selling, H.; Sjöbloem, K.-L.; Steyer, S.; Taccarello, D.; Xiang, H. *A position paper of international experts "The long term storage of radioactive waste: safety and sustainability*". International Atomic Energy Agency IAEA,Vienna, **2003**.
4. Apted, M.; Ahn, J. *Multiple-barrier geological repository design and operation strategies for safe disposal of radioactive materials. Geological repository systems for safe disposal*. Woodhead Publishing Limited, **2010**, 3.
5. Bernadzikowski, T. A.; Allender, J. S.; Butler, J. L.; Gordon, D. E.; Gould, Jr., T. H.; Stone, J. A. *The evaluation and selection of candidate high-level waste forms.* US Department of Energy Report DOE/TIC 11611; Savannah River Operations Office: Aiken, SC, **1982**.
6. Hench, L.L.; Clark, D.E.; Campbell, J. *High level waste immobilisation forms.* Nuclear and chemical waste management, **1984**, *5*, 149.
7. Roth, G.; Weisenburger, S. *Vitrification of high-level liquid waste: glass chemistry, process chemistry and process technology.* Nucl. Eng. Des., **2000**, *202*, 197.
8. Vance, E.R.; Perera, D.S.; Moricca, S.; Aly, Z.; Begg, B.D. *Immobilisation of ^{129}I by encapsulation in tin by hot-pressing at 200°C.* J. Nucl. Mater., **2005**, *341*, 93.
9. Carter, M.L.; Gillen, A.L.; Olufson, K.; Vance, E.R. *HIPed tailored hollandite waste forms for the immobilization of radioactive Cs and Sr.* J. Am. Ceram. Soc., **2009**, *92,* 1112.
10. Lumpkin, G.R. *Ceramic waste forms for actinides*. Elements, **2006**, *2*, 365.
11. Ewing, R.C. *Ceramic matrices for plutonium disposition.* Prog. Nucl. Ener., **2007**, *49*, 635.
12. Donald, I.W.; Metcalfe, B.L.; Taylor, R.N.J. *Review: the immobilisation of high level radioactive wastes using glasses and ceramics.* J. Mater. Sci., **1997**, *32*, 5851.
13. Donald, I.W. *Waste immobilization in glass and ceramic based hosts: Radioactive, toxic and hazardous wastes.* John Wiley & Sons Ltd, Chichester, West Sussex, United Kingdom, **2010**.
14. Burakov, B.E.; Yagovkina, M.A.; Zamoryanskaya, M.V.; Petrova, M.A.; Domracheva, Y.V.; Kolesnikova, E.V.; Nikolaeva, L.D.; Garbuzov, V.M.; Kitsay, A.A.; Zirlin, V.A. *Behavior of actinide host-phases under self-irradiation: zircon, pyrochlore, monazite, and cubic zirconia doped with Pu-238.* In: Krivovichev, S.V. (ed.): Minerals as Advaced Materials, Springer (Berlin, Heidelberg), **2008**, 209.
15. Deissmann, G.; Neumeier, S.; Modolo, G.; Bosbach, D. *Durability of potential plutonium wasteforms under repository conditions.* Mineral. Mag., **2012**, *76(8)*, 2911.

16. Carter, M.L.; Stewart, M.W.A.; Vance, E.R.; Begg, B.D.; Moricca, S.; Tripp, J. *HIPed tailored ceramic waste forms for the immobilization of Cs, Sr, and Tc.* Proceedings GLOBAL 2007, Boise, ID, USA, **2007**, 1022.
17. Angeli, F.; McGlinn, P.; Frugier, P. *Chemical durability of hollandite ceramic for conditioning cesium.* J. Nucl. Mater., **2008**, *380*, 59.
18. Hartmann, T.; Alaniz, A.J.; Antonio, D.J. *Fabrication and properties of technetium-bearing pyrochlores and perovskites as potential waste forms.* Procedia Chem., **2012**, *7*, 622.
19. Nenhoff, T.M.; Krumhansl, J.L.; Gao, H.H.; Rajan, A.; McMahon, K. *Iodine waste form summary report.* Sandia National Laboratories Report SAND, **2007**, 6202.
20. Gras, J.M.; Do Quang, R.; Masson, H.; Lieven, T.; Ferry, C.; Poinssot, C.; Debes, M.; Delbecq, J.M. *Perspectives on the closed fuel cycle - Implications for high-level waste matrices.* J. Nucl. Mater., **2007**, *362*, 383.
21. Dacheux, N.; Clavier, N.; Podor, R. *Versatile monazite: resolving geological records and solving challenges in materials science. Monazite as a promising long-term radioactive waste matrix: benefits of high-structural flexibility and chemical durability.* Am. Mineral., **2013**, *98(5-6)*, 833.
22. Schlenz, H.; Heuser, J.; Neumann, A.; Schmitz, S.; Bosbach, D. *Monazite as a suitable actinide waste form.* Z. Kristallogr. Cryst. Mater., **2013**, *228(3)*, 113.
23. Clavier, N.; Podor, R.; Dacheux, N. *Crystal chemistry of the monazite structure.* J. Eur. Ceram. Soc., **2011**, *31(6)*, 941.
24. Poitrasson, F.; Oelkers, E.; Schott, J.; Montel, J.-M. *Experimental determination of synthetic $NdPO_4$ monazite end-member solubility in water from 21°C to 300°C: implications for rare earth element mobility in crustal fluids.* Geochim. Cosmochim. Acta, **2004**, *68(10)*, 2207.
25. Oelkers, E.H.; Montel, J.-M. *Phosphates and nuclear waste storage.* Elements, **2008**, *4*, 113.
26. Ewing, R.C.; Wang, L. *Phosphates as nuclear waste forms.* Rev. Mineral. Geochem., **2002**, *48(1)*, 673.
27. Meldrum, A.; Boatner, L.A.; Weber, W.J.; Ewing, R.C. *Radiation damage in zircon and monazite.* Geochim. Cosmochim. Acta, **1998**, *62*, 2509.
28. Meldrum, A.; Boatner, L.A.; Ewing, R.C. *A comparison of radiation effects in crystalline ABO_4-type phosphates and silicates.* Mineral. Mag., **2000**, *64*, 185.
29. Ewing, R.C.; Meldrum, A.; Wang, L.M.; Wang, S. *Radiation induced amorphization.* Rev. Min.. Geochem., **2000**, *39*, 319.
30. Boatner, L.A. *Synthesis, structure, and properties of monazite, pretulite, and xenotime*. Rev. Mineral. Geochem., **2002**, *48*, 87.
31. Weber, W.J.; Navrotsky, A.; Stefanovsky, S.; Vance, E.; Vernaz, E. *Materials science of high-level nuclear waste immobilization.* MRS Bull., **2009**, *34*, 46.
32. Wing, B.A.; Ferry, J.M.; Harrison, M. *Prograde destruction and formation of monazite and allanite during contact and regional metamorphism of pelites: petrology and geochronology.* Contributions to Mineralogy and Petrology, **2003**, *145*, 228.
33. Kohn, M.J.; Malloy, M.A. *Formation of monazite via prograde metamorphic reactions among common silicates; implications for age determinations*. Geochim. Cosmochim. Acta, **2004**, *68*, 101.

34. Cuney, M.; Mathieu, R. *Extreme light rare earth element mobilization by diagenetic fluids in the geological environment of the Oklo natural reactor zones, Franceville basin, Gabon.* Geol., **2000**, *28*, 743.
35. Sudre, O.H.; Marshal, D. B.; Morgan, P. E. D. *Monazite-based thermal barrier coatings.* United States Patent, (US 6,863,999 B1), **2005**.
36. Anfimova, T.; Li, Q.; Jensen, J.O.; Bjerrum, N.J. *Thermal stability and proton conductivity of rare earth orthophosphate hydrates.* Int. J. Electrochem. Sci., **2014**, *9*, 2285.
37. Yu, R.; De Jonghe, L.C. *Proton-transfer mechanism in* $LaPO_4$. J. Phys. Chem., **2007**, *C(111)*, 11003.
38. Takitaa, Y.; Sanoa, K.; Murayab, T.; Nishiguchia, H.; Kawataa, N.; Itoa, M.; Akbaya, T.; T., I. *Oxidative dehydrogenation of iso-butane to iso-butene II. Rare earth phosphate catalysts*. Appl. Catal., **1998**, *A: General(170)*, 23.
39. Kumar, V.; Singh, S.; Kotnala, R.K.; Chawla, S. $GdPO^4{:}Eu^{3+}$ *nanoparticles with intense orange red emission suitable for solar spectrum conversion and their multifunctionality*. J. Lumin., **2014**, *146*, 486.
40. Rodriguez-Liviano, S.; Becerro, A.I.; Alcantara, D.; Grazu, V.; de la Fuente, J.M.; Ocana, M. *Synthesis and properties of multifunctional tetragonal Eu:*$GdPO_4$ *nanocubes for optical and magnetic resonance imaging applications.* Inorg. Chem., **2013**, *52(2)*, 647.
41. Montel, J.M.; Razafimahatratra, D.; Ralison, B.; De Parseval, P.; Thibault, M.; Randranja, R. *Monazite from mountain to ocean: a case study from Trolognaro (Fort-Dauphin), Madagascar.* Eur. J. Mineral., **2011**, *23*, 745.
42. Ni, Y.; Hughes, J.M.; Mariano, A.N. *Crystal chemistry of the monazite and xenotime structures.* Am. Mineral., **1995**, *80*, 21.
43. Shannon, R.D. *Revised effective ionic radii and systematic studies of interatomic distances in halides and chalcogenides.* Acta Crystallogr, **1976**, *A32*, 751.
44. Brandt, F.; Neumeier, S.; Schuppik, T.; Arinicheva, Y.; Bukaemskiy, A.; Modolo, G.; Bosbach, D. *Conditioning of minor actinides in lanthanum monazite ceramics: A surrogate study with europium.* Prog. Nucl. Energy, **2014**, *72*, 140.
45. Ewing, R.W., W.; Clinard, F. *Radiation effects in nuclear waste forms for high-level radioactive waste.* Prog. Nucl. Energ., **1995**, *29*, 63.
46. Heuser, J.; Bukaemskiy, A.A.; Neumeier, S.; Neumann, A.; Bosbach, D. *Raman and infrared spectroscopy of monazite-type ceramics used for nuclear waste conditioning.* Prog. Nucl. Energy, **2014**, *72*, 149.
47. Oelkers, E.H.; Poitrasson, F. *An experimental study of the dissolution stoichiometry and rates of a natural monazite as a function of temperature from 50 to 230 °C and pH from 1.5 to 10.* Chem. Geol., **2002**, *191*, 73.
48. Kretzschmar, R.; Schäfer, T. *Metal retention and transport on colloidal particles in the environment.* Elements, **2005**, *1*, 205.
49. Schäfer, T.; Huber, F.; Seher, H.; Missana, T.; Alonso, U.; Kumke, M.; Eidner, S.; Claret, F.; Enzmann, F. *Nanoparticles and their influence on radionuclide mobility in deep geological formations.* Applied Geochemistry, **2012**, *27(2)*, 390.
50. Claparede, L.; Clavier, N.; Dacheux, N.; Moisy, P.; Podor, R.; Ravaux, J. *Influence of crystallization state and microstructure on the chemical durability of cerium-neodymium mixed oxides.* Inorg. Chem., **2011**, *50(18)*, 9059.
51. Szenknect, S.; Mesbah, A.; Horlait, D.; Clavier, N.; Dourdain, S.; Ravaux, J.; Dacheux, N. *Kinetics of Structural and Microstructural Changes at the Solid/Solution Interface during*

Dissolution of Cerium(IV)–Neodymium(III) Oxides. J. Phys. Chem. C, **2012**, *116(22)*, 12027.

52. Horlait, D.; Tocino, F.; Clavier, N.; Dacheux, N.; Szenknect, S. *Multiparametric study of* $Th_{1-x}Ln_xO_{2-x/2}$ *mixed oxides dissolution in nitric acid media.* J. Nucl. Mater., **2012**, *429 (1-3)*, 237.
53. Du Fou de Kerdaniel, E.; Clavier, N.; Dacheux, N.; Terra, O.; Podor, R. *Actinide solubility-controlling phases during the dissolution of phosphate ceramics.* J. Nucl. Mater., **2007**, *362(2-3)*, 451.
54. Saraf, M.; Kumar, P.; Kedawat, G.; Dwivedi, J.; Vithayathil, S.A.; Jaiswal, N.; Kaipparettu, B.A.; Gupta, B.K. *Probing highly luminescent europium-doped lanthanum orthophosphate nanorods for strategic applications.* Inorg Chem, **2015**, *54(6)*, 2616.
55. Yan, Z.-G.; Zhang, Y.-W.; You, L.-P.; Si, R.; Yan, C.-H. *Controlled synthesis and characterization of monazite type monocrystalline nanowires of mixed lanthanide orthophosphates.* Solid State Commun., **2004**, *130(1-2)*, 125.
56. Du, A.; Wan, C.; Qu, Z.; Wu, R.; Pan, W. *Effects of texture on the thermal conductivity of the* $LaPO_4$ *monazite.* J. Am. Ceram. Soc., **2010**, *93(9)*, 2822.
57. Du, A.B.; Qu, Z.X.; Wan, C.L.; Han, R.B.; Pan, W. *Effects of processing parameters of SPS on the densification and texture of* $LaPO_4$ *ceramics*. Key Eng. Mater., **2008**, 368-372, 1059.
58. Wang, J.; Zhou, Y.; Lin, Z. *First-principles elastic stiffness of* $LaPO_4$ *monazite*. Appl. Phys. Lett., **2005**, *87(5)*, 051902.
59. Mesbah, A.; Clavier, N.; Elkaim, E.; Gausse, C.; Kacem, I.B.; Szenknect, S.; Dacheux, N. *Monoclinic form of the rhabdophane compounds:* $REEPO_4{\cdot}0.667H_2O$. Cryst. Growth. Des., **2014**, *14(10)*, 5090.
60. Mesbah, A.; Clavier, N.; Elkaim, E.; Szenknect, S.; Dacheux, N. *In pursuit of the rhabdophane crystal structure: from the hydrated monoclinic* $LnPO_4{\cdot}0.667H_2O$ *to the hexagonal* $LnPO_4$ *(Ln = Nd, Sm, Gd, Eu and Dy).* J. Solid State Chem., **2017**, *249*, 221.
61. Mooney, R.C.L. *X-ray diffraction study of cerous phosphate and related crystals.* Acta. Cryst., **1950**, *3*, 337.
62. Lucas, S.; Champion, E.; Bregiroux, D.; Bernache-Assollant, D.; Audubert, F. *Rare earth phosphate powders* $RePO_4{\cdot}nH_2O$ *(Re=La, Ce or Y)—Part I. Synthesis and characterization*. J. Solid State Chem., **2004**, *177(4-5)*, 1302.
63. Clavier, N.; Dacheux, N.; Wallez, G.; Quarton, G. *Hydrothermal methods as a new way of actinide phosphate preparation.* Mater. Res. Soc. Symp. Proc., **2007**, *985*, 169.
64. Assaaoudi, H.; Ennaciri, A.; Rulmont, A. *Vibrational spectra of hydrated rare earth orthophosphates.* Vib. Spectrosc., **2001**, *25*, 81.
65. Gausse, C.; Szenknect, S.; Qin, D.W.; Mesbah, A.; Clavier, N.; Neumeier, S.; Bosbach, D.; Dacheux, N. *Determination of the Solubility of Rhabdophanes* $LnPO_4{\cdot}0.667H_2O$ *(Ln = La to Dy).* Eur. J. Inorg. Chem., **2016**, *28*, 4615.
66. Jonasson, R.C. *DTA study of the rhabdophane to monazite transformation in rare earth (La-Dy) phosphates.* Thermochim. Acta, **1986**, *108*, 65.
67. Arinicheva, Y.; Bukaemskiy, A.; Neumeier, S.; Modolo, G.; Bosbach, D. *Studies on thermal and mechanical properties of monazite-type ceramics for the conditioning of minor actinides.* Prog. Nucl. Energy, **2014**, *72*, 144.

68. Neumeier, S.; Arinicheva, Y.; Clavier, N.; Podor, R.; Bukaemskiy, A.; Modolo, G.; Dacheux, N.; Bosbach, D. *The effect of the synthesis route of monazite precursors on the microstructure of sintered pellets.* Prog. Nucl. Energy, **2016**, *92*, 298.
69. Terra, O.; Clavier, N.; Dacheux, N.; Podor, R. *Preparation and characterization of lanthanum–gadolinium monazites as ceramics for radioactive waste storage.* New J. Chem., **2003**, *27(6)*, 957.
70. Rai, D.; Felmy, A.R.; Fulton, R.W. *Solubility and ion activity product of* $AmPO_4$• $xH_2O(am)$. Radiochim. Acta, **1992**, *56*, 7.
71. Keller, C.; Walter, K.H. *Darstellung, Gitterkonstanten und chemische Eigenschaften einiger ternärer Oxide des Plutoniums, Americiums und Curiums vom Typ* $Me^{III}X^{V}O_4$. J. Inorg. Nucl. Chem., **1965**, *27*, 1253.
72. Bjorklund, C.W. *The preparation of* PuP_2O_7 *and* $PuPO_4$. J. Am. Chem. Soc., **1958**, *79(24)*, 6347.
73. Perrière, L.; Bregiroux, D.; Naitali, B.; Audubert, F.; Champion, E.; Smith, D.S.; Bernache-Assollant, D. *Microstructural dependence of the thermal and mechanical properties of monazite* $LnPO_4$ *(Ln=La to Gd).* J. Eur. Ceram. Soc., **2007**, *27(10)*, 3207.
74. Mikeska, K.R.B., Stephen J.; Grise, Steven L. *Corrosion of ceramics in aqueous hydrofluoric acid.* J. Am. Ceram. Soc., **2000**, *83(5)*, 1160.
75. Luttge, A.; Arvidson, R.S.; Fischer, C. *A stochastic treatment of crystal dissolution kinetics. Elements*, **2013**, *9(3)*, 183.
76. Ziouane, Y.; Arab-Chapelet, B.; Lalleman, S.; Leturcq, G. *Effect of the microstructural morphology on* UO_2 *powders.* Procedia Chem., **2016**, *21*, 319.
77. Diaz-Guillén, J.A.; Fuentes, A.F.; Gallini, S.; Colomer, M.T. *A rapid method to obtain nanometric particles of rhabdophane* $LaPO_4{\cdot}nH_2O$ *by mechanical milling.* J. Alloys Compd., **2007**, 427(1-2), 87.
78. Bregiroux, D.; Terra, O.; Audubert, F.; Dacheux, N.; Serin, V.; Podor, R.; Bernache-Assollant, D. *Solid-state synthesis of monazite-type compounds containing tetravalent elements.* Inorg. Chem., **2007**, *46(24)*, 10372.
79. Wang, R.; Pan, W.; Chen, J.; Fang, M.; Jiang, M.; Cao; Z. *Microstructure and mechanical properties of machinable* $Al_2O_3/LaPO_4$ *composites by hot pressing.* Ceram. Int., **2003**, *29*, 83.
80. Bregiroux, D.; Lucas, S.; Champion, E.; Audubert, F.; Bernache-Assollant, D. *Sintering and microstructure of rare earth phosphate ceramics* $REPO_4$ *with RE=La, Ce or Y.* J. Eur. Ceram. Soc., **2006**, *26(3)*, 279.
81. Messamy, H.; Riwotzki, K.; Kornowski, A.; Naused, S.; Haase, M. *Wet-chemical synthesis of doped colloidal nanomaterials particles and fibers of* $LaPO_4$*:Eu,* $LaPO_4$*:Ce, and* $LaPO_4$*:Ce,Tb.* Adv. Mater., **1999**, *11(10)*, 840.
82. Patra, C.R.; Gabashvili, A.; Patra, S.; Jacob, D.S.; Gedanken, A.; Landau, A.; Gofer, Y. *Microwave approach for the synthesis of rhabdophane-type lanthanide orthophosphate (Ln = La, Ce, Nd, Sm, Eu, Gd and Tb) nanorods under solvothermal conditions.* New J. Chem., **2005**, *29(5)*, 733.
83. Schatzmann, M.T.; Mecartney, M.L.; Morgan, P.E.D. *Synthesis of monoclinic monazite,* $LaPO_4$ *by direct precipitation.* J. Mater. Chem., **2009**, *19(32)*, 5720.
84. Park, J.; Joo, J.; Kwon, S.G.; Jang, Y.; Hyeon, T. *Synthesis of monodisperse spherical nanocrystals.* Angew. Chem. Int. Ed., **2007**, **46(25)**, 4630.

85. Klinkenberg, M.; Neumeier, S.; Bosbach, D. *Institute of energy and climate research IEK-6: Nuclear waste management & reactor safety report 2009/2010 Material science for nuclear waste management.* Forschungszentrum Jülich, **2011**, 90.
86. Liu, X.; Gao, Z.; Sun, J.; Shen, J. *Fabrication of lanthanide phosphate nanocrystals with well-controlled morphologies by layer-by-layer adsorption and reaction method at room temperature.* Cryst. Growth Des., **2009**, *9(8)*, 3707.
87. Hikichi, Y.; Tanimura, Y.; Suzuk, S. *Sintering and properties of monazite-type* $CePO_4$*.* J. Am. Ceram. Soc., **1990**, *73(12)*, 3594.
88. Bregiroux, D.; Audubert, F.; Charpentier, T.; Sakellariou, D.; Bernache-Assollant, D. *Solid-state synthesis of monazite-type compounds* $LnPO_4$ *(Ln=La to Gd).* Solid State Sci., **2007**, 9(5), 432.
89. Cho, I.-S.; Choi, G.K.; An, J.-S.; Kim, J.-R.; Hong, K.S. *Sintering, microstructure and microwave dielectric properties of rare earth orthophosphates,* $RePO_4$ *(Re=La, Ce, Nd, Sm, Tb, Dy, Y, Yb).* Mater. Res. Bull., **2009**, *44(1)*, 173.
90. Morgan, P.E.D.; Housley, R.M.; Davis, J.B.; DeHaan, M.L. *Chemical and ceramic methods toward safe storage of actinides. Rockwell Scientific, 1049, Camino Dos Rios,Thousand Oaks, CA 91360 USA* (Final technical report Contract No. DE-FG07-96ER45617), **2005**.
91. Hernández, T.; Martín, P. *Effect of the phosphorous/cerium ratio in the properties of sintered Ce-monazite.* J. Alloys Compd., **2008**, *466(1-2)*, 568.
92. Rajesh, K.; Sivakumar, B.; Pillai, P.K.; Mukundan, P.; Warrier, K.G.K.; Nair, V.R. *Synthesis of nanocrystalline lanthanum phosphate for low temperature densification to monazite ceramics.* Mater. Lett., **2004**, *58(11)*, 1687.
93. Zhao, X.; Teng, Y.; Yang, H.; Huang, Y.; Ma, J. *Comparison of microstructure and chemical durability of* $Ce_{0.9}Gd_{0.1}PO_4$ *ceramics prepared by hot-press and pressureless sintering.* Ceram. Int., **2015**, *41(9),* 11062.
94. Potanina, E.; Golovkina, L.; Orlova, A.; Nokhrin, A.; Boldin, M.; Sakharov, N. *Lanthanide (Nd, Gd) compounds with garnet and monazite structures. Powders synthesis by "wet" chemistry to sintering ceramics by Spark Plasma Sintering.* J. Nucl. Mater., **2016**, *473*, 93.
95. Ma, J.; Teng, Y.; Wu, L.; Zhang, K.; Huang, Y.; Zhao, X.; Wang, G. *Effect of sintering technique on mechanical property and chemical durability of* $Ce_{0.5}Pr_{0.5}PO_4$ *ceramics.* Ceram. Int., **2015**, *41(10)*, 14597.
96. Bregiroux, D.; Audubert, F.; Bernache-Assollant, D. *Densification and grain growth during solid state sintering of* $LaPO_4$*.* Ceram. Int., **2009**, *35(3)*, 1115.
97. Bingham, P.A.; Hand, R.J.; Stennett, M.C.; Hyatt, N.C.; Harrison, M.T. *The use of surrogates in waste immobilization studies: A case of plutonium.* Mater. Res. Soc. Symp. Proc., **2008**, *1107*, 421.
98. *CRC Handbook of Chemistry and Physics* 72nd Ed. CRC Press, Boca Raton, Section 8, **1991-1992**, 17.
99. Yang, P.; Quan, Z.; Li, C.; Hou, Z.; Wang, W.; Lin, J. *Solvothermal synthesis and luminescent properties of monodisperse* $LaPO_4$*:Ln (Ln=*Eu^{3+}*,* Ce^{3+}*,* Tb^{3+}*) particles.* J. Solid State Chem., **2009**, *182(5)*, 1045.
100. Oertel, A.; Lengler, C.; Walther, T.; Haase, M. *Photonic properties of inverse opals fabricated from lanthanide-doped* $LaPO_4$ *nanocrystals.* Chem. Mater., **2009**, *21(16)*, 3883.
101. Senden, T.; Rabouw, F.T.; A., M. *Photonic effects on the radiative decay rate and luminescence quantum yield of doped nanocrystals.* ACS Nano, **2015**, *9(2)*, 1801.

102. Terra, O.D., N.; Audubert, F.; Podor, R. *Immobilization of tetravalent actinides in phosphate ceramics.* J. Nucl. Mater., **2006**, *253(1 – 3)*, 224.
103. Gramaccioli, C.M.; Segalstad, T.V. *A uranium- and thorium-rich monazite from a south-alpine pegmatite at Piona,* Italy. Am. Mineral., **1978**, *63(197)*, 757.
104. Harrison, T.M.; Catlos, E.J.; Montel, J.M. *U-Th-Pb dating of phosphate minerals.* Rev. Mineral. Geochem., **2002**, *48(1)*, 524.
105. Donald, I.W.; Metcalfe, B.L.; Taylor, N.J. Review. *The immobilization of high level radioactive wastes using ceramics and glasses.* J. Mater. Sci., **1997**, *32*, 5851.
106. Popa, K.; Konings, R.J.M. *High-temperature heat capacities of $EuPO_4$ and $SmPO_4$ synthetic monazites.* Thermochim. Acta, **2006**, *445(1)*, 49.
107. Ushakov, S.V.; Helean, K.B.; Navrotsky, A.; Boatner, L.A. *Thermochemistry of rare-earth orthophosphates.* J. Mater. Res., **2001**, *16(9)*, 2623
108. Huittinen, N.; Arinicheva, Y.; Schmidt, M.; Neumeier, S.; Stumpf, T. *Using Eu^{3+} as an atomic probe to investigate the local environment in $LaPO_4$-$GdPO_4$ monazite end-members.* J. Colloid Interface Sci., **2016**, *483*, 139.
109. Popa, K.; Konings, R. J. M.; Geisler, T. *High-temperature calorimetry of $(La_{1-x}Ln_x)PO_4$ solid solutions.* J. Chem. Thermodyn., **2007**, *39*, 236.
110. Neumeier, S.; Kegler, P.; Arinicheva, Y.; Shelyug, A.; Kowalski, P.M.; Schreinemachers, C.; Navrotsky, A.; Bosbach, D. *Thermochemistry of $La_{1-x}Ln_xPO_4$-monazites (Ln=Gd, Eu).* J. Chem. Thermodynamics, **2017**, *105*, 396.
111. Podor, R. *Raman spectra of the actinide bearing monazites.* Eur. J. Mineral. , **1995**, *7*, 1353.
112. Konings, R.J.M.; Walter, M.; Popa, K. *Excess properties of the $(Ln_{2-2x}Ca_xTh_x)(PO_4)_2$ (Ln = La, Ce) solid solutions.* J. Chem. Thermodyn., **2008**, *40*, 1305.
113. Popa, K.; Cologna, M.; Martel, L.; Staicu, D.; Cambriani, A.; Ernstberger, M.; Raison, P. E.; Somers, J. *$CaTh(PO_4)_2$ cheralite as a candidate ceramic nuclear waste form: Spark Plasma Sintering and physicochemical characterisation.* J. Eur. Ceram. Soc., **2016**, *36(16)*, 4115.
114. Bregiroux, D.; Terra, O.; Audubert, F.; Dacheux, N.; Serin, V.; Podor, R.; Bernache-Assollant, D. *Solid-state synthesis of monazite-type compounds containing tetravalent elements.* Inorg. Chem., **2007**, *46*, 10372.
115. Burakov, B.E.; Yagockina, M. A.; Garbuzov, V. M.; Kitsay, A. A.; Zirlin, V. A. *Self-irradiation of monazite ceramics: Contrasting behavior of $PuPO_4$ and $(La,Pu)PO_4$ doped with Pu-238.* Mater. Res. Soc. Symp. Proc., **2004**, *824*, 219.
116. Aloy, A.S.; Kovarskaya, E.N.; Koltsova, T.I.; Samoylov, S.E.; Rovnyi, S.I.; Medvedev, G.M.; Jardine, L.J. *Immobilization of Am-241, formed under plutonium metal conversion, into monazite-type ceramics.* Am. Soc. Mechan. Engin., **2002**, 1833.
117. Bregiroux, D.; Belin, R.; Valenza, P.; Audubert, F.; Bernache-Assollant, D. *Plutonium and americium monazite materials: Solid state synthesis and X-ray diffraction study.* J. Nucl. Mater., **2007**, *366*, 52.
118. Weigel, F.; Haug, H. *Zur Kenntnis des Curium(III)phosphats.* Radiochim. Acta, **1965**, *4(4)*, 227.
119. Holliday, K.S.; Babelot, C.; Walther, C.; Neumeier, S.; Bosbach, D.; Stumpf, T. *Site-selective time resolved laser fluorescence spectroscopy of Eu and Cm doped $LaPO_4$.* Radiochim. Acta, **2012**, *100*, 189.

120. Hobart, D.E.; Begun, G. M.; Haire, R. G.; Hellwegel, H. E. *Raman spectra of the trans-plutonium orthophosphates and trimetaphosphates.* J. Raman Spectrosc., **1983**, *14(1)*, 59.
121. Bamberger, C.E.; Haire, R.G.; Begun, G.M.; Hellwege, H.E. The synthesis and characterization of crystalline phosphates of thorium, uranium and neptunium. J. Less Common Met., **1984**, *102(2)*, 179.
122. Glorieux, B.; Jorion, F.; Montel, J. M.; Matecki, M.; Deschanels, X.; Coutures, J. P. *Investigation of plutonium-239 conditioning in monazite and brabantite matrices: Synthesis and characterization.* Proc. ATALANTE 2004, Nîmes (France), **2004**, *O32 – 04*, 1.
123. Begg, B.D.; Vance, E.R.; Conradson, S.D. *The incorporation of plutonium and neptunium in zirconolite and perovskite.* J. Alloys Compd., **1998**, *271-273*, 221.
124. Popa, K.; Raison, P. E.; Martel, L.; Martin, P. M.; Prieur, D.: Solari, P. L.; Bouëxière, D.; Konings, R. J. M.; Somers, J. *Structural investigations of* Pu^{III} *phosphate by X-ray diffraction, MAS-NMR and XANES spectroscopy.* J. Solid State Chem., **2015**, *230*, 169.
125. Jardin, R.; Pavel, C. C.; Raison, P. E.; Bouëxière, D.; Santa-Cruz, H.; Konings, R. J. M.; Popa, K. *The high-temperature behaviour of* $PuPO_4$ *monazite and some other related compounds*. J. Nucl. Mater., **2008**, *378*, 167.
126. Popa, K.; Colineau, E.; Wastin, F.; Konings, R. J. M. *The low-temperature heat capacity of* $(Pu_{0.1}La_{0.9})PO_4$. Solid State Commun., **2007**, *144*, 74.
127. Zhang, Y.; Vance, E. R. *Plutonium in monazite and brabantite: Diffuse reflectance spectroscopy study*. J. Nucl. Mater., **2008**, *375*, 311.
128. Deschanels, X.; Picot, V.; Glorieux, B.; Jorion, F.; Peuget, S.; Roudil, D.; Jégou, C.; Broudic, V.; Cachia, J. N.; Advocat, T.; Den Auwer, C.; Fillet, C.; Coutures, J. P.; Hennig, C.; Scheinost, A. *Plutonium incorporation in phosphate and titanate ceramics for minor actinide containment.* J. Nucl. Mater., **2006**, *352(1 – 3)*, 233.
129. Schulz, W.W. *The chemistry of americium*. ERDA Critical Review Series, TID-26971; Technical Information Center, Energy Research and Development Administration, Oak Ridge, Tennessee **1976**.
130. Dinnebier, R.E. *Rietveld refinement from powder diffraction data.* Comission on powder diffraction, International Union of chrystallography, Newsletter, **2001**, 26.
131. Mohhanan, K.; Sharma, S.K. *A Raman spectral study of forsterite-monticellite solid solutions.* Am. Mineral., **1993**, *78*, 42.
132. Gouadec, G.; Colomban, P. *Raman spectroscopy of nanostructures and nanosized materials.* J. Raman Spectrosc., **2007**, *38(6)*, 598.
133. Ruschel, K.; Nasdala, L.; Kronz, A.; Hanchar, J.M.; Többens, D.M.; Škoda, R.; Finger, F.; Möller, A. *A Raman spectroscopic study on the structural disorder of monazite–(Ce).* Miner. Petrol., **2012**, *105*, 41.
134. Holliday, K.; Finkeldei, S.; Neumeier, S.; Walther, C.; Bosbach, D.; Stumpf, T. *TRLFS of* Eu^{3+} *and* Cm^{3+} *doped* $La_2Zr_2O_7$*: A comparison of defect fluorite to pyrochlore structures.* J. Nucl. Mater., **2013**, *433(1-3)*, 479.
135. Huittinen, N., Scheinost, A. C., Wilden, A., Arinicheva Y. Cm^{3+} *incorporation in* $La_{1-x}Gd_xPO_4$ *monazites: a TRLFS and XAFS study*. Ninth international conference on nuclear and radiochemistry– NRC9 Helsinki, Finland, **2016**.
136. Huittinen, N.; Arinicheva, Y.; Kowalski, P.M.; Vinograd, V.L.; Neumeier, S.; Bosbach, D. *Probing structural homogeneity of* $La_{1-x}Gd_xPO_4$ *monazite-type solid solutions by combined spectroscopic and computational studies*. J. Nucl. Mater., **2017**, *486*, 148.

137. Bosbach, D.; Luckscheiter, B.; Brendebach, B.; Denecke, M.A.; Finck, N. *High level nuclear waste glass corrosion in synthetic clay pore solution and retention of actinides in secondary phases.* J. Nucl. Mater., **2009**, *385(2)*, 456.
138. Fernandes, M.M.; Stumpf, T.; Rabung, T.; Bosbach, D.; Fanghänel, T. *Incorporation of trivalent actinides into calcite: A time resolved laser fluorescence spectroscopy (TRLFS) study.* Geochim. Cosmochim. Acta, **2008**, *72(2)*, 464.
139. Skerencak, A.; Panak, P.J.; Hauser, W.; Neck, V.; Klenze, R.; Lindqvist-Reis, P.; Fanghänel, T. *Hydration of* Cm^{3+} *in aqueous solution from 20 to 200 °C. A time-resolved laser fluorescence spectroscopy study.* Radiochim. Acta, **2009**, *97*, 385.
140. Stumpf, T.; Bauer, A.; Coppin, F.; Fanghänel, T.; Kim, J.I. *Inner-sphere, outer-sphere and ternary surface complexes: a TRLFS study of the sorption process of Eu(III) onto smectite and kaolinite.* Radiochim. Acta, **2002**, *90*, 345.
141. Tits, J.; Stumpf, T.; Rabung, T.; Wieland, E.; Fanghänel, T. *Uptake of Cm(III) and Eu(III) by calcium silicate hydrates: a solution chemistry and time-resolved laser fluorescence spectroscopy study.* Environ. Sci. Technol., **2003**, *37*, 3568.
142. Fernandes, M.M.; Schmidt, M.; Stumpf, T.; Walther, C.; Bosbach, D.; Klenze, R.; Fanghanel, T. Site-selective time-resolved laser fluorescence spectroscopy of Eu^{3+} in calcite. J. Colloid Interface Sci., **2008**, *321(2)*, 323.
143. Huittinen, N.; Rabung, T.; Schnurr, A.; Hakanen, M.; Lehto, J.; Geckeis, H. *New insight into Cm(III) interaction with kaolinite – Influence of mineral dissolution.* Geochim. Cosmochim. Acta, **2012**, *99*, 100.
144. Bünzli, J.-C.G. *Luminescent probes. in Lanthanide probes in life, chemical and earth sciences,* Elsevier, Amsterdam **1989**.
145. Binnemans, K. *Interpretation of europium(III) spectra.* Coord. Chem. Rev., **2015**, *295*, 1.
146. Edelstein, N.; Klenze, R.; Fanghanel, T.; Hubert, S. *Optical properties of Cm(III) in crystals and solutions and their application to Cm(III) speciation.* Coord. Chem. Rev., **2006**, *250(7-8)*, 948.
147. Horrocks, W.D.; Sudnick, D.R. *Lanthanide ion probes of structure in biology. Laser induced luminescence decay constants provide a direct measure of the number of metal-coordinated water molecules.* J. Am. Chem. Soc., **1979**, *101(2),* 334.
148. Kimura, T.; Choppin, G.R. *Luminescence study on determination of the hydration number of Cm(III).* J. Alloys Compd., **1994**, *213/214*, 313.
149. Gaur, A.; Shrivastava, B.D.; Nigam, H.L. *X-Ray Absorption Fine Structure (XAFS) spectroscopy – A review.* Proc. Indian Natn. Sci. Acad., **2013**, *79 (4 B)*, 921.
150. Newville, M. *Fundamentals of XAFS.* Consortium for Advanced Radiation Sources University of Chicago, Chicago, IL, **2004**.
151. *NIST-JANAF Thermochemical Tables.* American Inst. of Physics **1998**.
152. Robie, R.A.; Hemingway, B.S.; Fisher, J.R. *Thermodynamic properties of minerals and related substances at 298.15 K and 1 bar (105 Pa) pressure and at higher temperatures*. Geol. Surv. Bull. 1452, U.S. Geological Survey, U.S. Government Printing Office, Washington, DC, **1978**.
153. Yungman, V.S. *Thermal constants of substances.* Begell House, **1999.**
154. Navrotsky, A.; Green, D.J. *Progress and new directions in calorimetry: A 2014 perspective*. J. Am. Ceram. Soc., **2014**, 97(11), 3349.
155. Navrotsky, A. *Mineralogy, materials science, energy, and environment: A 2015 perspective.* Am. Mineral., **2015**, *100(4)*, 674.

156. Navrotsky, A. *Progress and new directions in high temperature calorimetry revisited.* Phys. Chem. Minerals., **1997**, *24*, 222.
157. Navrotsky, A. *High-temperature oxide melt calorimetry of oxides and nitrides.* J. Chem. Thermodyn., **2001**, *33(8)*, 859.
158. Ushakov, S.V.; Navrotsky, A.; Green, D.J. *Experimental approaches to the thermodynamics of ceramics above 1500°C.* J. Am. Ceram. Soc., **2012**, *95(5),* 1463.
159. Sarge, S.M.; Höhne, G.W.H.; Hemminger, W.F. *Calorimetry: fundamentals, instrumentation and applications.* Wiley-VCH Verlag GmbH & Co KGaA, Weinheim **2014**.
160. Levchenko, A.; Marchin, L.; Parlouer, P.L.; Navrotsky, A. *The new high-temperature Setaram AlexSYS calorimeter and thermochemistry of alpha-$CuMnO_4$.* ITAS Bull., **2009**, 2, 91.
161. Popa, K.; Sedmidubský, D.; Beneš, O.; Thiriet, C.; Konings, R.J.M. *The high-temperature heat capacity of $LnPO_4$ (Ln=La, Ce, Gd) by drop calorimetry*. J. Chem. Thermodyn., **2006**, *38(7)*, 825.
162. Popa, K.; Jutier, F.; Wastin, F.; Konings, R.J.M. *The heat capacity of $NdPO_4$.* J. Chem. Thermodyn., **2006**, *38(11)*, 1306.
163. Navrotsky, A.; Lee, W.; Mielewczyk-Gryn, A.; Ushakov, S.V.; Anderko, A.; Wu, H.; Riman, R.E. *Thermodynamics of solid phases containing rare earth oxides.* J. Chem. Thermodyn., **2015**, *88*, 126.
164. Gavrichev, K.S.; Gurevich, V.M.; Ryumin, M.A.; Tyurin, A.V.; Komissarova, L.N. *Heat capacity and thermodynamic functions of $SmPO_4$ at 10 –1600 K.* Geochem. Int., **2015**, *53(7)*, 607.
165. Gavrichev, K.S.; Gurevich, V.M.; Ryumin, M.A.; Tyrin, A.V.; Komissarova, L.N. *Low-temperature heat capacity and thermodynamic properties of $PrPO_4$.* Geochem. Int., **2016**, *54(4)*, 362.
166. Blanca Romero, A.; Kowalski, P.M.; Beridze, G.; Schlenz, H.; Bosbach, D. *Performance of DFT+U method for prediction of structural and thermodynamic parameters of monazite-type ceramics.* J. Comput. Chem., **2014**, *35(18)*, 1339.
167. Ushakov, S.; Navrotsky, A.; Farmer, J.M.; Boatner, L.A. *Thermochemistry of the alkali rare-earth double phosphates, $A_3RE(PO_4)_2$.* J. Mater. Res., **2004**, *19(07)*, 2165.
168. Beridze, G.; Birnie, A.; Koniski, S.; Ji, Y.; Kowalski, P.M. *DFT + U as a reliable method for efficient ab initio calculations of nuclear materials.* Prog. Nucl. Energy, **2016**, *92*, 142.
169. Hirsch, A.; Kegler, P.; Alencar, I.; Ruiz-Fuertes, J.; Shelyug, A.; Peters, L.; Schreinemachers, C.; Neumann, A.; Neumeier, S.; Liermann, H.P.; Navrotsky, A.; Roth, G. *Structural, vibrational, and thermochemical properties of the monazite-type solid solution $La_{1–x}Pr_xPO_4$.* J. Solid State Chem., **2017**, *245*, 82.
170. Mogilevsky, P. *On the miscibility gap in monazite–xenotime systems.* Phys. Chem. Miner., **2007**, *34(3)*, 201.
171. Li, Y.; Kowalski, P.M.; Blanca-Romero, A.; Vinograd, V.; Bosbach, D. *Ab initio calculation of excess properties of $La_{1-x}(Ln,An)_xPO_4$ solid solutions*. J. Solid State Chem., **2014**, *220*, 137.
172. Kowalski, P.M.; Li, Y. *Relationship between the thermodynamic excess properties of mixing and the elastic moduli in the monazite-type ceramics.* J. Eur. Ceram. Soc., **2016**, *36(8)*, 2093.

173. Thiriet, C.; Konings, R.J.M.; Wastin, F. *Low temperature heat capacity of $PuPO_4$.* J. Nucl. Mater., **2005**, *344(1-3),* 56.
174. Beneš, O.; Popa, K.; Reuscher, V.; Zappia, A.; Staicu, D.; Konings, R.J.M. *High temperature heat capacity of $PuPO_4$ monazite-analogue.* J. Nucl. Mater., 2011, *418(1-3),* 182.
175. Popa, K.; Shvareva, T.; Mazeina, L.; Colineau, E.; Wastin, F.; Konings, R.J.M.; Navrotsky, A. *Thermodynamic properties of $CaTh(PO_4)_2$ synthetic cheralite.* Am. Mineral., **2008**, *93(8-9)*, 1356.
176. Rawat, D.; Phapale, S.; Mishra, R.; Dash, S. *Thermodynamic studies on charge-coupled substituted synthetic monazite.* J. Nucl. Mater., **2017**, *487*, 406.
177. Trocellier, P. *Immobilization of radionuclides in single-phase crystalline waste forms: a review on their intristic properties and long term behavior*. Ann. Chim. Sci. Mater., **2000**, *25*, 321.
178. Morgan, P.E.D.M., D. B. *Ceramic composites of monazite and alumina.* J. Am. Ceram. Soc., **1995**, *70 (161)*, 1553.
179. Hikichi, Y.; Ota, T.; Hattori, T. *Thermal, mechanical and chemical properties of sintered monazite-(La, Ce, Nd or Sm).* Mineral. J., **1997**, *19(3)*, 123.
180. Du, A.; Wan, C.; Qu, Z.; Pan, W. *Thermal conductivity of monazite-type $REPO_4$ (RE=La, Ce, Nd, Sm, Eu, Gd).* J. Am. Ceram. Soc., **2009**, *92(11)*, 2687.
181. Lasaga, A.C.S., J. M.; Gapjor, J.; Burch, T. E.; L. Nagy, K. L. *Chemical weathering rate laws and global geochemical cycles.* Geochim. Cosmochim. Acta, **1994**, *58(10)*, 2361.
182. *USDOE MCC-1 static test: nuclear waste materials handbook.* US-report-No. DOE/TIC 11400, material Characterization centre: Hanford **1984**.
183. Pierce, E.M.; McGrail, B.P.; Martin, P.F.; Marra, J.; Arey, B.W.; Geiszler, K.N. *Accelerated weathering of high-level and plutonium-bearing lanthanide borosilicate waste glasses under hydraulically unsaturated conditions*. Appl. Geochem., **2007**, *22*, 1841.
184. Sales, B.C.; White, C.W.; Boatner, L.A. *A comparison of the corrosion characteristics of synthetic monazite and borosilicate glass containing simulated nuclear defense waste*. Nucl. Chem. Waste Man., **1983**, *4*, 281.
185. Ishida, M.; Kikuchi, K.; Yanagi, T.; Terai, R. *Leaching behavior of crystalline phosphate waste forms*. Nucl. Chem. Waste Man., **1986**, *12*, 127.
186. Langmuir, D. *Aqueous environmental geochemistry.* Prentice Hall, **1997**, 1.
187. Teng, Y.; Wang, X.; Huang, Y.; Wu, L.; Zeng, P. *Hot-pressure sintering, microstructure and chemical durability of $Ce_{0.5}Eu_{0.5}PO_4$ monazite ceramics*. Ceram. Int., **2015**, *41(8)*, 10057.
188. Boatner, L.; Abraham, M.; Rappaz, M. *Analogs of monazite for the storage of radioactive wastes.* Trans. Am. Nucl. Soc., **1980**, *35*, 186.
189. Neumeier, S.; Arinicheva, Y.; Heuser, J.M.; Kowalski, P.M.; Kegler, P.; Schlenz, H.; Bosbach, D.; Deissmann, G. *New insights into phosphate based materials for the immobilisation of actinides.* Radiochim. Acta, **2017**, 105(11), 961.
190. Arinicheva, Y.N., S.; Brandt, F.; Bosbach, D.; Deissmann, G. *Dissolution kinetics of synthetic $LaPO_4$-monazite in acidic media.* MRS Adv., **2018**, *3(21),*1133.
191. Roncal-Herrero, T.; Rodríguez-Blanco, J.D.; Oelkers, E.H.; Benning, L.G. *The direct precipitation of rhabdophane ($REEPO_4{\cdot}nH_2O$) nano-rods from acidic aqueous solutions at 5–100 °C.* J. Nanopart. Res., **2011**, *13(9)*, 4049.

192. Babelot, C.; Bukaemskiy, A.; Neumeier, S.; Modolo, G.; Bosbach, D. *Crystallization processes, compressibility, sinterability and mechanical properties of La-monazite-type ceramics.* J. Eur. Ceram. Soc., **2017**, *37(4),* 1681.
193. Cherniak, D.J.; Pyle, J.; Rakovan, J. *Synthesis of REE and Y phosphates by Pb-free flux methods and their utilization as standards for electron microprobe analysis and in design of monazite chemical U-Th-Pb dating protocol.* Am. Mineral., **2004**, *89*, 1533.
194. Amelinckx, S.; van Dyck, D.; van Landuyt, J.; van Tendeloo, G. *Handbook of Microscopy, Applications in Materials Science. Solid-State Physics and Chemistry in Applications*, **1997**, VCH Verlagsgesellschaft mbH, Weinheim.
195. Wiss, T.; Thiele, H.; Janssen, A.; Papaioannou, D.; Rondinella, V. V.; Konings, R. J. M. *Recent results of microstructural characterization of irradiated light water reactor fuels using scanning and transmission electron microscopy*. JOM, **2013**, *64(12),* 1390.
196. Rasband, W.S. *ImageJ.* U. S. National Institutes of Health, Bethesda, Maryland, USA, http://imagej.nih.gov/ij/, **2016**.
197. Podor, R.; Clavier, N.; Ravaux, J.; Claparede, L.; Dacheux, N.; Wakai, F. *In situ HT-ESEM observation of* CeO_2 *grain growth during sintering.* J. Am. Ceram. Soc. **2012**, *95(11)*, 3683.
198. Podor, R.; Pailhon, D.; Ravaux, J.; Brau, H.P. *Development of an integrated thermocouple for the accurate sample temperature measurement during high temperature environmental scanning electron microscopy (HT-ESEM) experiments.* Microsc. Microanal., **2015**, *21(2),* 307.
199. Webb, S.M. *SIXpack: a graphical user interface for XAS analysis using IFEFFIT*. Phys. Scr., **2005**, *T115*, 1011.
200. Zunger, A.; Wei, S.; Ferreira, L.G.; Bernard, J.E. *Special quasirandom structures*. Phys. Rev. Lett., **1990**, *65(3),* 353.
201. Giannozzi, P.; Baroni, S.; Bonini, N.; Calandra, M.; Car, R.; Cavazzoni, C.; Ceresoli, D.; Chiarotti, G.L.; Cococcioni, M.; Dabo, I.; Dal Corso, A.; Fabris, S.; Fratesi, G.; de Gironcoli, S.; Gebauer, R.; Gerstmann, U.; Gougoussis, C.; Kokalj, A.; Lazzeri, M.; Martin-Samos, L.; Marzari, N.; Mauri, F.; Mazzarello, R.; Paolini, S.; Pasquarello, A.; Paulatto, F.; Sbraccia, C.; Scandolo, S.; Sclauzero, G.; Seitsonen, A.P.; Smogunov, A.; Umari, P.; Wentzcovitch, R.M. *QUANTUM ESPRESSO: a modular and open-source software project for quantum simulations of materials*. J. Phys. Condens. Matter **2009**, *21*, 395502.
202. Gale, J.D. *GULP: A computer program for the symmetry-adapted simulation of solids.* J. Chem. Soc., Faraday Trans., **1997**, *93(4)*, 629.
203. Girard, S.; Gale, J.D.; Mellot-Draznieks, C.; Fe´rey, G. *Derivation of interatomic potentials for gallophosphates from the* $GaPO_4$*-quartz structure: transferability study to gallosilicates and zeotype gallophosphates.* Chem. Mater., **2001**, *13*, 1732.
204. Ji, Y.; Kowalski, P.M.; Neumeier, S.; Deissmann, G.; Kulriya, P.K.; Gale, J.D. *Atomistic modeling and experimental studies of radiation damage in monazite-type* $LaPO_4$ *ceramics.* Nuclear Instruments and Methods in Physics Research Section B: Beam Interactions with Materials and Atoms, **2017**, *393*, 54.
205. Kowalski, P.M.; Ji, Y.; Li, Y.; Arinicheva, Y.; Beridze, G.; Neumeier, S.; Bukaemskiy, A.; Bosbach, D. *Simulation of ceramic materials for nuclear waste management: case of* $La_{1-x}Eu_xPO_4$ *solid solution.* Nucl. Instrum. Meth., **2017**, *B(393)*, 68.

206. Ditmars, D.A.; Ishihara, S.; Chang, S.S.; Bernstein, G.; West, E.D. *Enthalpy and heat-capacity standard reference material: synthetic sapphire (aAl2O3) from 10 to 2250 K.* J. Res. Nat. Bur. Stand., **1982**, *87*, 59.
207. Lashley, J.C.; Hundley, M.F.; Migliori, A.; Sarrao, J.L.; Pagliuso, P.G.; Darling, T.W.; Jaime, M.; Cooley, J.C.; Hults, W.L.; Morales, L.; Thoma, D.J.; Smith, J.L.; Boerio-Goates, J.; Woodfield, B.F.; Stewart, G.R.; Fisher, R.A.; Phillips, N.E. *Critical examination of heat capacity measurements made on a quantum design physical property measurement system.* Cryogenics, **2003**, *43*, 369.
208. Navrotsky, A. *Progress and new directions in high temperature calorimetry.* Phys. Chem. Minerals., **1977**, *2*, 89.
209. Navrotsky, A.; Kleppa, O.J. *A calorimetric study of molten Na_2MoO_4-MoO_3 mixtures at 970°K.* Inorg. Chem., **1967**, *6(11)*, 2119.
210. Arbeck, D.; Haussühl, E.; Bayarjagal, L.; Winkler, B.; Paulsen, N.; Haussühl, S.; Milman, V. *Piezoelastic properties of retgersite determined by ultrasonic measurements*. Eur. Phys. J. B, **2009**, *73(2)*, 167.
211. Yadawa, P.K.; Singh, D.; Pandey, D.K.; Yadav, R.R. *Elastic and acoustic properties of heavy rare-earth metals.* The Open Acoustics Journal, **2009**, *2*, 61.
212. Levy, M.; Bass, H.E.; Stern, R.R.; Furr, L.; Keppens, V. *Handbook of elastic properties of solids, liquids, and gases: elastic properties of solids: biological and organic materials.* Earth and Marine Sciences, Academic Press, Oxford, **2001**, III.
213. Thust, A.; Arinicheva, Y.; Haussühl, E.; Ruiz-Fuertes, J.; Bayarjargal, L.; Vogel, S.C.; Neumeier, S.; Winkler, B.; Vance, L. *Physical properties of $La_{1-x}Eu_xPO_4$, $0 \leq x \leq 1$, monazite-type ceramics.* J. Am. Ceram. Soc., **2015**, *98(12)*, 4016.
214. Dacheux, N., de Kerdaniel, E.D.F., Clavier, N., Podor, R., Aupiais, J., Szenknect, S. *Kinetics of dissolution of thorium and uranium doped britholite ceramics.* J. Nucl. Mater., **2010**, *404*, 33.
215. Neeway, J.; Abdelouas, A.; Grambow, B.; Schumacher, S. *Dissolution mechanism of the SON_{68} reference nuclear waste glass: New data in dynamic system in silica saturation conditions.* J. Nucl. Mater., **2011**, *415(1)*, 31.
216. Finkeldei, S.; Brandt, F.; Rozov, K.; Bukaemskiy, A.A.; Neumeier, S.; Bosbach, D. *Dissolution of ZrO_2 based pyrochlores in the acid pH range: A macroscopic and electron microscopy study.* Appl. Geochem., **2014**, *49*, 31.
217. Kulik, D.A.; Wagner, T.; Dmytrieva, S.V.; Kosakowski, G.; Hingerl, F.F.; Chudnenko, K.V.; Berner, U.R. *GEM-Selektor geochemical modeling package: revised algorithm and GEMS3K numerical kernel for coupled simulation codes*. Comput. Geosci., **2012**.
218. Johnson, J.W.; Oelkers, E.H.; Helgeson, H.C. *SUPCRT92: A software package for calculating the standard molal thermodynamic properties of minerals, gases, aqueous species, and reactions from 1 to 5000 bar and 0 to 1000°C.* Comput. Geosci., **1992**, *18(7).*
219. Thoenen, T.; Hummel, W.; Berner, U.; Curti, E. *The PSI / Nagra Chemical Thermodynamic Database 12 / 07, (14).* PSI Bericht Nr. 14-04, **2014**.
220. Tardy, Y.; Vieillard, P. *Relationships among Gibbs free energies and enthalpies of formation of phosphates, oxides and aqueous ions.* Contrib. Mineral. Petrol., **1977**, *63*, 75.
221. Feick, G.; Hainer, R.M. *On the thermal decomposition of ammonium nitrate. Steady-state reaction temperatures and reaction rate.* J. Am. Chem. Soc., **1954**, *76(22)*, 5860.

222. Silva, E.N.; Ayala, A.P.; Guedes, I.; Paschoal, C.W.A.; Moreira, R.L.; Loong, C.K.; Boatner, L.A. *Vibrational spectra of monazite-type rare-earth orthophosphates*. Opt. Mater., **2006**, *29(2-3)*, 224.
223. Dacheux, N.; Brandel, V.; Genet, M. *Synthesis and Characterization of mixed-valence uranium orthophosphate − $U(UO_2)(PO_4)_2$*. New J. Chem., **1995**, *19*, 15.
224. https://youtu.be/grbbeHT1vlo.
225. https://youtu.be/ucUEgP0TTvg.
226. Dutta, S.K.; Spriggs, R.M. *Grain growth in fully dense ZnO*. J. Am. Ceram. Soc., **1970**, *53(1)*, 61.
227. Bernache-Assollant, D. *Chimie-physique du frittage*. Hermes Eds, Paris **1993**.
228. Mullins, W.W.; Vinals, J. *Scaling in linear bubble models of grain growth.* Acta metall. mater., **1993**, *41(5)*, 1359.
229. Maître, A.; Beyssen, D.; Podor, R. *Modelling of the grain growth and the densification of SnO_2-based ceramics.* Ceram. Int., **2008**, *34(1)*, 27.
230. Srolovitz, D.J.A., M. P.; Grest,G. S.; Sahni, P. S. *Computer simulation of grain growth - III. Influence of particle dispersion.* Acta Metall. Mater., **1984**, *32*, 1429.
231. Te´tard, F.B.-A., D.; Champion, E.; Lortholary, P. *Grain growth kinetics of Li_3PO_4-doped calcium carbonate.* Solid State Ionics, **1997**, *101-103*, 517.
232. Podor, R.; Clavier, N.; Ravaux, J.; Claparede, L.; Dacheux, N.; Bernache-Assollant, D. *Dynamic aspects of cerium dioxide sintering: HT-ESEM study of grain growth and pore elimination.* J. Eur. Ceram. Soc., **2012**, *32(2)*, 353.
233. Zhu, H.; Averback, R.S. *Sintering of nano-particle powders: simulations and experiments.* Mater. Maufacturing Process., **1996**, *11*, 905.
234. Lee, E.J.H.; Ribeiro, C.; Longo, E.; Leite, E.R. *Growth kinetics of tin oxide nanocrystals in colloidal suspensions under hydrothermal conditions*. Chem. Phys. Chem., **2005**, *6*, 690.
235. Nkou Bouala, G.I.; Clavier, N.; Léchelle, J.; Mesbah, A.; Dacheux, N.; Podor, R. *In situ HT-ESEM study of CeO_2 nano-ripening: toward a control of nanostructure*. Ceram. Intern., **2015**, *41*, 14703.
236. Fang, Z.Z.; Wang, H.; Kumar, V. *Coarsening, densification, and grain growth during sintering of nano-sized powders—A perspective*. Intern. J. Refract. Met. & Hard Mater., **2017**, *62*, 110.
237. Chaim, R.; Levin, M.; Shlayer, A.; Estournes, C. *Sintering and Densification of Nanocrystalline Ceramic Oxide Powders: A Review.* Adv. Appl. Ceram., **2008**, *107*, 159.
238. Xing, P.; Zhuang, Y.; Tu, G.; Guo, J. *High temperature dephosphorization behavior of monazite concentrate with charred coal.* Trans. Nonferrous Met. Soc. China, **2010**, *20(12)*, 2392.
239. Frondel, C. *Systematic mineralogy of uranium and thorium.* Geological survey bulletin 1064 United States government printing office, Washington, **1958**.
240. Pan, Y.; Fleet, M.E.; Macrae, N.D. *Oriented monazite inclusions in apatite porphyroblasts from the Hemlo gold deposit*, Ontario, Canada. Mineral Mag., **1993**, *57*, 697.
241. Gavrichev, K.S.; Ryumin, M.A.; Tyurin, A.V.; Gurevich, V.M.; Komissarova, L.N. *Refined heat capacity of $LaPO_4$ in the temperature range 0–1600K*. Thermochim. Acta., **2008**, *474(1-2)*, 47.
242. Wallez, G.; Raison, P.E.; Dacheux, N.; Clavier, N.; Bykov, D.; Delevoye, L.; Popa, K.; Bregiroux, D.; Fitch, A.N.; Konings, R.J. *Triclinic-cubic phase transition and negative*

expansion in the actinide IV (Th, U, Np, Pu) diphosphates. Inorg. Chem., **2012**, *51(7)*, 4314.

243. Downs, R.T.; Hall-Wallace, M. *The American Mineralogist crystal structure database*. Am. Mineral., **2003**, *88(1)*, 247.
244. Elliott, R.J.; Harley, R.T.; Hayes, W.; Smith, S.R.P. *Raman scattering and theoretical studies of Jahn-Teller induced phase transitions in some Rrare-earth compounds*. Proc. Royal Soc. A, **1972**, *328(1573)*, 217.
245. Raison, P.E.; Jardin, R.; Bouëxière, D.; Konings, R.J.M.; Geisler, T.; Pavel, C.C.; Rebizant, J.; Popa, K. *Structural investigation of the synthetic* $CaAn(PO_4)_2$ *(An = Th and Np) cheralite-like phosphates.* Phys. Chem. Miner., **2008**, *35(10)*, 603.
246. Gausse, C.; Szenknect, S.; Qin, D.W.; Mesbah, A.; Clavier, N.; Neumeier, S.; Bosbach, D.; Dacheux, N. *Determination of the solubility of rhabdophanes* $LnPO_4$*•0.667*H_2O *(Ln = La to Dy).* Eur. J. Inorg. Chem., 2016, 4615.
247. Shannon, R.D. Revised effective ionic radii and systematic studies of interatomie distances in halides and chaleogenides. Acta Cryst., **1976**, *A32*, 751.
248. Geisler, T.; Popa, K.; Konings, R.J.M. *Evidence for lattice strain and non-ideal behavior in the* $(La_{1-x}Eu_x)PO_4$ *solid solution from X-ray Diffraction and vibrational spectroscopy*. Front. Earth Sci., **2016**, 4, 1.
249. David, F. Thermodynamic properties of lanthanide and actinide ions in aqueous solution. J. Less-Common Met., **1986**, *121*, 27
250. Ochiai, A.; Utsunomiya, S. *Crystal chemistry and stability of hydrated rare-earth phosphates formed at room temperature.* Minerals, **2017**, *7(5)*, 84.
251. Huittinen, N. *Sorption of trivalent actinides onto gibbsite, γ-alumina, and kaolinite - A spectroscopic study of An(III) interactions at the mineral-water interfaces*. Ph.D. Thesis, University of Helsinki, Finland, **2013**.
252. Holliday, K.; Handley-Sidhu, S.; Dardenne, K.; Renshaw, J.; Macaskie, L.; Walther, C.; Stumpf, T. *A new incorporation mechanism for trivalent actinides into bioapatite: a TRLFS and EXAFS study.* Langmuir, **2012**, *28(8)*, 3845.
253. Arinicheva Y.; Popa, K.; Scheinost, A. C.; Rossberg, A; Dieste-Blanco, O.; Raison, P; Cambriani, A.; Neumeier, S.; Somers, J.; Bosbach, D. *Structural investigations of (La,Pu)PO4 monazite solid solutions: XRD and XAFS study.* J. Nucl. Mater., **2017**, *493*, 404.
254. Bregiroux, D.; Audubert, F.; Charpentier, T.; Sakellariou, D.; Bernache-Assollant, D. *Solid-state synthesis of monazite-type compounds* $LnPO_4$ *(Ln = La to Gd).* Solid State Sci., **2007**, *9*, 432.
255. Hikichi, Y.; Nomura, T. *Melting temperatures of monazite and xenotime*. J. Am. Ceram. Soc., **1987**, *70(10)*, 252.
256. Rossberg, A.R., T.; Bernhard, G. *Complexation of uranium(VI) with protocatechuic acid – application of iterative transformation factor analysis to EXAFS spectroscopy*. Anal. Bioanal. Chem., **2003**, *376(5)*, 631.
257. Prieur, D.C.-N., U.; Vitova, T.; Somers, J. *Local and Electronic Structure of Americium-Bearing* PuO_2*.* Eur. J. Inorg. Chem., **2013**, *9*, 1518.
258. Funke, H.S., A. C.; Chukalina, M. *Wavelet analysis of extended X-ray absorption fine structure data.* Phys. Rev. B, **2005**, *B71*, 094110.
259. Scavini, M.C., M.; Allieta, M.; Brune, M.; Ferrero, C. *Probing complex disorder in* $Ce_{1-x}Gd_xO_{2-x/2}$ *using the pair distribution function analysis.* Chem. Mat., **2012**, *24*, 1338

260. Martin, P.G., S.; Valot, C.; Carlot, G.; Ripert, M.; Blanc, P.; Hennig, C. *XAS study of $(U_{1-y}Pu_y)O_2$ solid solutions.* J. Alloys Compd., **2007**, *444*, 410.
261. Ellis, D.E.T., J.; Warschkow, O.; Jiang, M.; Gonzalez, G. B.; Okasinski, J. S.; Bedzyk, M. J.; Rossi, A. M.; Eon, J. G. *A theoretical and experimental study of lead substitution in calcium hydroxyapatite.* Phys. Chem. Chem. Phys., **2006**, *8*, 967.
262. Henderson, C.M.B.; Redfern, S. A. T.; Smith, R. I.; Knight, K. S.; Charnock, J. M. *Composition and temperature dependence of cation ordering in Ni-Mg olivine solid solutions: a time-of-flight neutron powder diffraction and EXAFS study*. Am. Mineral. , **2001**, *86*, 1170.
263. Scheinost, A.C. *Diffuse reflectance spectra of Al substituted goethite: A ligand field approach.* Clays Clay Miner., **1999**, *47*, 156.
264. Scheinost, A.C.; Stanjek, H.; Schulze, D. G.; Gasser, U.; Sparks, D. L. *Structural environment and oxidation state of Mn in goethite-groutite solid-solutions*. Am. Mineral., **2001**, *86*, 139.
265. Hazemann, J. L.; Manceau, A.; Sainctavit, P.; Malgrange, C. *Structure of the alpha-$Fe_xAl_{1-x}OOH$ solid solution. Evidence by polarized EXAFS for an epitaxial growth of hematite-like clusters in Fe-diaspore.* Phys. Chem. Miner., **1992**, *19*, 25.
266. Vantelon, D.; Montarges-Pelletier, E.; Michot, L. J.; Briois, V.; Pelletier, M.; Thomas, F. *Iron distribution in the octahedral sheet of dioctahedral smectites. An FeK-edge X-ray absorption spectroscopy study.* Phys. Chem. Miner., **2003**, *30*, 44.
267. Arinicheva, Y.; Lozano Rodriguez, M.J.; Neumeier, S.; Scheinost, A.C.; Clavier, N.; Bosbach, D. *Structural studies on $(La,Eu)PO_4$ solid solutions by infrared, Raman and X-ray absorption spectroscopy.* ATAS 2014 proceedings, **2014**.
268. Cheng, J.; Navrotsky, A. *Enthalpies of formation of $LaBO_3$ perovskites (B = Al, Ga, Sc, and In).* J. Mater. Res., **2011**, *18(10),* 2501.
269. Hildenrand, J.H. *Solubility. XII. Regular solutions.* J. Am. Chem. Soc., **1929**, *51*, 66.
270. Ganguly, J. *Thermodynamic modelling of solid solutions.* EMU Notes in Mineralogy, **2001**, *3(3)*, 37.
271. Glynn, P. *Solid-solution solubilities and thermodynamics: sulfates, carbonates and halides.* in: C.N. Alpers, J.L. Jambor, D.K. Nordstrom (Eds.), Sulfate Minerals: Crystallography, Geochemistry, and Environmental Significance, Mineral. Soc. Am., **2000**, 481.
272. Thiriet, C.; Konings, R.J.M.; Javorský, P.; Magnani, N.; Wastin, F. *The low temperature heat capacity of $LaPO_4$ and $GdPO_4$, the thermodynamic functions of the monazite-type $LnPO_4$ series*. J. Chem. Thermodyn., **2005**, *37(2)*, 131.
273. Kowalski, P.M.; Beridze, G.; Vinograd, V.L.; Bosbach, D. *Heat capacities of lanthanide and actinide monazite-type ceramics.* J. Nucl. Mater., **2015**, *464*, 147.
274. Shih, P.Y. *Properties and FTIR spectra of lead phosphate glasses for nuclear waste immobilization.* Mater. Chem. Phys., **2003**, *80(1)*, 299.
275. Day, D.E.; Wu, Z.; Ray, C.S.; Hrma, P. *Chemically durable iron phosphate glass wasteforms.* J. Non-Cryst. Solids, **1998**, *241*, 1.
276. Matzke, H.; Vernaz, E. *Thermal and physicochemical properties important for the long term behavior of nuclear waste glasses*. J. Nucl. Mater., **1993**, *201*, 295.
277. Campbell, J.; Hoenig, C.; Bazan, F.; Ryerson, F.; Guinan, M.; Van Konynenburg, R.; Rozsa, R. Properties of SYNROCK-D nuclear waste form: a state of the art review. Lawrence Livemore National Laboratory, **1982**.

278. Vassen, R.; Cao, X.; Tietz, F.; Basu, D.; Stoever, D. *Zirconates as new materials for thermal barrier coatings.* J. Am. Ceram. Soc., **2000**, *83(8)*, 2023.
279. Chung, H.-Y.; Weinberger, M.B.; Yang, J.-M.; Tolbert, S.H.; Kaner, R.B. *Correlation between hardness and elastic moduli of the ultraincompressible transition metal diborides* RuB_2, OsB_2, *and* ReB_2. Appl. Phys. Lett., 2008, 92(26), 261904.
280. Brandt, F.; Bosbach, D.; Krawczyk-Bärsch;; E., A., T.;; Bernhard, G. *Chlorite dissolution in the acid pH-range: a combined microscopic and macroscopic approach.* Geochim. Cosmochim. Acta, **2003**, *67*, 1451.
281. Horlait, D.; Tocino, F.; Clavier, N.; Dacheux, N.; Szenknect, S. *Multiparametric study of* $Th_{1-x}Ln_xO_{2-x/2}$ *mixed oxides dissolution in nitric acid media.* J. Nucl. Mater., **2012**, *429*, 237.
282. Chou, L.; Wollast, R. *Study of weathering of albite at room-temperature and pressure with a fluidized-bed reactor.* Geochim. Cosmochim. Acta, **1984**, *48*, 2205.
283. Knauss, K.G.; Thomas, J.W. *Muscovite dissolution kinetics as a function of pH and time at 70°C. Geochim.* Cosmochim. Acta, **1989**, *53*, 1493.
284. Wehrli, B. *Monte Carlo simulations of surface morphologies during mineral dissolution*. J. Colloid Interface Sci., **1989**, *132*, 230.
285. Casey, W.H.; Bunker, B. *Leaching of mineral and glass surfaces during dissolution*. Rev. Miner. Geochem., **1990**, *23*, 397.
286. Luettge, A.; Arvidson, R.S.; Fischer, C. *A stochastic treatment of crystal dissolution kinetics.* Elements, **2013**, *9*, 183.
287. Veilly, E. *Comparative behavior of britholites and monazite-brabantite solid solutions during dissolution tests: a combined experimental and DFT approach*. Inorg. Chem., **2008**, *47*, 10971.
288. Locker, L.D.; de Bruy, P.L. *The kinetics of dissolution of II-VI semiconductor compounds in monoxidizing acids.* J. Electrochem. Soc., **1969**, *116(12)*, 1658.
289. Lasaga, A.C. *Chemical kinetics of water-rock interactions*. J. Geophys. Res. Solid Earth., **1984**, *89(B6)*, 4009.
290. Lasaga, A.C. *Rate laws of chemical reactions*. Rev. Miner., **1981**, *8*, 1.
291. Deng, Y. *Effect of pH on the reductive dissolution rates of iron(III) hydroxide by ascorbate.* Langmuir, **1997**, *13(6)*, 1835.
292. Born, C.A.; Queneau, P.B.; Ronzio, R.A. *Processing of wolframite-cassiterite concentrate for brannerite removal.* Trans Soc. Min. Eng. , **1975**, AIME *258*, 218.
293. Gogoleva, E.M. *The leaching kinetics of brannerite ore in sulfate solutions with iron(III).* . J. Radioanal. Nucl. Chem., **2012**, *293*, 183.
294. Cetiner, Z.S.; Wood, S.A.; Gammons, C.H. *The aqueous geochemistry of the rare earth elements. Part XIV. The solubility of rare earth element phosphates from 23 to 150 °C.* . Chem. Geol., **2005**, *217*, 147.

Acknowledgements

Firstly, I would like to express my sincere gratitude to my doctoral supervisor Prof. Dirk Bosbach for the opportunity to pursue my doctoral research at Forschungszentrum Jülich (IEK-6) and for his continuous support of my scientific undertakings.

I am especially thankful to my scientific advisor Dr. Stefan Neumeier for discovering my professional potential and helping me to develop it by his inspiring leadership, extensive mentoring on a daily basis, patience, motivation, sharing immense knowledge and research ideas as well as by his personal support throughout the doctoral studies and advises for my subsequent career steps.

I want to thank Prof. Georg Roth for being the second reviewer of my PhD thesis, constructive discussion on this work and the opportunity to gain experience in single crystal growth at his institute.

I would like to acknowledge my IEK-6 colleagues, Prof. Giuseppe Modolo, Dr. Guido Deissmann, Dr. Piotr Kowalski and his group, Prof. Evgeny Alekseev and his group, Dr. Philip Kegler, Dr. Andrey Bukaemsky, Dr. Victor Vinograd, Dr. Martina Klinkenberg, Dr. Felix Brandt, PD Dr. Hartmut Schlenz and his group, Mr. Christian Schreinemachers, for sharing their scientific expertise, constant readiness to discuss and their friendly support in planning of experiments, evaluation of results and preparation of scientific publications, which formed the basis of this work. I own my gratitude to Dr. Stefan Neumeier, Dr. Guido Deissmann, Dr. Andrey Bukaemsky and Dr. Victor Vinograd also for proofreading this work and their valuable improvement suggestions. I thank Mr. Fabian Sadowski for ICP-MS measurements and Ms. Jacqueline Holthausen for samples preparation.

My sincere thanks also go my colleagues from the BMBF project for the extensive scientific exchange resulting in a number of publications, and namely, Dr. Nina Huittinen and Prof. Thorsten Stumpf (Institute of Resource Ecology, HZDR Dresden) for the opportuninty to learn the time resolved laser fluorescence spectroscopy method, Dr. Andreas C. Scheinost, Dr. André Rossberg and Dr. M. Janeth Lozano-Rodriguez (ESRF) for the introduction into EXAFS technique and Dr. Anja Thust and Prof. Björn Winkler for the collaboration on physical properties of monazites.

I would also like to thank Prof. Nicolas Dacheux and Dr. Nicolas Clavier, my external mentors within the HITEC program, as well as Dr. Renaud Podor, Dr. Adel Mesbah and their colleagues at the Interface of materials in Evolution Laboratory (LIME), ICSM Marcoule, France, who provided me an opportunity to join their team in the frame of the HITEC Go program. The research stay at ICSM Marcoule was a very fruitful collaboration, which allowed me to gain a broad experience in the field of ceramics processing and characterization.

I am very grateful to Dr. Karin Popa, Dr. Oliver Dieste Blanco, Dr. Philippe Raison, Dr. Andrea Cambriani and Dr. Joseph Somers (European Commission, Joint Research Centre, Karlsruhe, Germany) for the possibility to take part in the exciting research on Pu incorporation in the monazite ceramics in the frame of the TALISMAN and the ACTUSLAB programs. Without their scientific expertise and precious support as well the laboratory facilities of the JRC it would not be possible to conduct this research.

I would like to thank Prof. Alex Christian Hoffmann (University of Bergen, Norway) and Dr. Crina Silvia Ilea (Christian Michelsen Research (CMR), Norway) for their mentoring as well as for the possibility to finalise the results of my PhD work during my research stay at the University of Bergen in the frame of the exchange program supported by the E.ON Stipendienfonds.

I am deeply grateful to Prof. Wilhelm Keim, who encouraged the decisive turning point in my career and life as well as my further endeavors. I would like to thank Ms. Renate Keim and Prof. Wilhelm Keim for their private and professional advices, supporting me from my very first days in Germany. Prof. Wilhelm Keim will always be in my heart and memories.

Last but not least, I am especially thankful to my family for their continuous love and care, unconditional support, patience and encouragement, without which I would not have come this far. Special thanks to my mother, Anna, who has inspired me through her own example to pursue a career in chemistry. Finally, I would like to thank my husband, Kim, and my family-in-law for beeing extremely supportive and patient throughout this entire challenging journey.

This work was supported by the German Federal Ministry of Education and Research (BMBF; grant-no: 02NUK021A and 02NUK021B), the HITEC – the Graduate School in Energy and Climate Research at the Forschungszentrum Jülich, the E.ON Stipendienfonds, the European FP7

TALISMAN project (JRP-No.: TALI-C06-11) under contract with the European Commission, and the JRC-ITU Actinide User Laboratory (grant-no: AUL-2016-18-195).

Band / Volume 446
Aging and Degradation Behavior of Electrode Materials in Solid Oxide Fuel Cells (SOFCs)
X. Yin (2018), x, 103 pp
ISBN: 978-3-95806-374-7

Band / Volume 447
TRENDS 2017
Transition to Renewable Energy Devices and Systems
D. Stolten, R. Peters (Eds.) (2018), 206 pp
ISBN: 978-3-95806-376-1

Band / Volume 448
3D simulation of impurity transport in a fusion edge plasma using a massively parallel Monte-Carlo code
J. Romazanov (2018), xvi, 149 pp
ISBN: 978-3-95806-377-8

Band / Volume 449
Projektbericht Adelheid – aus dem Labor heraus in die Lüfte
R. Peters, J. Pasel, R. C. Samsun, A. Tschauder, C. Wiethege, F. Scharf, D. Stolten (2018), xxi, 321 pp
ISBN: 978-3-95806-378-5

Band / Volume 450
Microstructure and Thermomechanical Properties of $SrTi_{1-x}Fe_xO_{3-\delta}$ Oxygen Transport Membranes and Supports
R. Oliveira Silva (2019), vi, 148 pp
ISBN: 978-3-95806-381-5

Band / Volume 451
Sodium Ion Conducting Ceramics for Sodium Ion Batteries
S. Naqash (2019), vii, 134 pp
ISBN: 978-3-95806-382-2

Band / Volume 452
Quantitative Analyse der Trocknungsverläufe von Katalysatordispersionen
F. Scheepers (2019), VIII, 191 pp
ISBN: 978-3-95806-384-6

Band / Volume 453
Neue Optionen für einen wirtschaftlichen Betrieb von Wasserstoffzügen durch Nutzung der LOHC-Technologie?
P. Wasserscheid, T. Grube, D. Sternfeld, M. Essl, M. Robinius, D. Stolten (2019), II, 88 pp
ISBN: 978-3-95806-386-0

Band / Volume 454
Reformierung von BtL-Kraftstoffen für die HT-PEFC in luftfahrttechnischen Systemen
C. Wilbrand (2019), IV, 312 pp
ISBN: 978-3-95806-387-7

Band / Volume 455
Entwicklung von thermischen Spritzprozessen für fortschrittliche Schutz- und Funktionsschichten
G. Mauer (2019), vi, 57 pp
ISBN: 978-3-95806-388-4

Band / Volume 456
Columnar Structured Thermal Barrier Coatings Deposited by Axial Suspension Plasma Spraying
D. Zhou (2019), VI, 126 pp
ISBN: 978-3-95806-391-4

Band / Volume 457
Modellierung zeitlich aufgelöster Ladeenergienachfragen von batterie-elektrischen Fahrzeugen und deren Abbildung in einem Energiesystemmodell
J. F. Linßen (2019), VIII, 189 pp
ISBN: 978-3-95806-395-2

Band / Volume 458
Synthesis and Analysis of Spinel Cathode Materials for High Voltage Solid-State Lithium Batteries
A. Windmüller (2019), iv, 142 pp
ISBN: 978-3-95806-396-9

Band / Volume 459
Monazite-type ceramics as nuclear waste form: crystal structure, microstructure and properties
Y. Arinicheva (2019), 194 pp
ISBN: 978-3-95806-397-6

Weitere ***Schriften des Verlags im Forschungszentrum Jülich*** unter
http://wwwzb1.fz-juelich.de/verlagextern1/index.asp

Energie & Umwelt / Energy & Environment
Band / Volume 459
ISBN 978-3-95806-397-6

Mitglied der Helmholtz-Gemeinschaft

JÜLICH
Forschungszentrum